Identification of synthetic lethal interactions with the KRAS oncogene for targeted cancer treatment

Kimberly Jane Morgan
ORCID: 0000-0001-7871-2583

Doctor of Philosophy
March 2021

The Walter and Eliza Hall Institute of Medical Research
Department of Medical Biology
Faculty of Medicine, Health and Dentistry
The University of Melbourne

Submitted in total fulfilment of the degree of Doctor of Philosophy

Abstract

Cancer is a major public health issue globally, ranking as the second most common cause of death. Molecularly targeted therapies, focused on exploiting tumour cell dependency on certain oncogenic driver mutations for growth and survival, have greatly improved patient outcomes. However, despite these advances, some of the most frequent oncogenic mutations in cancer, such as those found in KRAS, are extremely challenging to target directly. One promising strategy to expand the range of actionable targets for cancer drug development is the exploitation of synthetic lethal interactions. Synthetic lethality is the term used to describe the death of cells in response to the co-existing disruption of two genes, neither of which is lethal alone. In this setting, targeting a gene that is synthetic lethal with a cancer-relevant mutation has the potential to induce the death of vulnerable cancer cells while leaving healthy cells unaffected.

With this background in mind, my lab participated in a focused ENU mutagenesis screen in zebrafish with the aim of identifying genes that are essential for high rates of cell proliferation during endodermal organ development but not required by quiescent tissues. This yielded mutants that exhibited either 'cell death' or 'growth arrest' phenotypes in the liver, intestine and pancreas. I investigated two of the underlying mutant genes, *ahctf1* and *rnpc3*, for their capacity to engage in synthetic lethal interactions with the *kras* oncogene.

In Chapter 3, I investigated the impact of *ahctf1* heterozygosity on the growth and survival of $Kras^{G12V}$-expressing hepatocytes in a zebrafish model of hepatocellular carcinoma (HCC), *TO(kras^{G12V}). ahctf1* encodes Elys, a multifunctional nucleoporin with essential roles in nuclear pore assembly and mitosis. I found that *ahctf1* heterozygosity impairs nuclear pore formation, mitotic spindle assembly and chromosome segregation, leading to DNA damage and activation of Tp53-dependent and Tp53-independent cell death pathways which reduced tumour burden. Importantly, *ahctf1* heterozygosity did not impact normal liver development, advancing ELYS as an attractive target for cancer therapy with a viable therapeutic window.

In Chapter 4, I examined if *rnpc3* heterozygosity also reduced tumour burden in the *TO(kras^{G12V})* model. *rnpc3* encodes 65K, a unique protein component of the U12-dependent spliceosome, a specialised splicing machinery required for the correct splicing of a very small percentage (3.7%) of genes. In hepatocytes expressing *kras^{G12V}*, *rnpc3* heterozygosity reduced the number of cells in S phase of the cell cycle and increased cell death, together reducing tumour burden, without affecting normal tissue. These studies indicate that *ahctf1* and *rnpc3* are synthetic lethal partners with the *kras^{G12V}* oncogene and could be suitable targets for drug development.

In Chapter 5, I demonstrated that the zebrafish model of HCC is a powerful platform for testing novel therapeutics. I evaluated the efficacy of PRMT5 and KAT6A/B inhibitors early in

their development, and also demonstrated that a putative small molecule inhibitor of U12-dependent splicing developed in the Heath laboratory was highly effective in reducing tumour growth and worthy of future investigation.

In conclusion, my studies revealed two promising new targets for cancer treatment. I also demonstrated that the zebrafish HCC model is highly amenable to pharmacological inhibition and provides a valuable system for the pre-clinical examination of drug treatments *in vivo*.

Declaration

This is to certify that:

i. This thesis comprises only my original work towards the degree of Doctor of Philosophy, except where indicated in the Preface.
ii. Due acknowledgement has been made in the text to all other material presented.
iii. The thesis is fewer than 100,000 words in length, exclusive of figures, tables, bibliographies and appendices.

Kimberly Morgan

Preface

In accordance with the regulations governing the degree of Doctor of Philosophy at the University of Melbourne, I hereby submit that:

Chapter 3
Dr. Alexandra Garnham performed RNA sequencing data analysis. I conducted sample collection, RNA isolation and library preparation, thus I estimate my contribution to the RNA-sequencing experiment to be 70%. The chapter represents 95% of my own work.

Chapter 4
This chapter represents 100% of my own work.

Chapter 5
Dr. Alexandra Garnham performed RNA sequencing data analysis. I conducted sample collection, RNA isolation and library preparation, thus I estimate my contribution to the RNA-sequencing experiment to be 70%. The chapter represents 95% of my own work.

Acknowledgements

My PhD has been an incredibly challenging but intellectually engaging and exciting experience that would not have been possible without the support of many people. Completing my PhD at WEHI, surrounded by support and encouragement, both scientifically and personally has been an extraordinary privilege that I will always be grateful for.

First and foremost, I would like to thank my amazing supervisors Assoc Prof. Joan Heath and Dr. Karen Doggett. You have taught me a tremendous amount over the years, I am so appreciative that you took me on as a young and inexperienced Honours students and gave me the opportunity to work as a Research Assistant and travel before commencing my PhD. Thank you for giving me my start in science and inspiring me to persevere and overcome all the challenges I have been presented with. Your tireless support, endless cups of tea and generosity with your time has made this experience all the more enjoyable. Our discussions and your constructive feedback have helped me acquire the skills to be a successful scientist. It has been an absolute pleasure working with you for the past 5 years, I am so lucky for both your mentorship and friendship.

To past and present members of the Heath lab, Stephen Mieruszynski, Janine Coates, Fansuo Geng and Tanya de Jong-Curtain, thank you for always being so supportive and helpful. Starting as part of the small tight-knit Development and Cancer Division and now in the Epigenetic and Development Division, I really appreciate how everyone is always welcoming, willing to share ideas and give advice. Thanks to everyone for always accepting my baking with smiles and appreciation. The collaborative culture at WEHI has made it a great place to work, where I am constantly inspired by the amazing science surrounding me.

I would also like to thank my PhD committee, Tracy Putoczki, Brendon Monahan and Andy Cox for their valuable suggestions and kind words of encouragement. None of this work would have been possible without all the aquarium staff Tyson Blanch, Bryan Ko, Cameron Mackey, Elizabeth Grgacic and Dora McPhee, as well as the weekend feeders who continue to take such great care of all my zebrafish. I am also incredibly grateful for everyone in the imaging department who were absolutely instrumental in teaching me everything about microscopy and imaging analysis. Thank you especially to Lachlan Whitehead who helped write many of the ImageJ macros to process and quantitate my different imaging experiments, making my life much easier. I would also like to thank Ellen Tsui in histology who helped me perfect my vibratome and cryosectioning techniques.

My PhD experience has been greatly enriched by all the wonderful friends I have made at WEHI. I am especially thankful to Sophia Mah, Helen McRae, Zoe Grant and Sabrina Lewis for their friendship inside and outside of the lab and always checking in on me. I have always had so much fun, especially at student retreats and footy with you all.

Finally, I am so grateful for my Mum and Dad, who always encouraged me to follow my dreams. Thank you for always listening to me enthusiastically recount my latest results or talk about the newest technique I learnt, even if you do not understand it. You have always instilled confidence in me when I have needed it the most. I always appreciate your endless care, support and love. Thank you also to my sister Jessica for always providing me distractions when I was working too much, even when I stubbornly insisted I was too busy, I wouldn't have made it this far without you.

Abbreviations

2-CLiP	2-Colour Liver Pancreas
aDMA	asymmetric dimethylarginine
ahctf1	AT hook containing transcription factor 1
ALL	acute lymphoblastic leukemia
ALPS	ArgGAP1 lipid packing sensor
AML	acute myeloid leukemia
APC/C	anaphase-promoting complex/cyclosome
bp	base pair
BRPF1/2/3	bromodomain and PHD finger containing 1/2/3
BSA	bovine serum albumin
CBP	CREB-binding protein
Cdc6	cell division cycle 6
CDK-1	cyclin-dependent 1
CDKN2A	cyclin-dependent kinase inhibitor 2A
CDKs	cyclin-dependent kinases
cDNA	complementary DNA
Cdt1	chromatin licencing and DNA replication factor 1
ChiP-seq	chromatin immunoprecipitation sequencing
CML	chronic myeloid leukemia
CRISPR	clustered regularly interspaced short palindromic repeats
DDK	DBF4-dependent kinase
DEGs	differentially expressed genes
DMBA	7,12-dimethylbenz[a]anthracene
DMSO	dimethyl sulfoxide
DNA	deoxyribonucleic acid
dpf	days post fertilisation
EAF6	Esa1-associated factor 6
EdU	5-ethynyl-2'-deoxyuridine
EGFP	enhanced green fluorescent protein
Elys	embryonic large molecule derived from yolk sac
EM	electron microscopy
EMT	epithelial-mesenchymal transition
ENU	N-ethyl-N-nitrosourea

fabp10	fatty acid binding protein 10
FCS	fetal calf serum
FDA	Food and Drug Administration
FDR	false discovery rate
FG-nups	phenylalanine-glycine nucleoporins
γ-TuRC	γ-tubulin ring complex
GAF	GAGA factor
GDP	guanosine diphosphate
GTP	guanosine triphosphate
GWAS	genome wide association studies
h	hour
HBV	hepatitis B virus
HCC	hepatocellular carcinoma
HCV	hepatitis C virus
hpf	hours post fertilisation
ING5	inhibitor of growth 5
KAT6A/B	lysine acetyltransferases 6A/B
kDa	kilodalton
KRAS	Kirsten rat sarcoma
MAPK	mitogen-activated protein kinase
Mcm2-7	mini-chromosome maintenance 2-7 complex
MDa	megadalton
min	minute
MMA	mono-methylarginine
MNNG	N-methyl-N'-nitro-N-nitrosoguanidine
mpf	months post fertilisation
mRNA	messenger RNA
MTAP	methylthioadenosine phosphorylase
NE	nuclear envelope
NES	nuclear export signals
NLS	nuclear localisation signals
nm	nanometre
NPC	nuclear pore complex
NTF	nuclear transport factor
NUMA	nuclear mitotic apparatus protein

nup	nucleoporin
O/N	overnight
ORC	origin recognition complex
PARP	poly(adenosine diphosphate [ADP]-ribose) polymerase
PBAP	polybromo-containing Brahma-associated proteins
PBS	phosphate buffered saline
PBST	PBS + 0.1% (w/v) Tween-20
PCR	polymerase chain reaction
PFA	paraformaldehyde
PLK-1	polo-like 1
PP1	protein phosphate 1
pre-mRNA	precursor messenger RNA
pre-RC	pre-replication complex
PRMT5	protein arginine methyltransferase 5
RanBP2	Ran-binding protein 2
RanGTP	Ran GTPase activating protein
RAS	rat sarcoma
RNA	ribonucleic acid
RNAi	RNA interference
rnpc3	RNA-binding region containing 3
RT	room temperature
RT-qPCR	reverse transcriptase-quantitative polymerase chain reaction
SAH	S-adenosylhomocysteine
SAM	S-adenosylmethionine
sDMA	symmetric dimethylarginine
SEM	standard error of the mean
shRNA	short hairpin RNA
SINE	selective inhibitor of nuclear export
siRNAs	short interfering RNAs
snRNA	small nuclear RNA
snRNP	small nuclear ribonucleoproteins
T-ALL	T-cell acute lymphoblastic leukemia
TACE	transcatheter arterial chemoembolization
TCGA	The Cancer Genome Atlas
TEAZ	transgene electroporation of adult zebrafish

TNBC	triple-negative breast cancer
TOPIIα	topoisomerase IIα
TP53	tumour suppressor protein 53
XPO1	exportin 1
zPDX	zebrafish patient-derived xenografts
µg	microgram
µL	microlitre
µm	micrometre
µM	micromolar

Table of Contents

List of Figures

List of Tables

1 Literature review

1.1 The burden of cancer

Cancer is the second leading cause of death globally, accounting for almost 10 million mortalities in 2020. One in eight men and one in eleven women are estimated to die from the disease. More than 50 million people have been diagnosed with cancer in the past five years, with one in five people developing cancer during their lifetime[1]. Significant disparities in cancer incidence and mortality rates exist between higher and lower-income countries, due to different access to healthcare and treatment. Based on projected population aging and growth, the burden of cancer is set to increase by more than 56% by 2040, to a predicted 30.2 million cases[1].

1.1.1 Hepatocellular carcinoma

Liver cancer represents a major public health issue, as it is the sixth most common cancer and the third leading cause of cancer-related mortality worldwide (Figure 1.1)[1]. There were an estimated 906,000 cases diagnosed in 2020 and this is projected to surpass 1.4 million cases globally in 2040. Hepatocellular carcinoma (HCC) is the most prevalent form of liver cancer, accounting for 85-90% of all cases[2]. The incidence of HCC is highest in South-East Asian and sub-Saharan African countries and is rapidly increasing in developing countries including America[3].

The geographical distribution of HCC mainly reflects that of chronic viral hepatitis. Chronic hepatitis B virus (HBV) infection is the most frequent aetiology of HCC in Eastern Asian and most African countries, excluding Northern Africa, where hepatitis C virus (HCV) infection is more prevalent[4,5]. In most Western countries, including America, HCV is the leading cause of HCC. Overall, up to 80% of HCC cases worldwide are attributable to chronic HBV and HCV[3].

Additional predisposing risk factors for HCC development include chronic alcohol consumption, aflatoxin B1 exposure, diabetes and obesity (Figure 1.2)[6]. Hepatocarcinogenesis induced by these various causes is a complex multistep process, which typically occurs in the context of liver cirrhosis[2]. Cirrhotic hepatocytes undergo chronic cycles of necrosis and regeneration, leading to the development of chromosomal instability and dysplastic nodules. Genetic and epigenetic alterations progressively accumulate in a background of increased inflammation and fibrosis, ultimately resulting in malignant transformation and the initiation of HCC[7,8].

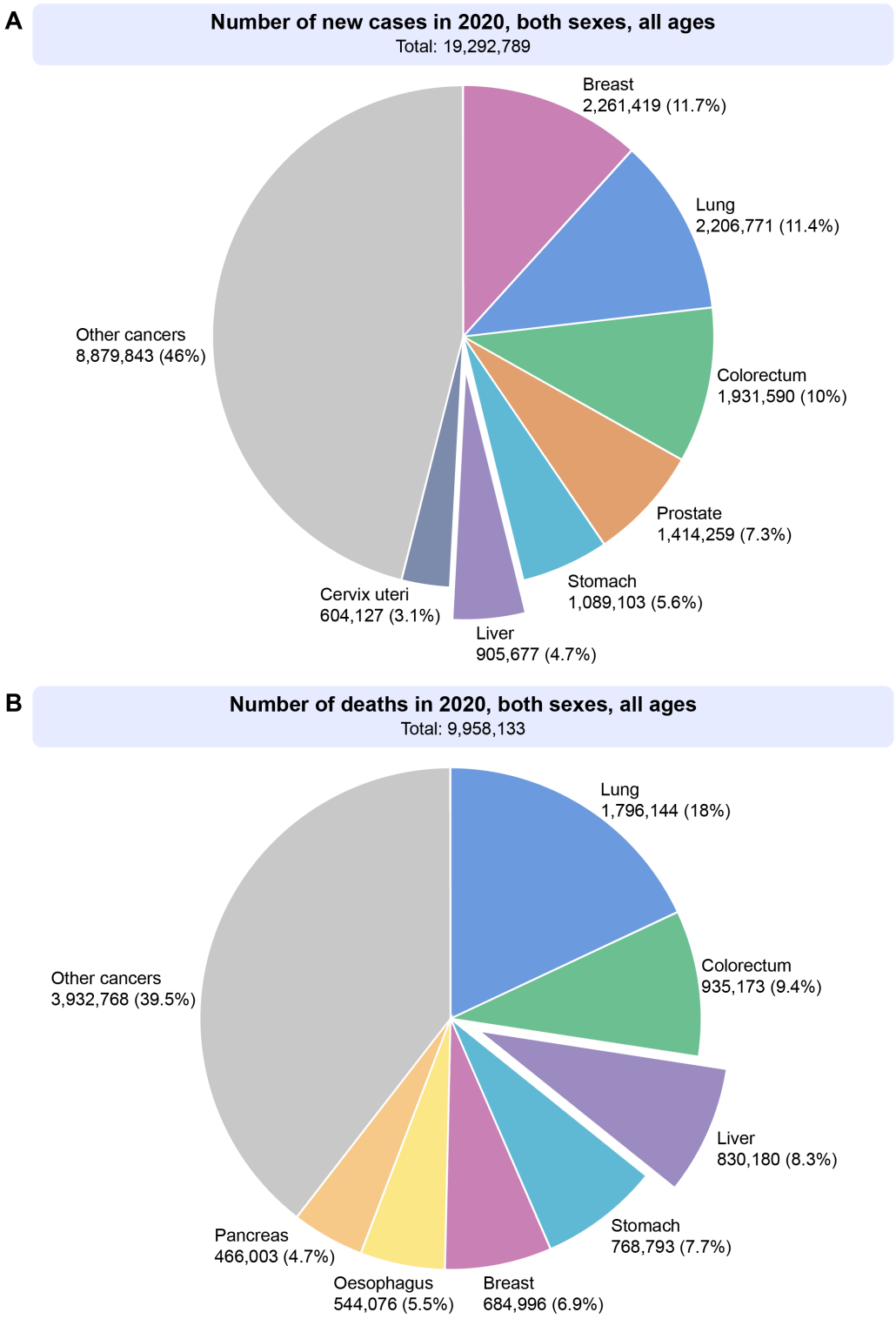

Figure 1.1 Global cancer incidence and mortality in 2020

A. Population weighted average of cancer type incidence globally in 2020. Liver cancer is the sixth most commonly diagnosed cancer. **B.** Population weighted average of cancer type mortalities globally in 2020. Liver cancer is the third leading cause of cancer-related deaths. Data from GLOBOCAN 2020[1].

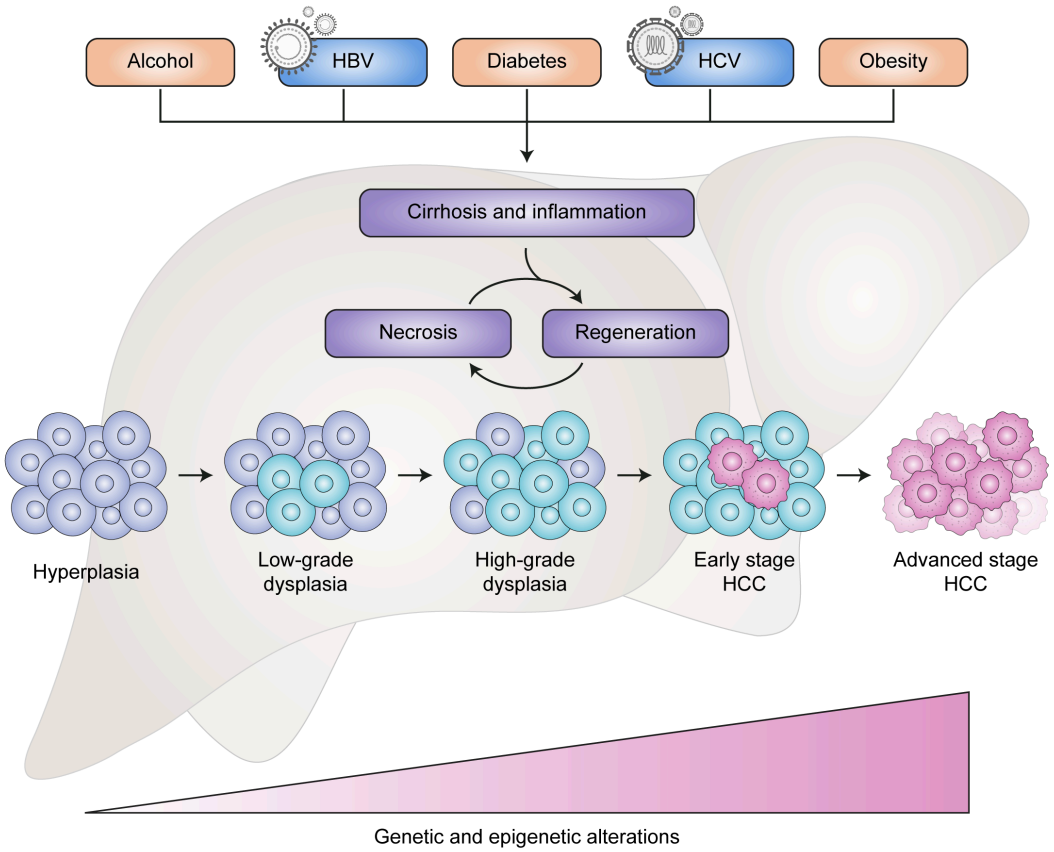

Figure 1.2 Mechanisms of hepatocarcinogenesis

Alcohol consumption, HBV, diabetes, HCV and obesity are significant risk factors contributing to hepatocarcinogenesis. These factors induce cirrhosis and inflammation which cause chronic cycles of hepatocyte necrosis and regeneration. This fosters the development of chromosomal instability and dysplastic nodules. Genetic and epigenetic alterations progressively accumulate resulting in malignant transformation and ultimately HCC[6-8].

HBV: hepatitis B virus, HCC: hepatocellular carcinoma, HCV: hepatitis C virus.

1.1.2 Genetic landscape of HCC

Genome-wide association studies (GWAS) have delineated the landscape of genetic alterations that contribute to hepatocarcinogenesis with an average of 60 somatic alterations detected in coding regions of the genome per tumour[9]. The most frequent mutations that occur during HCC affect *TERT* (60%), *TP53* and *CTNNB1* (25-30%)[9,10]. *TERT* promoter mutations impacting telomere maintenance, are the earliest recurrent mutation detected in HCC. The prevalence of *TERT* mutations remains stable between early and advanced stage HCC, suggesting that *TERT* acts as a gatekeeper of malignant transformation[11]. In contrast, *TP53* and *CTNNB1* mutation frequencies increase with tumour stage, indicating a role of TP53 inactivation and WNT-β-catenin pathway dysregulation in HCC progression[10]. Epigenetic modifiers and chromatin remodelling factors (*ARID1A, ARID2, KMT2A, KMT2B, KMT2C*), plus other members of the WNT-β-catenin pathway (*AXIN1*) and tumour suppressors (*RB1, KEAP1*) are also recurrently altered in HCC[2].

1.1.3 RAS signalling in HCC

The RAS family of small GTPases are the most commonly mutated oncogenes in cancer[12]. Activating mutations in RAS isoforms, *KRAS*, *HRAS* and *NRAS*, result in constitutive GTPase activity, sustaining signalling cascades that promote cellular proliferation, survival and differentiation (Figure 1.3)[13]. In this manner, RAS signalling plays a pivotal role in malignant transformation and tumour progression, including in HCC. Specifically, mutations in *KRAS* and *NRAS* are found in 5% and 3% of HCC tumours respectively[13]. Additionally, inactivating mutations in the RAS inhibitor, *RPS6KA3*, have been identified in 7% of HCC cases[9]. *RASSF1A* and *NORE1A* methylation in HCC tumours further promotes RAS pathway activation[14]. Enhanced RAS signalling in HCC may also be attributable to overexpression of *IGF2* and alterations in upstream signalling receptors such as *VEGFA* and *FGF19*[10]. In total, 50% of HCCs exhibit aberrant RAS/RAF/MAPK signalling and enhanced activation of RAS pathways is universally observed in human HCC tumours relative to non-neoplastic hepatocytes[15,16]. Moreover, activation of RAS signalling, through MAPK14, is also implicated in resistance to molecular targeted therapies for HCC[17]. Specifically, treatment with the multikinase inhibitor sorafenib, induces upregulation of MAPK14 which activates both RAF-MEK-ERK and PI3K-PDK1-AKT signalling cascades, contributing to the development of drug resistance.

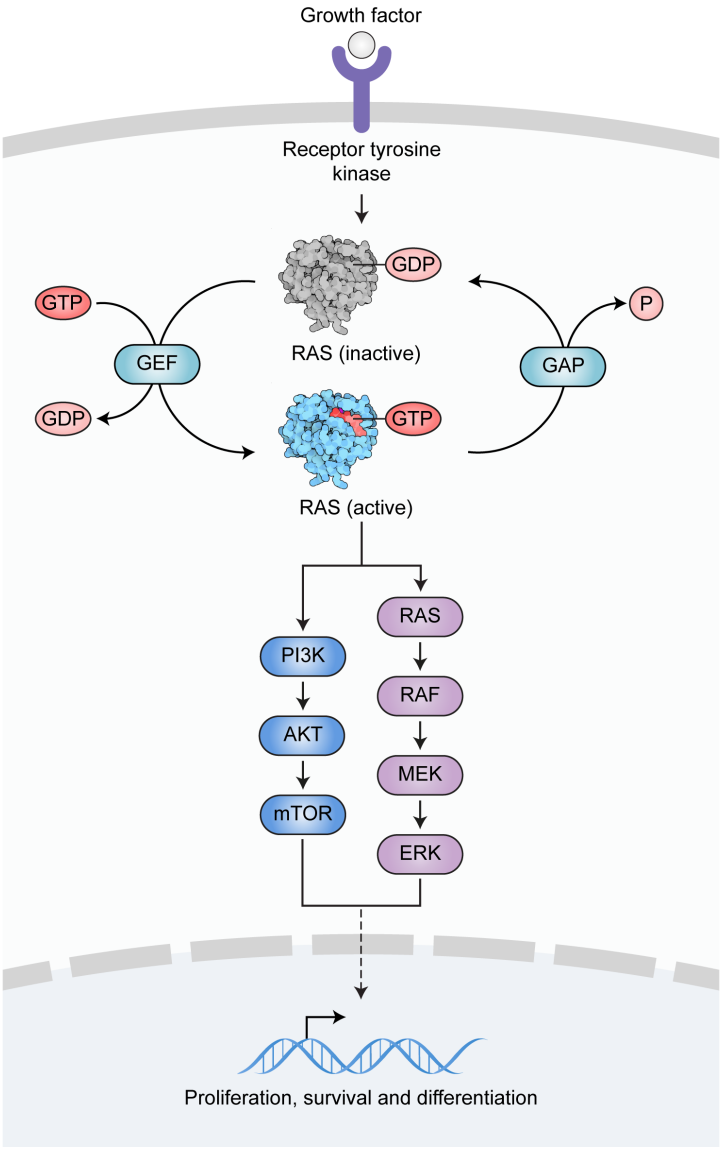

Figure 1.3 RAS signalling pathway

Simplified representation of the RAS signalling pathway shows that RAS responds to extracellular stimuli such as growth factor binding to receptor tyrosine kinases. This triggers the recruitment of GEFs that catalyses the exchange of GDP to GTP, converting RAS to an active GTP-bound state. This activates multiple downstream effectors including RAF-MEK-ERK and PI3K-PDK1-AKT cascades resulting in enhanced proliferation, survival and differentiation. GAPs increase the rate of GTP hydrolysis, returning RAS to its inactive GDP-bound state[13]. Oncogenic mutations of *RAS* genes result in constitutive activation of downstream pathways driving malignant transformation. Protein Data Bank entry: 5p21[18].

GAPs: GTPase activating proteins, GDP: guanosine diphosphate; GEFs: Ras GTPase exchange factors, GTP: guanosine triphosphate.

1.1.4 TP53 mutation in HCC

The tumour suppressor protein, TP53 is often termed the 'guardian of the genome' due to its central role in responding to cellular stresses such as DNA damage and oncogene expression[19]. Activation of TP53 can prevent tumourigenesis through regulating a diverse array of processes including cell cycle arrest, senescence, DNA repair, apoptosis, cellular metabolism and autophagy (Figure 1.4)[20,21]. These functions are crucial for tumour suppression, as well as mediating responses to cancer therapies. Consequently, *TP53* is the most frequently dysregulated gene in tumourigenesis and *TP53* mutations are found in 30% of HCC cases[10,20]. TP53 exhibits a variable mutation spectrum, dependent on HCC aetiology. For example, exposure to Aflatoxin B1 is specifically associated with TP53 R249S mutation[22]. Amplification/overexpression of TP53 negative regulators *MDM2/MDM4* and recurrent mutations in *ARF* also contribute to TP53 dysfunction in HCC[10]. TP53 mutation status is also of clinical significance, with TP53 alterations associated with reduced overall survival[23].

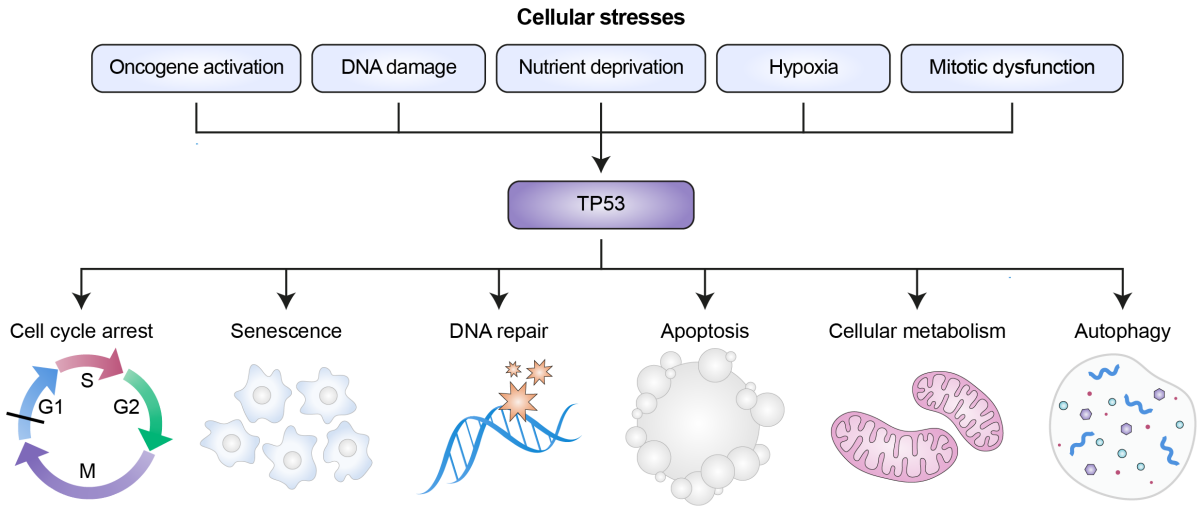

Figure 1.4 TP53 activating signals and responses that are important for tumour suppression

TP53 plays a central role in responding to cellular stresses, such as oncogene activation, DNA damage, nutrient deprivation, hypoxia and mitotic dysfunction. Activated TP53 can modulate diverse cellular processes that are important for suppressing tumour development. This includes promoting cell cycle arrest, senescence, DNA repair, apoptosis, altering cellular metabolism and activating autophagy[20,21]. Figure adapted from Vousden et al., 2007[24].

1.1.5 Molecular classification of HCC

Integrative analysis of genomic, transcriptomic and epigenomic profiling of tumours has provided the basis for the molecular classification of HCC subtypes. Two distinct molecular HCC subtypes have been identified: the proliferation and non-proliferation subclasses, each representing approximately 50% of cases (Figure 1.5)[25,26]. The proliferation subclass of HCC is associated with HBV infection and is characterised by mutations in *TP53,* chromosomal instability and *FGF19* amplification. Another common molecular feature of this subclass is activation of RAS, mTOR, MET, IGF and Notch signalling cascades. Clinically, patients in the proliferation subclass exhibit increased tumour recurrence after resection and lower overall survival rates[27]. HCV and alcohol-related HCCs typically cluster within the non-proliferation HCC subclass. *CTNNB1* mutations are the dominant molecular feature of this subclass, resulting in dysregulation of the WNT-β-catenin pathway[28]. HCC tumours in the non-proliferation subclass display a less aggressive phenotype and consequently are associated with a better prognosis[29]. Clinical translation of these molecular HCC classifications for improved patient management and outcomes has yet to be achieved.

	Proliferation subclass	Non-proliferation subclass
Genetic and epigenetic features	*TP53* mutation Chromosomal instability 11q13 amplification (*FGF19* and *CCND1*) 17p loss	*CTNNB1* mutation *TERT* promoter mutation Chromosome 7 amplification *CDKN2A* methylation
Deregulated pathways	mTOR MET RAS IGF Notch	WNT-β-catenin
Clinical phenotype	Higher HBV prevalence Poorly differentiated Higher serum AFP levels Higher frequency of vascular invasion Worse outcome	Higher HCV prevalence and alcohol exposure Moderately-to-well differentiated Lower serum AFP levels Lower frequency of vascular invasion Better outcome

Figure 1.5 Molecular classification of HCC subtypes

Schematic representation of molecular classification of HCC. HCC can be classified into two major subclasses on the basis of genetic and epigenetic features, deregulated pathways and clinical phenotype. The proliferation class is associated with a poor prognosis, TP53 mutation and activation of classic oncogenic signalling cascades (such as RAS-MAPK and AKT-mTOR pathways). In contrast, the non-proliferation class is associated with better outcomes and is defined by *CTNNB1* mutation and WNT-β-catenin pathway activation[30]. Figure adapted from Llovet et al., 2018[30].

AFP: α-fetoprotein; HBV: hepatitis B virus; HCV: hepatitis C virus.

1.1.6 Treatments for HCC

Despite improved understanding of the molecular pathogenesis of HCC and recent advances in systemic therapies, the 5-year survival rate of HCC remains a low 18%[31]. Early stage HCC can often be treated curatively by surgical resection, liver transplantation or local ablation[32]. However, as a consequence of the lack of surveillance programs to enable early HCC detection, these potential curative treatments are applicable to less than 30% of newly diagnosed patients[33]. Therapeutic options for HCC treatment are restricted by the existence of underlying concomitant liver disease, particularly cirrhosis, that reduces the effectiveness or prevents the use of conventional treatments such as chemotherapy[34]. In patients with intermediate stage HCC, transcatheter arterial chemoembolization (TACE) can extend median overall survival to 26 months[35,36].

In 2007, the multikinase inhibitor sorafenib, became the first drug approved by the FDA for systemic treatment of HCC (Figure 1.6). In patients with advanced HCC, sorafenib can modestly improve median overall survival from 7.9 to 10.7 months, with a tumour overall response rate of 2-3%[37]. However, sorafenib does not prevent tumour recurrence after curative resection or ablation and some patients do not respond to treatment[38]. Subsequent phase III trials of other targeted therapies developed in the decade since sorafenib approval repeatedly failed to demonstrate survival benefits in patients. These include trials for brivanib (FGFR and VEGFR inhibitor)[39], sunitinib (KIT, VEGFR and PDGFR inhibitor)[40], linifanib (VEGFR and PDGFR inhibitor)[41] and erlotinib (EGFR inhibitor)[42] in the first line setting, and brivanib[43] and everolimus (mTOR inhibitor)[44] in the second-line setting. These negative trial outcomes were attributable to an array of factors including marginal anti-tumour potency, liver toxicity, flaws in trial design, challenges in patient molecular stratification and lack of biomarker-based enrichment[45,46]. The trend of disappointing phase III trial results was interrupted by the success of regorafenib, a multi-kinase inhibitor, as a second-line treatment for HCC[47]. Treatment with regorafenib after patients progressed on sorafenib, extends median overall survival from 7.8 months to 10.6 months[47]. Thereafter, another multi-target tyrosine kinase inhibitor, lenvatinib was found to be non-inferior to sorafenib as a first-line treatment[48]. Cabozantinib (MET inhibitor)[49] and ramucirumab (VEGFR2 inhibitor)[50] were also shown to be effective in the second-line setting. Additionally, immune checkpoint inhibitors, including pembrolizumab[51], nivolumab[52] and ipilimumab[53] have received accelerated FDA approval and are now being incorporated into HCC treatment. Such emerging immunotherapies are a particularly promising approach for cancer treatment. Whilst these advancements in molecular targeted therapies for HCC have improved patient outcomes, the impacts on overall survival have been modest and incremental, with median survival of advanced stage HCC patients remaining around 1 year[30]. Thus, there is a major requirement for the development of new therapeutic strategies to improve HCC clinical outcomes.

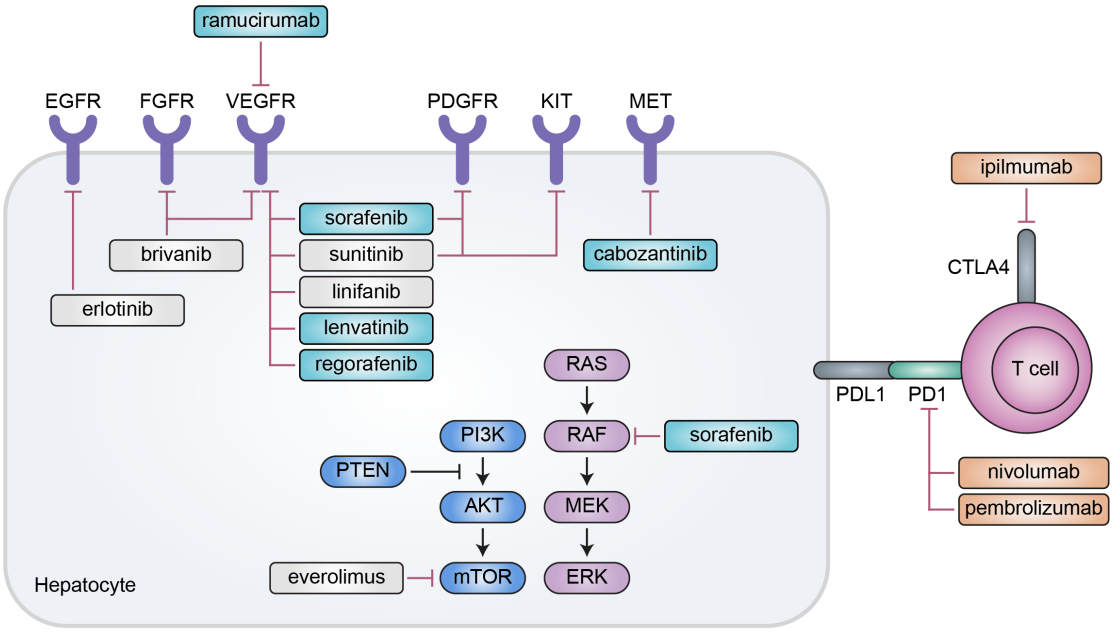

Figure 1.6 Molecular targeted therapies for HCC

Turquoise boxes indicate drugs with positive results from phase III trials (sorafenib, lenvatinib, regorafenib, ramucirumab and cabozantinib). Grey boxes indicate drugs with negative results from phase III trials (brivanib, erlotinib, sunitinib, linifanib and everolimus). Orange boxes indicate drugs currently in development for HCC that have received accelerated FDA approval for which clinical trials are ongoing (ipilimumab, nivolumab, pembrolizumab). Figure adapted from Llovet et al., 2018[30].

CTLA4: cytotoxic T lymphocyte protein 4; EGFR: epidermal growth factor receptor; FGFR: fibroblast growth factor receptor; PDGFR: platelet-derived growth factor receptor; PDL1: programmed cell death ligand 1; PD1: programmed cell death protein 1; VEGFR: vascular endothelial growth factor receptor.

1.2 Molecularly targeted cancer therapy

Advances in understanding the genomic alterations that contribute to tumourigenesis have revolutionised cancer treatment by facilitating the development of molecularly targeted therapies focused on drugging gene products recurrently altered in tumour cells. Genomic alterations that occur during malignant transformation create an increased dependence on certain genes and induce a stress phenotype or altered cellular state that can be therapeutically exploited to achieve selective cytotoxicity of malignant cells[54].

1.2.1 Oncogene and non-oncogene addiction

The success of many molecularly targeted cancer therapies is underpinned by oncogene addiction, whereby tumour cells are sensitive to inhibition of a single dominant-acting oncogene (Figure 1.7)[55,56]. A considerable number of cancers exhibit dependence on certain oncogenic driver mutations for growth and/or survival. For example, *in vivo* mouse models of myelocytic leukemia induced by the *Bcr-Abl* oncogene are dependent on its continued expression for maintenance of the neoplastic state[57]. This addiction has been exploited clinically in patients with chronic myeloid leukemia (CML) through treatment with the ABL inhibitor imatinib[58]. Imatinib treatment has dramatically extended the median overall survival of CML patients to more than 10 years[59], demonstrating the remarkable therapeutic efficacy of targeting oncogene addiction.

However, this approach is limited to cancers which harbour actionable oncogenic mutations. Some of the most frequently mutated oncogenes, such as RAS, are difficult to directly target therapeutically owning to a perceived lack of accessible drug-binding pockets[12], although recent advancements have been made with allele-specific $KRAS^{G12C}$ covalent inhibitors[60,61]. Other oncogenes, such as the transcription factor MYC, lack specific active sites for small molecule inhibition, and their predominant nuclear localisation precludes monoclonal antibody targeting[62]. Additionally, it is challenging to develop therapeutics against loss of function mutations in tumour suppressor genes including *TP53*. Subsequent identification of non-oncogene addiction in malignant cells has further expanded the range of potential therapeutic targets for cancer treatment beyond those directly altered in tumours, helping to overcome these limitations.

Non-oncogene addiction is defined as a state in which cancer cells exhibit an increased dependency on genes which are not inherently oncogenic to sustain a malignant phenotype[54,63]. Oncogenic transformation resulting in sustained proliferation induces various cell stresses, including replicative and oxidative stress[64]. Consequently, tumour cells are more reliant on compensatory cellular pathways and processes for growth and survival. In this paradigm, the supporting gene or pathway is not mutated in cancer nor oncogenic in its own right; nonetheless, its function is essential to maintain the tumourigenic state. As normal cells do not require these genes to the same extent for viability, this dependency can be therapeutically exploited[54,63].

1.2.2 Synthetic lethal therapies for cancer

Non-oncogene addiction constitutes a form of synthetic lethality, which has emerged as a promising tool for cancer drug development[65]. Synthetic lethality describes the death of cells in response to the co-existing disruption of two genes, neither of which is lethal alone[66,67]. Thus, targeting a gene that is synthetic lethal to a cancer-relevant mutation should kill only cancer cells while healthy cells are unaffected. The clinical usefulness of this approach is exemplified by the use of poly(adenosine diphosphate [ADP]-ribose) polymerase (PARP) inhibitors to treat tumours harbouring mutations in the breast cancer susceptibility genes, *BRCA1*/*BRAC2*[68,69]. *BRCA1*/*BRAC2* mutant cells are deficient in DNA repair by homologous recombination; PARP inhibition in this background induces apoptosis specifically in tumour cells whilst normal cells are spared[70,71]. This selective cytotoxicity of PARP inhibitors is achieved through both catalytic inhibitory and DNA trapping activity[72,73]. In ovarian cancer patients with *BRCA1*/*BRAC2* mutations, treatment with the PARP inhibitor olaparib significantly extends median progression free survival from 5.5 to 19.1 months[74]. PARP inhibitors have also received FDA approval for *BRCA1*/*BRAC2* mutant breast, pancreatic and prostate cancers[75].

This resounding success has fuelled the search for other clinically relevant pairwise combinations, and there has been a particular focus on identifying genes whose loss of function confers synthetic lethality with difficult to target oncogenes. Numerous synthetic lethal screens involving mutant *RAS* utilizing RNA interference (RNAi) technology have been performed[76-78]. However, the synthetic lethal hits uncovered by these studies display limited overlap and reproducibility[79]. This may be attributable to problems with library quality, off target effects of RNAi technologies and lack of robustness of synthetic lethal interactions in different cellular and genetic contexts[79,80]. The advent of CRISPR/Cas9 screens has renewed enthusiasm in synthetic lethal screening by helping to overcome these limitations by facilitating the construction of high-fidelity libraries that enable complete knockdown with minimal off-target effects[81,82]. Subsequently, multiple screens have been performed in different RAS mutant cell lines, revealing genetic vulnerabilities and suggesting optimal drug combination strategies to maximize therapeutic responses[83-86]. However, these findings require further mechanistic validation before successful translation into the clinic.

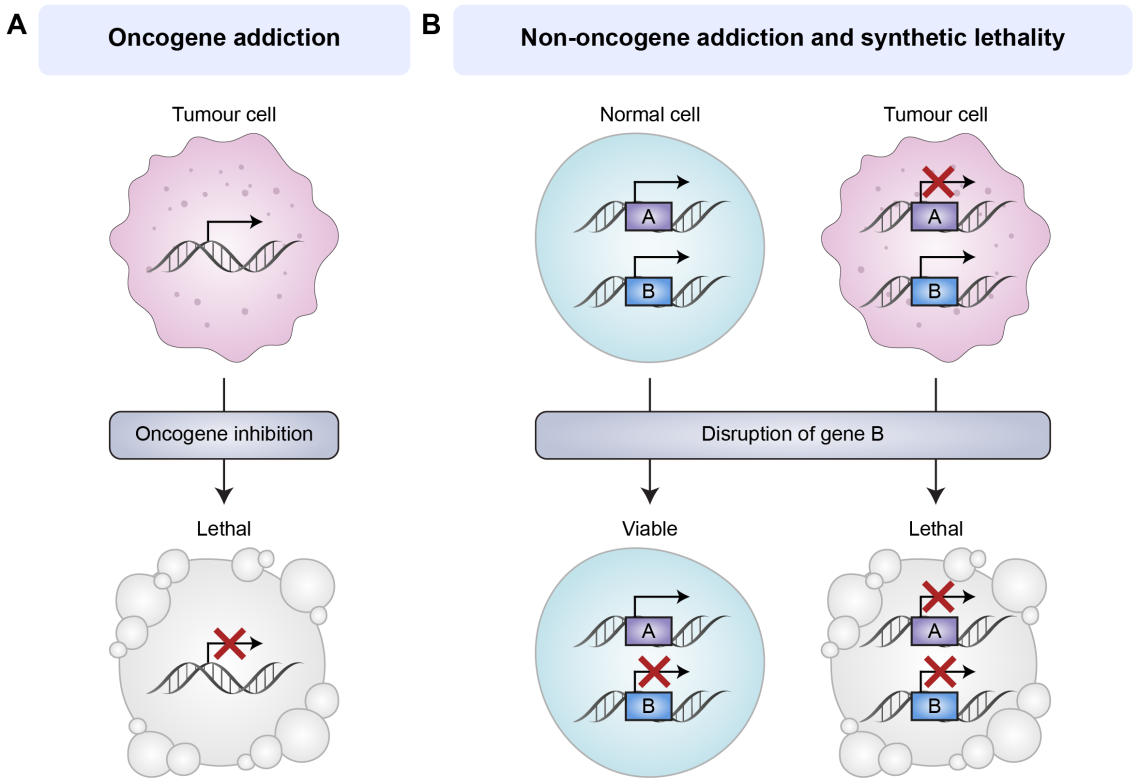

Figure 1.7 Exploiting oncogene addiction, non-oncogene addiction and synthetic lethality for cancer therapy

A. Oncogene addicted tumour cells depend on continuous oncogenic signalling for their survival. For example, mutation of KRAS or MYC enhances proliferation and drives malignant transformation and progression. Cells are reliant on these activated oncogenic proteins to maintain their malignant properties, therefore, oncogene inhibition results in tumour cell lethality. **B.** Non-oncogene addicted tumour cells exhibit an increased dependency on gene products which are not themselves mutated to compensate for oncogene-induced stress phenotypes. This creates a therapeutic vulnerability that can be exploited through synthetic lethality. Synthetic lethality is defined as the death of cells in response to the co-existing disruption of two genes, neither of which is lethal alone. In this instance, disruption of gene B expression does not affect the viability of normal cells. However, in tumour cells which harbour gene A mutations, the co-disruption of gene B expression results in cell death. Figure adapted from O'Neil et al., 2017[67].

1.2.3 Drug resistance to targeted therapies

Whilst molecular targeted cancer therapies have transformed patient outcomes, the emergence of drug resistance continues to be the principal limiting factor to achieving complete cures in patients. After an initial reduction in tumour burden in response to drug treatment, tumour cells often acquire resistance through multiple mechanisms resulting in disease relapse. For example, both amplification and mutation of *Bcr-Abl* confers resistance to the ABL-inhibitor imatinib in patients with CML[87]. Clinical resistance has also been observed to PARP inhibitors due to secondary mutations in *BRCA1/BRCA2* which restore partial DNA homologous recombination repair competency[88]. Combination therapies can limit the emergence of resistance, however unless complete tumour ablation is achieved, evolving drug resistance is inevitable[89]. Additionally, determining the optimal combination of drugs is a formidable challenge due to tumour cell heterogeneity. To overcome the lack of direct actionable targets in some tumours and the evolution of resistance, the identification of novel cancer therapeutic targets is urgently required to improve patient outcomes. In this thesis, I test the hypothesis that the identification of genes that are indispensable for the rapid proliferation of cells during zebrafish development provides a powerful platform for discovering genes relevant to cancer.

1.3 The relationship between development and cancer

1.1.1 Developmental signalling pathways are recapitulated in cancer

Embryonic development requires precise spatiotemporal control of cell proliferation, differentiation, migration and death for the formation of a viable organism. Signalling cascades crucial for development and tissue homeostasis, such as Wnt, Hedgehog and Notch pathways, are often dysregulated in a variety of pathologies including cancer (Figure 1.8)[90,91].

Wnt-β-catenin signalling is critical in embryogenesis for axis patterning, regulation of cell proliferation, migration and polarity, cell fate specification and self-renewal in stem cells[92]. Aberrations in Wnt signalling pathway genes are a common occurrence in a diverse range of cancer types. This is exemplified by mutation of the tumour suppressor gene *APC* in 72% of colorectal cancers, resulting in disruption of the β-catenin destruction complex, in turn promoting the transcription of WNT target genes that contribute to tumour initiation, growth and metastasis[93,94].

The Hedgehog signalling pathway is also integral in development and is frequently dysregulated in cancer. During embryonic development, Hedgehog signalling contributes to limb patterning, organogenesis, osteogenesis, stem cell maintenance and proliferation[95]. Dysregulation of the Hedgehog pathway contributes to malignant transformation and progression through the activation and nuclear localisation of GLI transcription factors which promote expression of target genes involved in proliferation, survival and angiogenesis[96,97]. Notably, 90% of basal cell carcinomas exhibit loss-of-function mutations in *PTCH1*, resulting in constitutive Hedgehog pathway activity[98].

Notch, similar to Wnt and Hedgehog pathways, is also crucial during embryonic development and disrupted in tumourigenesis. Notch signalling, via transmembrane ligands and receptors, controls cell fate determination, stem cell self-renewal potential and is essential for central nervous system and cardiovascular development[99,100]. The first demonstration of a role of Notch signalling in cancer was the identification of a chromosomal translocation in T-cell acute lymphoblastic leukaemia (T-ALL) that generates constitutively active NOTCH1[101]. Subsequently, over 50% of T-ALL cases have been found to harbour *NOTCH1* activating mutations[102]. Notch signalling during tumourigenesis is linked to both oncogenic and tumour suppressive functions, dependent upon the tissue and cellular context[103-105].

The pivotal role of Wnt, Hedgehog and Notch signalling alterations in the initiation and progression of several malignancies, has attracted great interest in the development of strategies for the therapeutic modulation of these pathways. Several WNT pathway agonists and small molecule inhibitors have been identified, however, none of these have yet received clinical approval[94,106]. More positive progress has been achieved in clinical trials of Hedgehog pathway inhibitors for cancer treatment. This includes FDA approval of the SMO inhibitors vismodegib and sonidegib for basal cell carcinoma[107,108]. Numerous modulators of Notch signalling have also been developed, including antibody therapies and small molecule inhibitors, and evaluation in clinical trials is ongoing[109]. The promising outcomes achieved in the therapeutic targeting of developmental pathways dysregulated in cancer suggests that further investigation of processes essential for development may provide valuable insights into tumourigenesis that can be of therapeutic benefit.

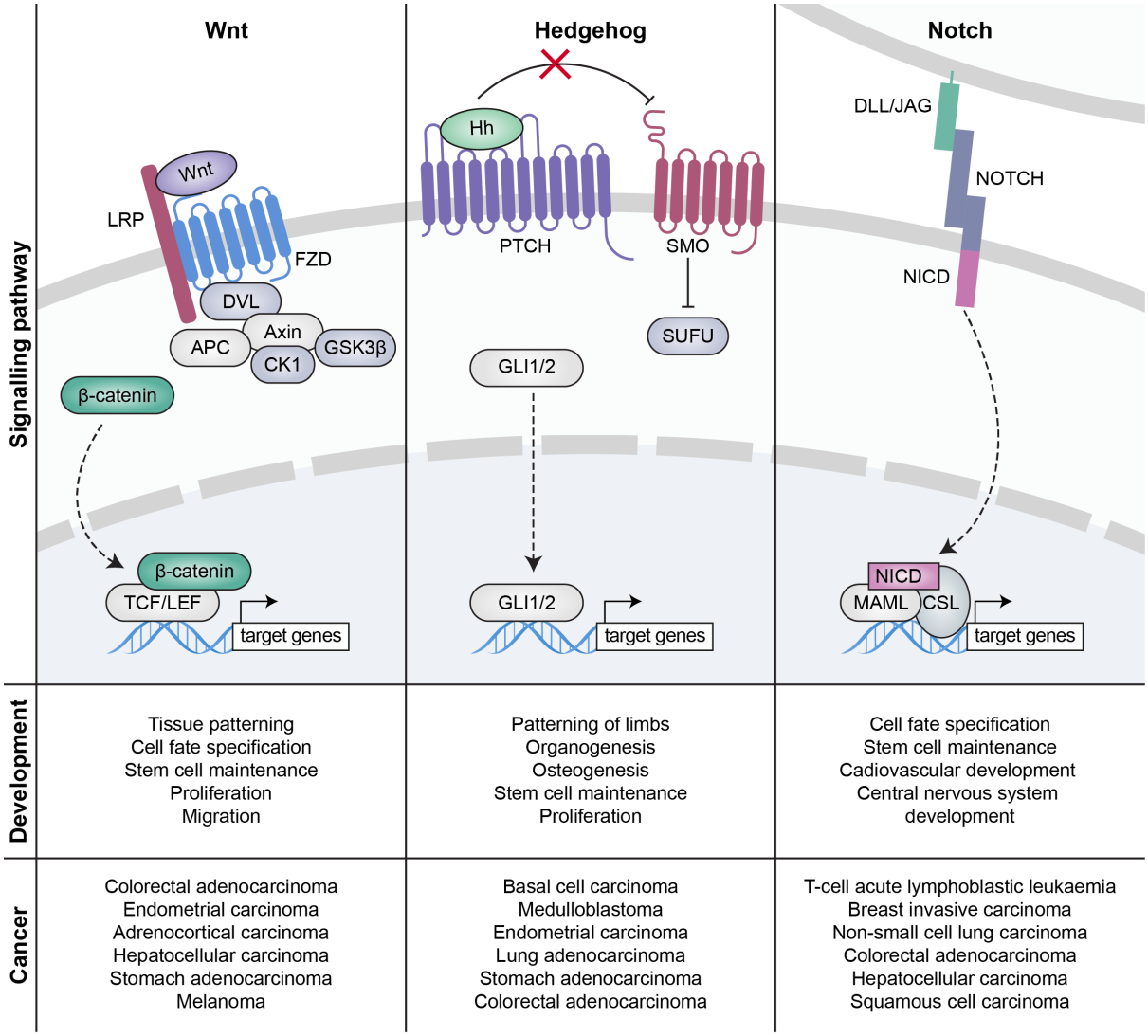

Figure 1.8 Signalling pathways important during development are frequently activated in cancer

Wnt, Hedgehog and Notch signalling pathways are involved in many critical aspects of embryogenesis and dysregulation of these pathways contributes to malignant transformation and progression of a diverse array of cancers. Signalling through these cascades is initiated by binding of a ligand to a plasma membrane receptor. This activates downstream effectors, culminating in translocation of factors to the nucleus where they promote transcription of target genes.

Wnt proteins bind and activate their receptor FZD and co-receptor LRP. This complex recruits DVL and a destruction complex composed of APC, AXIN1, GSK3β and CK1 to the plasma membrane, inhibiting β-catenin proteolysis. Subsequently, β-catenin accumulates in the cytoplasm and translocates to the nucleus, where it associates with TCF/LEF to activate transcription of pro-proliferation target genes, such as Cyclin D and MYC[106].

Binding of Hh relieves the inhibitory effect of the PTCH receptor on SMO. This inhibits SUFU, enabling activation and nuclear translocation of GLI1/2 to promote the transcription of pro-proliferation target genes, such as MYCN and FGF[97].

The Notch pathway is activated by NOTCH ligand binding to adjacent receptor-presenting cells. This induces NICD cleavage, allowing it to translocate to the nucleus and associate with MAML and CSL to activate transcription of target genes VEGF and CDKN1A[103]. Figure adapted from Aiello et al., 2016[90].

APC: adenomatous polyposis coli; CK1: casein kinase 1; CSL: CBF1/suppressor of hairless/LAG-1; DLL: delta-like; DVL: dishevelled; FZD: frizzled; GSK3β: glycogen synthase kinase 3 β; Hh: hedgehog; JAG: jagged; LEF: lymphoid enhancer binding factor; LRP: lipoprotein receptor protein; MAML: mastermind-like; NICD: notch intracellular domain; PTCH: patched; SMO: smoothened; SUFU: suppressor of fused; TCF: T-cell specific transcription factor.

1.3.1 Shared characteristics of cells in developing tissues and cancer cells

In addition to the recapitulation of developmental signalling pathways, key characteristics of cells in developing tissues are shared with cancer cells (Figure 1.9). Throughout embryonic development cells exhibit rapid proliferation, vigorous angiogenesis, tightly regulated apoptosis and extensive migratory capacity. These properties also define malignant cells, with sustained proliferative signalling, evading growth suppressors, enabling replicative immortality, resisting cell death, activating invasion and metastasis and inducing angiogenesis identified as hallmarks of cancer[110,111].

Early development is characterised by repeated and rapid cell proliferation to ultimately generate all the tissues of multicellular organisms. Hallmark capabilities of cancer cells similarly enable vigorous proliferation through a diverse array of mechanisms. Tumour cells deregulate proliferative signalling pathways, sustaining positively acting growth-stimulatory signals and circumventing anti-growth signals. Additionally, tumour cells acquire limitless replicative potential, bypassing cell cycle control mechanisms and upregulating telomerase to become immortal and chronically proliferative[110,111].

Migratory capacity is also a common biological capability exhibited by cells during both embryogenesis and tumourigenesis. Epithelial-mesenchymal transition (EMT) during embryonic development is fundamental for implantation, gastrulation and organogenesis[112]. EMT describes the process wherein epithelial cells lose their apicobasal polarity and intercellular junctions and gain mesenchymal cell phenotypes, including enhanced migratory capacity. The EMT process is activated in cancer, playing a central role in malignant progression, conferring tumour cell invasiveness and dissemination[113].

Another characteristic shared by cells in development and cancer is angiogenesis. The expansion of blood vasculature networks is necessary during embryogenesis to supply growing tissues with nutrients and oxygen and remove metabolic by-products. Tumour cells are similarly dependent on growing their vascular network to obtain sufficient blood supply and metabolic support. Indeed, inducing angiogenesis is critical for the survival and growth of solid tumours beyond a few millimetres in size[114].

Apoptosis plays an integral role in embryonic development and defects in programmed cell death also contribute to malignant transformation. Precise control of apoptosis is critical for cavitation, tube and vesicle formation and tissue remodelling during development[115]. For instance, apoptosis must be tightly regulated to enable formation of the neural tube and to eliminate interdigital webbings. Tumour cells routinely evade cell death via downregulation or mutation of pro-apoptotic proteins and upregulation of anti-apoptotic proteins enabling prolonged survival[116]. Given the many commonalities between embryogenesis and tumourigenesis, greater understanding of processes essential for development may uncover novel therapeutic strategies for improved cancer treatments.

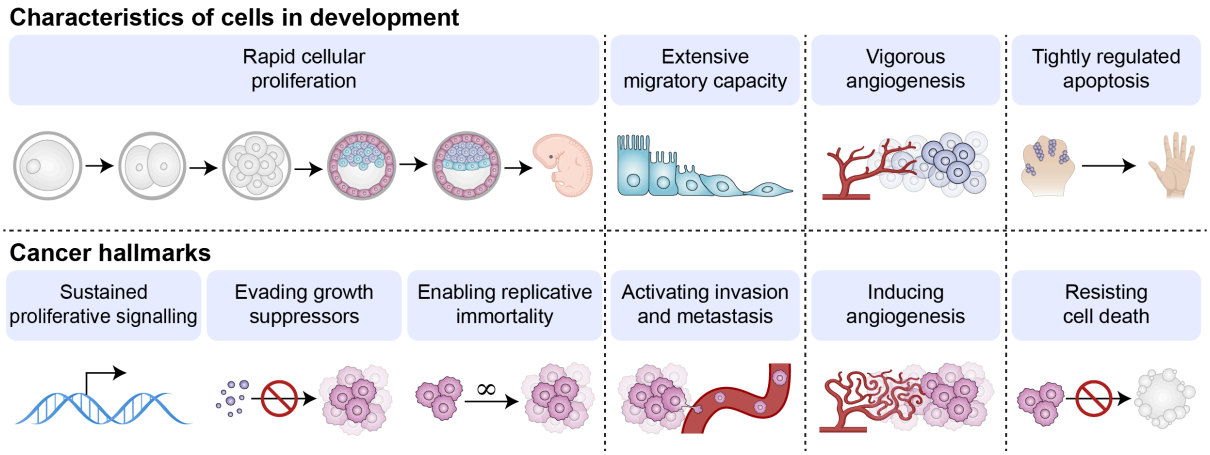

Figure 1.9 Similarities between characteristics of cells during development and cancer hallmarks

Embryonic development is characterised by rapid cellular proliferation, extensive migratory capacity of cells, vigorous angiogenesis and tightly regulated apoptosis. These properties are also recognised as fundamental biological capabilities of cancer cells, with sustained proliferative signalling, evading growth suppressors, enabling replicative immortality, activating invasion and metastasis, inducing angiogenesis and resisting cell death identified as hallmarks of cancer[110,111]. These similarities reflect the close relationship between embryogenesis and tumourigenesis and underpin the idea that the same genes may be involved in the regulation of these processes.

1.4 The zebrafish as a model system for studying human disease

1.4.1 The emergence of zebrafish as a model organism

Zebrafish (*Danio rerio*) offer an ideal *in vivo* vertebrate system for investigating the close relationship between development and cancer. As early as the 1930s, zebrafish were used as a model of embryonic development[117,118]. This initial focus reflects the inherent attributes of zebrafish, notably, the rapid, ex-utero development of optically transparent embryos and larvae. At just 24 hours post fertilisation (hpf) embryos have a beating heart and functioning neurological system with a recognisable vertebrate body plan (Figure 1.10)[119]. Additional advantages of zebrafish include their small size, fast maturation time and fecundity, which facilitates large studies and high-throughput assays[120]. Subsequently, zebrafish have risen to prominence as a valuable model system for studying human disease.

1.4.2 Relevance of zebrafish for modelling human diseases

Despite nearly 400 millions of years of divergent evolution and some quite apparent differences in physiology, genomic sequencing has revealed a high degree of genetic conservation between humans and zebrafish[121]. Approximately 70% of protein-coding human genes have a zebrafish orthologue and 84% of genes known to be associated with human disease have a zebrafish counterpart[122,123]. Moreover, epigenetic marks as well as DNA methylation and histone modification machinery are highly conserved[124]. This has firmly established the value of the zebrafish model as an indispensable tool for advancing understanding of human pathologies. A wide array of diseases are now modelled in zebrafish, including hereditary diseases, neurodegenerative diseases such as amyotrophic lateral sclerosis, anaemia, infection, inflammation, immunological disorders, metabolic syndromes and toxicology[125]. Of greatest relevance to this project is the use of zebrafish to recapitulate mechanisms relevant to human cancer.

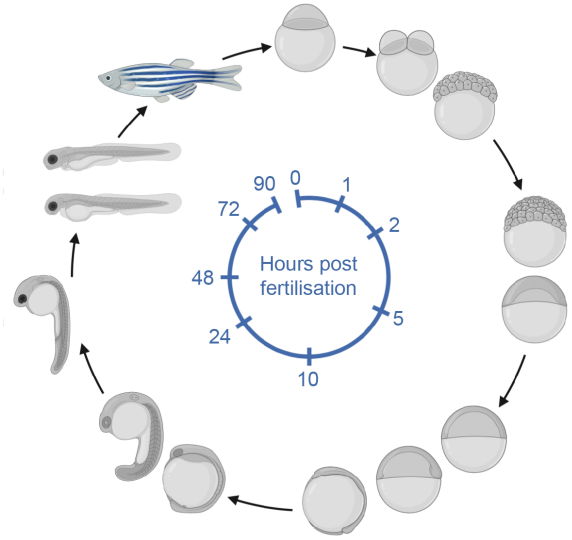

Figure 1.10 Schematic representation of zebrafish embryonic development

Zebrafish develop *ex utero* from a one-cell zygote with a large yolk. Gastrulation commences from 5 hours post fertilisation (hpf) and segmentation and organogenesis begins at around 10 hpf. At 24 hpf embryos have a beating heart, functioning neurological system and recognisable vertebrate body plan. The larval period from 72 hpf is characterised by rapid proliferation, especially of endodermal organs. Zebrafish reach sexual maturity at 3 months post fertilisation (mpf)[119].

1.4.3 Zebrafish as a model of human cancer

Zebrafish cancer models, developed through a variety of methods (Figure 1.11), exhibit remarkable similarities to human tumours at the histological, gene expression and genomic levels[126]. Exposure to mutagens, such as N-methyl-N'-nitro-N-nitrosoguanidine (MNNG), 7,12-dimethylbenz[a]anthracene (DMBA) and N-ethyl-N-nitrosourea (ENU), has been used to induce a wide spectrum of tumours in zebrafish[127]. However, this approach results in the appearance of sporadic tumours in different organs with low frequency and prolonged latency. Consequently, transgenic techniques have been widely utilised to overcome these limitations.

The relative ease with which 1-cell stage zebrafish embryos can be injected with DNA constructs has resulted in the creation of numerous transgenic lines that recapitulate human cancers[128,129]. The first genetically engineered cancer model in zebrafish was of T-ALL, driven by overexpression of the mouse oncogene c-myc, specifically in lymphoid cells[130]. Since then, transgenic technology has been used to successfully model a diverse range of malignancies including melanoma, sarcoma, pancreatic and liver cancer[131-133]. In addition to these cancer models, several transgenic and mutant lines have been developed to enable observation of oncogenic processes *in vivo*. These include the vascular fluorescence reporter line *Tg(fli:EGFP)* and the *casper* mutant which retains much of its embryonic transparency throughout adulthood[134,135]. These models, coupled with the application of inducible strategies for gene expression, have further broadened the possibilities for analysis of human malignancies[136,137]. As too have new methods, such as the recently developed transgene electroporation in adult zebrafish (TEAZ) which allows rapid combinatorial genetic modelling of complex genotypes to efficiently recapitulate human tumours[138].

The development of xenograft models in zebrafish has further facilitated investigation of tumour invasion, metastasis and angiogenesis[139,140]. Prior to the development of the adaptive immune system at 2-3 weeks post fertilisation, human or mouse cells can be readily transplanted into zebrafish[141,142]. This technology, combined with fluorescent labelling of cells has enabled convenient and detailed imaging of tumours, allowing for *in vivo* visualisation of cancer growth and migration at single-cell resolution[126]. Since the first successful xenografts of human metastatic melanoma cells into zebrafish in 2005, the field has rapidly evolved and models based on engraftment of patient-derived tumour cells have been developed[143,144]. Pioneering work, using patient-derived gastrointestinal tumour cells, has demonstrated that zebrafish xenotransplantation models can be used for real-time imaging of metastasis[145]. Genetically immunodeficient lines have also been recently established to enable xenotransplantation of human patient samples into adult zebrafish[146].

Site directed mutagenesis, achieved for example, through the CRISPR-Cas9 system, has further expanded the potential of cancer modelling in zebrafish, enabling modification of multiple genes simultaneously to better reflect the complex mutational landscape of

tumours[147,148]. Together, these zebrafish cancer models offer unique insights into human cancer biology and hold immense promise as *in vivo* platforms for drug discovery[149-151]. The utility of zebrafish for precision oncology applications is also rapidly emerging with transplantation-based zebrafish cancer avatars permitting testing of a wide array of drugs to inform clinical descision[120,152].

The clinical utility of zebrafish cancer models is exemplified by extensive studies on melanoma. Expression of human oncogenic $BRAF^{V600E}$ under the control of the melanocyte-specific promoter *mitfa*, results in the development of melanocytic nevi in adult zebrafish and in melanoma formation on a *tp53* mutant background[153]. Subsequently, the *mitfa:* $BRAF^{V600E}$*,* $tp53^{M214K}$ model has been widely used as a platform for screening, facilitating *in vivo* discovery of modulators of melanoma. For instance, the histone methyltransferase SETDB1 was identified as an oncogene which cooperates with *BRAF to* accelerate melanoma formation[154]. Furthermore, zebrafish melanoma models have revealed that reactivation of neural crest development pathways is critical for initiation of melanoma growth and drives invasion[155-157]. Consequently, a chemical screen of 2,000 compounds was performed in zebrafish embryos to identify suppressors of neural crest progenitors which may be beneficial for melanoma treatment. Treatment with leflunomide, an inhibitor of DHODH (dihydroorotate dehydrogenase) was found to abrogate neural crest development in zebrafish embryos by inhibiting transcriptional elongation and have an anti-proliferative effect on human melanoma cell lines and mouse xenografts[155]. Identification of transcriptional elongation as a novel therapeutic target has directly led to human clinical trials, emphasising the power of the zebrafish system[155,158-161]. Moreover, the suitability of zebrafish for *in vivo* imaging of tumour cell dynamics has provided important insight into melanoma. In particular, imaging of melanoma xenografts in adult zebrafish has revealed that adipocytes are major drivers of melanoma progression, directly donating fatty acids to tumour cells, which modulates metabolism[162]. Taken together, these studies demonstrate the immense potential of zebrafish cancer models for understanding mechanisms of malignant transformation, progression and drug discovery.

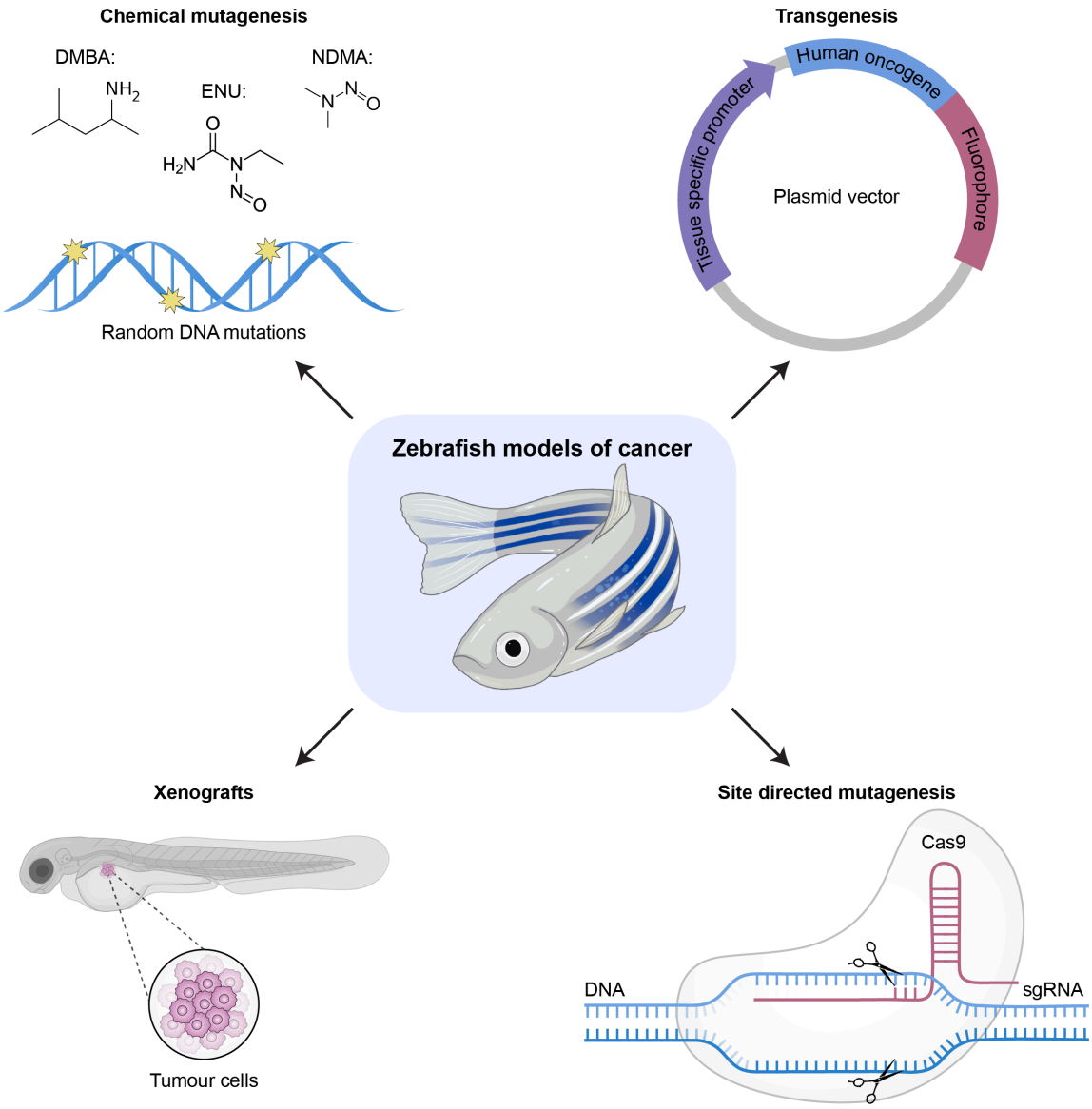

Figure 1.11 Methods for generating zebrafish models of cancer

Zebrafish have emerged as a valuable vertebrate system in which to model human cancer. Exposure to chemical mutagens DMBA (7,12-dimethylbenz[a]anthracene), ENU (N-ethyl-N-nitrosourea) and MNNG (N-methyl-N'-nitro-N-nitrosoguanidine) induce random DNA mutations which can lead to tumour development. Numerous cancer models have been developed through transgenesis, enabling expression of human oncogenes (or their zebrafish counterparts), often under the control of a zebrafish tissue-specific promoter and fused to a fluorophore enabling *in vivo* imaging of tumourigenesis. Site-directed mutagenesis technologies such as CRISPR/Cas9 gene editing have further expanded the potential of modelling cancer in zebrafish. Additionally, xenotransplantation of human tumours cells into zebrafish provides a valuable system to directly visualise tumour metastasis in larvae prior to development of the adaptive immune system.

1.4.4 Zebrafish models of HCC

Zebrafish models are very useful for studying HCC because liver developmental pathways are evolutionarily conserved in vertebrates[163,164]. Consequently, several zebrafish HCC models have been developed, allowing insight into the pathogenesis of liver cancer and acting as a platform for drug screening. Early experiments utilising chemical mutagenesis approaches revealed similar histopathological features and significant conservation of zebrafish and human liver tumour signalling pathways[165-167]. Indeed, comparative oncogenomic approaches have shown that zebrafish and human liver tumours possess similar molecular hallmarks which correlate with tumour progression, including upregulation of cell cycle genes and negative regulators of apoptosis[168]. Carcinogenic chemical treatment induces liver tumours at a range of frequencies after a long latency. For example, DMBA exposure leads to the development of hepatic neoplasms in 30% of zebrafish at 9 months of age, whereas MNNG induces liver tumours at a lower incidence of 7% at 1 year of age[169,170].

Multiple transgenic zebrafish models of HCC, driven by constitutive or inducible oncogene expression, have since been developed (Table 1.1). Constitutive expression systems often resulted in severe tumours and early lethality, impeding complete tumour characterisation and necessitating a switch to inducible systems. For instance, UHRF1 overexpression causes DNA hypomethylation leading to the development of HCC in 76% of zebrafish by 20 dpf[171]. Cre-loxP, GAL4/UAS, mifepristone and tetracycline inducible systems have been successfully exploited in zebrafish, enabling spatiotemporal control of oncogene expression to investigate tumour initiation, progression and regression[165]. Specifically, tetracycline inducible zebrafish HCC models have been established through oncogenic *myc*, *xmrk* and *kras* expression[172-175]. With expression signatures correlating with advanced stages of human HCC[167], these models mimic the cellular and signalling events observed in human HCC of different aetiologies, proving to be an invaluable resource to better understand the complexities underlying tumourigenesis[132].

Of direct relevance to this project are zebrafish HCC models driven by expression of oncogenic *kras*^{G12V}. These elegant models, developed in the laboratory of Professor Zhiyuan Gong at the National University of Singapore, utilise the liver-specific *fabp10* (fatty acid binding protein 10) promoter to restrict the expression of a *EGFP-kras*^{G12V} transgene to hepatocytes. *Tg(fabp10:EGFP-kras*^{G12V}*)* zebrafish that constitutively express *kras*^{G12V}, develop HCC spontaneously between 2 and 12 weeks and this is accelerated upon *tp53* loss[173]. To exert synchronous control over the timing and potency of oncogene expression, various conditional transgenic models were subsequently developed to enable inducible *kras*^{G12V} expression in the liver, including the *Tg(fabp10:rtTA2s-M2;TRE2:EGFP-kras*^{G12V}*)* line (Figure 1.12)[176]. This transgenic line was generated via co-microinjection of two gene cassettes, p*fabp10-rtTA2s-M2* and p*TRE2-EGFP-kras*^{G12V} into one-cell stage embryos. Thousands of injected embryos were then raised to adulthood and one F0 zebrafish identified with the transgenes positioned close enough in the genome to always be inherited together without recombination. In this

model, herein denoted *TO(kras^{G12V})*, the doxycycline-inducible expression of a *EGFP-kras^{G12V}* transgene leads to the accumulation of a constitutively active, EGFP-tagged oncogenic form of Kras specifically in hepatocytes resulting in hyperplasia[176].

The flexibility of the model has been exploited by the application of various treatment regimes in both larvae and adults. Comparative transcriptomic analysis has shown that the gene expression profile of oncogenic *kras^{G12V}* hepatocytes isolated from 8 dpf larval zebrafish (treated with 20 µg/mL doxycycline for 5 days) strongly resembles that of early-stage human HCC, with elevated expression of RAS/RAF/MAPK target genes such as *FGFR4*, *ETV4*, *EPHA2*, *DUSP6* and *SPRY* and DNA damage response genes *GADD45B*, *CCND1* and *H2AX1*[177]. In adult fish, induced expression of *kras^{G12V}* by doxycycline treatment (starting at 4 mpf, treated with alternating doses of 10 and 20 mg/L doxycycline bi-weekly) results in HCC development at 100% penetrance 1.5 months post induction[178]. The immune system, particularly neutrophils and macrophages, plays a major role in tumour progression in this model, and this is also a feature of human HCC[179,180]. Similarly, sex hormone-induced differences in tumour onset are observed in zebrafish HCC models, reflecting the gender disparity in human HCC, with an increased prevalence in males[178,181,182]. Thus, this model provides a clinically relevant *in vivo* platform for the study of human cancer and the discovery of new therapeutic strategies.

Table 1.1 Zebrafish transgenic models of HCC

Construct	Expression system	Liver pathology	Reference
***zfBLP1* (zebrafish)**	Constitutive	Hyperplasia	183
***zfMcl-1a* (zebrafish)**	Constitutive	Hyperplasia	183
HCV + TAA (human)	Constitutive	Steatosis, cirrhosis, HCC	184
***ORFA* (human)**	GAL4/UAS	Delayed onset of liver tumours	185
***kras*^{G12V} (zebrafish)**	Constitutive	Hyperplasia, hepatocellular adenoma, HCC	173
***kras*^{G12V} + *tp53*^{M214K} (zebrafish)**	Constitutive	Hyperplasia, hepatocellular adenoma, HCC	173
***xmrk* (xiphophorus)**	Tet-on inducible	Hyperplasia, hepatocellular adenoma, HCC	175
HBx + HCV (human)	Tet-off inducible	Intrahepatic cholangiocarcinoma	186
***kras*^{G12V} (zebrafish)**	Mifepristone inducible	Hyperplasia, HCC	174
***Myc* (mouse)**	Tet-on inducible	Hyperplasia, HCC	172
HBx + AFB1 (human)	Constitutive	Hepatitis, steatosis, hyperplasia	187
HBx + *tp53*^{M214K} (zebrafish)	Constitutive	Chronic inflammation, steatosis, bile duct dilation, hyperplasia, dysplasia, HCC	188
HBx + *src* (human/zebrafish)	Constitutive	Chronic inflammation, steatosis, bile duct dilation, dysplasia, HCC	188
***src* (zebrafish)**	Constitutive	Chronic inflammation, steatosis, bile duct dilation, hyperplasia, dysplasia, HCC	188
***src* + *tp53*^{M214K} (zebrafish)**	Constitutive	Steatosis, bile duct dilation, hyperplasia, dysplasia, HCC	188
***kras*^{G12V} (zebrafish)**	Tet-on inducible	Hyperplasia, hepatocellular adenoma, HCC	176
***kras*^{G12V} + *rhoa*^{G14V} (zebrafish)**	Tet-on inducible	Hyperplasia, hepatocellular adenoma, HCC	176
***kras*^{G12V} + *rhoa*^{T19N} (zebrafish)**	Tet-on inducible	HCC	176
***kras*^{G12V} + *rhoa* (zebrafish)**	Tet-on inducible	Hyperplasia, hepatocellular adenoma, HCC	176
***edn1* (zebrafish)**	Constitutive	Steatosis, bile duct dilation, hyperplasia, HCC	189
***UHRF1* (human)**	Constitutive	Atypical cells, dysplastic foci, HCC	171

***UHRF1* + *tp53*^{M214K} (human/zebrafish)**	Constitutive	Atypical cells, HCC	171
***ctnnb1* (xenopus)**	Constitutive	Atypical cells, HCC	190
***Myc* + *xmrk* (mouse/xiphophorus)**	Tet-on inducible	HCC	191
***myca* (zebrafish)**	Mifepristone inducible	Hyperplasia, hepatocellular adenoma, HCC	192
***myca* + *tp53*^{M214K} (zebrafish)**	Mifepristone inducible	Hyperplasia, HCC	192
***mycb* (zebrafish)**	Mifepristone inducible	Hyperplasia, HCC	192
***kras*^{G12V} (zebrafish)**	Mifepristone inducible Cre-lox recombination	Hepatoblastoma, hepatocellular adenoma, HCC	193
***nras*^{Q61K} (zebrafish)**	Constitutive	Intrahepatic cholangiocarcinoma	194
***tgfb1a* (zebrafish)**	Mifepristone inducible	Hyperplasia, intrahepatic cholangiocarcinoma, hepatocellular adenoma, HCC	195
***RPIA* (human)**	Constitutive	Steatosis, hyperplasia, dysplasia, HCC	196
***ctnnb1* (xenopus)**	Cre-lox recombination	HCC	197
***kras*^{G12V} + L-ARKO (zebrafish)**	Tet-on inducible and Cas9-CRSIPR gene editing	Hyperplasia, hepatocellular adenoma, HCC	198
***xmrk* + CreER (xiphophorus)**	Tet-on inducible and Cre-lox recombination	HCC	199
HBx + *src* + *tp53*^{M214K} (zebrafish)	Constitutive	HCC	200
***xmrk* + *Twist1a-ER*^{T2} (xiphophorus)**	Tet-on inducible and tamoxifen inducible	Metastatic HCC	201

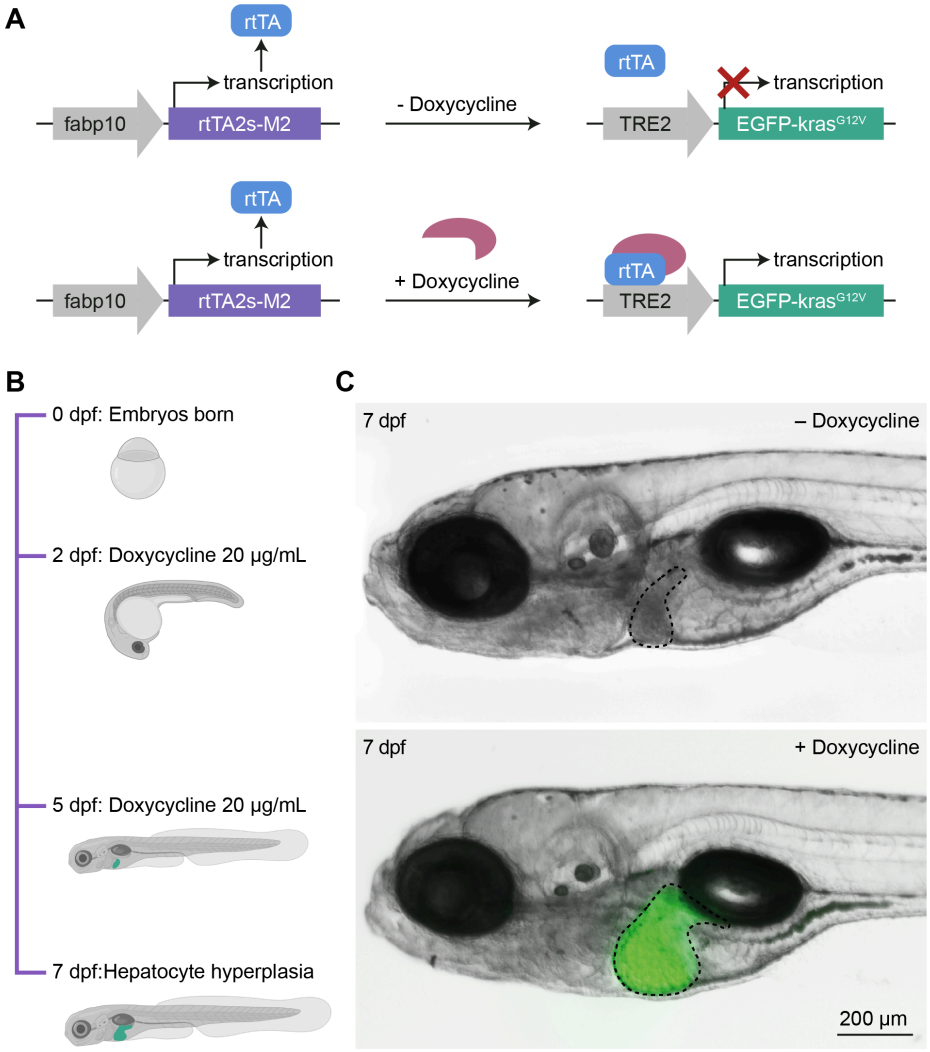

Figure 1.12 *TO(kras^{G12V})* model of HCC

A. The *TO(kras^{G12V})* transgenic line contains two gene cassettes, the *fabp10-rtTA2s-M2* and the downstream *TRE2-EGFP-kras^{G12V}*. The *fabp10* promoter drives the liver-specific expression of rtTA. In the absence of doxycycline, the rtTA protein cannot bind the TRE and hence EGFP-Kras^{G12V} is not expressed. In the presence of doxycycline, the rtTA protein can bind to the TRE, initiating the transcription of *EGFP-kras^{G12V}*. **B.** Protocol for doxycycline induction in *TO(kras^{G12V})* larvae. **C.** Brightfield images of untreated and doxycycline-treated *TO(kras^{G12V})* larvae at 7 dpf. Dashed line in upper panel indicates the normal liver. In response to doxycycline (lower panel), liver-specific EGFP-Kras^{G12V} expression results in hepatocyte hyperplasia and considerable liver enlargement. The expression of EGFP fluorescence permits the accurate quantitation of liver volume by 2-photon microscopy.

dpf: days post fertilisation; EGFP: enhanced green fluorescent protein; fabp10: fatty acid binding protein 10; rtTA: reverse tetracycline-controlled transactivator; TRE: tetracycline response element.

1.4.5 Genetic screens in zebrafish

The overarching paradigm underlying this thesis is that genes that are critical for the rapid growth and proliferation of cells during development are also likely to be essential for the growth and proliferation of cancer cells, thereby providing novel targets for cancer treatment. Also taken into account in this approach is an appreciation that the genetic pathways that drive the growth of developing organs are usually downregulated in adult animals, only to be reactivated again within the same organ(s) when the adult organism develops cancer. Therefore, to prosecute this argument in the context of liver cancer, my goal was to investigate genes that are indispensable for the huge expansion of the endoderm-derived digestive organs (liver, pancreas and intestine) during development and test whether they are also critical in the context of liver cancer. To achieve this, I took advantage of several genes that had been shown by previous students in the Heath laboratory, using ENU mutagenesis and positional cloning, to be required for digestive organ development.

It was pioneering research by George Streisinger that first demonstrated that zebrafish are highly suitable for genetic analysis and screening[202]. Forward genetic screens involve inducing mutations at random in adult zebrafish via exposure to chemical, viral or transposon-based mutagens. These mutations are then bred to homozygosity in subsequent generations, at which point embryos are screened for phenotypes of interest (Figure 1.13). The first large-scale vertebrate zebrafish genetic screens, performed in Boston and Tübingen, using ENU as a mutagen, recovered over 6000 mutants in embryonic development, of which 1740 were retained[203,204]. The isolated mutants exhibited defects in circulation, formation of the major body axis, somites, forebrain, fins, eye and heart. However, only 12 mutants with abnormal endodermal phenotypes were identified, largely due to of the deep internal position of these organs compared to more prominent tissues and the relatively late stage of their development. One of these mutants, isolated in the Tübingen screen designated *flotte lotte* (*flo*^{ti262c})[205], is investigated in this thesis.

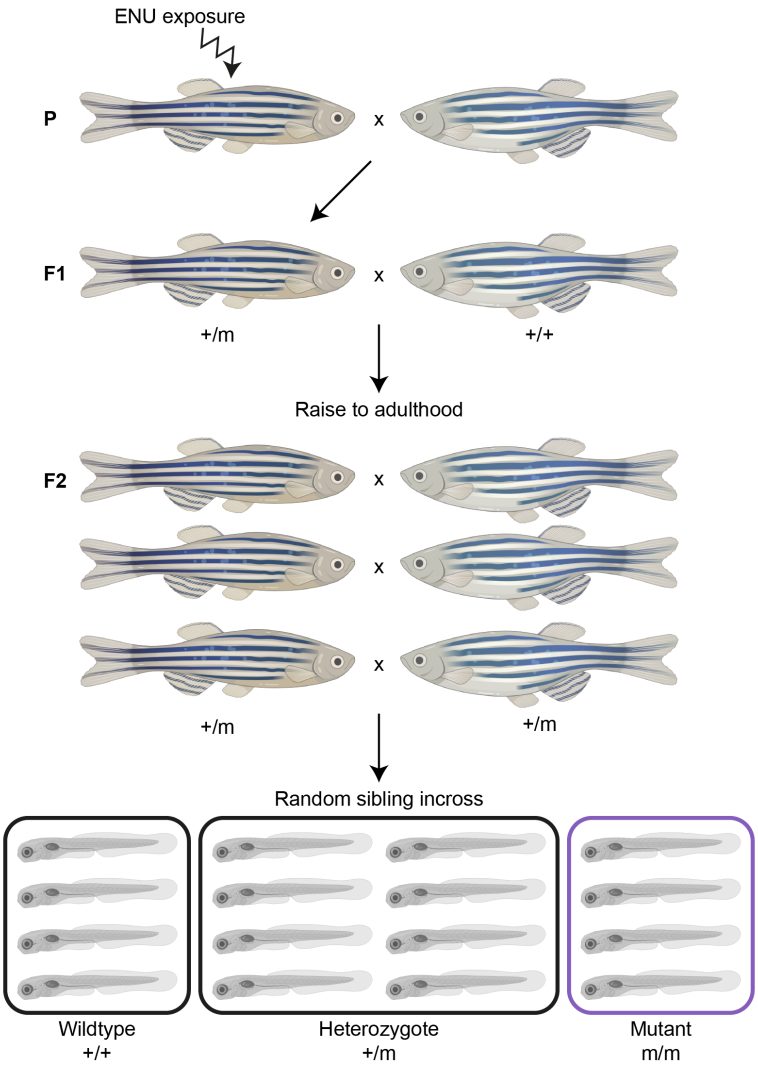

Figure 1.13 ENU mutagenesis screens in zebrafish

Adult male zebrafish are exposed to ENU (N-ethyl-N-nitrosourea) which introduces mutations randomly throughout the genome. Mutagenized fish are outcrossed to generate the F1 population. Subsequent in-crossing of siblings through two generations drives induced recessive mutations to homozygosity, producing one quarter mutant progeny in the F3 generation. Figure adapted from Patton et al., 2001[206].

1.4.6 A genetic screen to identify zebrafish mutants with disrupted endoderm organ development

As only a dozen mutants with endodermal abnormalities were recovered from the large-scale zebrafish mutagenesis screens[205,207], our laboratory participated in a focused, transgene-assisted screen to expand upon this collection[208]. To facilitate the identification of mutations affecting endodermal organ morphogenesis, the screen was performed on the *Tg(gutGFP)*^{s854} line. This transgenic zebrafish line expresses green fluorescent protein (GFP) throughout the developing liver, intestine and pancreas[209,210]. Over 100 mutants with abnormal GFP expression were recovered, 15 of which exhibited intestinal, liver and pancreas abnormalities. These included a second *flo* mutant allele *(flo*^{s871}*)*[211], along with a mutant designated *caliban (clbn*^{s846}*)*[212], which was also chosen for investigation in this study.

Bright-field microscopy and histological analysis showed that compared to the extensively folded and polarised intestinal epithelium in wildtype larvae, *flo* and *clbn* mutants have a thinner, unfolded intestinal epithelium and a smaller liver and pancreas. Both mutants also showed gross morphological defects within the highly proliferative cell compartments of the brain, eye and pharyngeal arches, whereas relatively quiescent tissues remained healthy. *flo* mutants were characterised by catastrophic levels of cell death in the developing intestinal epithelium[211,213], whereas *clbn* mutants displayed a growth arrest phenotype[212] (Figure 1.14). PhD students in the Heath laboratory, Tanya de Jong Curtain and Sebastian Markmiller, used positional cloning to identify the mutant genes underlying the observed phenotypes as *ahctf1,* which encodes Elys a component of the nuclear pore complex (NPC) in *flo,* and *rnpc3* which encodes 65K a component of the U12-dependent spliceosome in *clbn*[211,212].

1.5 Hypothesis and aims

Whilst both *ahctf1* and *rnpc3* homozygous mutants survive through early development due to maternal deposition of mRNA and protein in the yolk, mutation is ultimately lethal at 9-10 dpf. In contrast, heterozygous mutants have no gross morphological phenotypes under homeostatic conditions, achieving sexual maturity and exhibiting a normal lifespan. Together, these observations suggest that the functions of both *ahctf1* and *rnpc3* represent an Achilles heel of rapidly proliferating cells for which a viable therapeutic window exists and that may extrapolate to cancer. In order to address this hypothesis, the following specific aims of this PhD study were developed:

1. Determine whether the nucleoporin Elys provides a target for cancer treatment with a viable therapeutic window
2. Determine whether the 65K component of the U12-dependent spliceosome provides a target for cancer treatment with a viable therapeutic window
3. Establish the zebrafish model of HCC as a tractable, *in vivo* platform for testing novel cancer therapeutics

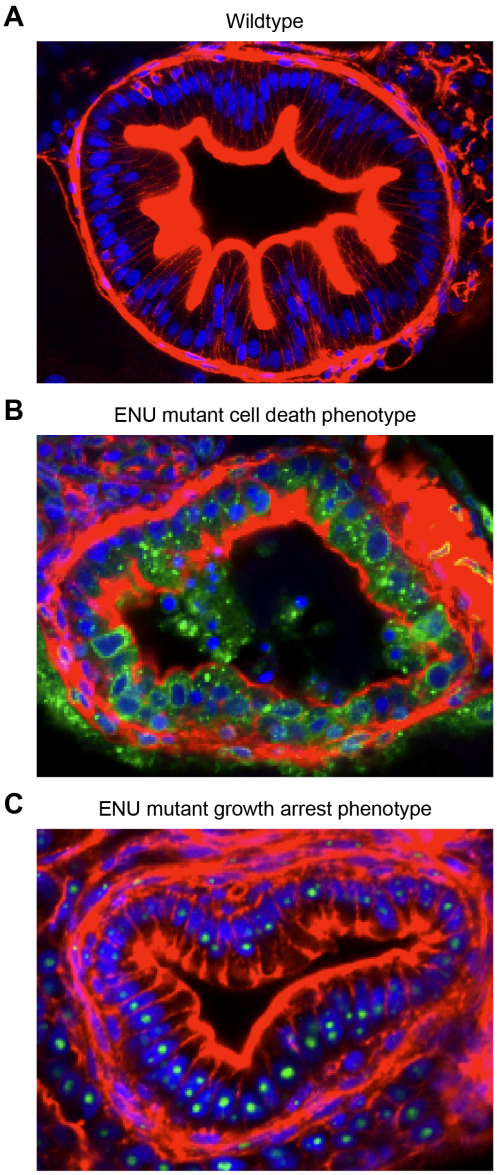

Figure 1.14 Phenotypes of zebrafish ENU endodermal mutants

Confocal imaging of 200 µm thick sections of the intestinal epithelium of 78 hpf larvae stained with rhodamine phalloidin (red) to mark F-actin and Hoechst 33342 (blue) marking DNA. **A.** In wildtype larvae the intestinal epithelium is elaborately folded and comprises polarised columnar cells with basally positioned nuclei. **B.** *flo* mutants generated in the Tübingen ENU mutagenesis screen exhibit a cell death phenotype exhibiting a thinner unfolded intestinal epithelium with large numbers of apoptotic cells in the lumen. mAb414 marking nuclear pore complexes are shown in green. **C.** *clbn* mutants generated in the Liver^{plus} ENU mutagenesis screen displayed a growth arrest phenotype, resulting in a thin intestinal epithelium. Fibrillarin marking nucleoli is shown in green.

2 Materials and methods

2.1 Zebrafish

2.1.1 Housing and ethics

Zebrafish were maintained at 28.5°C on a 12 h light/12 h dark cycle according to standard husbandry procedures of the WEHI Zebrafish Aquarium and then the University of Melbourne Zebrafish Aquarium. These procedures were based on those described in The Zebrafish Book[214]. All experiments were approved by the WEHI Animal Ethics Committee.

2.1.2 Zebrafish mutant and transgenic lines

The zebrafish mutant line *flo*, *ahctf1*^{ti262}, was generated in the Tübingen ENU mutagenesis screen[205], and has an C to T transition mutation creating a premature stop at codon 1319 of the *ahctf1* gene. The *ranbp2*^{s452}mutant line was generated in the Liver^{plus} ENU mutagenesis screen[208], and has a T to A transversion mutation introducing a premature stop codon in exon 19 of the *ranbp2* gene. The *clbn*, *rnpc3*^{s846} mutant line was also generated in the Liver^{plus} screen[208], and has a T to A transversion mutation resulting in a cryptic acceptor splice site at the -12 position of the 3' splice site of intron 13 of the *rnpc3* gene resulting in premature protein truncation. Subsequently, another *rnpc3* null allele became available from a commercial source, Znomics (RRID: ZFIN_ZDB-GENO-140806-3) and was used in this thesis. In this mutant line the *rnpc3* locus is disrupted by retroviral insertion into intron 1, resulting in undetectable mRNA transcripts[212]. The *tp53*^{M214K} mutant line, referred to as *tp53*$^{m/m}$, has a T to A missense mutation in the tp53 DNA binding domain, preventing activation of *tp53* target genes, and has been previously described[215].

The *Tg*(*fabp10:dsRed, ela3l:GFP*)^{gz12} transgenic line, referred to as *2-CLiP*, expresses dsRed in the liver and GFP in the exocrine pancreas but carries no oncogenic transgenes or mutations[216]. The *Tg(fabp10:rtTA2s-M2;TRE2:EGFP-kras*^{G12V}*)* line referred to as *TO(kras*^{G12V}*)* has been described previously[176]. The cell death reporter line (a gift of Dr Thomas Hall, Institute for Molecular Bioscience, University of Queensland), *Tg(actb2:SEC-Hsa.ANXA5-mKate2,cryaa:mCherry)*^{uq24rp}, referred to as *Annexin 5-mKate* constitutively expresses a fusion protein comprising Annexin 5 and the far-red fluorophore mKate[217].

2.1.3 Embryo production

Embryos were produced by natural spawning of mating pairs set up in breeder boxes. Embryos were collected and transferred into Petri dishes with E3 medium (5 mM NaCl, 0.17 mM KCl, 0.33 mM $CaCl_2$, 0.33 mM $MgSO_4$) and placed in a 28.5°C incubator. Embryos were transferred into E3 medium with 0.003% 1-Phenyl-2-thiourea (PTU; Sigma, #P7629) at 10-24 hpf to inhibit pigmentation and maintained at a density of 50 embryos per Petri dish. Embryos were inspected daily and dead embryos, debris and embryos with developmental defects such as oedemas were removed to prevent fungal and bacterial contamination.

2.1.4 Raising embryos to adulthood

Embryos to be raised to adulthood were maintained in E3 medium in Petri dishes at a density of 50 embryos in a 28.5°C incubator until 5 dpf. After 5 dpf, larvae were transferred into 3 L tanks and fed live *Paramecium* cultures twice daily. After approximately 14 dpf, larvae were fed a combination of *Paramecium* and *Artemia* (Primo Aquaculture). Between 21-28 dpf, zebrafish were transferred to the main aquarium system and fed *Artemia* and pellet feed (Primo Aquaculture). Fish generally reached sexual maturity at 3 months of age.

2.1.5 Inducing hepatocellular hyperplasia in zebrafish

To induce mutant Kras expression, *TO(kras^{G12V})* larvae were treated with 20 μg/mL doxycycline (Sigma, #D9891) at 2 dpf in E3 medium with 0.003% PTU (Sigma, #P7629) to suppress pigmentation. E3 medium was changed at 5 dpf and fresh doxycycline (final conc. 20 μg/mL) added.

2.1.6 Drug treatments in zebrafish

At 5 dpf, zebrafish larvae were treated with DMSO vehicle control (Sigma, #D2650) or various drugs (Table 2.1) serially diluted in E3 medium with 0.003% PTU (Sigma, #P7629). Larvae were monitored daily to assess drug toxicity. Morphological and molecular analyses were performed at 7 dpf.

Table 2.1 Drug treatment compounds

Drug	Description	Concentrations (μM)	Source/Reference
EPZ015666	PRMT5 inhibitor	00.01-10.00	Cancer Therapeutics, Ctx
Hit 1	U12-dependent splicing inhibitor screen hit	00.50-05.00	WEHI
Inactive	U12-dependent splicing inhibitor screen inactive analogue	00.50-05.00	WEHI
MEK162	MEK inhibitor	01.00-20.00	Selleckchem, #S7007
Selinexor (KPT-330)	XPO1 inhibitor	00.10-02.00	Karyopharm
WM-2474	KAT6A/B inactive analogue	01.00-10.00	Baell et al., 2018[218]
WM-8014	KAT6A/B inhibitor	01.00-10.00	Baell et al., 2018[218]

2.2 Histology and immunohistochemistry

2.2.1 Fixation of larvae

Larvae were anaesthetised with benzocaine (200 mg/L; Sigma, #PHR1158) and fixed O/N in 4% paraformaldehyde (PFA) in phosphate-buffered saline (PBS) at 4°C. After fixation, larvae were washed several times with PBS/0.1% Tween 20 and incubated in 30% sucrose in PBS O/N at 4°C.

2.2.2 Vibratome sectioning and immunofluorescence staining

Fixed larvae were aligned and embedded in Tissue-Tek cryomoulds (ProSciTech) in 4% low melting point agarose (Invitrogen, #16520100) and transverse sections taken at 200 µm intervals using a vibrating microtome (Leica VT 1000S). Sections were blocked with 1% BSA in PBS/0.3% Triton X-100 and incubated with 1:750 mAb414 (Abcam, #ab24609) at 4°C overnight. Sections were then incubated with 1:500 anti-mouse AF647 (Thermofisher, #A21235) and 1:500 Hoechst 33342 (Thermofisher, #62249) at room temperature for 1 h. Sections were mounted in Prolong Diamond Antifade Mountant (Thermofisher #P36961) with a coverslip. Image acquisition was performed using a Zeiss LSM880 Fast Airyscan Confocal microscope with a 63x objective. Excitation wavelengths for Hoechst and AF647 were 405 nm and 633 nm, respectively.

2.2.3 Cryostat sectioning and immunofluorescence staining

Fixed micro-dissected livers were aligned and embedded in Tissue-Tek cryomoulds (ProSciTech) in OCT (Milestone, #51420)and frozen on dry ice. The tissue was sectioned at 10 µm intervals using a Thermofisher Scientific Microm HM550 cryostat. Sections were washed with PBS before blocking with 10% FCS in PBS/0.3% Triton X-100. Incubation with primary antibodies was performed at 4°C O/N, while incubation with secondary antibodies was performed at RT for 1 h. Antibodies used in this work were: 1:2000 α-Tubulin DM1A (CST, #3873), 1:1000 γ-H2AX (Abcam, #ab11174), 1:250 cleaved caspase-3 (CST, #9664), 1:500 anti-rabbit AF647 (Thermofisher scientific, #A31573) and 1:500 anti-mouse AF647 (Thermofisher, #A21235). Prolong Diamond Antifade Mountant with DAPI (Thermofisher #P36962) was used for slide mounting. Image acquisition was performed using a Zeiss LSM880 Fast Airyscan Confocal microscope with a 63x objective. Excitation wavelengths for DAPI and AF647 were 405 nm and 633 nm, respectively.

2.2.4 EdU proliferation assay

To assess the percentage of cells in S phase of the cell cycle, 7 dpf zebrafish larvae were incubated in 2 mM EdU in E3 medium for 2 h followed by a further incubation in fresh E3 medium for 1 h. Larvae were euthanized using benzocaine (1000mg/L; Sigma, #PHR1158) prior to removal of the liver by dissection. Micro-dissected livers were fixed in PFA as previously described and permeabilised by incubation in PBST/0.5% Triton-X at 4°C O/N. EdU labelling was carried out using the Click-iT Edu Alexa Fluor 647 (AF647) imaging kit (Invitrogen,

#C10340) according to the manufacturer's instructions. The livers were co-stained with Hoechst 33342 (Thermofisher, #62249). Image acquisition was performed using an Olympus FVMPE-RS multiphoton microscope with a 25x objective and Olympus FV30-SW software, utilising a z-stack step size of 2 µm. Excitation wavelengths for Hoechst and AF647 were 950 nm and 1160 nm, respectively.

2.3 Imaging techniques

2.3.1 Brightfield microscopy

Larvae were anaesthetised with benzocaine (200 mg/L; Sigma, #PHR1158) and aligned in 1% agarose. Brightfield and epifluorescence images were acquired using a Nikon SMZ1500 fluorescent microscope with a DXM1200C camera and NIS Elements AR 3.06 software.

2.3.2 Two-photon microscopy

To quantitate liver volume, larvae were anaesthetized with benzocaine (200 mg/L; Sigma, #PHR1158) and aligned in 1% agarose. Image acquisition was performed using an Olympus FVMPE-RS multiphoton microscope with a 25x objective and Olympus FV30-SW software, utilising a z-stack step size of 2 µm. Excitation wavelengths for GFP and dsRed were 840 nm and 1100 nm, respectively.

2.3.3 Confocal microscopy

To assess apoptosis, *TO(kras^{G12V})*; *Annexin 5-mKate* zebrafish larvae (7 dpf) were fixed in PFA as previously described and livers isolated by micro-dissection. Image acquisition was performed using a Zeiss LSM 880 microscope with a 20x objective and ZEN software, utilising a step size of 2 µm. Excitation wavelengths for mKate and GFP were 561 nm and 860 nm, respectively.

2.4 Imaging analysis

2.4.1 Liver volumetric analysis

Volumetric analysis was performed in ImageJ by default thresholding of EGFP signal (for *TO(kras^{G12V})$^{T/+}$* larvae) or dsRed signal (for 2-*CLiP* larvae) and automatic processing with a macro that increased signal intensity with depth to compensate for the gradual decline in signal. Signal area was then calculated per slice and converted into volume by multiplication with z-stack step size (2 µm). Representative three-dimensional reconstructions of liver volume were generated using Imaris (v9.1.2) software by default surface rendering.

2.4.2 EdU proliferation analysis

The number of Hoechst 33342 and EdU positive nuclei was quantified using Arivis Vision4D software. The Segment Generation Blob Finder Feature was used to segment nuclei with an average diameter of 10 µm with the threshold set to 5.00%. A watershed algorithm was then

applied to identify object boundaries with the split sensitivity set to 55, allowing quantification of the total number of nuclei and EdU positive nuclei.

2.4.3 Cell death analysis

Volume of micro-dissected *TO(kras^{G12V})*; *Annexin 5-mKate* livers was quantified as described previously. Annexin 5-mKate signal, generated when the secreted Annexin 5-mKate fusion protein binds to phosphatidylserine on the inner leaflet of plasma membranes that are exposed during apoptosis, was quantified in ImageJ by 3D simple segmentation with a minimum object size of 10 pixels and the threshold set to 300.

2.4.4 Nuclear pore complex analysis

3D segmentation of nuclei was performed in ImageJ by default thresholding of Hoechst signal and 3D watershed detection. Morphological filtering was used to define the nuclear periphery as the 2 voxels surrounding nuclei. The cytoplasmic area was distinguished by subtraction of Hoechst 33342 nuclear signal and 3D segmentation of cells by default thresholding of EGFP signal (for *TO(kras^{G12V})$^{T/+}$*) or F-actin (for *TO(kras^{G12V})$^{+/+}$* stained with 1:200 Rhodamine phalloidin at the same time as secondary antibody incubations) and 3D watershed detection to define cell membranes. mAb414 fluorescence intensity was then calculated for the nuclear periphery and for the cytoplasm. NPC density was calculated by manual selection of nuclear surface area and automatic finding of mAb414 signal maxima for 5 nuclei per liver.

2.5 Molecular biology techniques

2.5.1 DNA isolation and genotyping

Zebrafish larvae (5 dpf) were anaesthetised with benzocaine (200 mg/L; Sigma, #PHR1158) and the tip of the tail fin clipped distal to blood circulation. Larvae were then placed in 150 µL of E3 medium with 0.003% PTU (Sigma, #P7629) in a 96-well plate until protein/RNA extraction or fixation at 7 dpf. Genomic DNA (gDNA) was extracted from fin clips by incubation at 95°C for 10 min in 20 µL of 50 mM sodium hydroxide (NaOH), followed by neutralization with 2 µL of 1 M Tris-HCl (pH 8.0).

7 dpf larvae or adult zebrafish were anaesthetised with benzocaine (200 mg/L) and fin clipped. gDNA was extracted by incubation at 95°C for 20 min in 50 µL of 50 mM sodium hydroxide (NaOH), followed by neutralization with 5 µL of 1 M Tris-HCl (pH 8.0).

Polymerase chain reaction (PCR) was performed using MyTaq HS Red Mix (Bioline, #25047). Oligonucleotides used for genotyping are listed in Table 2.2. PCR products were visualised by electrophoresis on 2% agarose gels.

Table 2.2 Zebrafish genotyping primer sequences

Gene	Forward (5'-3')	Reverse (5'-3')
ahctf1	TGACATGCATGCCCTCTCTG	TAGCTGCTCCTCGCTTACGT
EGFP-TO(kras)	ATGGTGAGCAAGGGCGAGGA	CGTCCTTGAAGAAGATGGTGCG
ranbp2	CGCCGATCAAGAGGACGAAA	TGTCCGCCGTAACACTACTC
rnpc3 wildtype	TTATGATTGATGCAGAAGCG	GGAGGTTTGTTTTGAAGCGA
rnpc3 mutant	ACAGACACAGATAAGTTGCTGGCC	GGAGGTTTGTTTTGAAGCGA
tp53 wildtype	AGCTGCATGGGGGGGAT	GATAGCCTAGTGCGAGCACACTCTT
tp53 mutant	AGCTGCATGGGGGGGAA	GATAGCCTAGTGCGAGCACACTCTT

For *ahctf1* larvae, a restriction fragment length polymorphism was used for genotyping as the *flo*^{ti262} mutation generated a novel Tsp45I restriction enzyme site. After PCR amplification of a 482 bp fragment containing the *ahctf1* mutation, restriction digest with 0.01 units/µL of Tsp45I (New England BioLabs, #R0583L) was performed for 3 h at 65°C before products were visualised by electrophoresis on 2% agarose gels.

2.5.2 RNA extraction

Total RNA was extracted from independent pools of micro-dissected zebrafish livers or individual livers using the RNeasy Micro Kit (QIAGEN, #74004) following the manufacturer's guidelines including DNAse treatment. RNA integrity was assessed by a High Sensitivity RNA ScreenTape assay (Agilent, #5067-5579) on a 2200 TapeStation.

2.5.3 cDNA synthesis

cDNA was generated from 1-10 µg RNA using the Superscript III First Strand Synthesis System (Invitrogen, #18080051) and oligo(dT) priming according to the manufacturer's instructions.

2.5.4 RT-qPCR

Reverse transcription-quantitative PCR (RT-qPCR) was performed using a SensiMix SYBR kit (Bioline, #QT605-05) on an Applied Biosystems ViiATM7 Real-Time PCR machine. Expression data were normalised by reference to *hrpt1*, *b2m* and *tbp*. LinRegPCR V11.0 was used for baseline correction, PCR efficiency calculation and transcript quantification analysis[219]. Relative expression levels were calculated by the $2^{-\Delta\Delta Ct}$ method and all results were expressed as the mean ± SEM of three independent biological replicates. Primer sequences are listed in Table 2.3.

Table 2.3 RT-qPCR primer sequences

Gene	Forward (5'-3')	Reverse (5'-3')
ahctf1	GGTGAGTCAGTGTGGGGAAC	CCAGCAGGGCATGAAGTGAT
b2m	GCGGTTGGGATTTACATGTTG	GCCTTCACCCCAGAGAAAGG
bad	AGCAGCACCTCACTGTTCCT	CCAGTTTCCAGCAAGTCCTC
bax	GGAGATGAGCTGGATGGAAA	GGGCCACTCTGATGAAGACA
bbc3 (puma)	GATGCCTTCAGCTTGGAC	GCCTGGACACTTCCTGTTCT
bcl2	GGATCGAGGAAAATGGAGGT	AAAACGGGTGGAACACAGAG
bclxl	CAACCATATTCAACCCTGGA	TTCTTGCGATTTCCTGCT
bid	ACCAGCGACCTACAGAGACC	TCTGCATTGACTGAAAGACCA
bik	TTGCTTCCACAGCTTCAAAA	ATGTAGTGCTGCGAGACCAG
bim	GCACTTTGATTTCCCTCAGC	TGGAGAAAGTCCGGTTCATC
cdkn1a (p21)	CAAGCCAAGAAGCGTCTAGTG	AACGGTGTCGTCTCTGGTTC
cdkn2a/b (p16)	CGAGGATGAACTGACCACAGC	CAACAGCCAAAGGTGCGTTAC
egfp	ATGGTGAGCAAGGGCGAGGA	CGTCCTTGAAGAAGATGGTGCG
hrpt1	GAGGAGCGTTGGATACAGA	CTCGTTGTAGTCAAGTGCAT
mdm2	TGACAAAGAAACTGGTAAGA	AAACATAACCTCCTTCATGGT
pmaip1 (noxa)	ATGGCGAAGAAAGAGCAAAC	TCATCGCTTCCCCTCCATTTG
rnpc3	AGGCCCTGAAGGAAACCAAT	TCAACCAGGGCAGTCACTTCA
tbp	CAGGCAACACACCACTTTAT	AAGTTTACGGTGGACACAAT
tp53	TCCACTCTCCCACCAACATC	GGGAACCTGAGCCTAAATCC
tp63	CGGCCTGTTTGGACTATTTC	ACTCCATGATGCCTTTCCAG
tp73	GGCCAATCCTCATCATCATC	TCCCTGAATGGTCTTCGTC
Δ113tp53	ATATCCTGGCGAACATTTGG	ACGTCCACCACCATTTGAAC

2.5.5 Library preparation and RNA-sequencing

RNA was isolated from individually micro-dissected livers as described previously and 100 ng per sample of RNA was used for RNA-sequencing library preparation using the TruSeq RNA Sample Prep Kit with Ribo-Zero depletion (Illumina) according to manufacturer's instructions. Indexed libraries were sequenced on a NextSeq 500 instrument (Illumina) to generate 80 bp paired-end reads and yielding ~20 million reads per sample. Bioinformatic analyses were conducted by Dr. Alexandra Garnham of the WEHI Bioinformatics Support Unit.

All samples were aligned to the GRCz11 build of the zebrafish genome using the align function from the Rsubread software package (v2.0.1)[220]. In all cases at least 75% of fragments (read pairs) were successfully mapped. All fragments overlapping genes were then counted using Rsubread's featureCounts function. Genes were identified using Ensembl annotation (v101). Differential expression analyses between the sample groups were then undertaken using the limma (v3.46.0)[221] and edgeR (v3.32.1)[222] software packages.

These data were generated over multiple sequencing runs, generating 2-3 technical replicates per sample. Prior to analysis all technical replicate samples were combined to form single samples. All genes labelled 'To Be Experimental Confirmed' (TEC) together with ribosomal RNAs (rRNAs) were then removed, and expression based filtering was performed using edgeR's filterByExpr function with default parameters. A total of 23,769 genes remained. Following gene filtering, sample composition was normalised using the TMM method[223].

To identify differentially expressed genes between the sample groups, the data was first transformed to log-counts per million (logCPM) with associated observation level precision weights using voom[224]. Sample weights were also calculated. For this analysis, loss of residual degrees of freedom was allowed for due to samples with a high proportion of genes with a count of 0. Linear models were then fit to the data and robust empirical bayes moderated t-statistics were utilized to identify differentially expressed genes[225]. This analysis was achieved through the application of edgeR's voomLmFit pipeline. The false discovery rate was controlled below 5% using the Benjamini and Hochberg method.

The gene set test was conducted with limma's cameraPR function with default parameters, and the associated barcode plot drawn with limma's barcodeplot function. Pathway analyses of the gene ontology (GO) and kyoto encyclopedia of genes and genomes (KEGG) databases were accomplished using limma's goana and kegga functions. The mean-difference plots were generated using limma's plotMD function, multi-dimensional scaling (MDS) plots with limma's plotMDS function, while the heatmaps were generated using the pheatmap software package (v1.0.12).

2.5.6 Protein extraction

Pooled micro-dissected zebrafish livers were lysed in RIPA buffer (20mM Hepes, pH 7.9, 150mM NaCl, 1mM MgCl2, 1% NP40, 10mM NaF, 0.2mM Na3VO4, 10mM β-glycerol phosphate) supplemented with cOmplete Proteinase Inhibitor (Roche, #11836170001) and PhosTOP phosphatase inhibitors (Roche, #04906837001). Samples were incubated for 30 min on ice and the extracts cleared by centrifugation at 13,000 rpm for 20min at 4°C. The protein concentration of samples was determined by Bicinchoninic Acid (BCA) protein assay (Thermo Fisher Scientific, #23227).

2.5.7 Western blot

25 µg of protein per lane were resolved on NuPAGE Novex Bis-Tris 4-12% polyacrylamide gels (Invitrogen, #NP0321BOX) and transferred onto nitrocellulose blotting membranes (Amersham Protran, #10600003). Membranes were blocked with 5% BSA in PBS for 1 h at RT. Primary antibodies used in this work were 1:500 anti-p53 (9.1) (Abcam, #ab77813) or 1:1000 anti-phospho-p44/42 MAPK (ERK1/2) (Tyr202/Tyr204) (CST, #4370) incubated O/N at 4°C and 1:1000 anti-GAPDH (14C10) (CST, #2118) and 1:1000 anti-α-Tubulin (DM1A) (CST, #3873) incubated for 1 h at RT. Secondary antibodies, goat anti-mouse HRP (Dako, #P0447) and goat anti-Rabbit HRP (Dako, #P0448), were used at 1:5000 and IRDye 680LT donkey anti-rabbit (LI-COR, #925-68023) and IRDye 800CW donkey anti-mouse (LI-COR, #925-32212) were used at 1:10000 and incubated with membranes for 1 h at RT. Membranes were developed using Amersham ECL Western Blotting Detection Kit (Cytiva, #RPN2108) and imaged on a Chemidoc Touch (Biorad) or using an Odyssey infrared imaging system (Licor). Relative protein quantitation was calculated based on normalised integrated intensity.

2.6 Statistics

2.6.1 General statistical analysis

Data are expressed as mean ± SEM unless indicated otherwise and the number of biological replicates indicating samples from individual animals for each experiment are stated in figure legends. *P*-values were calculated using unpaired t-tests (two-tailed, followed by Welch's correction) when comparing two groups, and by one-way ANOVA followed by Tukey's post-hoc test when comparing multiple groups.

The effect of drug treatments on liver volume was analysed by linear regression, regressing liver volume against drug concentration. All analysis was performed using GraphPad Prism version 9.0.0 (GraphPad software) and $p \leq 0.05$ was considered statistically significant.

3 Exploring components of the nuclear pore complex as potential cancer therapeutic targets

The focus of this chapter is the 252 kDa multidomain nucleoporin ELYS (embryonic large molecule derived from yolk sac), encoded by *AHCTF1* (*AT hook containing transcription factor 1).* Elys was initially identified in a cDNA subtraction screen as a putative transcription factor involved in mouse haematopoiesis[226]. Subsequently, Elys was shown to be essential for the proliferation and survival of inner mass cells during mouse embryonic development[227]. ELYS-deficient mice generated via homologous recombination in embryonic stem (ES) cells were observed to undergo apoptosis at E3.5 and were absorbed by E5.5. Significantly, Elys heterozygous blastocysts were morphologically indistinguishable from wildtype embryos with no differences in the number of apoptotic cells or *in vitro* blastocyst outgrowth rates apparent. Moreover, adult Elys heterozygous mice were healthy and fertile[227]. Immunoprecipitation experiments performed in *Xenopus* egg extracts identified Elys as an integral component of nuclear pore complexes (NPCs), interacting with the Nup107-160 complex and initiating nuclear pore assembly[228]. Consistent with this, functional screens in *C. elegans* revealed that the metazoan ortholog of Elys, Mel-28, is essential for nuclear integrity and postmitotic NPC formation[229-231].

Since then, Elys has been studied in many model systems, including in zebrafish. As mentioned in section 1.4.6, the Heath lab cloned and characterised the zebrafish development mutant *flo* (*flo*^{ti262c}), which was generated in the Tübingen ENU mutagenesis screen many years ago[205]. In independent studies, the Heath lab and the group of Michael Pack showed that the underlying mutant gene was *ahctf1*[211,213]. Homozygous *ahctf1* mutant larvae exhibit a small liver and pancreas, microphthalmia, impaired yolk absorption and rarely inflated swim bladders (Figure 3.1). In comparison to wildtype larvae, *ahctf1* mutants also display striking intestinal defects, with a thinner, unfolded and unpolarised intestinal epithelium with apoptotic cells present in the lumen[211,213,232-234]. Moreover, we and others showed that loss of Elys in zebrafish disrupts NPC formation and causes catastrophic levels of cell death in highly proliferative cell compartments while relatively quiescent tissues remain healthy (Figure 3.2)[211,213].

In this Chapter, I begin by reviewing what is already known about the functions of Elys and other components of the nuclear pore and their role in maintaining the integrity of proliferating cells. I then set out to determine whether the disruption of these functions in an *in vivo* model of zebrafish liver cancer, *TO(kras*^{G12V}*)*[176] as introduced in section 1.4.4, has any impact on the mutant Kras-fuelled growth and survival of hyperplastic hepatocytes.

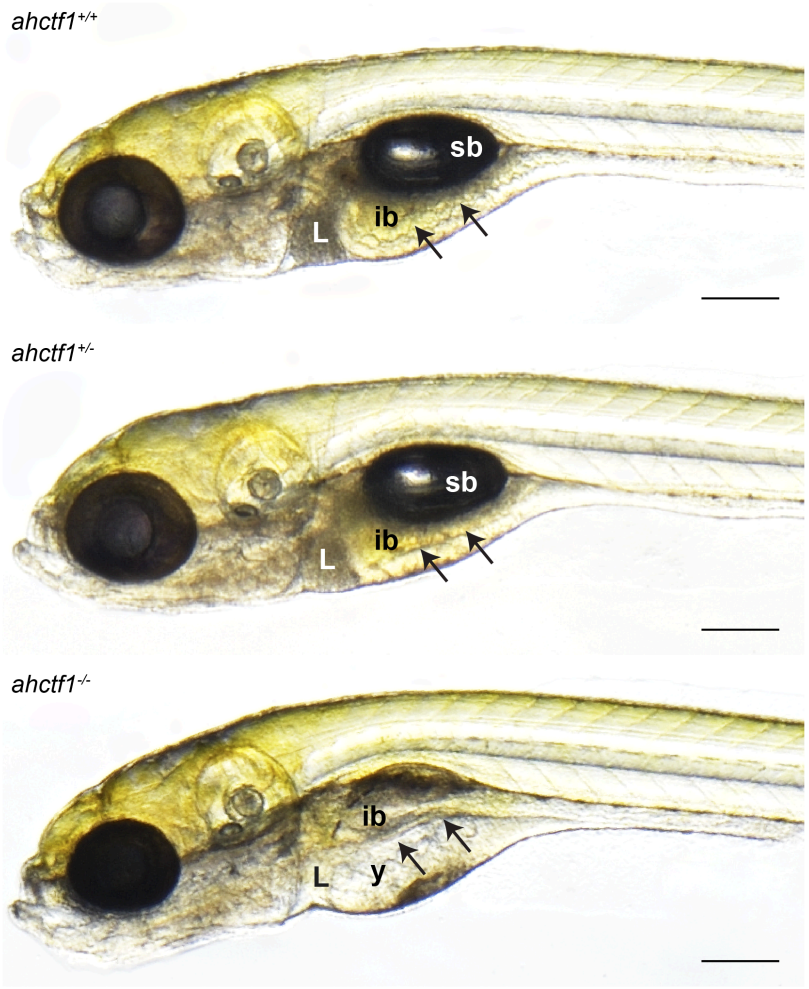

Figure 3.1 Gross morphology of *ahctf1* mutant larvae

Bright-field images of 7 dpf *flo/ahctf1* larvae. Compared to wildtype, *ahctf1*$^{-/-}$ larvae have a smaller head and liver, microphthalmia and fail to inflate the swim bladder or fully absorb the yolk. Whilst the intestinal epithelium (arrows) is thick and extensively folded in *ahctf1*$^{+/+}$ larvae, it is significantly thinner and unfolded in *ahctf1*$^{-/-}$ larvae. Meanwhile, *ahctf1*$^{+/-}$ larvae exhibit no phenotypic abnormalities. Scale bar 200 µm.

e: eye, ib: intestinal bulb, L: liver, sb: swim bladder, y: yolk.

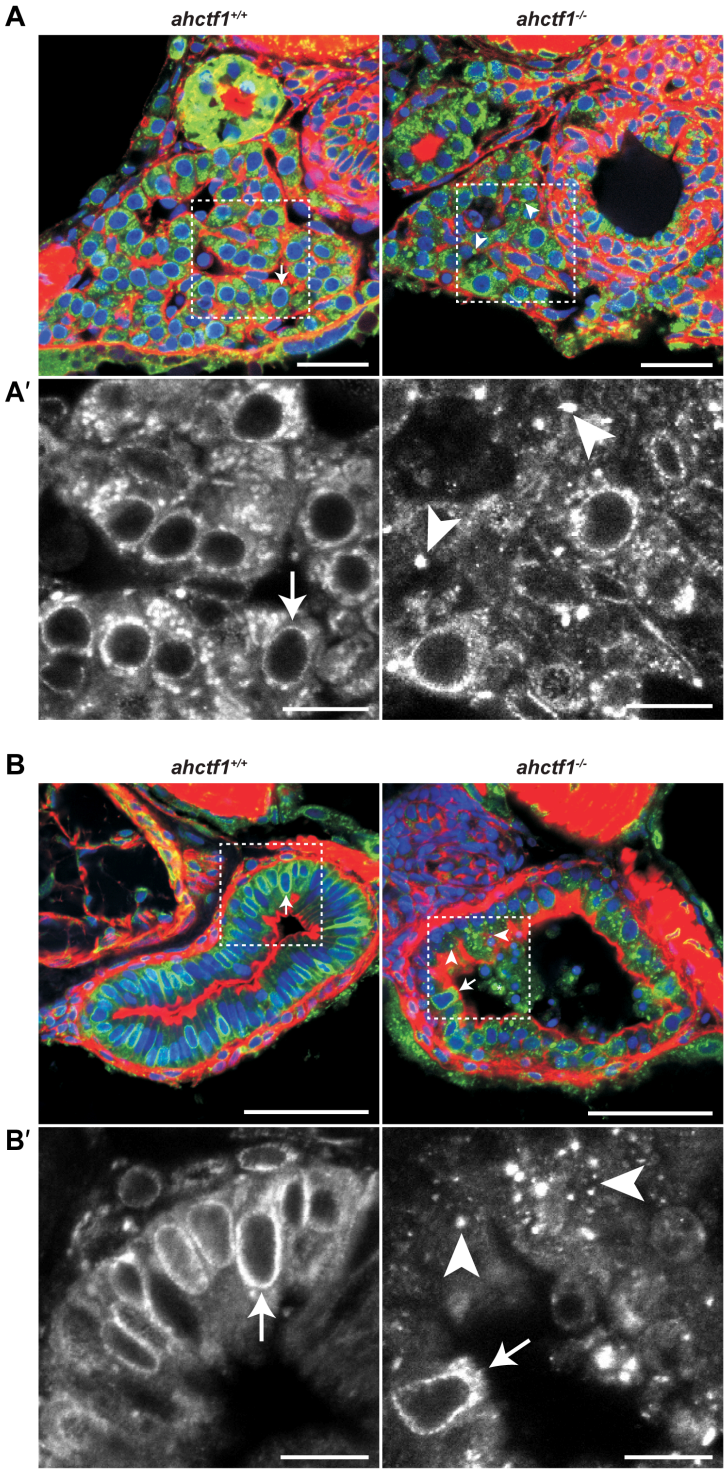

Figure 3.2 NPCs are aberrantly distributed in the digestive organs of *ahctf1* mutant larvae

Confocal imaging of 200 µm thick sections of 78 hpf larvae of the indicated *ahctf1* genotypes stained with rhodamine phalloidin (red) to mark F-actin, mAb414 (green) marking FG-nups and Hoechst (blue) marking DNA. **A.** In the liver of *ahctf1*$^{+/+}$ larvae, NPCs form a punctate ring of fluorescence around nuclei (arrow). In contrast, NPCs in *ahctf1*$^{-/-}$ larvae NPCs are severely disrupted and cytoplasmic aggregates of mAb414 are present (arrowheads). Scale bar 50 µm.

A'. Inset of mAb414 staining in larval liver. Scale bar 10 µm. **B.** Similarly, in the intestinal epithelium of *ahctf1*$^{+/+}$ larvae, NPCs are located in a punctate rim surrounding nuclei (arrow). In *ahctf1*$^{-/-}$ larvae NPCs are aberrantly distributed (arrowheads); however, rare cells displayed proper NPC association with the NE (arrow). The images shown in panel B are the same as those shown in Figure 1.14. **B'.** Inset showing higher magnification mAb414 staining of larval intestine. Scale bar 10 µm. Figure taken from de Jong-Curtain et al., 2009[211].

FG-nups: phenylalanine-glycine nucleoporins, NE: nuclear envelope, NPCs: nuclear pore complex.

3.1 Structure of the nuclear pore complex

Eukaryotic cells are characterised by the spatial segregation of various biological processes into dedicated membrane-bound enclosed organelles. Most prominently, the nuclear envelope (NE) separates DNA contained within the nucleus from the cytoplasm via a double membrane bilayer. Such compartmentalisation requires the transport of molecules and continuous exchange of materials, posing a considerable logistical challenge. Nucleocytoplasmic transport is accomplished through NPCs, which fuse the inner and outer nuclear membranes to form cylindrical channels, allowing bidirectional trafficking of molecules[235,236].

NPCs are amongst the largest and most complex proteinaceous assemblies in eukaryotic cells, with a molecular mass of approximately 60 MDa in yeast and 110 MDa in humans[235]. The overall shape and architecture of the NPC is highly conserved across eukaryotes, as first revealed by studies utilising electron microscopy (EM)[237-239]. NPCs are composed of multiple copies of at least 30 different proteins termed nucleoporins (nups) that are assembled in an octameric array (Figure 3.3-3.4)[240-242]. The major structural components of the NPC are the outer nuclear and cytoplasmic rings, inner ring, transmembrane proteins, as well as peripheral elements, the nuclear basket and cytoplasmic filaments. Phenylalanine-glycine (FG) repeat nups fill the central channel and mediate transport.

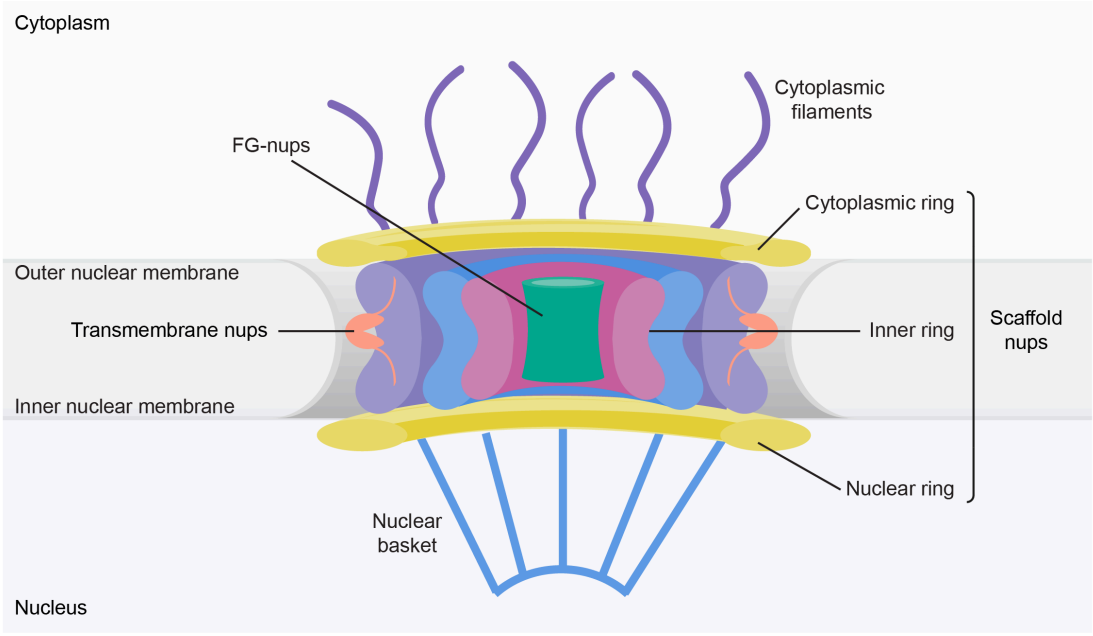

Figure 3.3 Overall structural organisation of the nuclear pore complex

Schematic representation of NPC architecture, depicting a cut away view. The NPC is the major gateway for transport between the nucleus and cytoplasm. Core structural elements of the NPC: the cytoplasmic ring, inner ring and nuclear ring form a stable scaffold. Transmembrane nups anchor the NPC to the NE. The cytoplasmic filaments and nuclear basket are formed by dynamic nups which shuttle on and off the NPC[235,243]. Figure adapted from Lin et al., 2019[235].

FG: phenylalanine-glycine, NE: nuclear envelope, NPC: nuclear pore complex; nups: nucleoporins.

	Saccharomyces cerevisiae		*Homo sapiens*	
Nup107-160 complex	Nup120	(16)	NUP160	(32)
	Nup85	(16)	NUP75	(32)
	Seh1	(16)	SEH1	(32)
	Nup145C	(16)	NUP96	(32)
	Sec13	(16)	SEC13	(32)
	Nup84	(16)	NUP107	(32)
	Nup133	(16)	NUP133	(32)
	-		NUP43	(32)
	-		NUP37	(32)
	-		ELYS†	(16)
Inner ring nups	Nup192	(16)	NUP205‡	(32)
	Nup188	(16)	NUP188‡	(16)
	Nic96	(32)	NUP93	(48)
	Nup157	(16)	NUP155	(48)
	Nup170	(16)		
	Nup53	(16)	NUP53	(32)
	Nup59	(16)		
	Nup57	(16)	NUP54	(32)
	Nup49	(32)	NUP58	(32)
	Nsp1*	(48)	NUP62*	(48)
	Nup100*	(16)		
	Nup116*	(16)	NUP98*	(48)
	Nup145N*	(16)		
Transmembrane nups	Ndc1	(16)	NDC1	(32)
	-		POM210	(32)
	-		POM121	(16)
	Pom152	(16)	-	
	Pom34	(16)	-	
	Pom33		-	
Cytoplasmic filaments	Gle2	(16)	RAE1	(48)
	Nup42	(8)	NUP42	(8)
	Nup82	(16)	NUP88	(16)
	Nup159	(16)	NUP214	(16)
	Gle1	(8)	GLE1	(8)
	-		NUP358	(32)
	-		ALADIN	(32)
	Dyn2	(16)	-	
Nuclear basket	Nup1	(8)	NUP153	(32)
	Nup2		NUP50	(16)
	Mlp1	(8)	TPR	(32)
	Mlp2	(8)		
	Nup60	(16)	-	

Figure 3.4 Molecular composition of nuclear pore complexes in *Saccharomyces cerevisiae* and *Homo sapiens*

Nups in yeast and human NPCs grouped by subcomplex. The single dagger (†) indicates that ELYS is only a component of the NUP107-160 complex on the nuclear side in humans. The double dagger (‡) indicates that NUP205 and NUP188 are also localised to the outer rings in humans. Asterisks (*) indicate that NUP68 and NUP98 and their homologues are also found as part of the cytoplasmic filaments and nuclear basket. Stoichiometries of nups indicated in parentheses. Figure adapted from Lin et al., 2019[235].

NPC: nuclear pore complex, nups: nucleoporins.

3.1.1 NUP107-160 complex

The major constituent of the outer cytoplasmic and nuclear rings of the NPC is the NUP107-160 complex, referred to as the Nup84 complex in yeast. The NUP107-160 complex is also known as the coat nucleoporin complex (CNC) or Y-complex due to its elongated shape reminiscent of the letter Y as revealed by negative-stain electron microscopy[244,245]. The stoichiometry of the Nup107-160 complex is variable across species. In humans 16 copies of the NUP107-160 complex are arranged in two concentric circles to form the outer rings, totalling 32 NUP107-160 complex copies per NPC[246]. This stoichiometry is reduced in algal and fungal NPCs, which possess 24 or 16 Nup107-160 complex copies respectively[247-249]. The NUP107-160 complex contains 10 distinct nups: SEC13, SEH1, NUP96, NUP75, NUP107, NUP160, NUP133, NUP37, NUP43 and ELYS[228,230,242,250-252] (Figure 3.5). 7 of these nups are conserved in S. cerevisiae (Sec13, Seh1, Nup145C, Nup85, Nup84, Nup120, and Nup133)[244,253]. Although NUP37 and ELYS homologues are found in some fungi, often the domain architecture is dramatically altered[254-256]. For example, fungal ELYS homologues lack chromatin-binding domains present in the human protein[255,257]. The NUP107-160 component NUP43 appears to be present only in metazoans[258]. Whilst all other NUP107-160 complex nups have a symmetrical distribution on both the nuclear and cytoplasmic sides of the NPC, ELYS is asymmetrically distributed, localised to the nuclear face of the outer ring only, and is therefore present in 16 copies, exhibiting half-fold stoichiometry compared to other NUP107-160 complex components as measured by mass spectrometry[259].

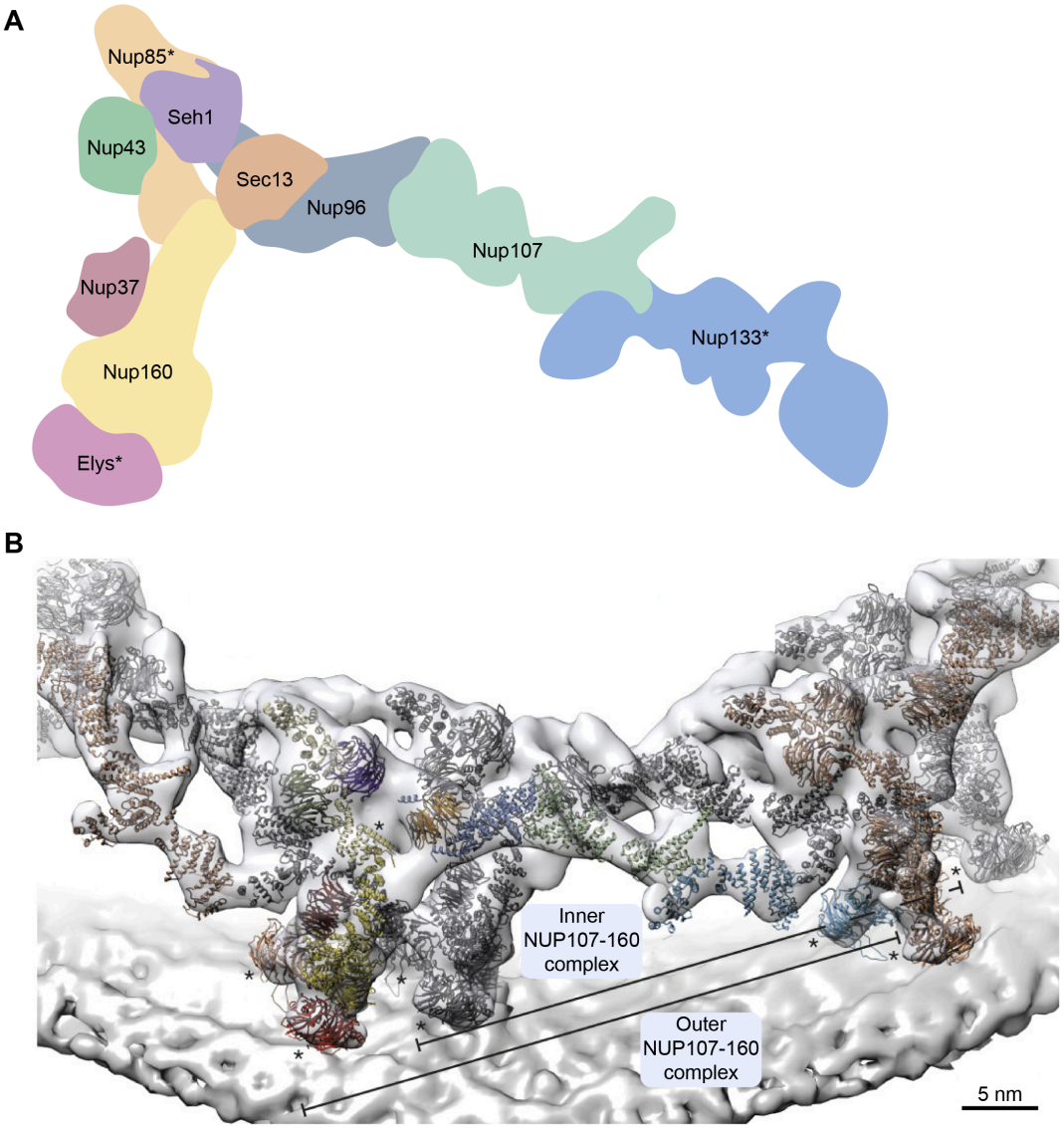

Figure 3.5 Structural architecture of the human NUP107-160 complex

A. The NUP107-160 complex is composed of SEC13, SEH1, NUP96, NUP75, NUP107, NUP160, NUP133, NUP37, NUP43 and ELYS. A total of 32 copies of the NUP107-160 complex are arranged in two concentric, reticulated rings to form the cytoplasmic and nuclear rings of the NPC. ELYS is asymmetrically distributed and localised to the nuclear ring only. Asterisks indicate nups that can be unambiguously positioned but have some uncertainty in their orientation. **B.** Segment of the nuclear ring of the NPC showing the staggered position of the inner and outer NUP107-160 complexes next to their anterior and posterior counterparts. Lines indicate position of each NUP107-160 complex. Figure from von Appen et al. 2015; Protein Data Bank entry: 5A9Q[246].

NPC: nuclear pore complex, nup: nucleoporin

3.1.2 Inner ring nucleoporins

The inner ring of the NPC is embedded within the NE and is primarily composed of the symmetric core nups: NUP53, NUP93, NUP155, NUP205, NUP188 and NUP98 (also known as the NUP93 complex in humans), as well as the channel nucleoporin heterotrimer (CNT) consisting of NUP54, NUP58 and NUP62 (also known as the NUP62 complex)[235,260]. Functionally, the inner ring stabilises the fused inner and outer nuclear membranes by connecting transmembrane nups to the NE and acts as the major tethering point for FG-nups[246,260].

3.1.3 Transmembrane nucleoporins

Similar to the inner ring, transmembrane nups (also known as pore membrane proteins, POMs) are positioned within the nuclear membranes and connect the core scaffold of the NPC to the NE. Transmembrane nups, including NDC1, POM121 and POM210 represent the least conserved and structurally characterised component of the NPC[235]. Whilst Ndc1 is conserved in yeast, direct homologs of human POM121 and POM210 are absent[240,242,261].

3.1.4 Nuclear basket

Electron microscopy initially revealed basket-like structures attached to the nuclear face of the NPC, termed the nuclear basket[262]. The nuclear basket is composed of NUP50, NUP153 and TPR that are anchored to the nuclear ring of the NPC, forming eight filaments that extend into the nucleus and are attached to a distal ring[235]. The nuclear basket provides anchoring sites for gene tethering and mRNA export factors, directly interacting with nucleocytoplasmic transport machinery and regulating chromatin organisation[263-265].

3.1.5 Cytoplasmic filaments

The asymmetric cytoplasmic filaments of the NPC are highly flexible, elongated filamentous structures that project out into the cytoplasm, and are composed of GLE1, RAE1, NUP42, NUP88, NUP98, NUP214, NUP358 and ALADIN[235]. Whilst most cytoplasmic filament nups are evolutionarily conserved, NUP358 (also known as RANBP2) is metazoan specific[266]. The cytoplasmic filaments function to channel incoming cargo from the cytoskeleton towards the nuclear interior and export cargo towards protein synthesis machinery. Additionally, the cytoplasmic filaments position and regulate the activity of DDX19, an ATP-dependent RNA helicase, which terminates mRNA export[267,268].

3.1.6 Phenylalanine-glycine repeat nucleoporins

FG-repeat nups contain extensive intrinsically disordered domains that are rich in phenylalanine-glycine repeats and form a meshwork permeability barrier that regulates the selective bidirectional transport of molecules[269,270]. FGrepeat nups, including NUP45, NUP54, NUP58, NUP62 and NUP98 line the central channel of the NPC and dynamically bind directly to shuttling transport receptors, participating in multiple low affinity, high specificity

interactions[271,272]. FG-repeats are also found within nuclear basket and cytoplasmic filament nups. In total, FG-repeat nups comprise one third of total NPC proteins[273].

3.2 Functions of the nuclear pore complex

Whilst the main function of the NPC is in mediating nucleocytoplasmic transport, it has become increasingly evident that NPCs have transport-independent roles. Nups can interact directly with chromatin while part of the NPC, impacting genome architecture and regulating gene expression[274]. Some nups also function to maintain genome integrity, coordinate mitosis and respond to DNA damage[275-280]. Additionally, in metazoans some nups exhibit dynamic localisation and are found both as part of the NPC and also in the nucleoplasm where they can interact with chromatin[243,281,282].

3.2.1 Nucleocytoplasmic transport

The growth and survival of cells is dependent on continuous molecular trafficking of proteins and RNAs between the cytoplasm and the nucleus. Translocation through the NPC is a very rapid process, with kinetic studies measuring transport rates of up to 1000 events per second within a single NPC[283,284]. Whilst ions and small molecules can diffuse freely through the NPC, molecules >40 kDa are actively transported. Nuclear transport factors (NTFs, also known as karyopherins) facilitate the transport of cargo along a RanGTP gradient (Figure 3.6)[236,285]. Importins and exportins are the two major classes of NTFs. Importins recognise and bind to nuclear localisation signals (NLS) of cargo proteins and mediate their passage through the NPC. Conversely, exportins bind to nuclear export signals (NES) to facilitate export of mRNA and specific proteins from the nucleus[286].

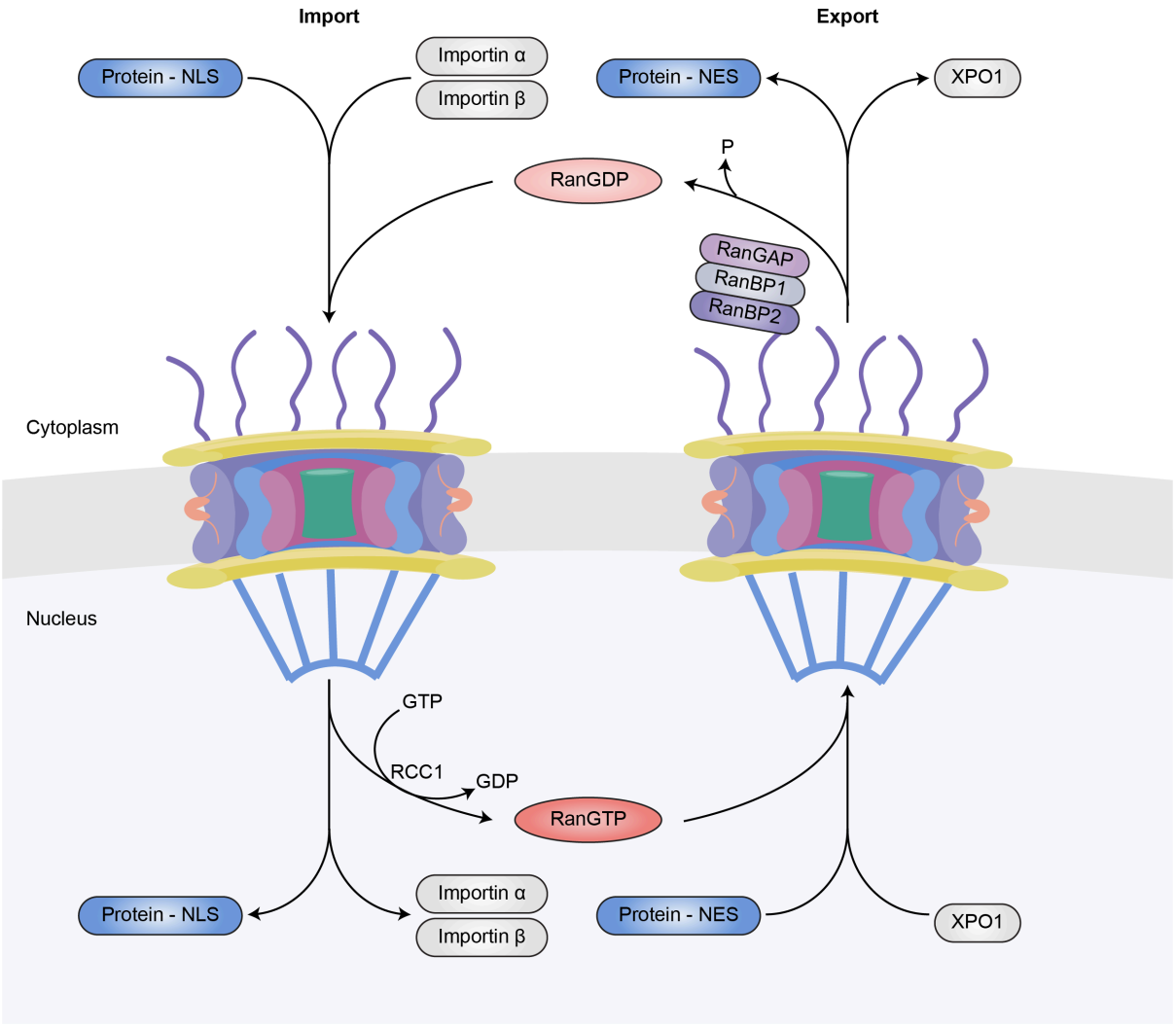

Figure 3.6 The RanGTPase cycle directs nucleocytoplasmic transport

The directionality of nucleocytoplasmic transport is regulated by the RanGTPase cycle. RanGTP is concentrated within the nucleus by RCC1, the Ran guanine-nucleotide exchange factor, which is bound to chromatin and mediates the exchange of GDP to GTP. RanGTP regulates the dissociation of imported cargo that carry a NLS from transport factors such as Importin α and β. Conversely, binding of RanGTP to XPO1 mediates export of cargo containing a NES. RanGAP, RanBP1 and RanBP2 as part of the cytoplasmic filaments of the NPC, cooperate to stimulate GTP hydrolysis of Ran and dissociation of exported cargo. This results in higher concentrations of RanGDP in the cytoplasm. Figure adapted from Clarke et al., 2008[287].

GDP: guanosine diphosphate, GTP: guanosine triphosphate, NES: nuclear export signal, NLS: nuclear localisation signal, NPC: nuclear pore complex, RanBP1: Ran-binding protein 1, RanBP2: Ran-binding protein 2, RanGAP: Ran GTPase activating protein, RCC1: Regulator of chromosome condensation 1, XPO1: exportin 1

3.2.2 Chromatin structure and gene regulation by the nuclear pore complex

In addition to their primary transport function, NPCs have emerged as central platforms for the regulation of gene expression by influencing chromatin architecture and mediating transcriptional output (Figure 3.7)[288,289]. As a dynamic nup with both DNA and chromatin binding domains[228,257,290], ELYS is capable of interacting with the genome both as part of the NPC and independently in the nucleoplasm. ChIP-seq analysis in *Drosophila* has revealed extensive genome-wide binding capacity of Elys, overlapping with the majority of peaks for Nup93, Nup98 and Nup107[291,292]. Whilst robust peaks for Elys, Nup98 and Nup107 were located at enhancers and promoters, consistent with a role in active transcription; peaks for Elys and Nup93 were enriched in polycomb-bound regions and at silenced H3K27Me3-marked loci[291,292]. Consistent with this, immunofluorescence staining of HeLa cells has demonstrated that Elys, along with other members of the Nup107-160 complex and Nup98, co-localise at multiple intranuclear foci[282]. Recruitment of Elys to chromatin is associated with chromatin decompaction mediated by the chromatin remodelling complex PBAP (polybromo-containing Brahma-associated proteins) and GAF (GAGA factor) which reduce nucleosome occupancy of target genes (Figure 3.8)[293]. Mel-28, the *C. elegans* homolog of Elys, has also been demonstrated to interact with chromatin modifiers, specifically, the swsn-2.2 component of the SWI/SNF (Switch/Sucrose Non-fermentable) chromatin remodelling complex[294].

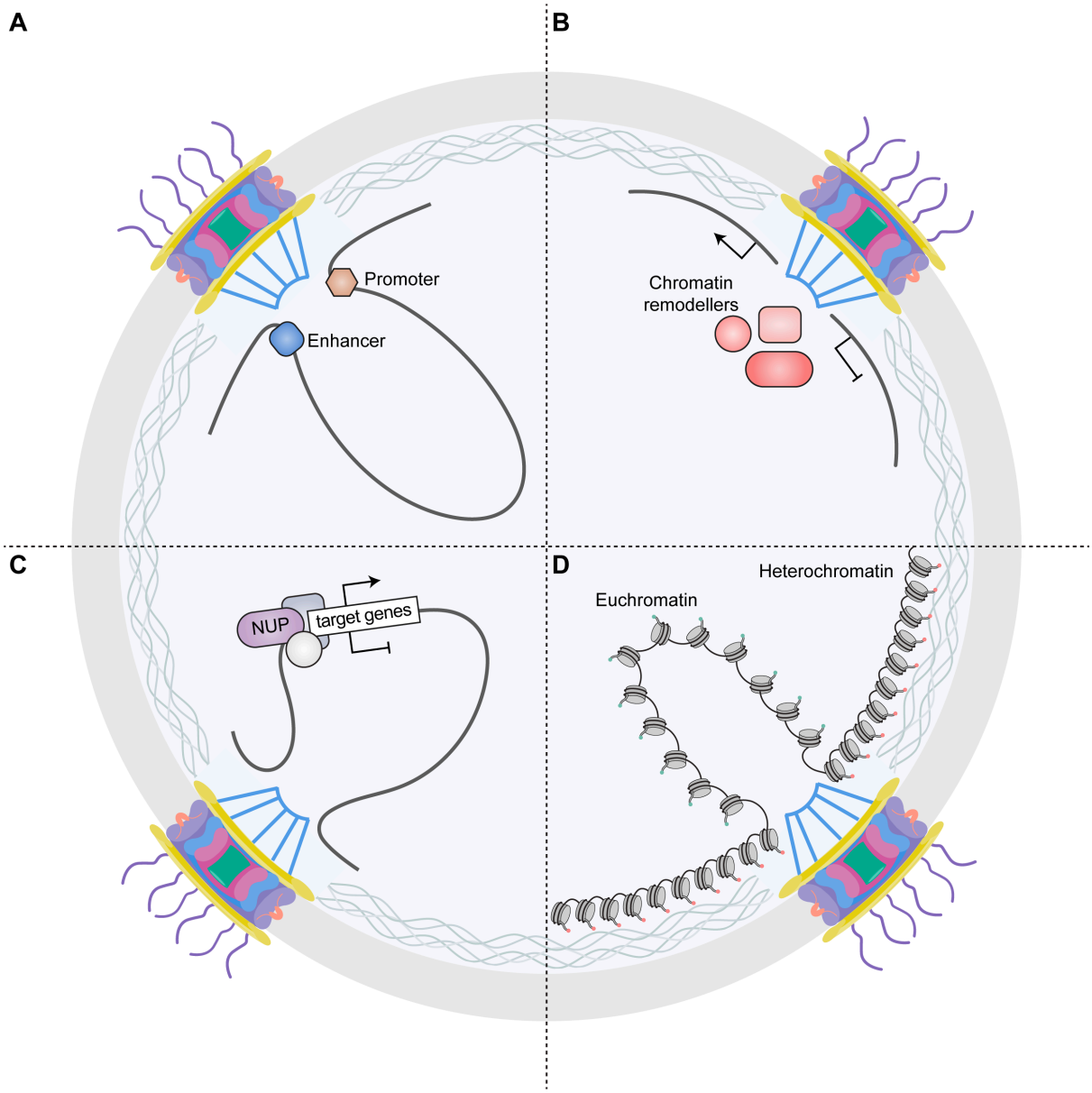

Figure 3.7 Nuclear pore complex mediated gene regulation

A. NPCs are able to bind to both enhancers and promoters to mediate enhancer-promoter looping for gene activation and transcriptional memory. **B.** NPCs recruit chromatin remodellers to the nuclear periphery to facilitate expression of target genes or to mediate gene repression **C.** Independent of the NPC, nups interact with the genome in the nucleoplasm, and associate with a variety of factors to both promote and repress target gene expression **D.** Heterochromatin that is transcriptionally inactive is localised to the nuclear periphery, except at NPCs which are associated with regions of decondensed euchromatin. Figure adapted from Buchwalter et al., 2019[288].

NPC: nuclear pore complex, nup: nucleoporin

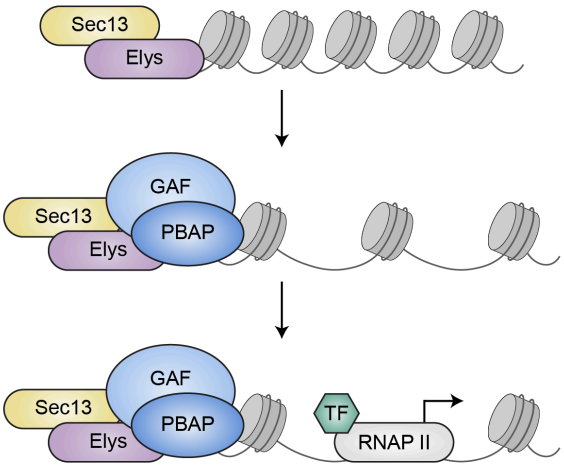

Figure 3.8 Nucleoporins regulate chromatin compaction and gene expression

Binding of the nups Elys and Sec13 to chromatin leads to the recruitment of the chromatin remodelling complex PBAP along with GAF. This triggers chromatin decompaction, reducing nucleosome occupancy to permit binding of transcriptional machinery and expression of target genes. Figure adapted from Kuhn et al., 2019[293]

GAF: GAGA factor, PBAP: polybromo-containing Brahma-associated proteins, RNAP II: RNA polymerase II, TF: transcription factors.

3.2.3 DNA repair by the nuclear pore complex

NPCs also function in the maintenance of genome integrity by facilitating DNA damage repair. In yeast, mutation of genes encoding components of the Nup84 complex (Nup84, Nup210, Nup133), inner ring (Nup170, Nup188) and nuclear basket nups (Mlp1, Mlp2) causes accumulation of DNA damage and enhanced sensitivity to DNA-damaging agents, including ionising radiation, UV-light exposure and topoisomerase I inhibitors[278,295,296]. Additionally, mutations in Nup84 complex components participate in synthetic lethal interactions with multiple DNA repair factors such as Rad27, Rad52, Mre11 and Srs2[296]. Collapsed replication forks and persistent DNA lesions such as double-strand breaks and eroded telomeres, are recruited to the NPC through SUMOylation events, further supporting a role of the NPC in mediating DNA repair[280,297-300]. Consistent with this, a genome-wide siRNA screen demonstrated that downregulation of NUP107-160 complex components (the vertebrate ortholog of the Nup84 complex) caused elevated levels of H2AX phosphorylation[301]. NUP153, a component of the nuclear basket, is also involved in repair of double-strand breaks, promoting nuclear localisation of 53BP1 and non-homologous end joining (NHEJ) repair[302,303].

3.2.4 Mitotic functions of nucleoporins

In eukaryotes which undergo open mitosis, the NE breaks down and NPCs are disassembled and then reassembled anew every cell cycle. Phosphorylation of NE proteins and nups by mitotic kinases PLK-1 (polo-like 1) and CDK-1 (cyclin-dependent 1) in late prophase triggers NE breakdown, NPC disassembly and lamina depolymerisation[304-306]. In particular, phosphorylation of NUP98 is required to initiate NPC disassembly during mitotic entry[305]. Whilst the majority of nups disassemble into stable subcomplexes that are dispersed throughout the cytoplasm, transmembrane nups are absorbed into the mitotic endoplasmic reticulum network[307,308]. Simultaneously, chromatin is condensed into chromosomes, a process facilitated by several factors including topoisomerase IIα (TOPIIα) and condensin complexes[309].

Following chromosome condensation, various nups are localised to mitotic structures where they contribute to proper spindle assembly and kinetochore function (Figure 3.9)[276,306]. NUP98 forms a complex with RAE1 and binds to microtubules, promoting spindle formation through interactions with the microtubule-associated protein NUMA (nuclear mitotic apparatus protein)[310,311]. The NUP107-160 complex localises to both spindle poles and kinetochores during mitosis[251,252,312], and interacts with the γ-tubulin ring complex (γ-TuRC) to promote Ran-dependent microtubule nucleation and polymerisation[313]. RNAi induced depletion of several NUP107-160 complex components causes chromosome misalignment during metaphase, reduced kinetochore tension and kinetochore-microtubule attachment defects[314]. ELYS also plays critical roles in mitotic progression and the maintenance of genome integrity (Figure 3.10). ELYS is found at outer kinetochores, colocalised with the kinetochore proteins CENP-B and NDC80, and at spindle poles during mitosis, contributing to proper spindle formation and chromosome segregation[228,229,231,315]. Accordingly, depletion of ELYS in

HeLa cells or *C. elegans* via RNAi leads to defects in chromosome condensation, kinetochore formation, spindle assembly and chromosome segregation as well as delayed cytokinesis with formation of mid-body microtubule structures[228,229,231]. NUP358 also has mitotic functions, and is recruited to kinetochores during prometaphase together with RanGAP1[316]. NUP358-RanGAP1 mediates the establishment of stable microtubule-kinetochore attachments which is critical for bipolar spindle formation and proper chromosome segregation[317,318].

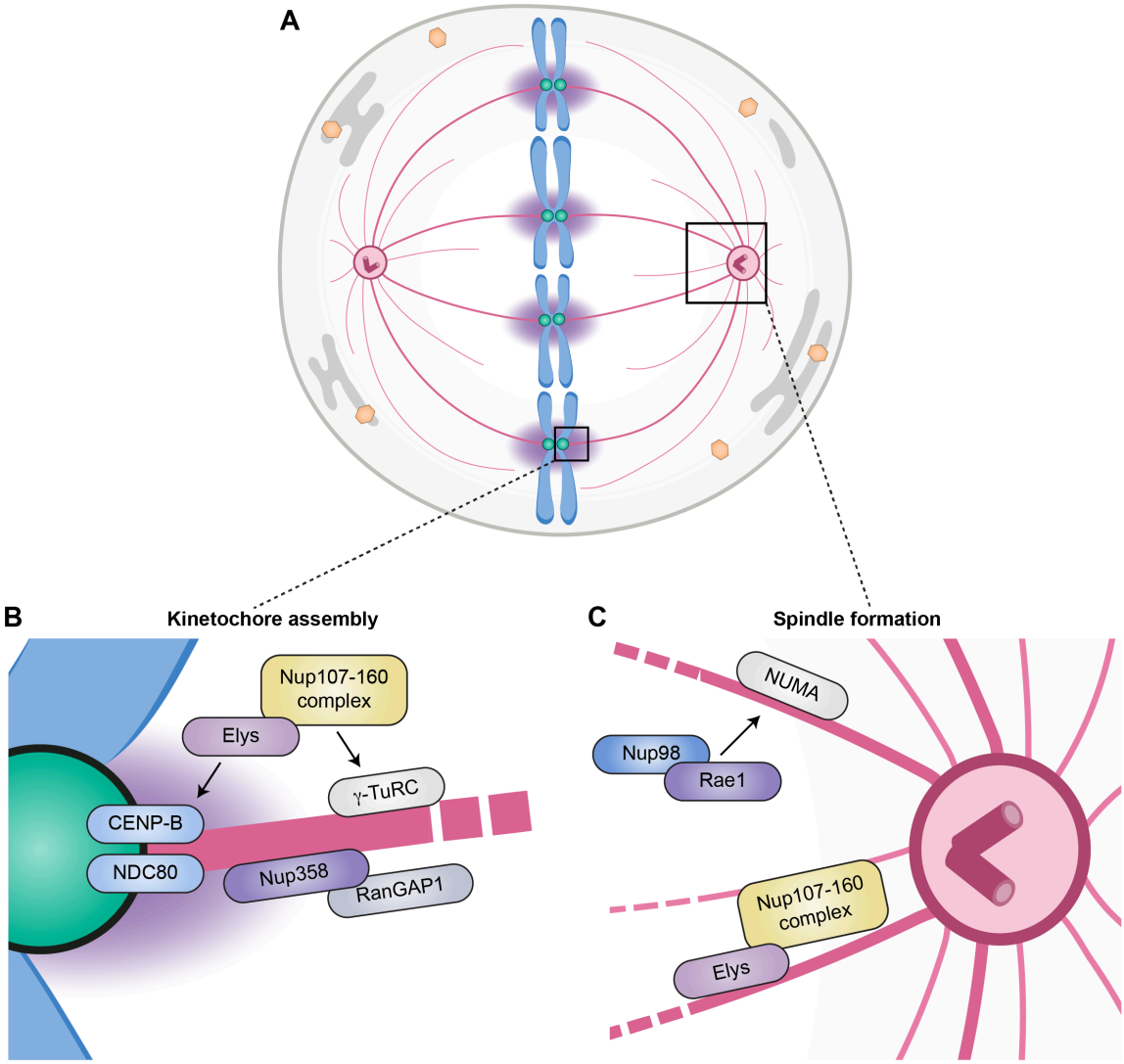

Figure 3.9 Mitotic functions of nucleoporins

A. During mitosis the NE breaks down and NPCs are disassembled. Whilst some nups are distributed throughout the cytoplasm and endoplasmic reticulum others are localised to THE kinetochore and spindles. **B.** Elys is recruited to the outer kinetochore through association with CENP-B and NDC80 whereas the Nup107-160 complex interacts with γ-TuRC, together promoting stable attachments between kinetochores and microtubules. Nup358 (also known as RanBP2) in complex with RanGAP1, is also localised to kinetochores and contributes to microtubule interactions. **C.** Nup98 and Rae1 function together with NUMA to mediate microtubule bundling. Elys and Nup107-160 are also localised to spindle poles and are involved in spindle formation. Figure adapted from Güttinger et al., 2009[306].

CENP-F: centromere protein F. γ-TuRC: γ-tubulin ring complex, NE: nuclear envelope, NPC: nuclear pore complex, NUMA: nuclear mitotic apparatus protein, nup: nucleoporin, RanGAP1: Ran GTPase-activating protein 1.

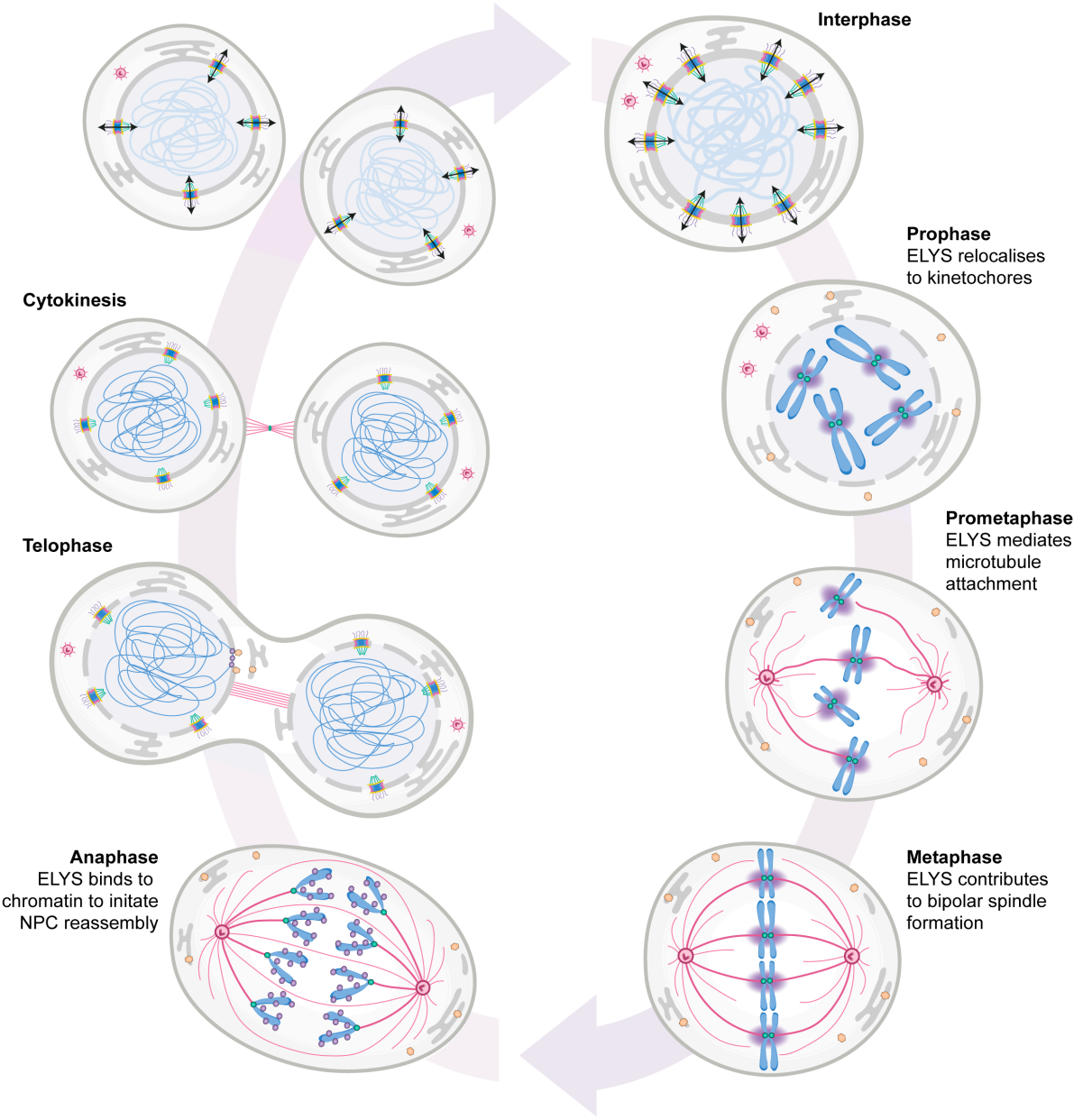

Figure 3.10 Elys functions throughout mitosis

After NEBD and NPC disassembly, most nups are redistributed throughout the cytoplasm and endoplasmic reticulum. However, Elys (shown in purple) relocalises to kinetochores, where it functions to mediate microtubule attachment contributing to proper bipolar spindle formation and chromosome segregation. During anaphase, Elys binds to chromatin to initiate postmitotic NPC reassembly. Subsequently, the restoration of nucleocytoplasmic trafficking enables the proper subcellular localisation of proteins and RNAs which is critical for proper function of eukaryotic cells.

NEBD: nuclear envelope breakdown, NPC: nuclear pore complex.

3.3 Dynamics of nuclear pore complexes throughout the cell cycle

Biogenesis of NPCs requires the ordered assembly of ~1000 individual proteins into a channel structure which must be integrated into the NE[319]. NPC formation occurs at two separate stages of the cell cycle, after mitosis to re-establish nuclear organisation and during interphase to allow nuclear growth. Postmitotic and interphase NPC assembly proceed via kinetically and mechanistically distinct multi-step pathways which are precisely regulated to maintain genome integrity.

3.3.1 Postmitotic nuclear pore complex assembly

After chromosome segregation, the NE is reformed and large numbers of NPCs are rapidly and simultaneously reassembled during mitotic exit to establish a functional nucleus in the daughter cells[307,320,321]. From late anaphase to telophase, when chromatids have fully separated, mitotic kinases are inactivated and phosphatases including protein phosphate 1 (PP1) are activated, facilitating chromatin decondensation as well as NE and NPC reassembly[322]. This process is also regulated by the relative levels of RanGTP, which promotes nuclear membrane fusion and NPC assembly and importin-β, which negatively regulates these events[323-325]. Elys initiates NPC assembly (Figure 3.11) by utilising its AT-hook DNA binding domain and a conserved C-terminal Arg-Arg-Lys (RRK) stretch to bind chromatin and nucleosomes[326,327]. From this tethered position, the N-terminal half of the Elys protein, consisting of β-propeller and α-helical domains, provides a scaffold for the preassembled Nup107-160 complex to bind[230,254,326,328]. Transmembrane nups Pom121 and Ndc1 are subsequently recruited along with membranes derived from the ER network[329]. Components of the Nup93 complex bind as individual nups, beginning with Nup53 and Nup155[330,331]. Nup93, Nup188 and Nup205 are then also incorporated to form the inner ring structure of the NPC[332]. Next, FG-nups are recruited before nuclear basket and cytoplasmic filament nups are the final components incorporated into the NPC[307,321]. In the absence of Elys, the NE can re-form at the end of mitosis, but it does so without NPCs, thereby precluding the movement of mRNAs and large proteins in and out of the nucleus[228,230]. Time-resolved three-dimensional electron microscopy of HeLa cells has revealed that NPC assembly and NE reformation occur concurrently through the radial dilation of nups within membrane fenestrations in ER sheets[320]. Ultimately, this enables establishment of an enclosed nuclear compartment punctuated by hundreds of transport channels within minutes of mitosis exit.

3.3.1.1 Coordination of replication licensing by Elys

In addition to its integral role in initiating postmitotic NPC assembly, Elys also coordinates the restoration of nucleocytoplasmic trafficking with replication licensing[328]. Replication origins, which are multiple discrete locations on DNA where bidirectional pairs of replication forks initiate, are assembled during the G1 phase of the cell cycle via the sequential loading of pre-replication complex (pre-RC) proteins onto chromatin[333,334]. Initially, the ORC (origin recognition complex) is recruited to replication origins, followed by Cdt1 (chromatin licencing and DNA replication factor 1) and Cdc6 (cell division cycle 6). Once these proteins are

assembled, the MCM (mini-chromosome maintenance) helicase complex, consisting of six subunits, MCM2-7, can bind to origins[334]. After nuclear assembly and before entry into S phase, licensing is shut down to ensure that DNA is replicated only once[335]. This is achieved through a combination of Cdt1 proteolysis as well as nuclear import of geminin, a Cdt1 inhibitor and CDKs (cyclin-dependent kinases) that phosphorylate and inactivate pre-RC components[336,337]. Subsequently, during S phase, helicases are activated by CDKs and DDK (DBF4-dependent kinase) resulting in DNA unwinding and initiation of DNA replication[334]. Thus, helicase loading and activation are temporally separated to enable precise regulation of DNA replication, ensuring faithful inheritance of the genome at each round of cell division (Figure 3.12). Experiments in *Xenopus* egg extracts, have revealed that Elys interacts with the Mcm2-7 complex on chromatin prior to replication initiation, to orchestrate NPC and nuclear reassembly with replication licensing[328]. Consistent with this, inhibition of Mcm2-7 loading onto chromatin via treatment with geminin, delays Elys association with chromatin and subsequently NPC assembly[328,338]. This suggests that interaction of Elys with the replication licensing system creates a feedback loop that promotes nuclear assembly and progression into S phase only once replication origin licensing is complete[328]. Mutation of Elys in both zebrafish and mice, reduces levels of chromatin bound Mcm2 and sensitises cells to replication stress[213,339], further supporting a function of Elys in preparing the genome for DNA replication and maintaining genome integrity.

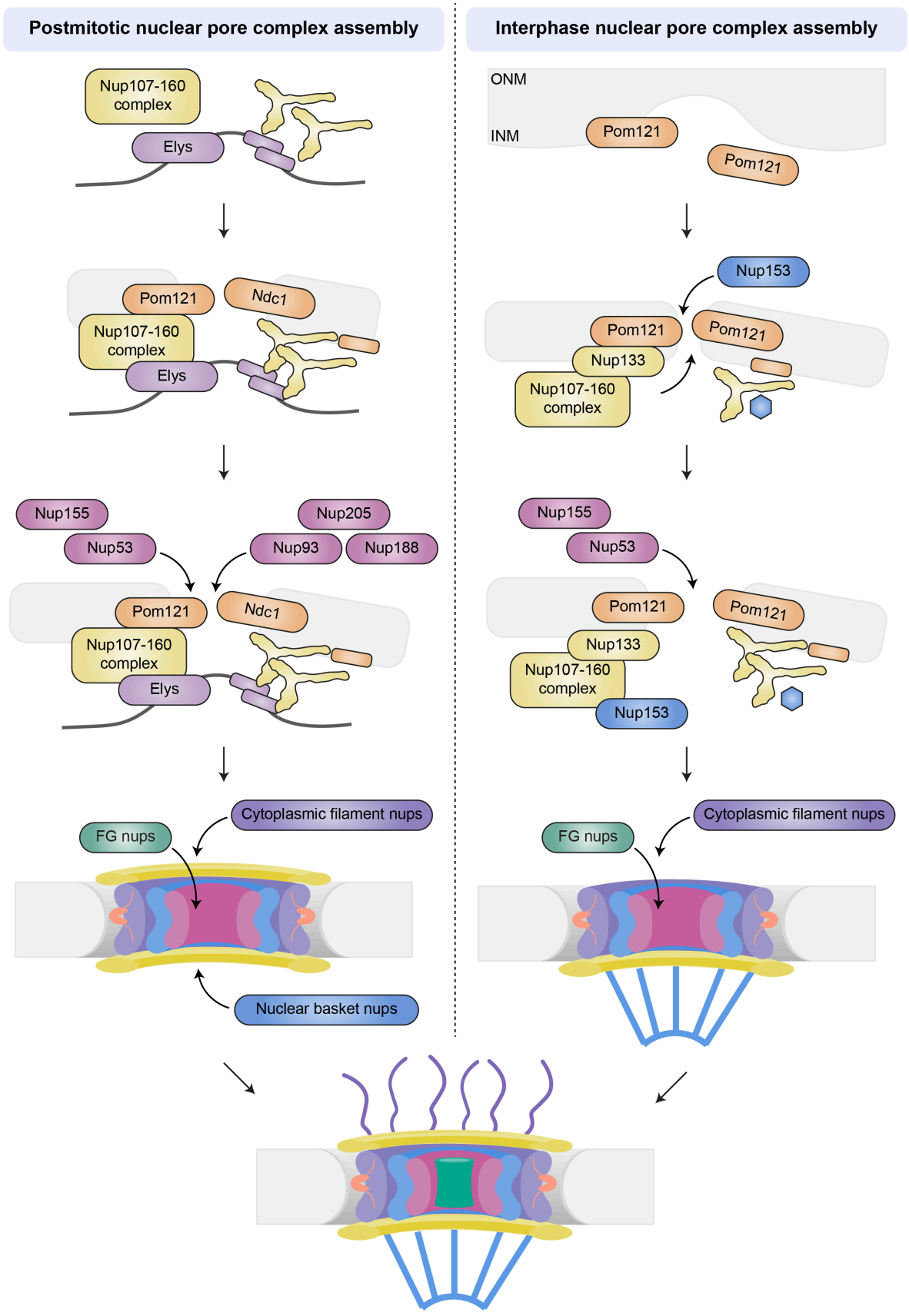

Figure 3.11 Postmitotic and interphase nuclear pore complex assembly are mechanistically distinct

Postmitotic NPC assembly is initiated by Elys binding to chromatin and recruiting the Nup107-160 complex. Transmembrane nups Pom121 and Ndc1 are the next to bind along with membranes derived from the ER network. Components of the Nup93 complex are incorporated individually to form the inner ring structure. FG-nups are subsequently recruited, before finally cytoplasmic filament and nuclear basket nups assemble. Postmitotic NPC assembly is very rapid, forming hundreds of NPCs within minutes of mitotic exit.

Interphase NPC assembly is Elys-independent and occurs via insertion of Pom121 into the intact NE, forming a dome-shaped evagination of the INM that grows to form a channel through the NE. Nuclear import of the nuclear basket nup Nup153 triggers the recruitment of the Nup107-160 complex via Nup133. Binding of these nups, along with Nup53 and Nup155 are proposed to induce and stabilise membrane curvature, facilitating NPC insertion into the NE. FG-nups and cytoplasmic filament nups are the final components recruited. Interphase NPC assembly occurs sporadically and lasts up to an hour.

FG: phenylalanine-glycine, INM: inner nuclear membrane, NE: nuclear envelope, nup: nucleoporin, NPC: nuclear pore complex, ONM: outer nuclear membrane.

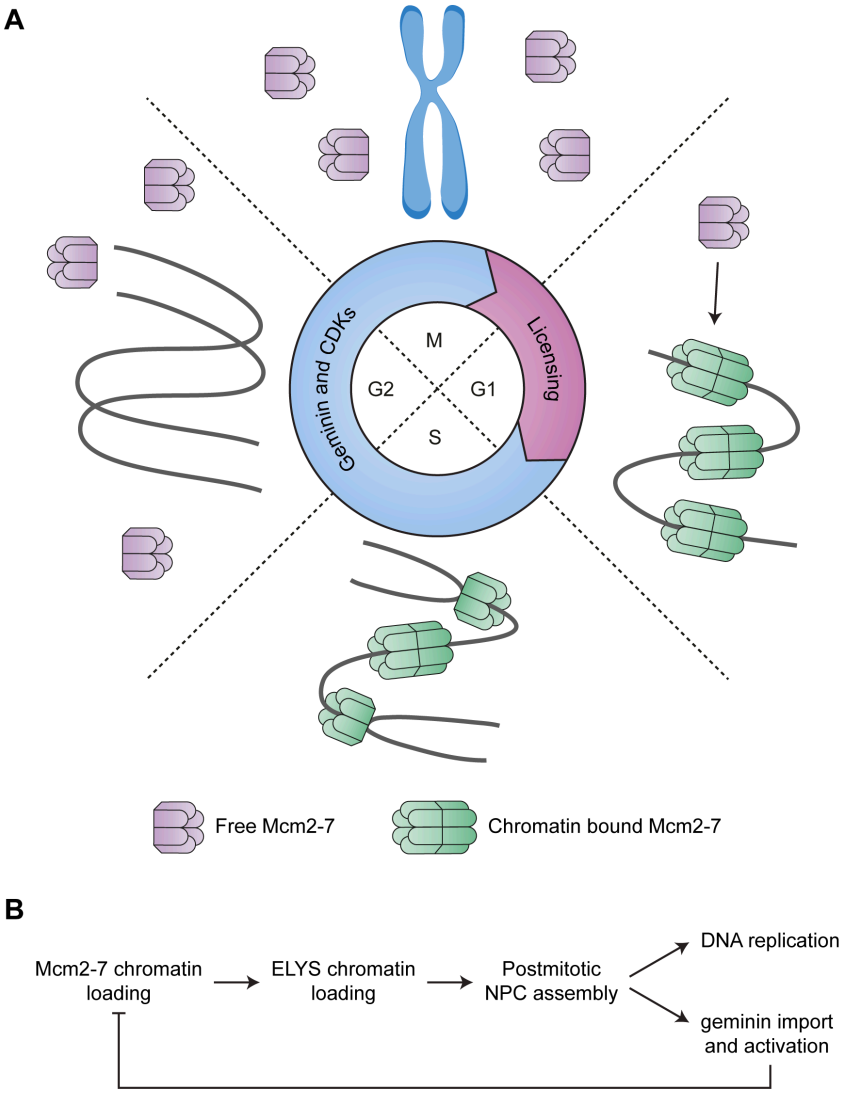

Figure 3.12 Elys coordinates replication licensing with nuclear pore reassembly

A. Mcm2-7 chromatin loading is tightly regulated throughout the cell cycle. During exit from mitosis the replication licensing system is activated and free Mcm2-7 complex is loaded onto chromatin to license potential replication origins. At the end of G1, nuclear import of geminin and CDKs inhibits further licensing. During S phase DNA is replicated and Mcm2-7 complexes are displaced. This ensures that DNA is replicated only once. Figure adapted from Blow et al., 2008[335]. **B.** Loading of Mcm2-7 onto chromatin promotes the association of Elys which initiates NPC assembly. Subsequent reformation of the nucleus and reestablishment of nucleocytoplasmic transport allows nuclear import of geminin and S phase kinases which shut down replication licensing and enable DNA replication. Figure from Gillespie et al., 2007[328].

CDKs: cyclin-dependent kinases, Mcm2-7: mini-chromosome maintenance 2-7 complex.

3.3.2 Interphase nuclear pore complex assembly

NPCs are also assembled during interphase, resulting in an approximate doubling of the number of NPCs in response to changes in cellular requirements and in preparation for the next cell division[340,341]. Interphase NPC assembly occurs sporadically and is a much slower process than postmitotic NPC assembly, lasting up to an hour[341,342]. Capturing these sporadic events is technically challenging, thus interphase assembly is less well characterised then postmitotic NPC assembly. Whilst Elys is critical for the initiation of postmitotic NPC assembly and recruitment of the Nup107-160 complex to reforming NPCs, RNAi-mediated knockdown has revealed it is dispensable for interphase assembly[340]. Instead, the transmembrane nup Pom121, which is localised to the inner nuclear membrane through its NE-binding domain and N-terminal clusters of NLSs, is specifically required for NPC formation during interphase[340,343]. Collation of high-resolution EM with live cell microscopy analysis has revealed that Pom121 inserts into the NE, fusing the inner and outer nuclear membranes via an inside-out extrusion, to trigger interphase NPC assembly (Figure 3.11)[344,345]. The nuclear import of the nuclear basket component Nup153 is required to recruit the Nup107-160 complex to the inner nuclear membrane[346]. Targeting of the Nup107-160 complex to new NPC assembly sites is mediated specifically by the ALPS (ArgGAP1 lipid packing sensor) domain of Nup133[340,341]. Such amphipathic helix domains induce membrane curvature and are also found in Nup160 and inner ring nups Nup53 and Nup155[347]. Together, recruitment of these nups is proposed to stabilise membrane evagination to facilitate insertion of pores into the intact NE[265,330,346]. Subsequently, peripheral nups that form the cytoplasmic ring, including Nup358, are the final components incorporated into newly formed interphase NPCs[344].

3.4 Nuclear pore complexes and disease

NPCs not only mediate nucleocytoplasmic transport but also have roles in a diverse array of essential cellular processes. As such, compromised function of several components of NPCs are associated with a broad spectrum of pathologies including tissue-specific disorders, neurodegenerative diseases, viral infections and various cancers.

3.4.1 Role of nucleoporin mutations in disease

The majority of nup homozygous knockout mice generated are embryonic lethal, demonstrating the essential function of NPCs for cell proliferation, growth and differentiation[348,349]. Therefore, it is somewhat surprising that mutations in nup genes have been identified in connection to highly tissue-specific disorders rather than causing global dysfunction. For instance, mutation of *NUP155* causes atrial fibrillation and sudden cardiac death[350]. Similarly, heterozygous mutations in *NUP37*, *NUP43* and *NUP188* were identified through whole exome sequencing as pathogenic variants in cardiovascular disease[351]. Mutation of nup genes have also been reported in a range of kidney diseases. In particular, biallelic *NUP107* mutations are associated with steroid-resistant nephrotic syndrome[352,353]. In addition, mutations in *NUP85*, *NUP93, NUP133, NUP160* and *NUP205* also cause nephrotic

syndrome by disrupting glomerulus development[354,355]. Another disease associated with nup mutation is Triple A syndrome, which is characterised by adrenal dysfunction, achalasia and alacrimia. Triple A syndrome is caused by mutations in the nup *AAAS* which cause ALADIN mislocalisation and impaired nuclear import of DNA repair proteins, resulting in hypersensitivity to oxidative stress[356,357]. These studies reveal an unanticipated diversity in nup function in distinct tissues, suggesting specialised roles of nups and NPCs in tissue-specific cellular processes that extend far beyond nucleocytoplasmic transport.

3.4.2 The nuclear pore complex in cancer

The earliest association between NPCs and disease was the identification of nups as part of chromosomal rearrangements occurring in leukemias. Gene fusions between transcription factors or kinases and nups including NUP98, NUP214, NUP358 and TPR are linked to tumourigenesis[264,358]. NUP98 was first identified as part of chromosomal translocations with Hoxa9 in AML patients[359]. Since then, NUP98 has been found fused to over 30 different partner genes in a wide variety of hematopoietic malignancies[360,361]. Oncogenicity of these chromosomal translocations is proposed to be mediated by aberrant transcriptional regulation by NUP98[360]. Similarly, NUP214 fusion with the chromatin binding proteins Dek and Set in AML is suggested to alter hematopoietic transcription patterns leading to leukemogenesis[264]. Both NUP358 and TPR fusions to tyrosine receptor kinases are also associated with hematopoietic malignancies. However, whether these chromosomal rearrangements are specific drivers of malignant transformation and progression remains to be established[348,358].

Alterations in nup expression have also been implicated in the development of cancer. For example, NUP88 is overexpressed in many cancers, including HCC, and is correlated with tumour aggressiveness[358,362,363]. Overexpression of NUP88 sequesters NUP98 and RAE1, preventing their interaction with the anaphase-promoting complex/cyclosome (APC/C) and thereby impairing mitotic checkpoint control and promoting aneuploidy[364]. Recently, a prominent role for POM121 in driving aggressiveness of advanced prostate cancer was described whereby over-expressed POM121 interacts directly with importin β to enhance the nuclear import of the oncogenes MYC and E2F1 and the prostate cancer-related transcription factors, AR and GATA2[365]. Targeting the POM121-importin β axis via pharmacological inhibition of importin β with importazole, significantly increased overall survival in prostate cancer mouse xenograft models[365]. Specific nups have also been demonstrated to contribute to tumourigenesis through their mitotic functions. Specifically, NUP358 is essential for the survival of BRAF(600E) and BRAF-mutant like colorectal cancer cells[366]. During mitosis, NUP358 relocalises to spindle microtubules and kinetochores where it is critical for mitotic progression and chromosome segregation[316-318,367]. BRAF-mutant cells are selectively vulnerable to NUP358 loss which exacerbates microtubule nucleation defects, inducing spindle perturbations and cell death. This sensitivity can be exploited therapeutically by treatment with vinorelbine, a microtubule poison, which was shown to induce cell death

specifically in BRAF-mutant cells both *in vitro* and *in vivo*[366]. Taken together, these data demonstrate that NPCs play a role in tumourigenesis through dysregulation of nucleocytoplasmic transport as well as via specialised roles of individual nups.

Therefore, the proper functioning of nups and NPCs may represent a vulnerability of malignant cells. In particular, the key cellular processes coordinated by Elys, as discussed previously (Figure 3.13) are critical for cell cycle progression, suggesting that it may be a promising target for therapeutic intervention in cancer. In this chapter, I explore whether reducing *ahctf1* gene dosage had an impact on hepatocyte hyperplasia and liver enlargement in the *TO(kras^{G12V})* zebrafish HCC model.

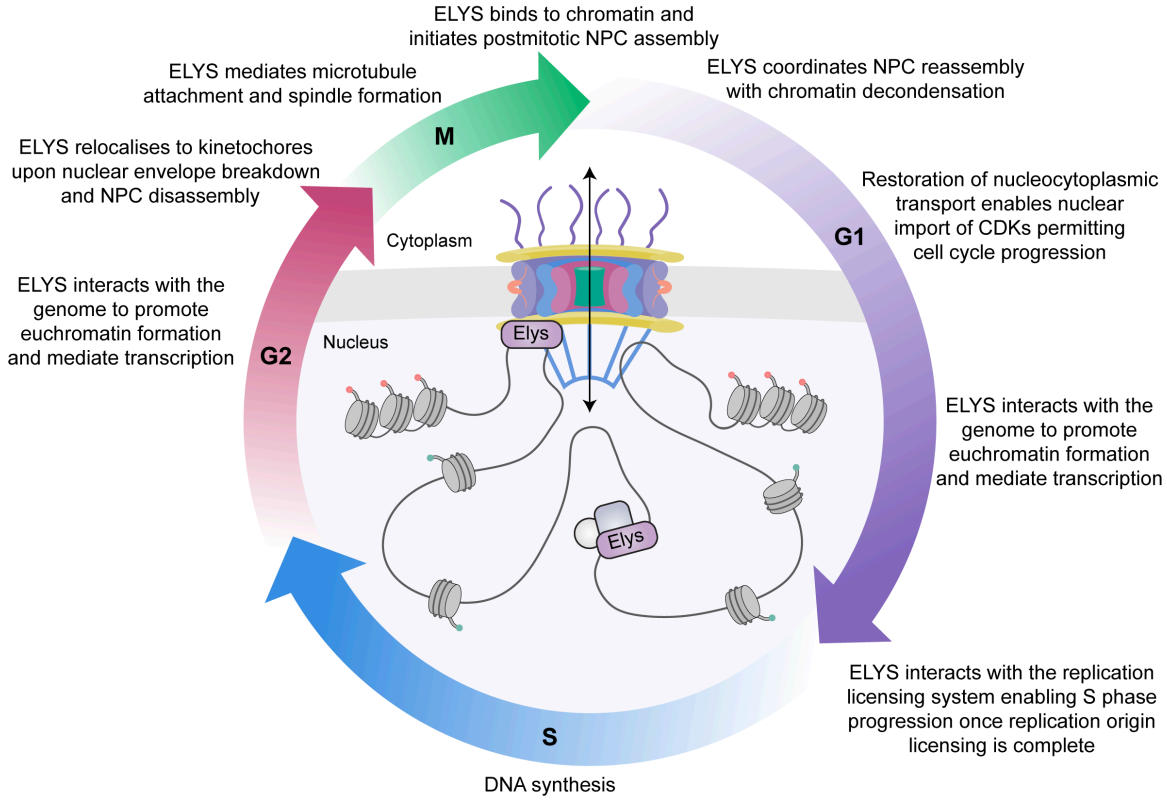

Figure 3.13 Elys functions throughout the cell cycle

Elys plays critical roles at several stages of the cell cycle in addition to its dynamic functions during mitosis. ELYS coordinates postmitotic NPC reassembly with replication licensing and chromatin decondensation. The restoration of nucleocytoplasmic transport enables nuclear import of CDKs, permitting cell cycle progression. Through Elys interactions with the replication licensing system, specifically Mcm2-7, entry into S phase is only permitted once licensing is shut down to protect genome integrity. During both G1 and G2, Elys interacts with the genome and chromatin modifiers as part of NPCs as well as in the nucleoplasm to regulate chromatin structure and gene expression. Thus, Elys is central to orchestrating many diverse cellular processes far beyond its canonical role in facilitating nucleocytoplasmic trafficking.

CDKs: cyclin-dependent kinases, Mcm2-7: mini-chromosome maintenance 2-7 complex, NEBD: nuclear envelope breakdown, NPC: nuclear pore complex.

3.5 Results

3.5.1 RNA-sequencing of *TO(kras^{G12V})* hepatocytes

One way to determine how closely the *TO(kras^{G12V})$^{T/+}$* zebrafish HCC model accurately recapitulates human HCC under my experimental conditions is to compare their mRNA expression profiles. Accordingly, I performed RNA-sequencing on individual 7 dpf micro-dissected livers to assess transcriptome-wide differences in mRNA levels between *TO(kras^{G12V})$^{T/+}$* hepatocytes expressing oncogenic Kras^{G12V} and control *TO(kras^{G12V})$^{+/+}$* hepatocytes. RNA was isolated and 100 ng per sample was used to generate sequencing libraries using the TruSeq RNA Sample Prep Kit with Ribo-Zero depletion (Illumina). Following Next Seq sequencing, differential expression analysis was performed by Dr. Alexandra Garnham of the WEHI Bioinformatics Support Unit (Figure 3.14). Using a false discovery rate (FDR) cut off of less than 0.05, expression of oncogenic Kras^{G12V} resulted in upregulation of 7185 genes and downregulation of 7032 genes compared to control hepatocytes. In a multi-dimension scaling plot, the samples are clustered by genotype, indicating similarities between samples of the same genotype. *TO(kras^{G12V})$^{T/+}$* hepatocytes showed significantly increased *kras* levels compared to control hepatocytes based on RPKM (reads per kilobase of transcript, per million mapped reads) values. The top 20 upregulated and downregulated genes ranked by significance, are shown in Table 3.1 and Table 3.2, respectively.

To understand if the differentially expressed genes (DEGs) shared common functions, KEGG pathway analysis was performed. This analysis tests if DEGs are over-represented in specific pathways and assigns a direction to expression of the pathway. The top 20 upregulated and downregulated KEGG pathways, ranked by significance, are shown in Table 3.3 and Table 3.4, respectively. The top-most upregulated KEGG pathways – spliceosome, DNA replication and cell cycle – indicate that expression of oncogenic Kras^{G12V} has a marked effect on pathways that support rapid rates of proliferation. The list of downregulated KEGG pathways includes numerous metabolic pathways, including carbon metabolism, glycolysis, tyrosine metabolism and glycine, serine and threonine metabolism. This likely reflects early stages of Kras^{G12V}-mediated metabolic reprogramming. Taken together, these data suggest that *TO(kras^{G12V})$^{T/+}$* hepatocytes exhibit considerable alterations in the expression of a broad range of genes and pathways that support rapid cell growth and tumourigenesis.

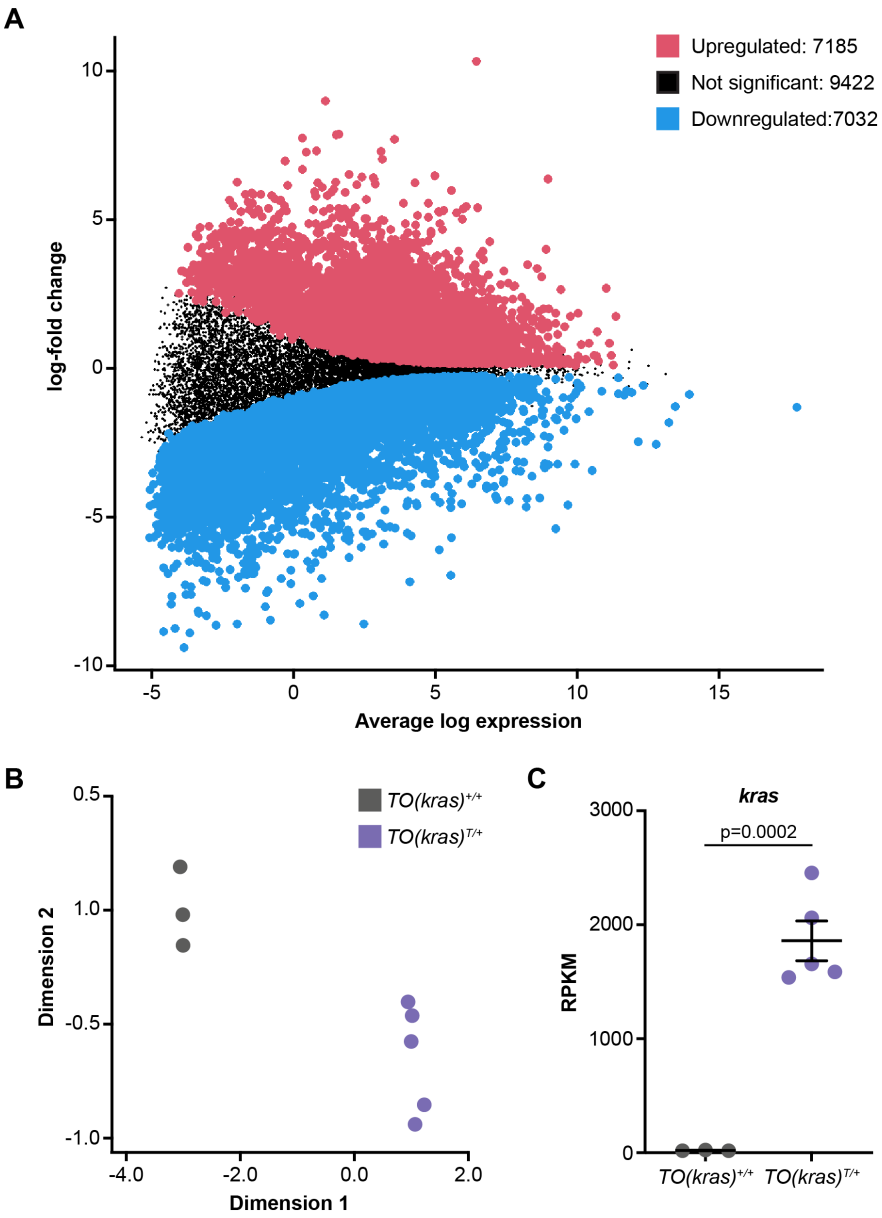

Figure 3.14 RNA-sequencing of *TO(kras^{G12V})* hepatocytes to understand the effects of oncogenic kras^{G12V} expression on transcriptome-wide mRNA levels

A. Mean difference plot of differentially expressed genes between *TO(kras^{G12V})$^{T/+}$* vs. *TO(kras^{G12V})$^{+/+}$*. Each point represents the average expression of a gene (x-axis) against its log-fold change (y-axis). Red dots indicate genes that are significantly upregulated in *TO(kras^{G12V})$^{T/+}$* hepatocytes and blue dots represent genes that are significantly downregulated in *TO(kras^{G12V})$^{T/+}$* hepatocytes based on a FDR<0.05. Black dots represent genes that are not statistically different. **B.** Multi-dimensional scaling plot showing segregation of *TO(kras^{G12V})$^{+/+}$* and *TO(kras^{G12V})$^{T/+}$* samples. **C.** *kras* expression in control *TO(kras^{G12V})$^{+/+}$* hepatocytes and *TO(kras^{G12V})$^{T/+}$* hepatocytes based on reads per kilobase of transcript, per million mapped reads (RPKM). Data are expressed as mean ± SEM, n≥3. Significance was calculated using a Student's t-test.

Table 3.1 Top 20 upregulated genes in *TO(kras^{G12V})$^{T/+}$* hepatocytes compared to control *TO(kras^{G12V})$^{+/+}$* hepatocytes

Gene	Log fold change	Average expression	False discovery rate
elovl1b	2.85	7.79	1.27E-20
shroom4	2.88	7.29	1.21E-19
slc51a	2.70	9.41	1.45E-19
itga3a	3.86	6.57	1.56E-19
si:ch211-137i24.10	3.14	8.74	5.96E-19
actr2a	1.79	7.38	1.22E-18
lamb1a	2.93	7.55	1.57E-18
epha2a	2.33	5.92	1.61E-18
pfn2l	1.76	7.98	4.89E-18
tmsb4x	1.90	10.01	5.57E-18
fstl1b	2.02	8.01	7.92E-18
cfl1	2.06	8.79	8.76E-18
enc3	1.79	6.23	9.39E-18
zgc:64106	3.14	6.13	1.12E-17
arhgap12b	2.32	6.40	1.12E-17
f10	2.06	8.99	1.19E-17
si:dkey-220k22.3	5.36	5.26	1.37E-17
hmgn2	2.46	8.03	2.19E-17
fxyd1	2.81	7.73	2.27E-17
efhd2	1.85	6.97	2.27E-17

Table 3.2 Top 20 downregulated genes in *TO(kras^{G12V})$^{T/+}$* hepatocytes compared to control *TO(kras^{G12V})$^{+/+}$* hepatocytes

Gene	Log fold change	Average expression	False discovery rate
krt91	-4.14	5.58	3.21E-23
isca1	-3.22	4.86	5.06E-22
krt17	-5.85	3.15	5.06E-22
slc6a9	-3.16	5.51	7.61E-21
got1	-3.00	7.28	7.79E-21
hsp70.3	-3.46	3.50	7.79E-21
cldne	-5.96	2.36	7.79E-21
me1	-3.86	3.40	5.06E-20
retreg1	-6.03	0.98	5.17E-20
abcc12	-2.69	5.46	1.17E-19
myhz1.1	-6.29	1.93	1.22E-19
hsp70l	-3.74	2.88	1.45E-19
TSTA3	-4.04	2.44	1.45E-19
slc38a5b	-2.54	5.34	1.65E-19
rbp4	-6.90	5.53	2.00E-19
abca12	-4.71	3.20	2.76E-19
mat2ab	-2.80	4.76	3.29E-19
si:ch211-125o16.4	-5.26	3.37	3.92E-19
bach1b	-2.20	5.37	4.34E-19
cldni	-4.06	2.88	5.57E-19

Table 3.3 Top 20 upregulated KEGG pathways in *TO(kras^{G12V})$^{T/+}$* hepatocytes compared to control *TO(kras^{G12V})$^{+/+}$* hepatocytes

KEGG pathway	P-value
Spliceosome	4.61E-17
DNA replication	1.38E-14
Cell cycle	2.33E-14
RNA transport	1.10E-13
Homologous recombination	3.16E-13
Proteasome	1.63E-11
Fanconi anemia pathway	9.10E-11
Base excision repair	1.50E-08
Oocyte meiosis	2.53E-08
Mismatch repair	4.95E-08
N-Glycan biosynthesis	6.52E-08
Ribosome	6.16E-07
Lysosome	1.07E-06
Basal transcription factors	1.66E-06
Nucleotide excision repair	4.35E-06
RNA polymerase	4.50E-06
Protein processing in endoplasmic reticulum	6.33E-06
Amino sugar and nucleotide sugar metabolism	7.74E-06
Ribosome biogenesis in eukaryotes	8.78E-06
Tight junction	1.63E-05

Table 3.4 Top 20 downregulated KEGG pathways in *TO(kras^{G12V})$^{T/+}$* hepatocytes compared to control *TO(kras^{G12V})$^{+/+}$* hepatocytes

KEGG pathway	P-value
Calcium signaling pathway	4.02E-09
Adrenergic signaling in cardiomyocytes	9.39E-09
Cardiac muscle contraction	1.77E-06
Carbon metabolism	3.18E-05
Glycolysis / Gluconeogenesis	3.95E-05
Neuroactive ligand-receptor interaction	5.27E-05
Adipocytokine signaling pathway	5.92E-05
Tyrosine metabolism	8.64E-05
PPAR signaling pathway	1.44E-04
Glycine, serine and threonine metabolism	2.19E-04
Biosynthesis of amino acids	2.38E-04
Pyruvate metabolism	2.59E-04
Cell adhesion molecules	3.64E-04
Starch and sucrose metabolism	4.92E-04
Glyoxylate and dicarboxylate metabolism	4.92E-04
FoxO signaling pathway	5.63E-04
Alanine, aspartate and glutamate metabolism	7.69E-04
Phenylalanine metabolism	7.88E-04
Ferroptosis	8.51E-04
Focal adhesion	8.62E-04

3.5.2 Gene expression changes in the *TO(kras^{G12V})$^{T/+}$* zebrafish HCC model are significantly correlated with the proliferation subclass of human HCC

To examine how accurately the *TO(kras^{G12V})* HCC model resembles human HCC, gene set analysis was performed. Changes in gene expression observed in *TO(kras^{G12V})$^{T/+}$* vs. *TO(kras^{G12V})$^{+/+}$* hepatocytes were compared with a published gene expression signature of the proliferation subclass of human HCC consisting of 358 genes[368]. The human HCC gene signature was strongly and significantly correlated with gene expression changes in the *TO(kras^{G12V})$^{T/+}$* zebrafish HCC model (Figure 3.15), with a 3.5-fold enrichment in upregulated genes and a 2.4-fold enrichment in downregulated genes. This data demonstrates that the zebrafish HCC model is a valuable platform for *in vivo* studies that is highly relevant to human disease.

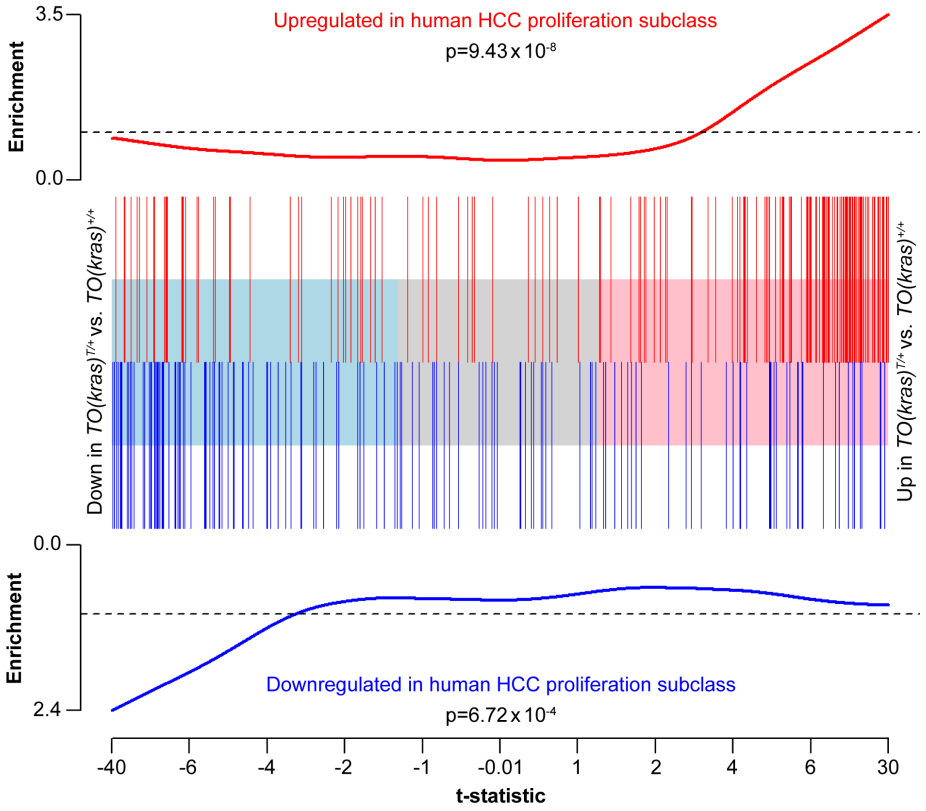

Figure 3.15 *TO(kras^{G12V})$^{T/+}$* hepatocyte gene expression changes correlate with the proliferation subclass of human HCC

Barcode plot showing correlation between gene expression changes in *TO(kras^{G12V})* hepatocytes due to the induced expression of oncogenic Kras^{G12V} with gene expression changes in the proliferation subclass of human HCC. X-axis shows the moderated t-statistic values of the *TO(kras^{G12V})$^{T/+}$* vs. *TO(kras^{G12V})$^{+/+}$* comparison. Red bars show upregulated genes and blue bars show downregulated genes within the proliferation subclass of human HCC as published by Chiang et al., 2008[368].

3.5.3 *ahctf1* mutation reduces *ahctf1* mRNA transcript expression

Having validated the *TO(kras^{G12V})* HCC model, I next investigated the role of Elys in a cancer setting by crossing *TO(kras^{G12V})$^{T/+}$* zebrafish with the ENU mutant *flo^{ti262c}* to generate the *ahctf1; TO(kras^{G12V})$^{T/+}$* line[176,205]. Heterozygous *ahctf1* mutation reduced *ahctf1* mRNA expression by 57% in larvae at 7 dpf (Figure 3.16). Meanwhile, *ahctf1* transcript expression was reduced by 90% in homozygous *ahctf1* mutant larvae. Both these results indicate that the premature stop codon encoded by the nonsense mutation in *ahctf1* triggers nonsense mediated decay, rather than expression of a truncated Elys protein.

3.5.4 *ahctf1* mutation reduces *kras^{G12V}*-driven hepatocyte hyperplasia

To determine the effect of *ahctf1* mutation on normal liver cells, I used the transgenic line denoted *2-CLiP* (2-Colour Liver Pancreas)[216]. *2-CLiP* larvae express dsRed fluorescence in the liver and EGFP fluorescence in the pancreas but they do not contain an oncogenic transgene and were used as a control for these studies and for many other experiments described in this thesis. In *ahctf1$^{+/+}$; 2-CLiP* larvae liver volume was an average of 2.08 x 10^6 ± 6.73 x 10^4 µm^3 at 7 dpf (Figure 3.17). *ahctf1* heterozygosity did not affect normal liver development. Strikingly, normal liver volume was reduced by 83% in *ahctf1$^{-/-}$; 2-CLiP* larvae, showing that when *ahctf1* expression is reduced markedly, hepatocytes cannot thrive.

Turning to the *TO(kras^{G12V})$^{T/+}$* model, induced expression of oncogenic Kras^{G12V} led to liver hyperplasia and a striking 3.8-fold increase in liver volume to 7.81x 10^6 ± 7.10 x 10^4 µm^3 in *ahctf1$^{+/+}$; TO(kras^{G12V})$^{T/+}$* larvae, demonstrating the potency of the oncogenic *kras^{G12V}* signal. Remarkably, this excess liver volume was reduced by 35% to 5.71x 10^6 ± 8.38 x 10^4 µm^3 in *ahctf1$^{+/-}$; TO(kras^{G12V})$^{T/+}$* larvae and even further restricted to 3.51x 10^6 ± 6.06 x 10^4 µm^3 in *ahctf1$^{-/-}$; TO(kras^{G12V})$^{T/+}$* larvae. Thus, a mild reduction in *ahctf1* gene dosage (50%) was sufficient to restrict tumour burden in livers expressing oncogenic *kras^{G12V}*, while having no effect on control livers. Therefore, these results suggest that moderately reduced *ahctf1* expression is a selective vulnerability of cancer cells indicative of a synthetic lethal interaction between *ahctf1* and *kras^{G12V}*.

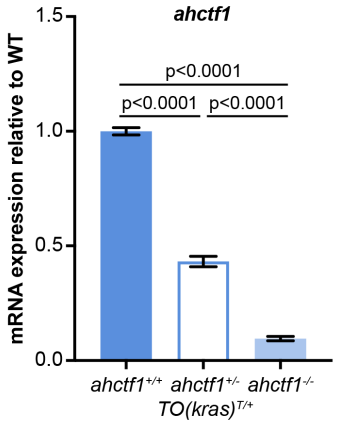

Figure 3.16 *ahctf1* mutation reduces *ahctf1* transcript expression

RT-qPCR analysis of pooled micro-dissected livers from *TO(kras^{G12V})$^{T/+}$* larvae of the indicated *ahctf1* genotype at 7 dpf. Heterozygous and homozygous mutation of *ahctf1* reduced expression of the *ahctf1* transcript by 57% and 90%, respectively, indicative of nonsense mediated decay. Data are expressed as mean ± SEM, n=3 biological replicates. Significance was calculated using a one-way ANOVA with Tukey's multiple comparisons test.

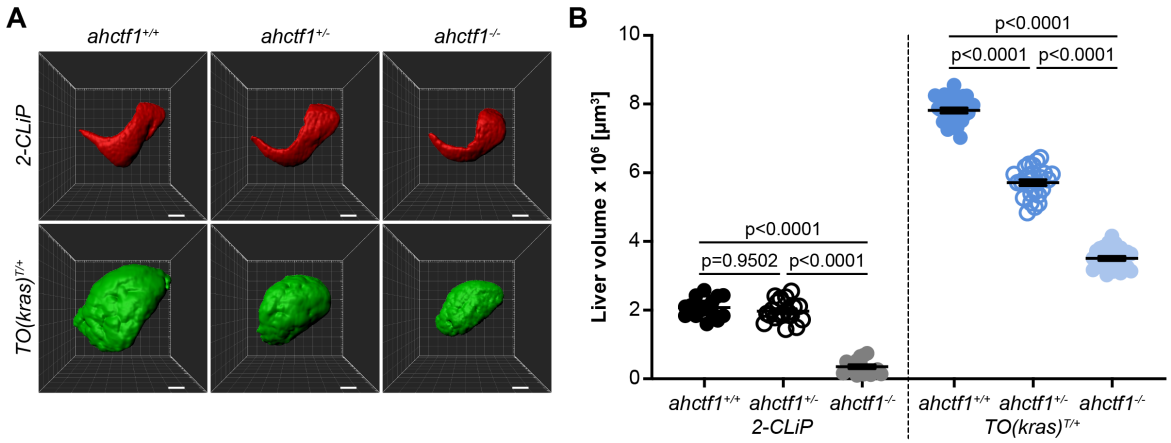

Figure 3.17 *ahctf1* mutation reduces *kras*^{G12V}-driven hepatocyte hyperplasia and liver enlargement

A. Representative three-dimensional reconstructions of *2-CLiP* and *TO(kras*^{G12V}*)*$^{T/+}$ livers of the indicated *ahctf1* genotype (7 dpf). Scale bar 25 µm. **B.** Liver volume in *2-CLiP* larvae was not impacted by *ahctf1* heterozygosity but was significantly reduced by homozygous *ahctf1* mutation. Upon induced expression of the *TO(kras*^{G12V}*)* transgene, *ahctf1* heterozygosity restricted liver hyperplasia and this affect was more pronounced in *ahctf1* homozygous mutant larvae. Data are expressed as mean ± SEM, n≥16. Significance was calculated using a one-way ANOVA with Tukey's multiple comparisons test.

3.5.5 Expression of *TO(kras^{G12V})$^{T/+}$* causes oncogene-induced stress that is increased by heterozygous *ahctf1* mutation

In the *TO(kras^{G12V})* model, tumour growth is dependent on the continuous forced expression of *kras^{G12V}* by frequent application of doxycycline treatment. Withdrawal of doxycycline results in reversion of the hyperplastic hepatocytes to the normal state[176]. Robust and relentless overexpression of *RAS* oncoproteins is frequently associated with oncogene-induced stress, leading to activation of TP53. To determine whether expression of *kras^{G12V}* caused oncogene-induced stress in our model, the levels of Tp53 protein in pooled lysates of micro-dissected *TO(kras^{G12V})$^{+/+}$* and *TO(kras^{G12V})$^{T/+}$* livers and the remaining bodies of the larvae were measured (Figure 3.18). No Tp53 signal was obtained from non-*kras^{G12V}*-expressing livers or the remaining larval body after liver removal. A weak Tp53 signal was detected in *ahctf1$^{+/+}$; TO(kras^{G12V})$^{T/+}$* livers, indicating a mild Tp53 response to expression of the *kras^{G12V}* oncogene. In *ahctf1$^{+/-}$; TO(kras^{G12V})$^{T/+}$* livers, a much stronger Tp53 signal (>3.5-fold) was detected. This demonstrates that a 50% loss in *ahctf1* gene dosage induces a more severe level of stress in the presence of oncogenic Kras^{G12V} than occurs in *ahctf1$^{+/+}$* livers.

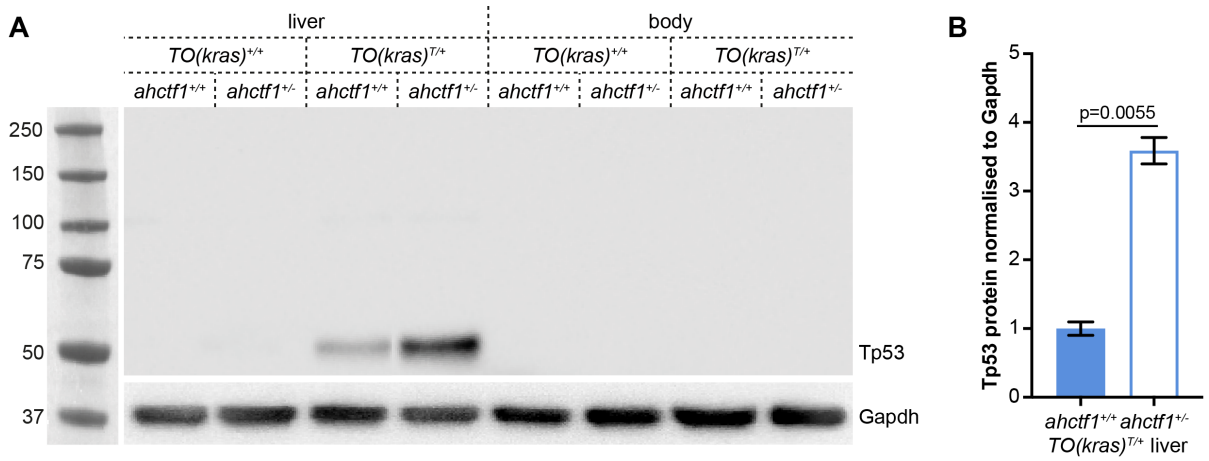

Figure 3.18 Tp53 protein levels are elevated in *ahctf1; TO(kras^{G12V})$^{T/+}$* hepatocytes

A. Representative western blot showing that a Tp53 protein signal is only detected in lysates of pooled micro-dissected livers expressing the *kras^{G12V}* transgene (lanes 3 and 4). Moreover, the Tp53 signal is markedly increased on a heterozygous *ahctf1* background, compared to that obtained on a wildtype *ahctf1* background. **B.** Quantification of Tp53 protein levels normalised by reference to the Gapdh loading control. The Tp53 signal is increased by 3.5-fold on the heterozygous *ahctf1* background. Data are expressed as mean ± SEM, n=3 independent experiments. Significance was calculated using a Student's t-test.

3.5.6 *tp53* mutation increases *kras*^{G12V}-driven hepatocyte hyperplasia and liver enlargement

Given Tp53 was upregulated by *TO(kras*^{G12V}*)*$^{T/+}$ expression and mutations disabling the TP53 tumour suppressor gene are common in HCC, the impact of *tp53* mutation on *kras*^{G12V}-driven liver hyperplasia was investigated. This was achieved using the *tp53*$^{M214K/M214K}$ mutant zebrafish line (hereafter referred to as *tp53*$^{m/m}$), which contains identical debilitating missense mutations in a position corresponding to a mutation hotspot in human *TP53*, together producing a complete loss of Tp53 function[215]. Abrogating Tp53 activity in *2-CLiP* larvae did not impact liver volume (Figure 3.19). In contrast, consistent with its well-established role as a tumour suppressor, heterozygous mutation of *tp53* in *TO(kras*^{G12V}*)*$^{T/+}$ larvae increased liver volume by 33% in comparison to *tp53*$^{+/+}$; *TO(kras*^{G12V}*)*$^{T/+}$ larvae. In *tp53*$^{m/m}$; *TO(kras*^{G12V}*)*$^{T/+}$ larvae liver hyperplasia was increased by 61%. These data suggest that Tp53 mutation enhances *kras*^{G12V}-driven liver hyperplasia, consistent with observations that *TP53* mutation in HCC patients is associated with poorer outcomes[23].

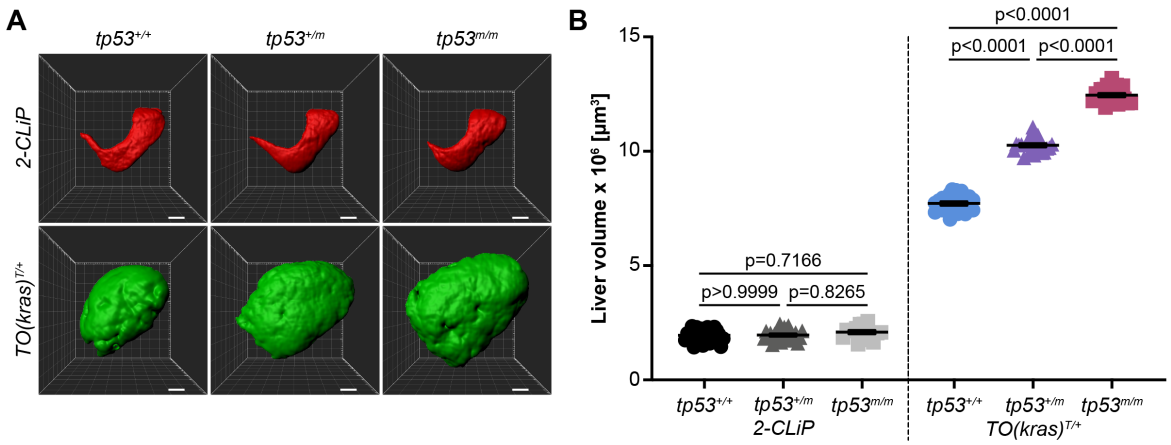

Figure 3.19 *tp53* mutation increases *kras*^{G12V}-driven hepatocyte hyperplasia and liver enlargement

A. Representative three-dimensional reconstructions of *2-CLiP* and *TO(kras*^{G12V}*)*$^{T/+}$ livers of the indicated *tp53* genotype. Scale bar 25 µm. **B.** Liver volume in *2-CLiP* larvae was not impacted by either heterozygous or homozygous *tp53* mutation at 7 dpf. Expression of *TO(kras*^{G12V}*)*$^{T/+}$ significantly increased liver volume and hyperplasia was further enhanced by *tp53* mutation. Data are expressed as mean ± SEM, n≥15. Significance was calculated using a one-way ANOVA with Tukey's multiple comparisons test.

3.5.7 *ahctf1* heterozygosity reduces hepatocyte hyperplasia and liver enlargement associated with combined *kras*^{G12V} and *tp53* mutation

To test whether activation of the Tp53 pathway was involved in the reduction of liver volume in *kras*^{G12V}-expressing larvae on a heterozygous *ahctf1* background, liver volume experiments were repeated in the presence and absence of Tp53 function.

Neither *ahctf1* heterozygosity alone or in combination with *tp53* mutation impacted on liver volume in *2-CLiP* larvae (Figure 3.20). Consistent with previous results, *ahctf1* heterozygosity restricted liver hyperplasia in *tp53*$^{+/+}$; *TO(kras*^{G12V}*)*$^{T/+}$ larvae. The complete abrogation of Tp53 activity in *ahctf1*$^{+/+}$; *tp53*$^{m/m}$; *TO(kras*^{G12V}*)*$^{T/+}$ larvae supported a large increase (60%) in liver volume compared to that of livers in *ahctf1*$^{+/+}$; *tp53*$^{+/+}$; *TO(kras*^{G12V}*)*$^{T/+}$ larvae, further indicating that Tp53 function normally restrains tumour growth and liver enlargement in this model. Interestingly, excess liver volume was reduced by 24% on an *ahctf1*$^{+/-}$; *tp53*$^{m/m}$; *TO(kras*^{G12V}*)*$^{T/+}$ background compared to liver volume observed on an *ahctf1*$^{+/+}$; *tp53*$^{m/m}$; *TO(kras*^{G12V}*)*$^{T/+}$ background. These data indicate that the reduced tumour burden observed in response to *ahctf1* heterozygosity likely involves both Tp53-dependent and Tp53-independent mechanisms.

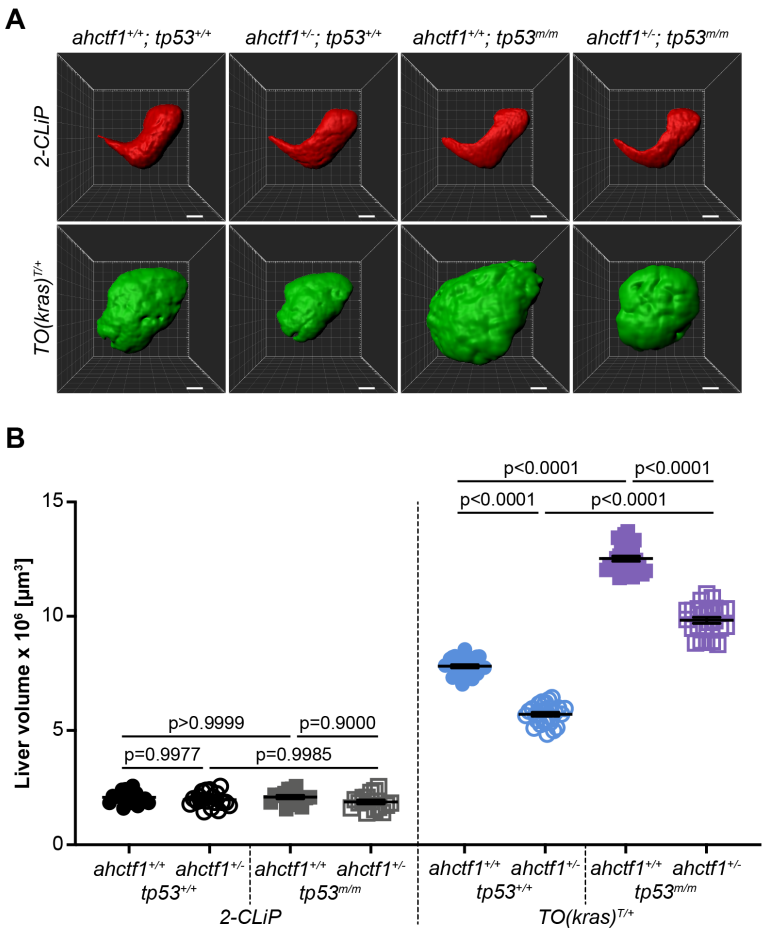

Figure 3.20 *kras*^{G12V} expression in the absence of Tp53 function (*tp53*$^{m/m}$) results in a greater increase in liver volume that is partially mitigated by *ahctf1* heterozygosity

A. Representative three-dimensional reconstructions of *2-CLiP* and *TO(kras*^{G12V}*)*$^{T/+}$ livers of the indicated *ahctf1* and *tp53* genotype. Scale bar 25 µm. **B.** Liver volume in *2-CLiP* larvae was not impacted by *ahctf1* heterozygosity or homozygous *tp53* mutation. However, in *TO(kras*^{G12V}*)*$^{T/+}$ larvae *ahctf1* heterozygosity significantly reduced liver volume in both Tp53 proficient and deficient larvae. Data are expressed as mean ± SEM, n≥20. Significance was calculated using a one-way ANOVA with Tukey's multiple comparisons test.

3.5.8 Heterozygous *ahctf1* mutation triggers cell death in *TO(kras^{G12V})$^{T/+}$* hepatocytes that is partially independent of Tp53 function

To examine if the restricted hyperplasia observed in response to heterozygous *ahctf1* mutation involved Tp53-dependent cell death, I employed a transgenic line, *Annexin 5-mKate* (gift of Dr Thomas Hall) that constitutively expresses a fusion protein comprising Annexin 5 and the far-red fluorophore mKate[217]. This fusion protein identifies cells undergoing apoptosis by binding to phosphatidylserine that is normally inaccessible on the inner leaflet of the plasma membrane but is exposed as the plasma membrane breaks down. This gives rise to discrete fluorescent puncta that can be captured by confocal imaging and quantified by automatic thresholding and 3D segmentation of fluorescence signal to calculate the number of Annexin 5 objects throughout the entire liver.

Annexin 5 fluorescent puncta were sparsely distributed throughout the livers of *ahctf1$^{+/+}$; tp53$^{+/+}$; TO(kras^{G12V})$^{T/+}$* larvae demonstrating that expression of *kras^{G12V}* is associated with low levels of cell death. There was a conspicuous increase in the number of fluorescent puncta throughout the livers of *ahctf1$^{+/-}$; tp53$^{+/+}$; TO(kras^{G12V})$^{T/+}$* larvae, giving rise to a 3.5-fold increase in the level of Annexin 5 fluorescent objects (Figure 3.21), demonstrating that in the context of *kras^{G12V}* expression, *ahctf1* heterozygosity increases cell death. To investigate the role of Tp53 function in these observations, the experiment also included larvae on a *tp53$^{m/m}$* background. Abrogating Tp53 function largely abolished apoptosis on an *ahctf1$^{+/+}$; tp53$^{m/m}$; TO(kras^{G12V})$^{T/+}$* background, with a 91% reduction in the amount of Annexin 5 fluorescence puncta throughout *ahctf1$^{+/+}$; tp53$^{m/m}$; TO(kras^{G12V})$^{T/+}$* livers. However, this marked reduction in cell death was partially mitigated by *ahctf1* heterozygosity with a 17.6-fold increase in the abundance of Annexin 5 fluorescence in *ahctf1$^{+/-}$; tp53$^{m/m}$; TO(kras^{G12V})$^{T/+}$* livers compared to *ahctf1$^{+/+}$; tp53$^{m/m}$; TO(kras^{G12V})$^{T/+}$*. Together these data show that while mutant *kras^{G12V}* expression results in the death of hepatocytes in the presence of wildtype Tp53, this is markedly suppressed on a *tp53$^{m/m}$* background, leading to an increase in tumour burden. However, *ahctf1* heterozygosity can partially mitigate this effect.

Airyscan imaging of cryosections of *TO(kras^{G12V})$^{T/+}$* livers immuno-stained with antibody to cleaved, active caspase-3 provided a complementary method to mark cell death (Figure 3.22). In the livers of *ahctf1$^{+/+}$; TO(kras^{G12V})$^{T/+}$* larvae, the percentage of cleaved caspase-3 positive cells was significantly higher than that found in the livers of *ahctf1$^{+/-}$; TO(kras^{G12V})$^{T/+}$* larvae and fragmented nuclei indicating apoptosis were also apparent. These experiments were performed only in *tp53$^{+/+}$* larvae.

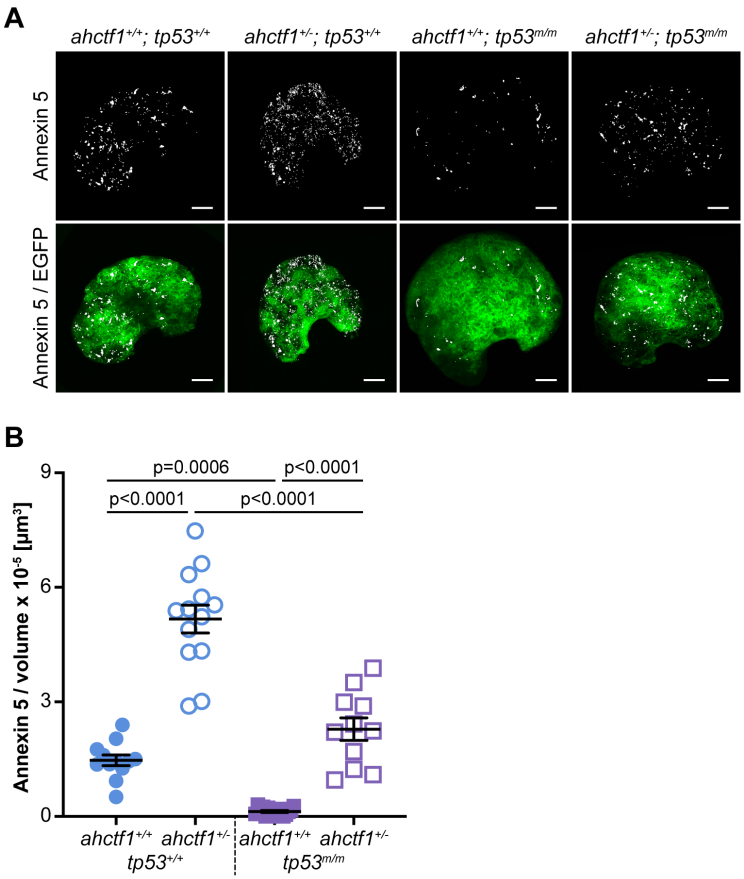

Figure 3.21 Heterozygous *ahctf1* mutation triggers cell death in *TO(kras^{G12V})$^{T/+}$* hepatocytes via Tp53-dependent and Tp53-independent pathways

A. Representative maximum intensity projection images of Annexin 5-mKate fluorescence, indicating cell death in *TO(kras^{G12V})$^{T/+}$* livers of the indicated *ahctf1* and *tp53* genotype. The volume of the liver is greatest in *ahctf1$^{+/+}$; tp53$^{m/m}$; TO(kras^{G12V})$^{T/+}$* larvae (3rd column), where Annexin 5-mKate fluorescence is almost completely suppressed. Scale bar 25 µm. **B.** Quantification of Annexin 5 fluorescent foci by automatic 3D simple segmentation of mKate signal. *ahctf1* heterozygosity increased cell death in Tp53 proficient larvae and to a lesser extent in Tp53 deficient larvae. Data are expressed as mean ± SEM, n≥11. Significance was calculated using a one-way ANOVA with Tukey's multiple comparisons test.

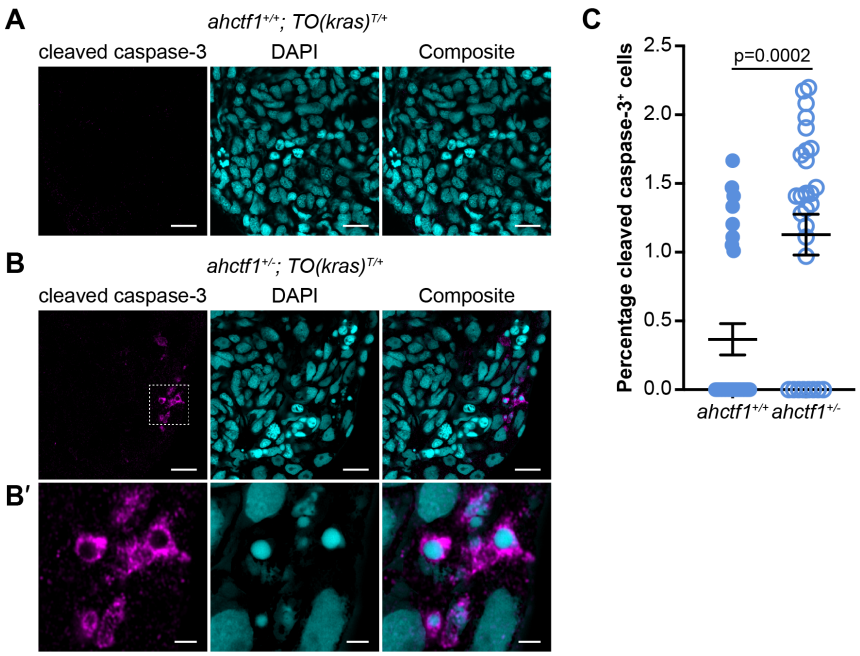

Figure 3.22 Heterozygous *ahctf1* mutation increases the number of *TO(kras^{G12V})$^{T/+}$* hepatocytes containing the cleaved, active form of caspase-3, denoting apoptosis

Representative Airyscan images of cryosections of *TO(kras^{G12V})$^{T/+}$* livers immuno-stained with cleaved caspase-3, to identify dying cells, and DAPI to stain DNA. **A.** In sections of *ahctf1$^{+/+}$; TO(kras^{G12V})$^{T/+}$* livers, no cleaved caspase-3 positive nuclei were observed in the majority of sections examined. Scale bar 5 µm. **B.** Cryosections of *ahctf1$^{+/-}$; TO(kras^{G12V})$^{T/+}$* livers exhibited cleaved-caspase-3 staining and fragmented nuclei with condensed chromatin. Scale bar 5 µm. **B′.** Inset showing multiple cleaved caspase-3 positive hepatocytes in sections of liver taken from *ahctf1$^{+/-}$, TO(kras^{G12V})$^{T/+}$* larvae. Scale bar 2 µm. **C.** Quantification of the percentage of cells positive for active cleaved caspase-3. Data are expressed as mean ± SEM, n=28. Significance was calculated using an unpaired t-test.

To investigate the mechanism by which cell death was occurring, I examined the mRNA expression levels of a set of direct *tp53* transcriptional target genes that are known to regulate apoptosis (Figure 3.23-3.24). The *tp53* targets, *pmaip1 (*formerly *noxa)* and *bbc3 (*formerly *puma)*, which encode the BH3-only sub-class of pro-apoptotic proteins, were upregulated >6.5-fold in *ahctf1*$^{+/-}$*; tp53*$^{+/+}$*; TO(kras*^{G12V}*)*$^{T/+}$ livers compared to *ahctf1*$^{+/+}$*; tp53*$^{+/+}$*; TO(kras*^{G12V}*)*$^{T/+}$ livers. Additionally, expression of other BH3-only encoding transcripts, *bim*, *bid*, *bik* and *bad* were also increased in *ahctf1*$^{+/-}$*; tp53*$^{+/+}$*; TO(kras*^{G12V}*)*$^{T/+}$ livers. *ahctf1* heterozygosity also upregulated expression of these transcripts in the absence of Tp53 function, but to a lesser extent. Transcripts encoding the pro-survival Bcl2 family members, Bcl2 and Bclxl were significantly downregulated in *ahctf1* heterozygous larvae in both Tp53 proficient and deficient larvae, compared to *ahctf1* wildtype controls. Finally, expression of transcripts encoding the pro-apoptotic, executioner protein Bax was also increased by *ahctf1* heterozygosity in *tp53*$^{+/+}$*; TO(kras*^{G12V}*)*$^{T/+}$ and *tp53*$^{m/m}$*; TO(kras*^{G12V}*)*$^{T/+}$ larvae. All these data are consistent with the relative levels of cell death observed in the Annexin 5-mKate experiments and suggest that Tp53 target genes play a central role in the cell death response. They are also consistent with *ahctf1* heterozygosity restricting *kras*^{G12V}-driven liver hyperplasia, at least in part, through activation of Tp53-dependent cell death pathways.

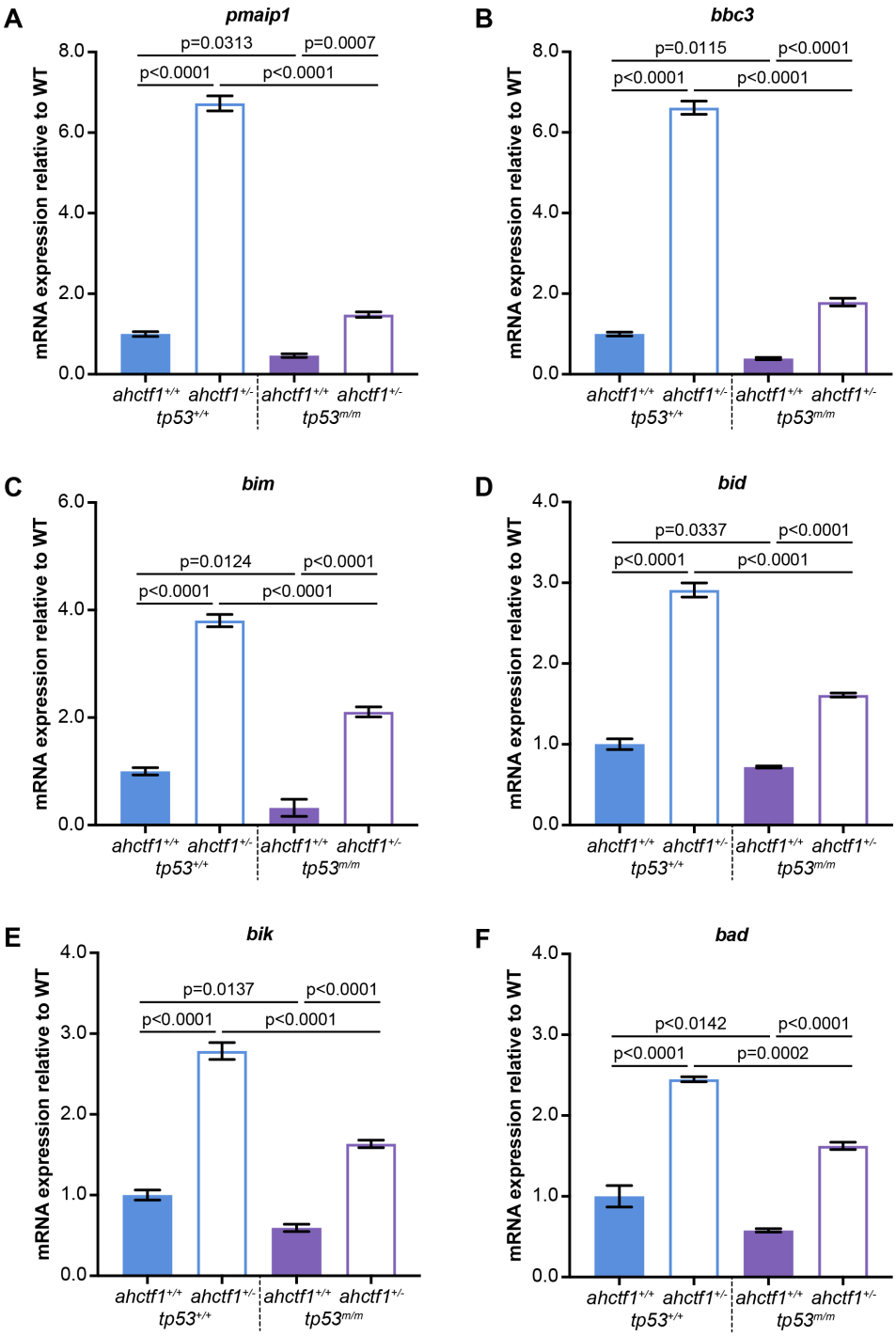

Figure 3.23 Heterozygous *ahctf1* mutation increases expression of genes encoding pro-apoptotic BH3 only proteins in *TO(kras^{G12V})$^{T/+}$* hepatocytes

RT-qPCR analysis of pooled micro-dissected livers from *TO(kras^{G12V})$^{T/+}$* larvae of the indicated *ahctf1* and *tp53* genotype. **A-F.** *ahctf1* heterozygosity increased levels of mRNAs for *pmaip1*, *bbc3*, *bim*, *bid*, *bik* and *bad,* encoding all six pro-apoptotic BH3 only proteins. More restricted upregulation of pro-apoptotic transcripts was also apparent in *ahctf1$^{+/-}$; tp53$^{m/m}$; TO(kras^{G12V})$^{T/+}$* larvae. Data are expressed as mean ± SEM, n=3 biological replicates. Significance was calculated using a one-way ANOVA with Tukey's multiple comparisons test.

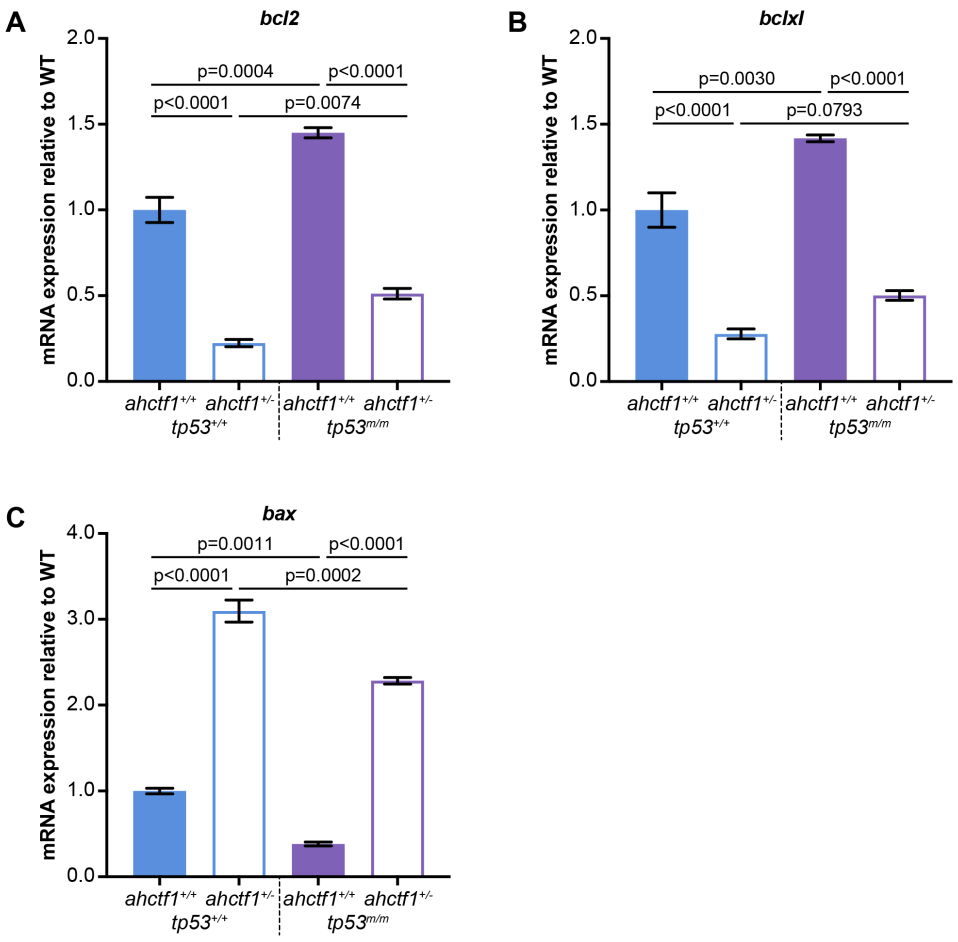

Figure 3.24 Heterozygous *ahctf1* mutation decreases expression of pro-survival genes and increases expression of pro-apoptotic *bax* in *TO(kras^{G12V})$^{T/+}$* hepatocytes

RT-qPCR analysis of pooled micro-dissected livers from *TO(kras^{G12V})$^{T/+}$* larvae of the indicated *ahctf1* and *tp53* genotype. **A,B.** *ahctf1* heterozygosity decreased levels of mRNA expression of pro-survival genes *bcl2* and *bclxl* in both Tp53 proficient and deficient larvae. **C.** In contrast, *ahctf1* heterozygosity upregulated transcript levels of pro-apoptotic *bax.* This observation was upheld even in the context of homozygous *tp53* mutation. Data are expressed as mean ± SEM, n=3 biological replicates. Significance was calculated using a one-way ANOVA with Tukey's multiple comparisons test.

3.5.9 Heterozygous *ahctf1* mutation increases expression of *tp53* family members

In the previous section, I demonstrated that heterozygous *ahctf1* promoted cell death in *TO(kras^{G12V})$^{T/+}$* livers even in the absence of Tp53 function. One possible explanation for this observation is that in the absence of Tp53, its closely related family members, Tp63 and Tp73 are recruited to perform some, or all, of its roles. Tp63 and Tp73 share considerable structural homology with Tp53, particularly within their DNA binding domains, and can activate common and distinct sets of target genes that cause cell cycle arrest, senescence and apoptosis[369,370]. To test this possibility, I carried out RT-qPCR analysis of *tp63* and *tp73* mRNA expression levels in *ahctf1$^{+/+}$; TO(kras^{G12V})$^{T/+}$* and *ahctf1$^{+/-}$; TO(kras^{G12V})$^{T/+}$* livers in the presence and absence of Tp53.

In these experiments, *tp53* mRNA expression levels were unaltered, irrespective of genotype. This is expected given Tp53 activity is known to be predominantly regulated at the post-transcriptional level and *tp53$^{m/m}$* is a point mutation affecting protein function/DNA binding ability not transcript levels. However, *ahctf1* heterozygosity produced a marked increase (>6-fold) in the expression of the *tp53* isoform, *Δ113tp53*, in the presence of wildtype Tp53 (Figure 3.25). *Δ113tp53* is a truncated *tp53* mRNA isoform that is transcribed from an alternative promoter in intron 4 of the zebrafish *tp53* gene. This promoter is only activated upon binding of the Tp53 protein itself so it provides a useful read-out of Tp53 activity[371]. Consistent with this, homozygous *tp53* mutation downregulated *Δ113tp53* transcripts and this was not impacted by *ahctf1* heterozygosity. *ahctf1* heterozygosity upregulated expression of *tp63* and *tp73* by 3.0-fold and 2.3-fold, respectively in *tp53$^{+/+}$; TO(kras^{G12V})$^{T/+}$* livers and this was further augmented by homozygous *tp53* mutation. Notably, both *tp63* and *tp73* transcripts were elevated in *tp53$^{m/m}$; TO(kras^{G12V})$^{T/+}$* livers suggesting they may compensate, at least in part, for the loss of Tp53 function.

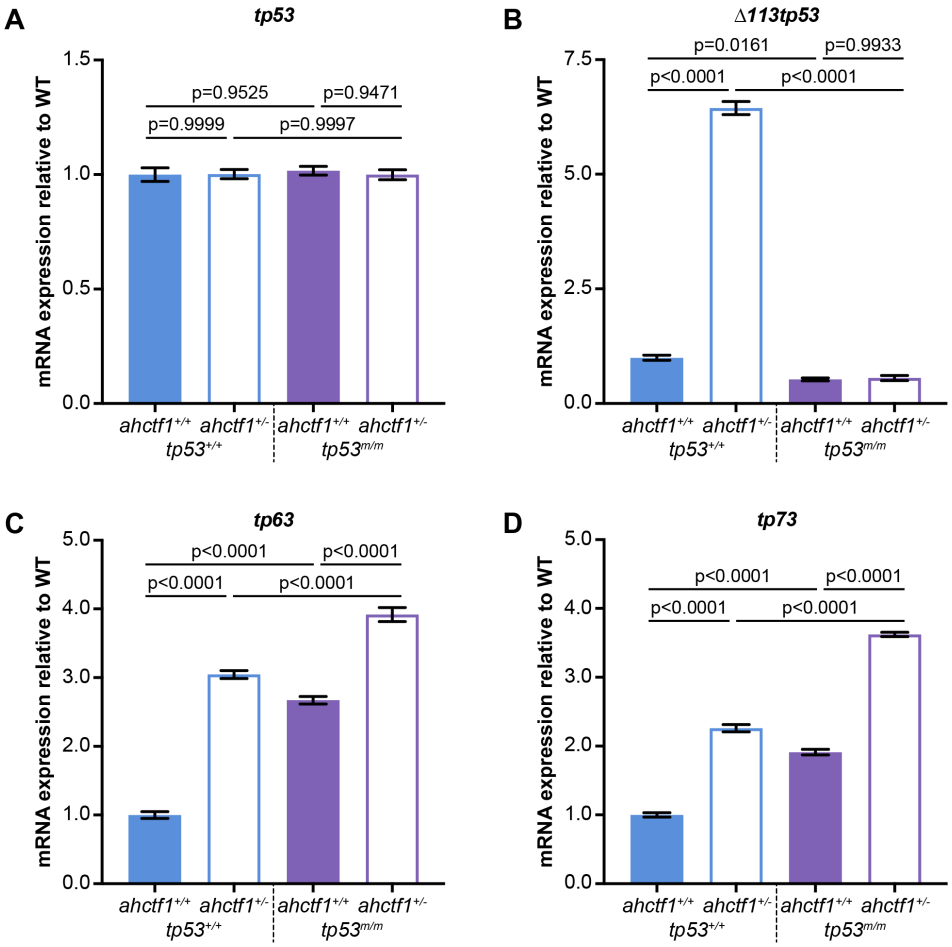

Figure 3.25 Heterozygous *ahctf1* increases mRNA expression of *tp53* family members in *TO(kras^{G12V})$^{T/+}$* hepatocytes

RT-qPCR analysis of pooled micro-dissected livers from *TO(kras^{G12V})$^{T/+}$* larvae of the indicated *ahctf1* and *tp53* genotype. **A.** Neither *ahctf1* heterozygosity alone or in combination with homozygous *tp53* mutation impacted mRNA expression levels of *tp53*. **B.** *ahctf1* heterozygosity upregulated expression of *Δ113tp53* in *tp53$^{+/+}$*; *TO(kras^{G12V})$^{T/+}$* livers. **C,D.** The levels of *tp63* and *tp73* mRNA expression were increased by homozygous *tp53* mutation, and this was augmented by *ahctf1* heterozygosity. Data are expressed as mean ± SEM, n=3 biological replicates. Significance was calculated using a one-way ANOVA with Tukey's multiple comparisons test.

3.5.10 Heterozygous *ahctf1* mutation disrupts the assembly of nuclear pore complexes in *TO(kras^{G12V})$^{T/+}$* hepatocytes

In the preceding sections, I demonstrated that tumour burden in *TO*(*kras^{G12V})* larvae was partially mitigated by *ahctf1* heterozygosity, which caused a significant increase in apoptosis in hepatocytes. This prompts the question of how a reduction in *ahctf1* gene dosage, and a corresponding reduction in Elys protein (which unfortunately could not be confirmed due to lack of available antibodies to the zebrafish Elys protein), causes an increase in apoptosis. As discussed in section 3.1, Elys plays different roles at multiple stages in the cell cycle, including the initiation of post-mitotic nuclear pore assembly. To determine whether this function was compromised in *ahctf1$^{+/-}$* larvae, the distribution and integrity of NPCS was examined by immunostaining vibratome sections with mAb414 antibody, which can recognise FG-repeat nucleoporins (Nup358, 214, 153 and 62) in mature NPCs.

Airyscan imaging of *TO(kras^{G12V})$^{+/+}$* hepatocytes showed that NPCs were located at the nuclear rim in a punctate pattern and this was not altered by *ahctf1* heterozygosity as quantified via 3D segmentation and morphological filtering of nuclear and cytoplasmic areas (Figure 3.26). By comparison, liver vibratome sections from *ahctf1$^{+/+}$; TO(kras^{G12V})$^{T/+}$* larvae exhibited a markedly increased mAb414 fluorescence intensity. Hepatocytes from *ahctf1$^{+/-}$; TO(kras^{G12V})$^{T/+}$* larvae displayed reduced mAb414 signal at the nuclear rim and there was a concomitant increase in cytoplasmic staining, which equated to a 21% reduction in the mean nuclear/cytoplasmic ratio of mAb414 fluorescence intensity.

Images acquired at the nuclear surface showed that NPC density was not affected by *ahctf1* heterozygosity in TO*(kras^{G12V})$^{+/+}$* hepatocytes (Figure 3.27). However, there was a 20% reduction in the number of NPCs in *ahctf1$^{+/-}$; TO(kras^{G12V})$^{T/+}$* hepatocytes compared to *ahctf1$^{+/+}$; TO(kras^{G12V})$^{T/+}$* hepatocytes, once again indicating a selective effect of *ahctf1* heterozygosity in hyperplastic cells. In addition, oncogenic Kras^{G12V} expression resulted in a 27% increase in nuclear volume compared to wildtype (Figure 3.28). *ahctf1* heterozygosity decreased nuclear size, but only in *TO(kras^{G12V})$^{T/+}$* hepatocytes. These results indicate that reduced levels of Elys protein are rate-limiting for the correct assembly of NPCs in hepatocytes expressing oncogenic Kras^{G12V}.

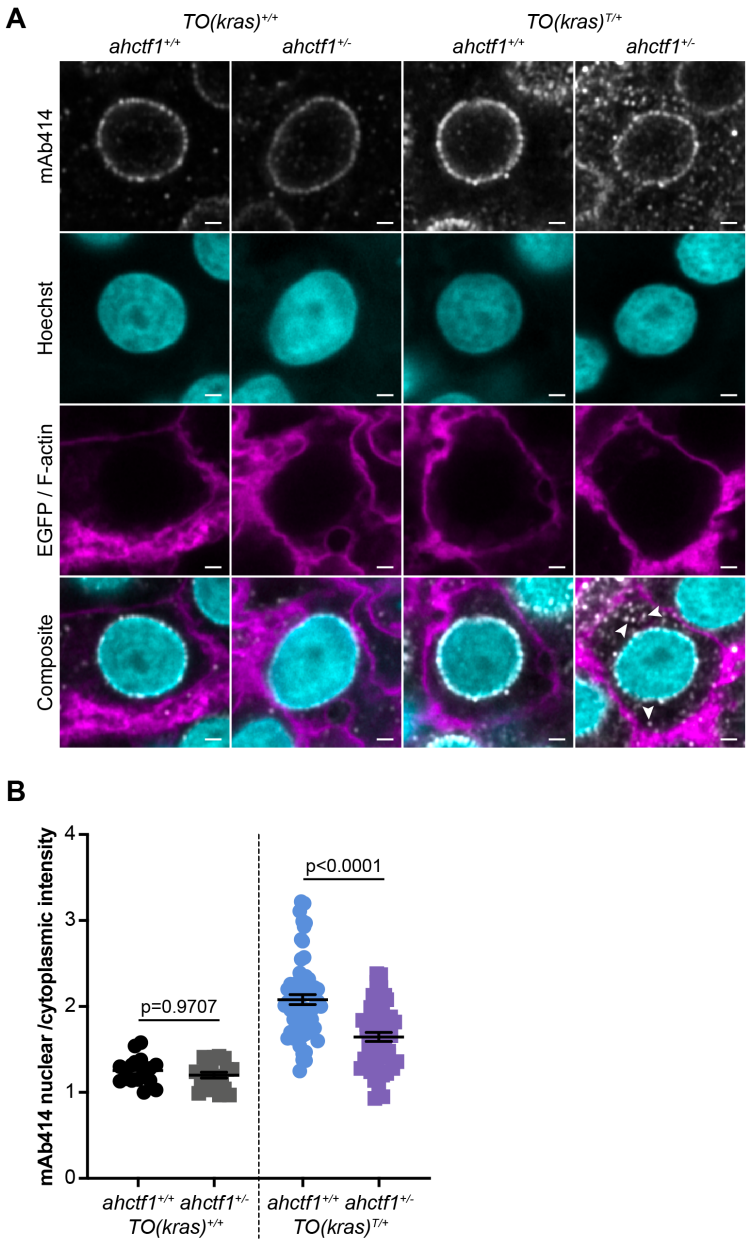

Figure 3.26 Heterozygous *ahctf1* mutation disrupts nuclear pore complexes in *TO(kras^{G12V})$^{T/+}$* hepatocytes

A. Representative Airyscan imaging of sections of liver of the indicated *ahctf1* and *TO(kras^{G12V})* genotype. Immunostaining with mAb414 identifies FG-nups, Hoechst 33342 fluorescent dye marks DNA and EGFP/F-actin marks the cell membrane/cytoskeleton. Arrowheads indicate cytoplasmic staining of mAb414. Scale bar 2 µm. **B.** Quantification of mean nuclear/cytoplasmic fluorescence intensity of mAb414. Fluorescence intensity in *TO(kras^{G12V})$^{+/+}$* hepatocytes was not affected by *ahctf1* heterozygosity. Fluorescence intensity was increased by 1.7-fold in *ahctf1$^{+/+}$; TO(kras^{G12V})$^{T/+}$* livers, compared to *ahctf1$^{+/+}$; TO(kras^{G12V})$^{+/+}$* livers. However, this increase in mean nuclear/cytoplasmic mAb414 fluorescence intensity was reduced by 21% in response to *ahctf1* heterozygosity. Data are

expressed as mean ± SEM, n≥18. Significance was calculated using a one-way ANOVA with Tukey's multiple comparisons test.

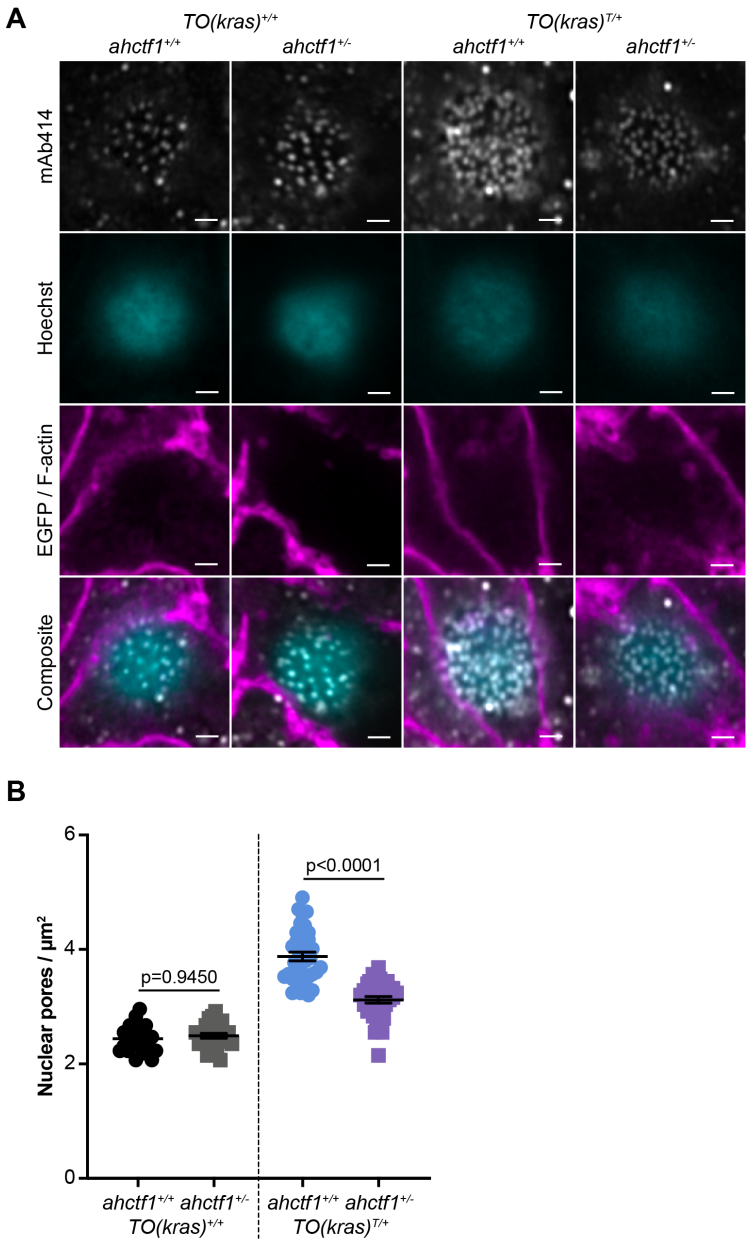

Figure 3.27 Heterozygous *ahctf1* mutation reduces nuclear pore complex density in *TO(kras^{G12V})$^{T/+}$* hepatocytes

A. Representative Airyscan imaging of the nuclear surface of hepatocytes of the indicated *ahctf1* and *TO(kras^{G12V})* genotype. Immunostaining with mAb414 identifies FG-nups, Hoechst 33342 fluorescent dye marks DNA and EGFP/F-actin marks the cell membrane/cytoskeleton. Scale bar 2 µm. **B.** Quantification of nuclear pore density at the surface of 5 nuclei per liver. *ahctf1* heterozygosity reduced nuclear pore number in *TO(kras^{G12V})$^{T/+}$* hepatocytes only. Data are expressed as mean ± SEM, n≥25. Significance was calculated using a one-way ANOVA with Tukey's multiple comparisons test.

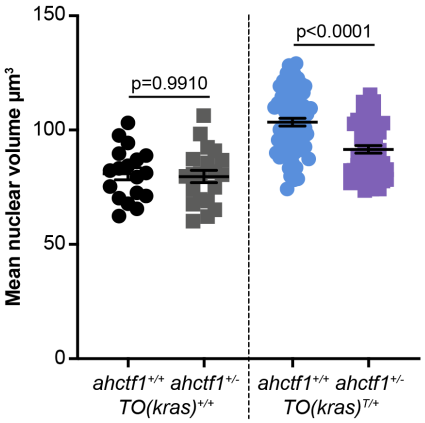

Figure 3.28 Heterozygous *ahctf1* mutation reduces nuclear volume in *TO(kras^{G12V})$^{T/+}$* hepatocytes

Nuclear volume was measured for an average of 35 nuclei per z-stack. *ahctf1* heterozygosity reduced nuclear volume specifically in *TO(kras^{G12V})$^{T/+}$* hepatocytes. Data are expressed as mean ± SEM, n≥25. Significance was calculated using a one-way ANOVA with Tukey's multiple comparisons test.

3.5.11 Heterozygous *ahctf1* mutation impairs mitotic spindle assembly and chromosome segregation in *TO(kras^{G12V})$^{T/+}$* hepatocytes

Elys function is also critical for proper spindle formation and chromosome segregation, so I assessed whether mitosis was affected by *ahctf1* heterozygosity using DAPI and α-tubulin staining of liver cryosections. Cells undergoing mitosis in *ahctf1$^{+/+}$; TO(kras^{G12V})$^{T/+}$* livers showed no defects with normal bipolar spindle formation at metaphase and complete chromosome segregation during anaphase (Figure 3.29). In contrast, *ahctf1$^{+/-}$; TO(kras^{G12V})$^{T/+}$* hepatocytes displayed abnormal mitosis, with multipolar spindles and misaligned chromosomes apparent at metaphase. Additionally, chromosome segregation was disrupted with multiple anaphase bridges formed. The distribution of cells observed at different mitotic stages was similar in *ahctf1$^{+/+}$* and *ahctf1$^{+/-}$* hepatocytes. In total, metaphase and anaphase was disrupted in 50% of *ahctf1$^{+/-}$; TO(kras^{G12V})$^{T/+}$* hepatocytes, whereas mitotic abnormalities were not observed in wildtype hepatocytes. Taken together, this data suggests that *ahctf1* is required for proper cell division.

3.5.12 Heterozygous *ahctf1* mutation leads to the accumulation of DNA damage in *TO(kras^{G12V})$^{T/+}$* hepatocytes

As chromosome segregation errors cause DNA damage, DNA damage was examined in *ahctf1*; *TO(kras^{G12V})$^{T/+}$* hepatocytes by staining with DAPI and γ-H2AX to mark DNA double-stranded breaks (Figure 3.30). Only 1% of *ahctf1$^{+/+}$; TO(kras^{G12V})$^{T/+}$* nuclei were positive for γ-H2AX. Conversely, DNA damage was markedly elevated in *ahctf1$^{+/-}$; TO(kras^{G12V})$^{T/+}$* hepatocytes with 6% of nuclei γ-H2AX positive. These data show that heterozygous *ahctf1* mutation has multiple impacts in *TO(kras^{G12V})$^{T/+}$* hepatocytes, including elevated levels of oncogene-induced stress, disrupted NPC assembly and impaired mitotic spindle assembly and chromosome segregation. Although some of these defects may be quite subtle or modest; collectively, disruption of these diverse cellular processes increase the proportion of highly stressed cells, resulting in DNA damage and ultimately apoptosis.

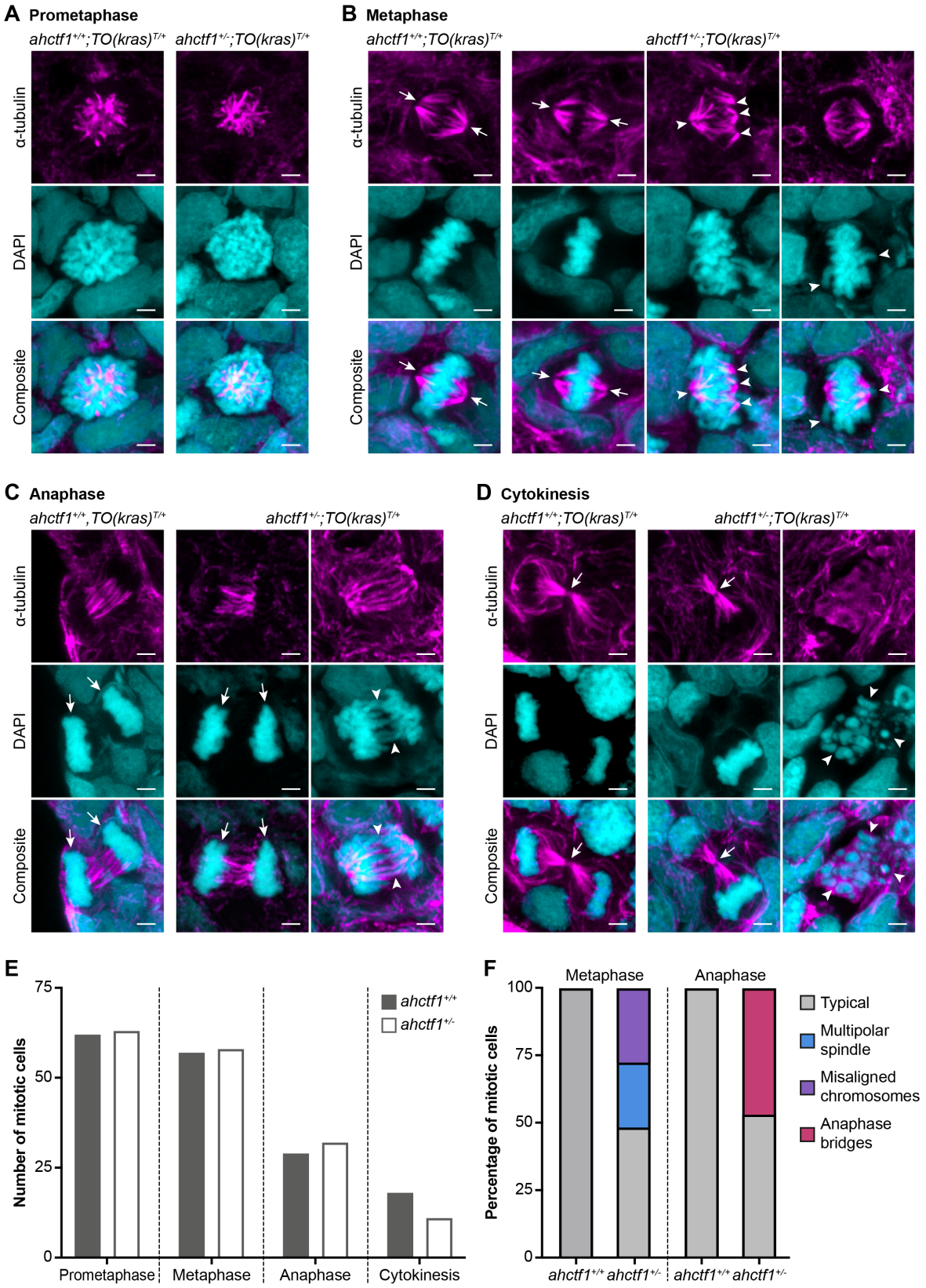

Figure 3.29 Heterozygous *ahctf1* mutation impairs mitotic spindle assembly and chromosome segregation in *TO(kras^{G12V})$^{T/+}$* hepatocytes

Representative Airyscan imaging of mitotic cells stained with α-tubulin antibody marking spindle microtubules and DAPI marking DNA in *TO(kras^{G12V})$^{T/+}$* micro-dissected liver cryosections of the indicated *ahctf1* genotype. Scale bar 2 µm. **A.** During prometaphase the NE breaks down and NPCs are disassembled. Elys relocates to kinetochores and DNA is condensed into chromosomes. Microtubules begin to randomly attach to chromosomes and dynamically change their length, resulting in α-tubulin staining that appears tangled. Prometaphase hepatocytes in both *ahctf1$^{+/+}$; TO(kras^{G12V})$^{T/+}$* and *ahctf1$^{+/-}$; TO(kras^{G12V})$^{T/+}$* larvae were very comparable and did not display any defects. **B.** At metaphase, chromosome pairs are fully condensed, aligned neatly in the centre of cells and a bipolar spindle is clearly established. *ahctf1$^{+/+}$; TO(kras^{G12V})$^{T/+}$* hepatocytes all exhibited proper spindle bipolarity (arrows). In contrast, whilst some *ahctf1$^{+/-}$; TO(kras^{G12V})$^{T/+}$* hepatocytes displayed bipolar spindles, other hepatocytes exhibited multipolar spindles (arrowheads). Another defect apparent was chromosome misalignment with some chromosomes not connected to the mitotic spindle (arrowheads). **C.** During anaphase, sister chromatids separate and move towards opposite spindle poles. As this stage progresses, Elys binds to chromatin. In *ahctf1$^{+/+}$; TO(kras^{G12V})$^{T/+}$* hepatocytes, chromatids were clearly defined and separate and elongation of interpolar microtubules was apparent (arrows). A portion of *ahctf1$^{+/-}$; TO(kras^{G12V})$^{T/+}$* hepatocytes displayed proper chromosome segregation. However, this was disrupted in some cells with anaphase bridges, that is a string of chromatin connecting the two segregating masses of chromosomes apparent (arrowheads). **D.** During cytokinesis, the final step of cell division, the cytoplasm is divided and two daughter cells are formed by a contractile actin ring with a bundled array of microtubule fibres. This structure was present in both *ahctf1$^{+/+}$; TO(kras^{G12V})$^{T/+}$* and *ahctf1$^{+/-}$; TO(kras^{G12V})$^{T/+}$* hepatocytes (arrows). However, instances of fragmented nuclei indicating cell death were observed in some *ahctf1$^{+/-}$; TO(kras^{G12V})$^{T/+}$* livers (arrowheads). **E.** Distribution of cells observed at different mitotic stages. N=92 livers, 326 cells. **F.** Quantification of the percentage of mitotic hepatocytes exhibiting an aberrant phenotype. N≥14.

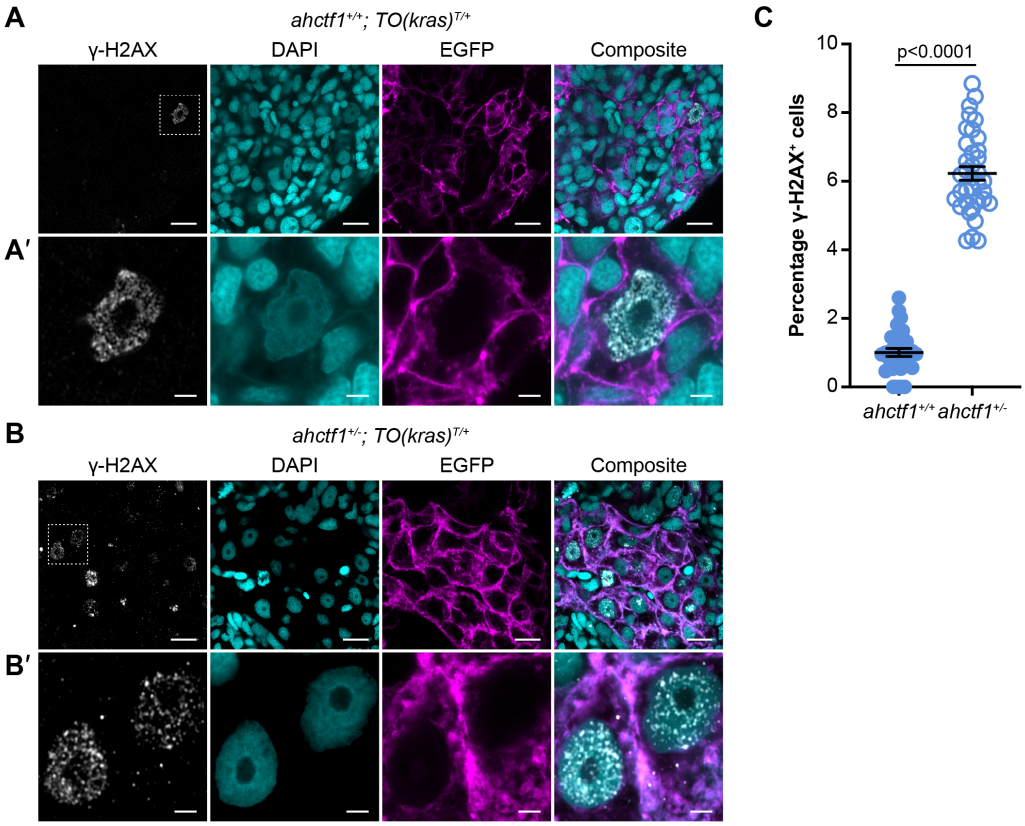

Figure 3.30 Heterozygous *ahctf1* mutation increases the number of *TO(kras^{G12V})$^{T/+}$* hepatocytes containing γ-H2AX , denoting DNA damage

Representative Airyscan images of cryosections of *TO(kras^{G12V})$^{T/+}$* livers immuno-stained with γ-H2AX, to identify DNA damage, DAPI to stain DNA and EGFP marking the cell membrane. **A.** In cryosections of *ahctf1$^{+/+}$; TO(kras^{G12V})$^{T/+}$* livers, γ-H2AX positive nuclei were rarely observed. Scale bar 5 µm. **A′.** Inset showing a single γ-H2AX positive nuclei in cryosections of liver taken from *ahctf1$^{+/+}$; TO(kras^{G12V})$^{T/+}$* larvae. Scale bar 2 µm. **B.** Cryosections of *ahctf1$^{+/-}$; TO(kras^{G12V})$^{T/+}$* livers exhibited multiple γ-H2AX positive nuclei. Scale bar 5 µm. **B′.** Inset showing multiple γ-H2AX positive hepatocytes in sections of liver taken from *ahctf1$^{+/-}$, TO(kras^{G12V})$^{T/+}$* larvae. Scale bar 2 µm. **C.** Quantification of the percentage of cells positive for γ-H2AX. Data are expressed as mean ± SEM, n≥31. Significance was calculated using an unpaired t-test.

3.5.13 Combined approaches targeting the nuclear pore completely restrict *kras^{G12V}*-driven liver hyperplasia

Having determined that heterozygous *ahctf1* mutation was effective in restricting *kras^{G12V}*-driven hepatocyte hyperplasia by impeding a number of cellular processes, I next examined whether the degree to which tumour burden was reduced could be enhanced by disrupting one or more of these processes further. In this section, I embarked on this question by utilising a different genetic mutation disrupting the nuclear pore. The opportunity to do this was presented by the Heath's lab's demonstration that one of our collection of endodermal organ mutants contained a *ranbp2* (encoding Nup358) mutation. The *ranbp2^{452}* mutant line was generated in the Liver^{plus} ENU mutagenesis screen (discussed in section 1.4.6). Homozygous *s452* mutants exhibited defects in the size and shape of the liver, pancreas and intestine as well as in other rapidly proliferating tissue compartments. Heterozygous larvae have no gross morphological phenotype. The mutant was shown to harbour a *ranbp2* mutation by Dr Fansuo Geng in the Heath lab, using homozygosity mapping[372,373] in collaboration with Associate Professor Kelly Smith and Professor Ben Hogan, then at the Institute for Medical Bioscience at the University of Queensland (Figure 3.31).

ranbp2 heterozygosity did not impact normal liver volume in *2-CLiP* larvae at 7 dpf (Figure 3.32). Induced expression of oncogenic Kras^{G12V} led to hepatocyte hyperplasia and a striking 4.9-fold increase in liver volume in *ranbp2$^{+/+}$; TO(kras^{G12V})$^{T/+}$* larvae. This excess liver volume was modestly reduced by 12% in *ranbp2$^{+/-}$; TO(kras^{G12V})$^{T/+}$* larvae.

In addition, *ranbp2* heterozygosity, alone or in combination with *ahctf1* mutation, did not affect liver growth in *2-CLiP* larvae (Figure 3.33). *ahctf1* heterozygosity alone reduced excess liver volume by 38% in *TO(kras^{G12V})$^{T/+}$* larvae, consistent with previous results. Significantly, *ranbp2$^{+/-}$; ahctf1$^{+/-}$* interacted synergistically to severely limit *kras^{G12V}*-driven liver hyperplasia. Hepatocyte hyperplasia and liver enlargement was completely blocked in *ranbp2$^{+/-}$; ahctf1$^{+/-}$; TO(kras^{G12V})$^{T/+}$* larvae returning to the liver volume observed in normal, non-hyperplastic *2-CLiP* livers. Therefore, these results suggest that cancer cells are selectively vulnerable to reduced expression of nups and impaired NPC function. The fact that combinatorial targeting of the NPC had no detrimental effects on *2-CLiP* larvae, suggests a therapeutic window that may be possible to exploit clinically.

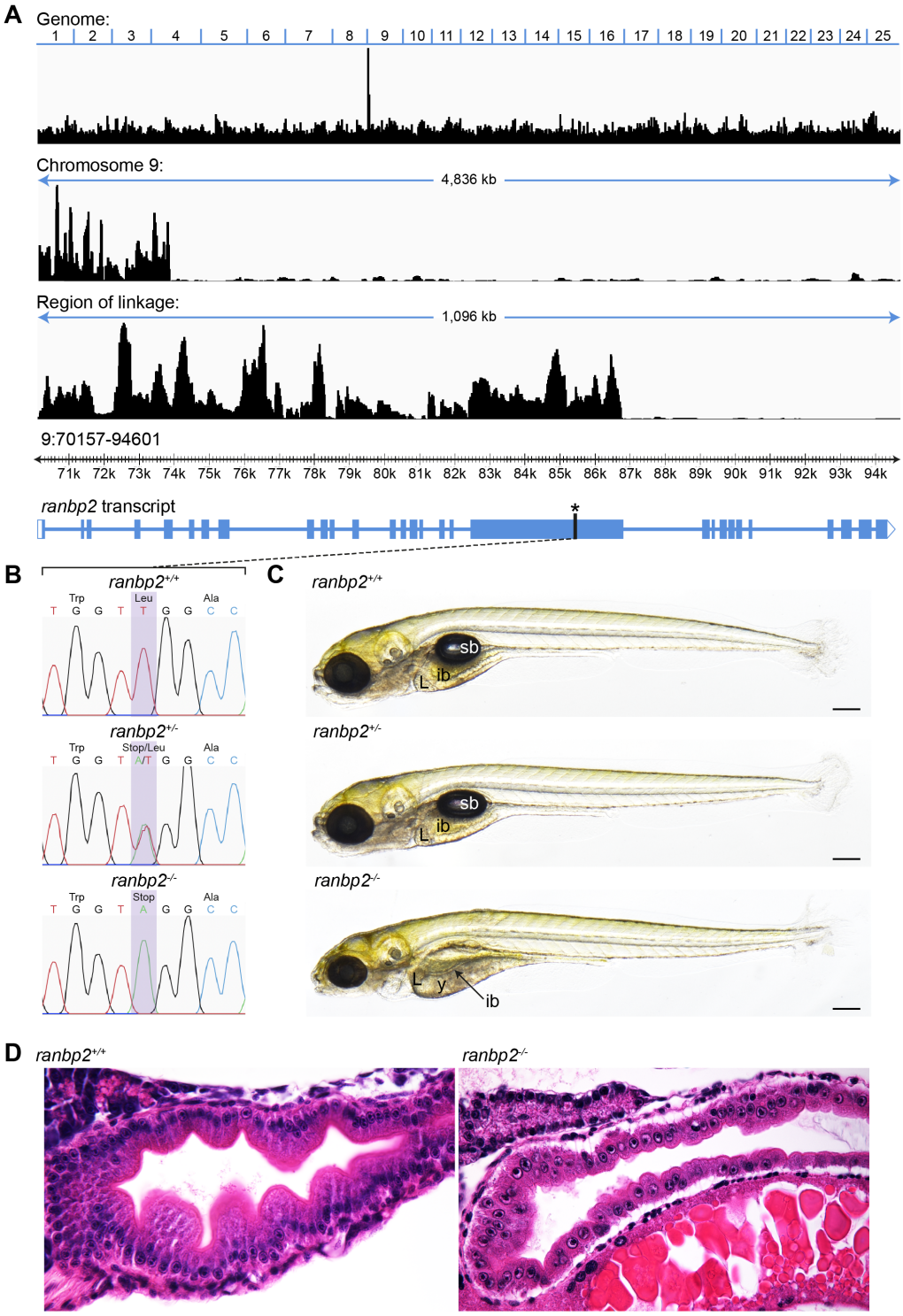

Figure 3.31 Genetic and phenotypic characterisation of the *ranbp2* mutant

A. Positional cloning of *s452* mutant using whole genome sequencing and homozygosity mapping. The genomic region containing the *s452* causal mutation is derived exclusively from the initial ENU mutated allele and is therefore defined by increased homozygosity. By analysing single nucleotide polymorphism homozygosity, the chromosomal region underlying the mutant phenotype can be efficiently identified. In *s452* mutants the region of linkage was

found in chromosome 9, corresponding to the *ranbp2* gene. Plot displays genomic homozygosity across 25 chromosomes, chromosome 9 and the region of linkage. The genome position of *ranbp2* within this region and a schematic of *ranbp2* transcript with the position of the mutation indicated (asterisk) are also shown. **B.** Sanger sequencing chromatographs confirming a T>A transversion mutation introducing a premature stop codon (TTG>TAG). **C.** Brightfield images of 7 dpf *ranbp2* larvae. Compared to wildtype, *ranbp2*$^{-/-}$ larvae have a thinner intestinal epithelium, smaller head and eye, cardiac oedema and fail to inflate the swim bladder or fully absorb the yolk. Meanwhile, *ranbp2*$^{+/-}$ larvae exhibit no phenotypic abnormalities. Scale bar 200 µm. **D.** Haematoxylin and Eosin-stained histology sections of 5 dpf *ranbp2* larvae. Whereas the intestinal epithelial cells in wildtype larvae are large and columnar with basally positioned nuclei, these cells in *ranbp2*$^{-/-}$ larvae are cuboidal with centrally positioned nuclei that contain prominent nucleoli. In wildtype, the rapid rate of cellular proliferation leads to the intestinal epithelium elaborating extensive folds, which in section are reminiscent of mammalian villi. Meanwhile, the intestinal epithelial cells in *ranbp2*$^{-/-}$ larvae are much fewer in number, and some exhibit blebbing at their apical membranes. The epithelium also fails to elaborate into folds in *ranbp2*$^{-/-}$ larvae.

ib: intestinal bulb, L: liver, sb: swim bladder, y: yolk.

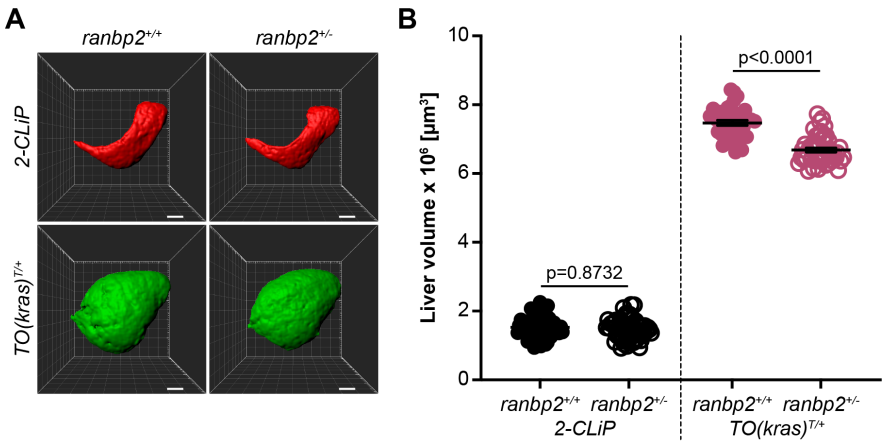

Figure 3.32 Heterozygous *ranbp2* mutation reduces liver volume in *TO(kras^{G12V})$^{T/+}$* larvae

A. Representative three-dimensional reconstructions of *2-CLiP* and *TO(kras^{G12V})$^{T/+}$* livers of the indicated *ranbp2* genotype. Scale bar 25 µm. **B.** Liver volume in *2-CLiP* larvae was not impacted by *ranbp2* heterozygosity. However, in *TO(kras^{G12V})$^{T/+}$* larvae *ranbp2* heterozygosity reduced excess liver volume by 12%. Data are expressed as mean ± SEM, n≥38. Significance was calculated using a one-way ANOVA with Tukey's multiple comparisons test.

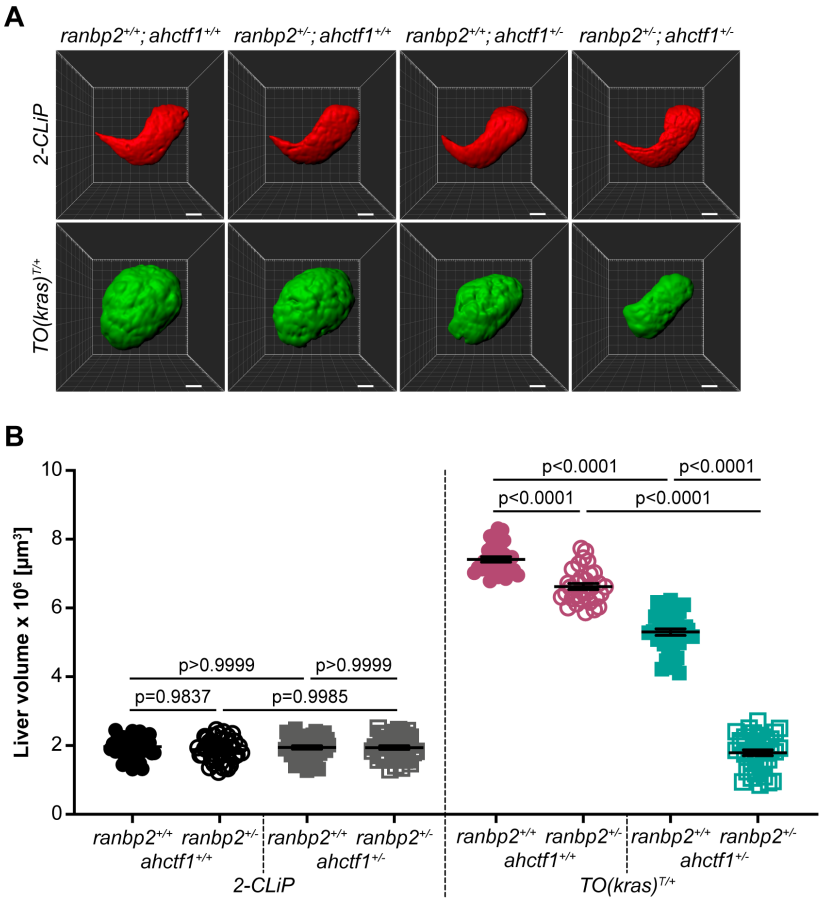

Figure 3.33 Combined heterozygous *ranbp2* and *ahctf1* mutation completely restricts *kras*^{G12V}-driven liver hyperplasia

A. Representative three-dimensional reconstructions of *2-CLiP* and *TO(kras*^{G12V}*)*$^{T/+}$ livers of the indicated *ranbp2* and *ahctf1* genotype. Scale bar 25 µm. **B.** Liver volume in *2-CLiP* larvae was not impacted by *ranbp2* heterozygosity alone, *ahctf1* heterozygosity alone or by combination of *ranbp2*$^{+/-}$ and *ahctf1*$^{+/-}$ genotypes. Induced expression of *TO(kras*^{G12V}*)*$^{T/+}$ caused hepatocyte hyperplasia and liver enlargement, with a 3.8-fold increase in liver volume in *ranbp2*$^{+/+}$*; ahctf1*$^{+/+}$*; TO(kras*^{G12V}*)*$^{T/+}$ larvae. *ranbp2* heterozygosity alone and *ahctf1* heterozygosity alone reduced excess liver volume by 13% and 38%, respectively in *TO(kras*^{G12V}*)*$^{T/+}$ larvae. The combination of the *ranbp2*$^{+/-}$ and *ahctf1*$^{+/-}$ genotypes produced a synergistic effect on liver volume, severely limiting *kras*^{G12V}-driven hepatocyte hyperplasia, returning liver volume to the level observed in *2-CLiP* larvae. Data are expressed as mean ± SEM, n≥30. Significance was calculated using a one-way ANOVA with Tukey's multiple comparisons test.

3.5.14 *NUP107-160* complex components are frequently overexpressed in human cancer samples

The *in vivo* pre-clinical data from the *TO(kras^{G12V})$^{T/+}$* model I have presented thus far suggests that hepatocarcinogenesis requires proper nuclear pore function. Various other approaches to investigating the relationship between cancer and nuclear pore function are consistent with this notion. For example, analysis of genome-wide CRISPR screens, curated in the DepMap portal, reveals that *AHCTF1* is essential for the viability of 805 out of 808 different human cancer cell lines[374,375]. The majority of *NUP107-160* complex members are also classified as common essential genes (Table 3.5). Common essential genes are those that rank amongst the topmost genes required for the sustained proliferation of at least 90% of cancer cell lines. Such genes are also likely to be essential for normal cells to proliferate. Moreover, examination of nup mRNA expression in The Cancer Genome Atlas (TCGA) datasets using the cBioPortal for Cancer Genomics[376,377] shows that *NUP107-160* complex components are frequently overexpressed in tumour samples with an mRNA expression z-score >2 in a diverse array of cancers (Table 3.6). Z-scores indicate the number of standard deviations away from the mean mRNA expression level of a given gene. Notably, *AHCTF1* is overexpressed in 32.24% of patient HCC samples and is also significantly upregulated in breast invasive carcinoma (27.54% of samples) and cholangiocarcinoma (36.11% of samples). In contrast, the *NUP107-160* complex was rarely under-expressed with mRNA expression z-score <-2 in an average of 2% of samples.

To explore the possibility that nup overexpression is associated with clinical outcomes, overall survival of patients was investigated by interrogating TCGA datasets. Median overall survival of HCC patients with increased expression (z-score >2) of components of the *NUP107-160* complex was 22.78 months, whereas survival of patients with *NUP107-160* complex expression z-scores <2 was 80.74 months (Figure 3.34). Similarly, overexpression of the *NUP107-160* complex components significantly reduced overall survival in brain lower grade glioma, breast invasive carcinoma, adrenocortical carcinoma, skin cutaneous melanoma, kidney renal papillary cell carcinoma and sarcoma patients (Figure 3.35). These data compliment my findings and suggest that targeting components of the nuclear pore may be a worthwhile strategy for a broad spectrum of cancers with the capacity to improve overall patient survival.

Table 3.5 DepMap portal gene essentiality CRISPR screens of *NUP107-160* complex components dependency in human cancer cell lines

NUP	Dependent cell lines (%)	Classification
AHCTF1	99.63	Common essential
NUP37	14.36	Not common essential
NUP43	99.88	Common essential
NUP85	100.00	Common essential
NUP98	97.65	Common essential
NUP107	96.29	Common essential
NUP133	100.00	Common essential
NUP160	97.77	Common essential
SEC13	100.00	Common essential
DNA1L	99.13	Common essential

Table 3.6 Percentage of TCGA PanCancer Atlas dataset samples with altered mRNA expression z-scores of *NUP107-160* complex components

TCGA study	*AHCTF1*		*NUP37*		*NUP43*		*NUP85*		*NUP98*	
	<-2	>2	<-2	>2	<-2	>2	<-2	>2	<-2	>2
AML	0.00	5.78	0.58	4.62	1.16	4.05	1.73	4.05	2.31	4.05
ACC	0.00	5.13	1.28	32.05	0.00	6.41	0.00	7.69	0.00	3.85
BLCA	0.98	10.81	0.98	6.39	3.93	4.42	0.25	13.76	10.57	5.16
LGG	0.19	5.45	0.97	4.67	1.95	2.92	0.00	6.81	3.50	4.28
BRCA	0.55	27.54	0.00	5.08	3.05	6.84	0.09	18.48	3.60	4.62
CESC	2.38	19.05	0.68	6.46	12.24	4.76	1.70	10.54	10.54	2.04
CHOL	5.56	36.11	2.78	2.78	0.00	2.78	0.00	8.33	11.11	5.56
COAD	3.89	6.08	0.34	4.39	4.22	4.39	2.20	8.61	3.72	5.07
DLBC	0.00	6.25	0.00	10.42	10.42	2.08	2.08	0.00	0.00	8.33
ESCA	0.55	14.36	0.00	5.52	1.66	7.73	2.76	16.57	6.08	3.87
GBM	0.00	3.13	0.00	4.38	5.00	1.88	0.00	4.38	1.88	3.75
HNSC	2.33	13.01	0.00	3.88	0.97	4.27	0.19	8.54	3.11	4.08
KICH	0.00	4.62	0.00	3.08	0.00	1.54	0.00	4.62	4.62	1.54
KIRC	1.57	3.92	0.20	7.25	6.08	2.16	0.98	4.51	0.59	4.31
KIRP	1.77	7.42	0.35	8.48	1.06	3.53	0.35	30.39	0.35	5.30
LIHC	0.82	32.24	0.00	6.01	0.55	6.83	0.00	18.31	2.46	3.28
LUAD	0.20	17.84	0.00	5.88	1.96	3.33	0.39	15.10	1.96	5.10
LUSC	0.41	15.29	0.21	6.61	2.89	8.47	0.41	13.43	5.58	2.69
MESO	4.60	11.49	2.30	9.20	16.09	0.00	0.00	8.05	3.45	2.30
OV	2.67	13.67	0.00	5.00	27.00	5.33	1.00	8.33	20.67	4.00
PAAD	1.13	7.91	0.56	4.52	7.34	1.69	2.26	7.91	3.95	3.95
PCPG	2.81	7.30	3.93	2.25	2.25	5.06	0.56	3.37	12.36	3.37
PRAD	1.42	6.49	0.81	6.09	3.45	2.23	0.41	5.48	0.81	2.84
SARC	0.40	6.32	1.19	11.46	1.19	12.25	0.79	10.28	3.56	5.14
SKCM	3.84	11.51	2.26	4.97	6.32	1.81	1.81	14.45	5.42	4.29
STAD	1.21	11.65	0.00	6.55	0.49	7.52	1.21	10.44	0.73	6.31
TGCT	2.01	11.41	0.00	10.74	0.00	7.38	0.00	14.77	0.00	2.68
THYM	2.52	10.08	2.52	4.20	1.68	1.68	0.00	2.52	3.36	3.36
THCA	3.82	5.02	2.41	3.01	2.81	3.01	2.01	4.02	2.21	3.61
UCS	0.00	3.51	7.02	8.77	3.51	14.04	8.77	31.58	0.00	3.51
UCEC	2.47	14.23	0.57	5.69	0.76	5.50	0.00	9.11	2.09	3.98
UVM	0.00	3.75	2.50	5.00	0.00	1.25	2.50	0.00	3.75	8.75

TCGA study	*NUP107*		*NUP133*		*NUP160*		*SEC13*		*SEH1L*	
	<-2	>2	<-2	>2	<-2	>2	<-2	>2	<-2	>2
AML	2.31	2.89	3.47	3.47	4.05	2.31	0.58	4.05	0.00	4.05
ACC	1.28	30.77	0.00	5.13	0.00	6.41	1.28	8.97	5.13	2.56
BLCA	0.49	14.00	0.25	10.32	0.25	4.91	0.49	17.69	0.74	12.53
LGG	0.58	5.06	2.92	3.11	2.53	3.50	1.17	4.28	2.33	4.67
BRCA	0.55	10.81	1.02	31.98	0.18	7.12	0.00	8.87	0.46	9.61
CESC	3.74	8.16	2.04	22.45	6.80	3.06	2.04	4.76	2.38	8.16
CHOL	0.00	11.11	0.00	50.00	0.00	0.00	0.00	0.00	8.33	0.00
COAD	3.04	4.56	2.87	8.11	1.69	4.56	0.00	4.05	3.21	2.70
DLBC	2.08	14.58	2.08	8.33	0.00	6.25	0.00	6.25	4.17	14.58
ESCA	0.55	11.60	1.10	16.57	0.00	5.52	1.66	2.21	2.76	11.05
GBM	1.88	6.88	3.13	5.63	0.00	4.38	0.00	6.88	5.00	5.63
HNSC	1.55	9.32	1.17	10.49	1.36	6.21	0.39	1.75	2.14	14.76
KICH	4.62	6.15	0.00	3.08	1.54	1.54	0.00	4.62	3.08	6.15
KIRC	1.18	7.45	2.75	2.94	2.16	3.14	0.59	2.35	2.75	4.31
KIRP	0.35	9.54	1.41	4.59	0.35	3.89	0.35	7.42	2.83	4.24
LIHC	0.27	7.92	1.09	30.60	0.00	5.46	0.55	8.47	2.73	6.83
LUAD	0.00	14.90	0.78	17.84	0.59	6.27	0.20	4.90	0.78	9.41
LUSC	0.21	10.33	1.24	16.53	0.00	5.17	1.86	2.69	0.21	7.85
MESO	1.15	10.34	1.15	11.49	0.00	3.45	3.45	4.60	0.00	5.75
OV	1.00	9.67	1.67	19.67	0.33	4.33	0.67	3.00	9.33	7.33
PAAD	2.26	6.78	1.69	6.78	2.82	3.95	0.00	3.95	6.78	10.17
PCPG	2.25	6.18	3.93	5.06	9.55	2.81	2.25	0.56	2.81	2.25
PRAD	1.62	5.07	3.25	3.65	1.42	1.83	1.62	5.07	2.43	5.68
SARC	0.79	16.60	2.37	7.91	0.00	5.53	0.00	9.09	0.00	8.70
SKCM	0.90	5.64	2.48	16.70	1.58	2.93	0.00	6.09	2.26	6.55
STAD	0.24	11.17	1.46	15.78	0.00	7.77	0.00	5.34	0.00	8.98
TGCT	0.00	25.50	0.00	5.37	0.67	4.03	0.67	8.72	0.00	6.04
THYM	3.36	2.52	0.84	10.92	2.52	4.20	3.36	1.68	0.84	0.84
THCA	3.82	1.41	3.41	4.22	4.02	2.21	0.80	5.22	1.81	3.41
UCS	0.00	19.30	0.00	15.79	0.00	3.51	0.00	1.75	0.00	3.51
UCEC	0.76	5.69	0.76	14.80	0.76	5.50	0.00	4.74	1.14	8.16
UVM	1.25	1.25	1.25	10.00	2.50	1.25	22.50	0.00	2.50	2.50

Heat-map based on percentage of TCGA samples with mRNA expression levels of Nup107-160 complex components overexpressed (Z-score >2: over 2 standard deviations above mean expression) or under-expressed (Z-score <-2: over 2 standard deviations below mean

expression). *NUP107-160* complex components are overexpressed in 7.48% of all samples. In particular, *AHCTF1* is overexpressed in 11.20% of all patient cancer samples and is significantly upregulated in breast invasive carcinoma (27.54% of samples) and liver hepatocellular carcinoma (32.24% of samples).

AML: acute myeloid leukemia, ACC: adrenocortical carcinoma, BLCA: bladder urothelial carcinoma, LGG: Brain lower grade glioma, BRCA: breast invasive carcinoma; CESC: cervical squamous cell carcinoma and endocervical adenocarcinoma, CHOL: cholangiocarcinoma, COAD: colon adenocarcinoma, DLBC: Lymphoid neoplasm diffuse large B-cell lymphoma, ESCA: oesophageal carcinoma, GBM: glioblastoma multiforme, HNSC: head and neck squamous cell carcinoma, KICH: kidney chromophobe, KIRC: kidney renal cell carcinoma, KIRP: kidney renal papillary cell carcinoma, LIHC: liver hepatocellular carcinoma, LUAD: lung adenocarcinoma, LUSC: lung squamous cell carcinoma, MESO: mesothelioma, OV: ovarian serous cystadenocarcinoma, PAAD: pancreatic adenocarcinoma, PCPG: pheochromocytoma and paraganglioma, PRAD: prostate adenocarcinoma, SARC: sarcoma, SKCM: skin cutaneous melanoma, STAD: stomach adenocarcinoma, TGCT: testicular germ cell tumours, THYM: thymoma, THCA: thyroid carcinoma, UCS: uterine carcinosarcoma, UCEC: uterine corpus endometrial carcinoma, UVM: uveal melanoma.

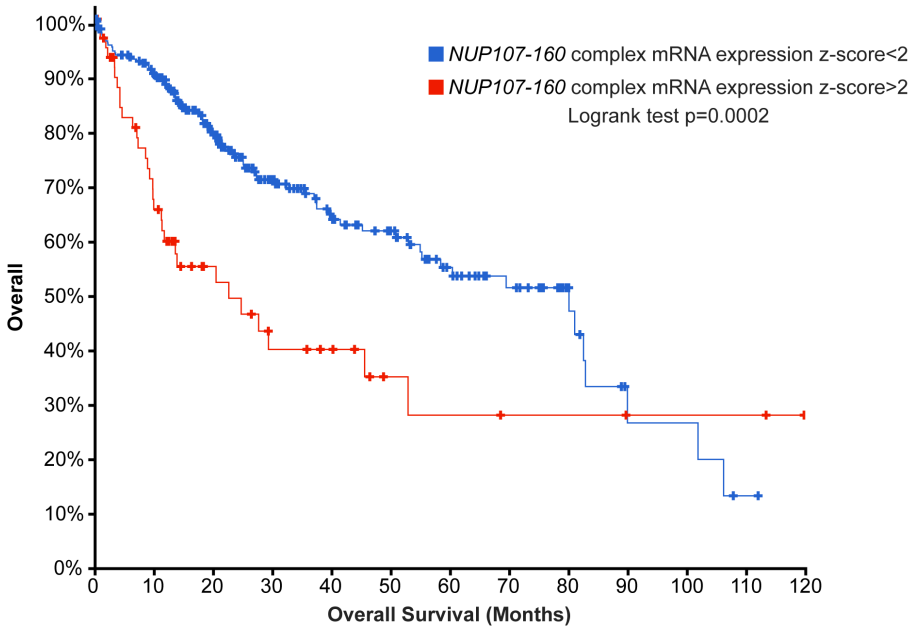

	Number of cases, Total	Number of cases, Deceased	Median Months Overall Survival
***NUP107-160* complex mRNA expression z-score<2**	287	89	80.74
***NUP107-160* complex mRNA expression z-score>2**	65	31	22.78

Figure 3.34 Overexpression of the *NUP107-160* complex is associated with reduced overall survival in HCC

Overall survival of TCGA HCC patients with mRNA expression z-scores >2 for one or more *NUP107-160* complex components (65 cases) and mRNA expression z-scores <2 for one or more *NUP107-160* complex components (287 cases). Notches indicate individual cases.

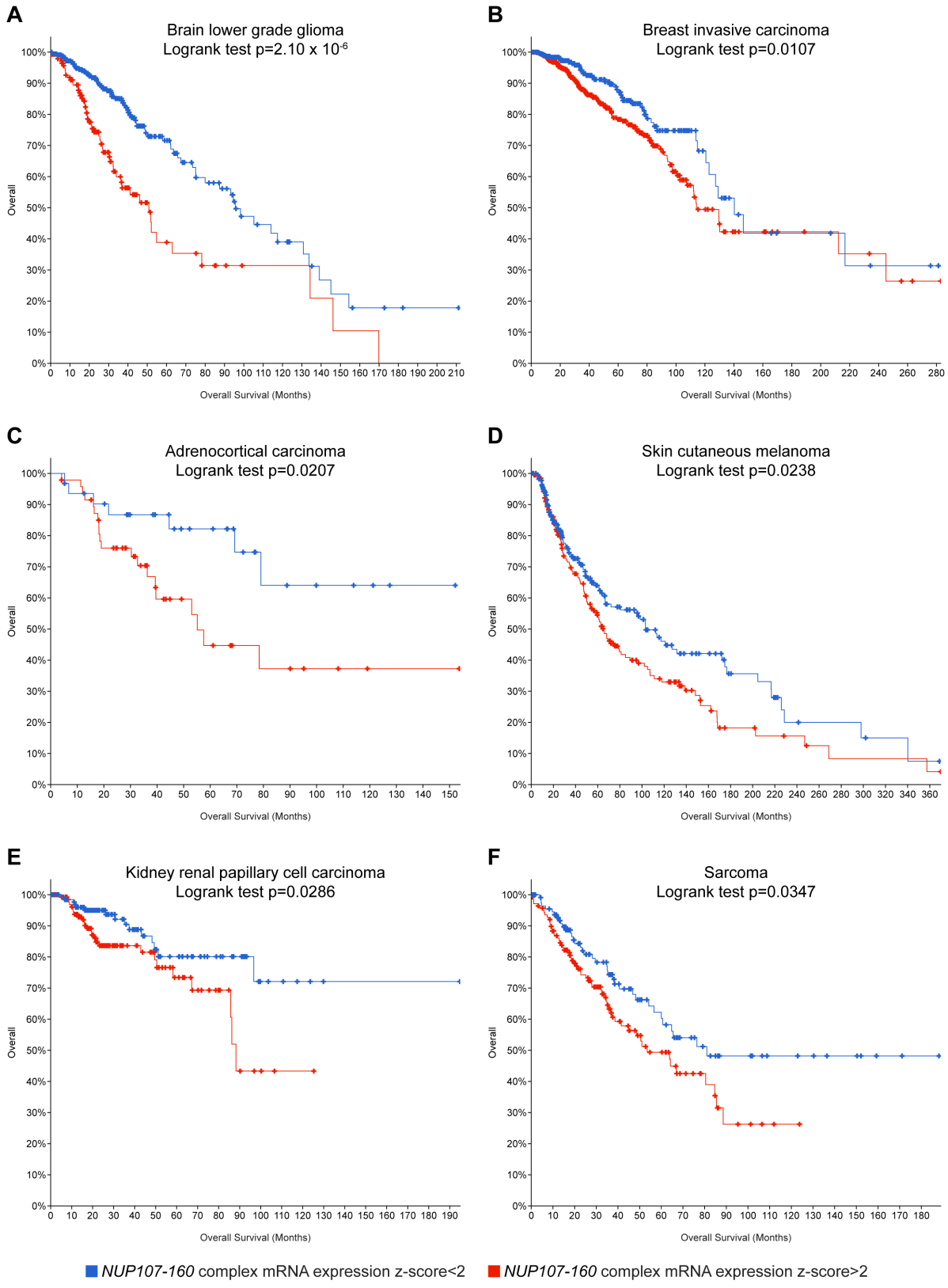

Figure 3.35 Overexpression of the *NUP107-160* complex is associated with reduced overall survival in diverse cancer types

A. Overall survival of TCGA brain lower grade glioma patients with *NUP107-160* complex mRNA expression z-scores >2 (151 cases) and z-scores <2 (362 cases). **B.** Overall survival of TCGA breast invasive carcinoma patients with *NUP107-160* complex mRNA expression z-scores >2 (669 cases) and z-scores <2 (413 cases). **C.** Overall survival of TCGA adrenocortical carcinoma patients with *NUP107-160* complex mRNA expression z-scores >2 (47 cases) and z-scores <2 (31 cases). **D.** Overall survival of TCGA skin cutaneous melanoma patients with *NUP107-160* complex mRNA expression z-scores >2 (198 cases) and z-scores <2 (227 cases). **E.** Overall survival of TCGA kidney renal papillary cell carcinoma patients with *NUP107-160* complex mRNA expression z-scores >2 (146 cases) and z-scores <2 (136 cases). **F.** Overall survival of TCGA sarcoma patients with *NUP107-160* complex mRNA expression z-scores >2 (139 cases) and z-scores <2 (114 cases).

3.6 Discussion

Components of NPCs represent promising candidates for therapeutic intervention in cancer due to their central role in mediating nucleocytoplasmic transport as well as transport-independent functions in DNA repair, genome regulation and mitosis. In this chapter, *ahctf1* heterozygosity is identified as participating in a synthetic lethal interaction with hyper-activation of the pro-proliferative, pro-survival RAS/RAF/MAPK signalling pathway to markedly reduce tumour burden in a genetically engineered zebrafish model of HCC. The therapeutic benefit of this mild (50%) reduction in *ahctf1* expression was caused, at least in part, by an increase in cell death. *ahctf1* heterozygosity produced a reduction in the density of nuclear pores, aberrant chromatid separation during mitosis and accumulation of DNA damage. These defects combined to activate Tp53-dependent and independent cell death pathways, explaining the observed reduction in tumour burden (Figure 3.36). Importantly, *ahctf1* heterozygosity had no adverse effects in the non-*kras*^{G12V}-expressing tissues in this model. These findings advance ELYS as an attractive target for cancer therapy with a viable therapeutic window.

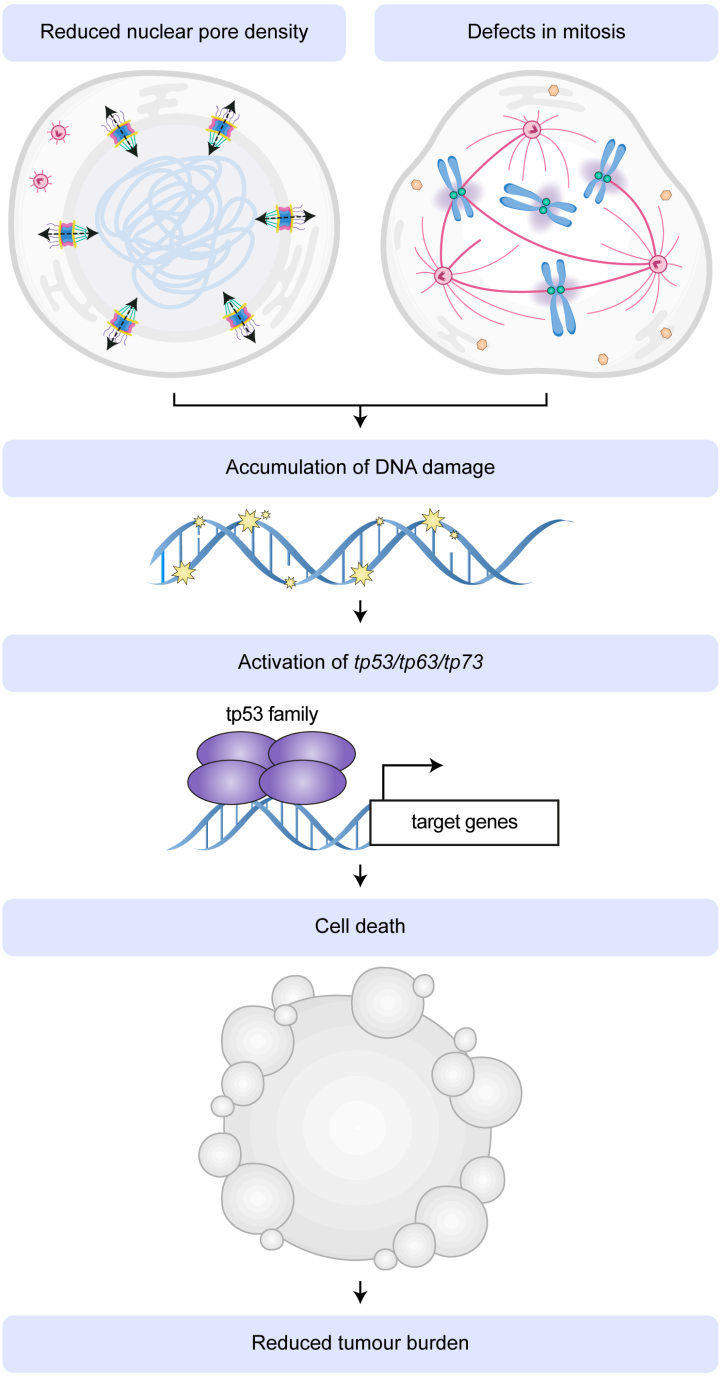

Figure 3.36 Schematic explaining the mechanism by which *ahctf1* heterozygosity reduces tumour burden

In the *TO(kras^{G12V})$^{T/+}$* HCC model, *ahctf1* heterozygosity results in a reduction in the density of nuclear pores and aberrant chromosome separation during mitosis, leading to the accumulation of DNA damage. These defects combine to activate Tp53 family members which trigger the apoptotic cell death pathway, ultimately reducing tumour burden.

There are several reasons why the *TO(kras^{G12V})* zebrafish HCC model provides a clinically relevant *in vivo* platform for the study of human cancer and the discovery of new therapeutic strategies[176]. Firstly, RAS/RAF/MAPK signalling is almost always hyper-activated in human HCC[15]. Secondly, the progressive accumulation of histopathologic features including irregular nuclei, cytoplasmic vacuolation and increased vascularisation that are characteristic of tumour progression in HCC are reproduced in the zebrafish model[167]. Thirdly, RNA-sequencing of *TO(kras^{G12V})$^{T/+}$* hepatocytes revealed that compared to control *TO(kras^{G12V})$^{+/+}$* hepatocytes, pathways required for rapid proliferation, such as DNA replication and cell cycle pathways are significantly upregulated. This is consistent with a previous comparative transcriptomic analysis on oncogenic *kras*^{G12V} hepatocytes isolated on the basis of GFP positivity and fluorescence-activated cell sorting (FACS) from larval zebrafish treated with doxycycline from 3 to 8 dpf, which revealed that the gene expression profile strongly resembles that of early-stage human HCC. *kras*^{G12V} hepatocytes exhibited elevated expression of RAS/RAF/MAPK target genes such as *FGFR4, ETV4, EPHA2, DUSP6* and *SPRY* and DNA damage response genes *CCND1* and *H2AX1*[177]. All these genes were also significantly upregulated in the RNA-sequencing experiment I performed.

In the *TO(kras^{G12V})* model, *ahctf1* heterozygosity partly mitigates against mutant Kras^{G12V}-driven hepatocyte hyperplasia, resulting in a decrease in tumour burden. Consistent with the literature, which demonstrates roles for the Elys protein in post-mitotic NPC reassembly, spindle formation and chromatid separation during mitosis, I found that *ahctf1* heterozygosity produced perturbations in all these processes, culminating in the accumulation of DNA damage. Taken together, these events would be expected to intensify oncogene-induced stress produced by expression of the Kras^{G12V} protein and provide a powerful stimulus to Tp53 activation. That this sequence of events is borne out is supported by results showing increased abundance of Tp53 protein and enhanced transcription of the pro-apoptosis genes, *pmaip1*, *bbc3* and *bax* as well as down regulation of the pro-survival genes, *bcl2* and *bclxl*. These observations support a mechanism whereby *ahctf1* heterozygosity and expression of mutant *kras^{G12V}* produce a synthetic lethal interaction that culminates in activation of a pro-apoptotic *tp53* transcriptional program that produces a reduction in tumour burden.

An important question from this is whether the promising therapeutic effect of partially inhibiting Elys function may be diminished in tumours unable to express wildtype Tp53 protein. This is a clinically relevant question since mutations in TP53, or amplification/overexpression of its negative regulators MDM2/MDM4, occur in 30% of HCC cases[10]. To investigate this further, experiments were repeated on a *tp53* mutant background. Remarkably, *ahctf1* heterozygosity still produced a 24% reduction in tumour burden and induced cell death in the complete absence of Tp53 function. Thinking about the mechanism of this effect, the possibility that loss of Tp53 function was compensated for by Tp63 and/or Tp73 was considered. These Tp53 family members share considerable structural homology

with Tp53, particularly within the DNA binding domain, and can activate common and distinct sets of target genes that cause cell cycle arrest, senescence and apoptosis[369,370]. For example, in response to DNA damage, Tp63 induces senescence and apoptosis in the same way as Tp53, via transcriptional induction of *cdkn1a*, *bbc3* and *pmaip1*[378]. *ahctf1* heterozygosity was demonstrated to upregulate *tp63* and *tp73* expression by 3.0-fold and 2.3-fold, respectively, and this was further enhanced by *tp53* mutation. These results suggest a mechanism through which *ahctf1* heterozygosity achieves a reduction in tumour burden in the absence of Tp53 function. Since TP63 and TP73 are rarely mutated in cancer[379], the possibility remains that inhibition of ELYS function may still produce a beneficial effect on tumour growth in patients harbouring TP53 mutations.

Recently, another research group reported that continuous rounds of nuclear pore assembly and disassembly are essential to sustain the behaviour of vigorously proliferating cells, including cancer cells[380], raising the possibility that nuclear pore components may provide useful targets for cancer treatment. In this study, Sakuma et al. used siRNAs targeting 28 out of 32 nucleoporin genes, including *AHCTF1*, to screen for reduced abundance of mature NPCs in the human melanoma-derived cell line, A375. Focusing on two nups exhibiting a severe reduction in NPC density, the authors showed that NUP160 and NUP93 are essential for NPC assembly and that inhibiting this process results in cell death. Importantly, they found that cancer cells exhibited an increased susceptibility to inhibition of NPC assembly, compared to normal cell lines derived from the retinal pigmental epithelium (RPE1) and human pulmonary fibroblasts that underwent reversible cell cycle arrest rather than apoptosis. This result is reminiscent of our findings in the zebrafish development mutant in which loss of *ahctf1* expression caused catastrophic levels of apoptosis in cells in highly proliferative compartments, such as the intestinal epithelium, while relatively quiescent cells survived[211]. This selective sensitivity to NPC assembly inhibition is supported by studies showing that quiescent cells exist for many years with the same set of assembled NPCs and generally maintain low levels of nup expression[381,382]. However, these studies have as yet underplayed the fact that many nups, including ELYS, also play critical roles outside of the NPC, including in mitotic progression, regulation of gene expression and the maintenance of genome integrity[279]. I expect these roles may also contribute to the vulnerability of cancer cells to disrupted nup function.

ELYS is a particularly strong candidate to contribute to the vulnerability of cancer cells due to its diverse functions throughout the cell cycle. My results compliment a growing body of evidence that carcinogenesis places persistently high demands on essential cellular genes, including those required for proper nuclear pore function, creating a vulnerability that may be therapeutically targeted without causing adverse effects on normal tissue[380,383]. Such a vulnerability has previously been demonstrated in BRAF mutated and BRAF-like (cells that do not contain a BRAF mutation but share a characteristic gene expression signature with BRAF

mutant cells) colorectal cancer cells which are selectively sensitive to Nup358 loss which exacerbates microtubule defects resulting in mitotic cell death[366].

In particular, ELYS remains the only nup identified with clearly defined chromatin-binding and DNA-binding domains which exhibits direct chromatin-binding activity[290]. ChIP-seq experiments have revealed widespread interactions between ELYS and both active and silent genomic loci[291,292]. Elys ChIP-seq binding peaks strongly overlap with and are more prominent than peaks for other chromatin associated nups including Nup93, Nup98 and Nup107. Therefore, it is tempting to speculate that Elys is a key mediator of nup-chromatin interactions, both at the nuclear periphery as part of NPCs as well as within the nucleoplasm. Thus, investigating the impact of *ahctf1* heterozygosity on Elys localisation and regulation of gene expression could help to provide further mechanistic insights into how *ahctf1* mutation restricts *kras*^{G12V}-driven liver hyperplasia.

The potential clinical utility of therapeutic strategies targeting NPCs is further supported by the demonstration that trans-heterozygosity of *ahctf1* and *ranbp2* produced a synergistic reduction in liver volume, bringing it back to the volume of non-hyperplastic livers. Notably, non-hyperplastic livers were completely unaffected by *ahctf1*, *ranbp2* trans-heterozygosity, indicating another potential synthetic lethal interaction that could be exploited by combinatorial drug treatments. Interrogation of TCGA datasets utilising the cBioPortal for Cancer Genomics, suggests that dependency on NPC function may extrapolate to other types of cancer and other nups[376,377]. Genes encoding components of the NUP107-160 complex were found to be frequently overexpressed in a diverse array of tumour types, reflecting the importance of multiple nups in sustaining malignant growth. In contrast, NUP107-160 complex nups were rarely under expressed, suggesting efficient NPC function is critical for the survival of rapidly proliferating cells. This raises the possibility that nups may be used as cancer biomarkers to facilitate early diagnosis, classify tumours and to inform prognostic predictions. Indeed, NUP88 has been discovered to be a cancer biomarker in ovarian and breast cancers defining a highly aggressive tumour phenotype[384,385]. The overexpression of nups in cancer underscores the potential value of targeting the nuclear pore for the efficacious treatment of numerous cancer types.

The dynamic and diverse functions of ELYS require its binding to nups and many other proteins, including components of kinetochore and replicative licensing complexes, as well as binding to chromatin in various states of condensation. The molecular topology of the ELYS protein and the structural basis for its diverse protein-protein and protein-DNA interactions are hitherto poorly defined. Crystal structures of ELYS have shown that the β-propeller and α-helical domains in the N-terminal half of the ELYS protein bind to NUP160, and cryo-electron microscopy has revealed the association of the ELYS C-terminal peptide with nucleosomes[257,327]. However, detailed molecular understanding awaits further high-resolution structural characterisation. While this will no doubt advance our understanding of

the multifunctional roles of ELYS and reveal the extent to which domains within the protein contribute to its function, it may not suggest opportunities to inhibit distinct regions on the protein for the purpose of disabling ELYS function therapeutically. As postulated by Sakuma et al.[380], the absence of discrete surfaces/catalytic pockets on ELYS and other globular nups may make it difficult to inhibit them with small molecules. Despite these challenges, new technologies are emerging that provide optimism that the problems may be overcome. For instance, carefully controlled targeting of degradation-tagged (d-Tag) ELYS molecules with proteolysis targeting chimeras (PROTACs) may offer opportunities for therapeutic development[386,387]. In view of the promising results I have reported in this chapter, I contend that future work directed towards developing drugs capable of disrupting Elys function for the purpose of cancer treatment is likely to be worthwhile.

4 Investigating U12-dependent splicing as a potential cancer therapeutic target

4.1 Introduction

As introduced in section 1.4.6, the importance of U12-dependent splicing to the maintenance of high rates of cellular proliferation was revealed by the identification of the zebrafish *caliban (clbn^{s846})* mutant line in the Liver^{plus} ENU mutagenesis screen[208]. This mutant was characterised by Sebastian Markmiller who demonstrated by positional cloning that the underlying mutant gene in *caliban* is *rnpc3* (*RNA-binding region containing 3*). This gene encodes the 65K protein component of the U12-dependent spliceosome[212]. Subsequently, another *rnpc3* null allele became available from a commercial source, Znomics (RRID: ZFIN_ZDB-GENO-140806-3), which is used throughout this thesis. In this mutant line the *rnpc3* locus is disrupted by retroviral insertion into intron 1, resulting in undetectable mRNA transcripts[212].

The accurate removal of introns from precursor messenger RNA (pre-mRNA) via splicing is essential for proper gene expression. The process of removing introns and ligating exons is catalysed by the spliceosome, a large dynamic complex consisting of both protein and small nuclear RNA (snRNA) molecules. Somewhat under-appreciated is that eukaryotic genomes contain two distinct classes of introns: U2-dependent and U12-dependent introns, also termed major and minor class introns respectively, that are excised by distinct spliceosomes[388,389]. Whilst U12-dependent splicing is required to remove less than 0.5% of introns, we and others have shown that it is critically important for cell growth and proliferation[212,390-392].

rnpc3 homozygous mutant larvae exhibit arrested development in the rapidly proliferating cells of the liver, pancreas and intestine, whereas relatively quiescent tissues are not impacted (Figure 4.1). RNA-seq analysis further revealed that *rnpc3*-deficient (*rnpc3*$^{-/-}$) larvae exhibited disrupted U12-dependent splicing leading to U12 intron retention and a transcriptome-wide impact on gene expression[212]. Meanwhile, heterozygous *rnpc3* larvae develop normally, reach sexual maturity and have a normal lifespan, indicating that a 50% reduction in *rnpc3* gene dosage has no detrimental outcomes.

Such developmental defects and impaired U12-dependent splicing are recapitulated in *Rnpc3*$^{-/-}$ mice. Constitutive deletion of *Rnpc3* results in pre-implantation lethality with *Rnpc3* mutant embryos failing to develop beyond the morula stage. However, mice heterozygous for *Rnpc3* achieve sexual maturity and exhibit a normal lifespan[390]. In further work from the Heath lab, conditional *Rnpc3 lox/lox* mice were generated by homologous recombination in ES cells. Tamoxifen induced Cre-mediated systemic deletion of *Rnpc3* in adult mice had the most profound impact on rapidly proliferating tissues, such as the hematopoietic compartment, thymus and gastrointestinal epithelium[390]. Histological and

immunocytochemical analysis revealed that loss of 65K induced apoptosis and reduced proliferation of intestinal epithelium cells. In addition, semi-quantitative RT-PCR showed that U12-dependent splicing was impaired upon *Rnpc3* deletion with an increase in U12-dependent intron retention[390].

Since *rnpc3* was demonstrated in the *caliban* zebrafish mutant[212], and later in mice[390], to be required to support the growth and division of cells in rapidly proliferating compartments, in this chapter I took advantage of the *TO(kras^{G12V})* zebrafish HCC model to determine whether 65K function in the U12-dependent spliceosome is also required by cancer cells .

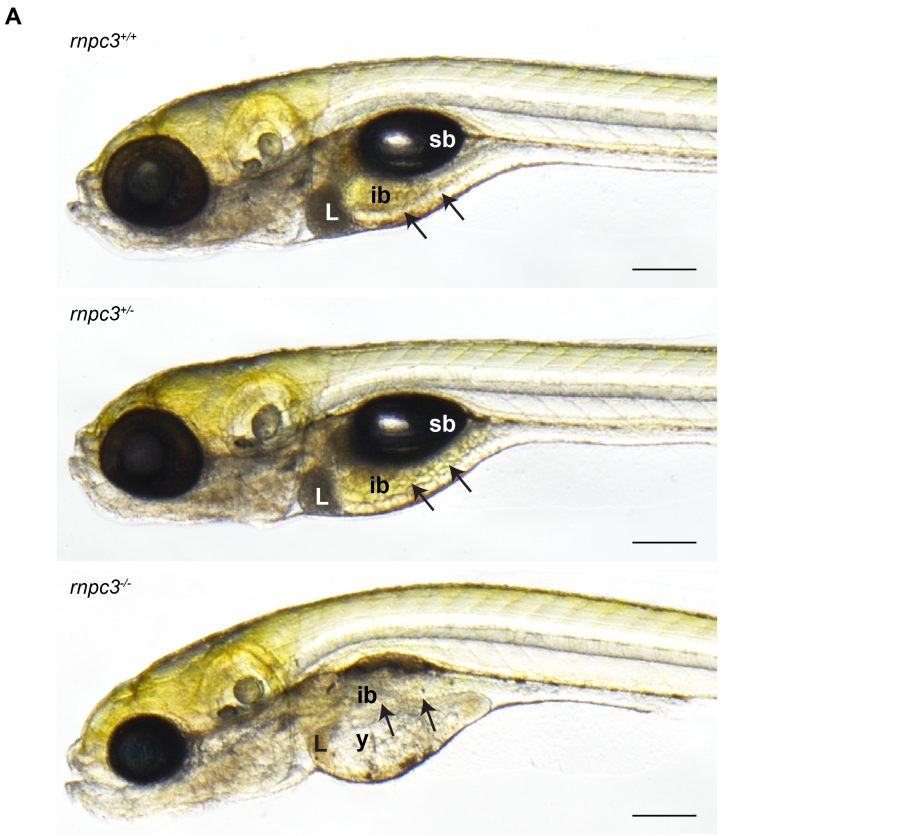

Figure 4.1 Gross morphology of *caliban/rnpc3^{s846}* mutant larvae

A. Bright-field images of 7 dpf *caliban/rnpc3^{s846}* mutant larvae. The intestinal epithelium is thick and extensively folded in *caliban/rnpc3$^{+/+}$* larvae and *rnpc3$^{+/-}$* larvae. In contrast, the intestinal epithelium in *rnpc3$^{-/-}$* larvae is significantly thinner and unfolded (arrows). Also, compared to wildtype, *rnpc3$^{-/-}$* larvae have a smaller head and liver, microphthalmia and fail to inflate the swim bladder or fully absorb the yolk. Meanwhile, *rnpc3$^{+/-}$* larvae exhibit no phenotypic abnormalities. Scale bar 200 µm. **B.** Schematic diagram of zebrafish 65K protein showing the position of the RRM domains. The *caliban, rnpc3^{s846}* mutant generated in the Liver^{plus} ENU mutagenesis screen has a premature stop codon within the RRM 2 domain required for interaction with the U12 snRNA. **C.** Schematic of human 65K protein showing domains required for interaction with the 59K protein and U12 snRNA.

ib: intestinal bulb, L: liver, RRM: RNA recognition motif, sb: swim bladder, y: yolk.

4.1.1 Splice site consensus sequences distinguish U2-dependent and U12-dependent introns

Since the discovery, in 1977, of intervening non-coding sequences in adenovirus genes, introns have been found in all eukaryotic genomes[393-395]. However, it was not until almost two decades later that a rare second type of introns was identified by their distinct splice site consensus sequences (Figure 4.2)[388,389]. Close to 99% of human introns, termed U2-dependent introns, have GT dinucleotides at the 5' splice site, AG dinucleotides at 3' splice site and a polypyrimidine tract upstream of the 3' splice site[396]. In contrast, the first U12-dependent introns identified had AT and AC as terminal dinucleotides at the 5' and 3' splice sites, respectively[397]. Subsequent studies, however, have revealed that U12-dependent introns are delineated by a longer 7 bp conserved sequence at the 5' splice site and a variable 3' splice site, sometimes having GT-AG and AT-AG terminal dinucleotides. In addition, U12-introns lack a polypyrimidine tract and instead contain a well conserved branch point sequence[398,399].

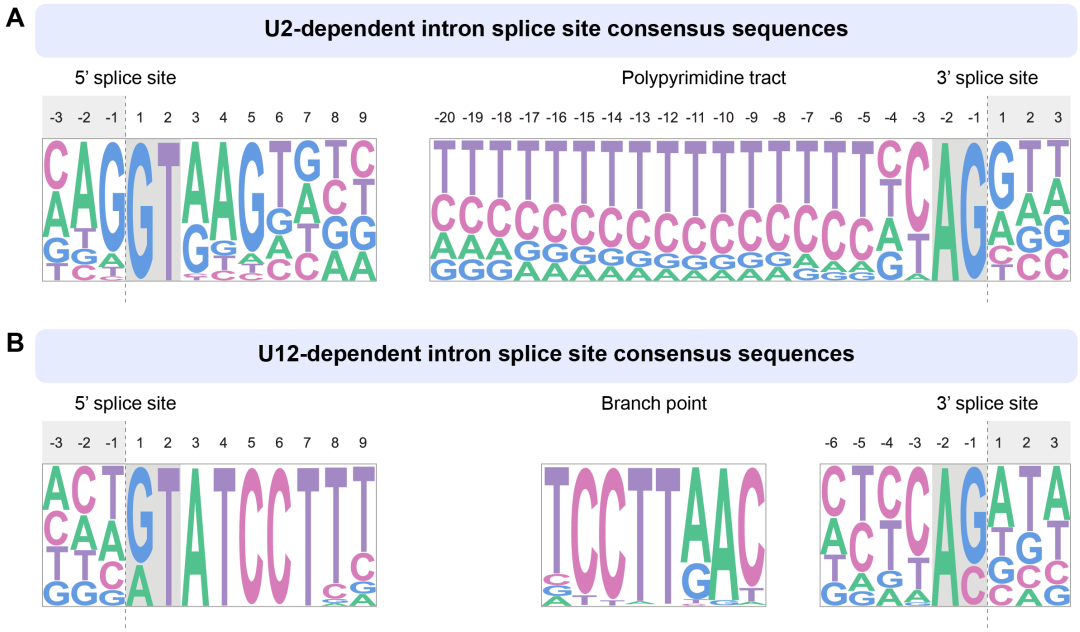

Figure 4.2 Splice site consensus sequences of human introns

Graphical representation of splice site consensus sequences in which letter size represents the probability of each nucleotide at that position. **A.** U2-dependent introns almost always have GT and AG as terminal dinucleotides at the 5' and 3' splice sites, respectively, in addition to a polypyrimidine tract adjacent to the 3' splice site. **B.** U12-dependent introns can have either GT and AG, AT and AC or AT and AG terminal dinucleotides at the 5' and 3' splice sites, respectively. The branch point sequence, upstream of the 3' splice site is also highly conserved. Figure adapted from Brent et al., 2004[398].

4.1.2 U2-dependent and U12-dependent introns are removed by distinct spliceosomes

Splicing occurs via a series of transesterification reactions that remove introns and ligate adjacent exons prior to translation (Figure 4.3)[400-403]. The spliceosome which catalyses these reactions, is assembled *de novo* on each intron of nascent mRNA[404,405]. Extensive x-ray crystallography and cryo-electron microscopy analyses have revealed that spliceosomes are composed of RNA-protein complexes known as small nuclear ribonucleoproteins (snRNPs) and non-snRNP proteins. The U2-dependent spliceosome consists of the snRNPs: U1, U2, U4, U5 and U6[404,406]. Similarly, the U12-dependent spliceosome contains 5 snRNPs, including the U5 snRNP which is a common component of both spliceosomes. The other snRNPs are highly similar to the U2-dependent spliceosome but unique to the U12-dependent spliceosome through their snRNAs: U11, U12, U4atac and U6atac (Figure 4.4). In addition, both spliceosomes are also composed of a range of associated proteins including a common set of seven Sm proteins (B/B', D3, D2, D1, E, F, G)[404,407].

The first steps in U2-dependent splicing are binding of the U1 snRNP to the 5' splice site, followed by U2 snRNP binding to the branchpoint sequence via direct base pairing (Figure 4.5)[408-410]. In contrast, the initial step of U12-dependent splicing is binding of U11/U12 together as a stable di-snRNP which simultaneously recognises the 5' splice site and branch point sequence[411]. The subsequent catalytic steps of splicing are essentially functionally analogous between U2-dependent and U12-dependent splicing and consequently, most protein components are shared in both spliceosomes[412,413]. However, 7 novel proteins unique to the U12-dependent spliceosome have been identified within the U11/U12 di-snRNP: 20K, 25K, 31K, 35K, 48K, 59K and 65K (Figure 4.6)[414,415]. These proteins contribute to the formation and stability of the U11/U12 di-snRNP enabling recognition and cooperative binding to U12-dependent introns. Specifically, the 48K protein directly interacts with U11 snRNA through a conserved CHHC-type zinc finger domain to stabilise binding to 5' splice sites[416,417]. The N-terminal region of 48K interacts with 59K, which in turn associates with 65K. The C-terminal RNA recognition motif of 65K binds to the 3' terminal stem loop of U12 snRNA, thereby forming a molecular bridge between the 5' and 3' splice sites of the intron[418]. These interactions are critical for proper di-snRNP formation and intron recognition. Consistent with this, RNAi-mediated knockdown of 48K in HeLa cells decreases abundance of U11/U12 di-snRNPs and impairs U12-dependent splicing[416].

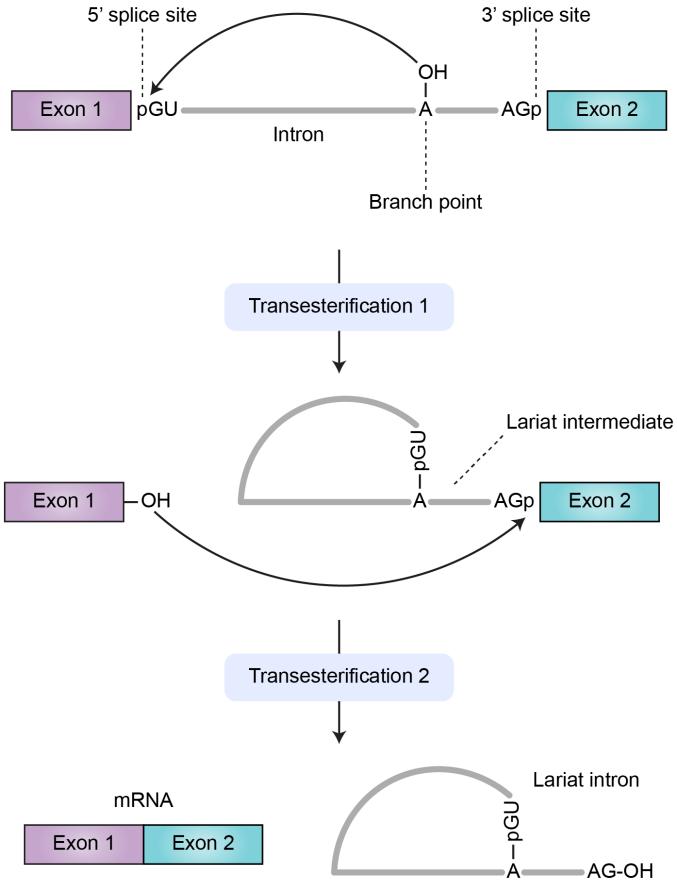

Figure 4.3 Pre-mRNA splicing occurs via sequential transesterification reactions

The first enzymatic step of splicing involves the branch point hydroxyl group attack of the 5' splice site phosphate. This results in 5' splice site cleavage and formation of a lariat intermediate. The second transesterification reaction results in 3' splice site cleavage, release of the lariat intron and exon ligation. Figure adapted from Bentley et al., 2014[419].

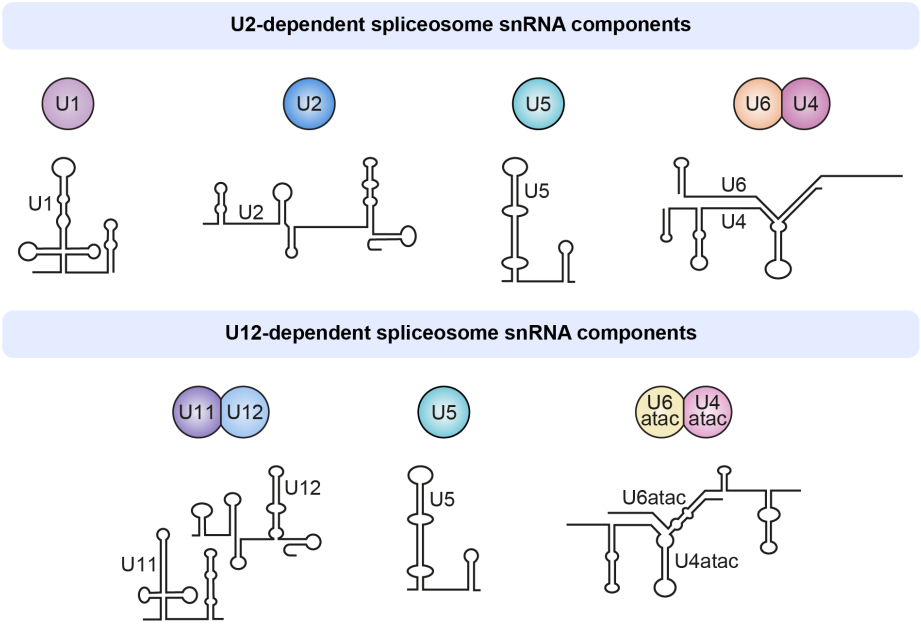

Figure 4.4 Small nuclear RNA components of the U2-dependent and U12-dependent spliceosomes

The U2-dependent spliceosome contains the snRNA components U1, U2, U4, U5 and U6. The U12-dependent spliceosome also contains the U5 snRNA in addition to U11, U12, U4atac and U6atac snRNAs, which are functionally equivalent to but distinct from their U2-dependent spliceosome counterparts. U6 and U4, U6atac and U4atac, as well as U11 and U12 snRNAs assemble with associated proteins into di-snRNPs. Figure adapted from Wahl et al., 2015[420].

snRNA: small nuclear RNA, snRNPs: small nuclear ribonuclear proteins.

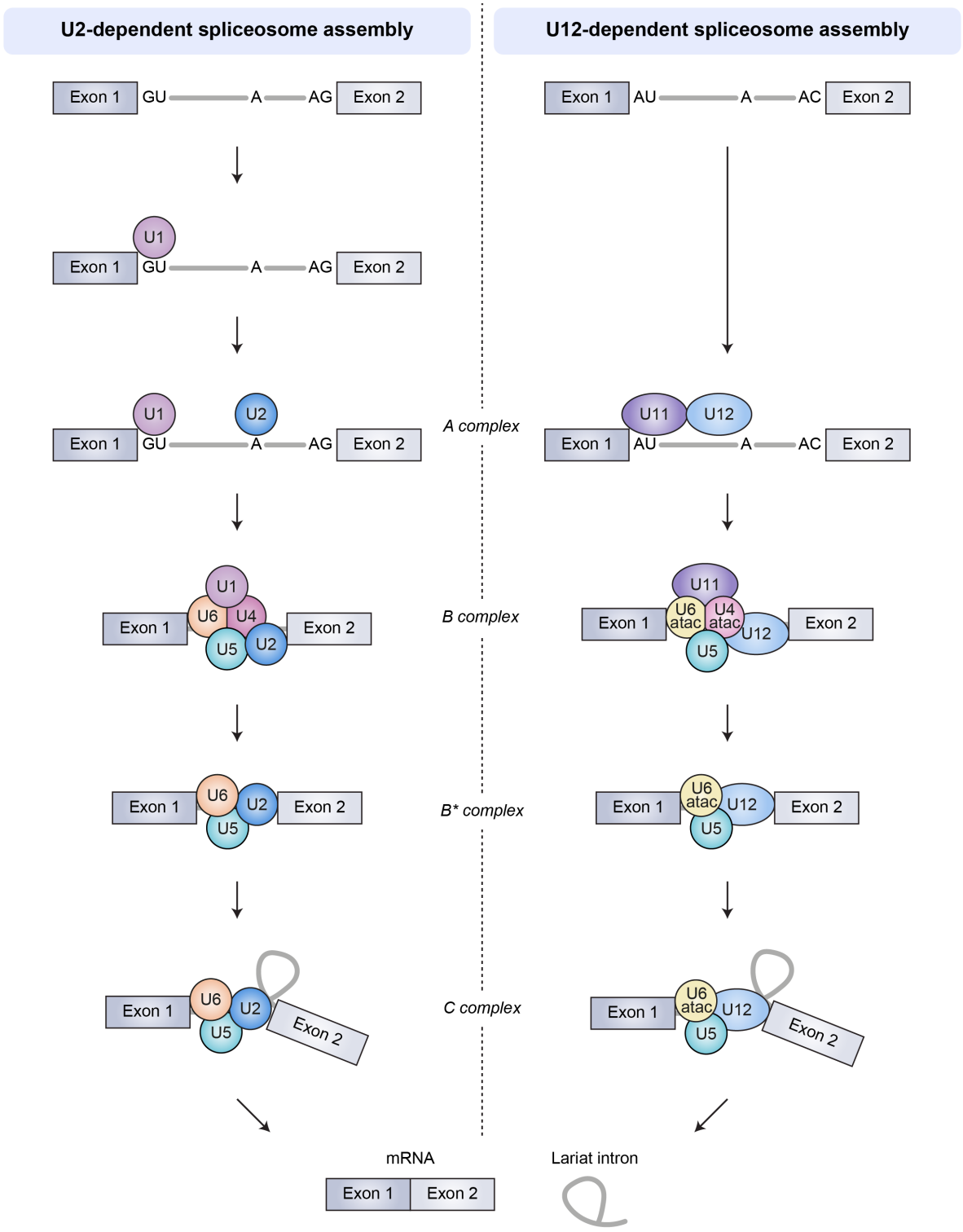

Figure 4.5 U2-dependent and U12-dependent spliceosome assembly

Overview of the interactions between snRNPs during various stages of spliceosome assembly and catalysis. U2-dependent splicing proceeds stepwise via base pairing of the U1 snRNP to the 5’ splice site. Next, the U2 snRNP binds at the branch point sequence. Subsequently, the preassembled tri-snRNP U4-U6.U5 is recruited. A series of structural rearrangements result in the release of U1 and U4 snRNPs and formation of a catalytically active complex.

Transesterification reactions then remove lariat introns to generate ligation of adjacent exons. Whilst U12-dependent splicing begins with binding of the U11/U12 di-snRNP as a single entity to the 5' splice site and branch point sequence, subsequent steps are similar to U2-dependent spliceosome assembly. Figure adapted from Will et al., 2005[413].

snRNP: small nuclear ribonuclear protein.

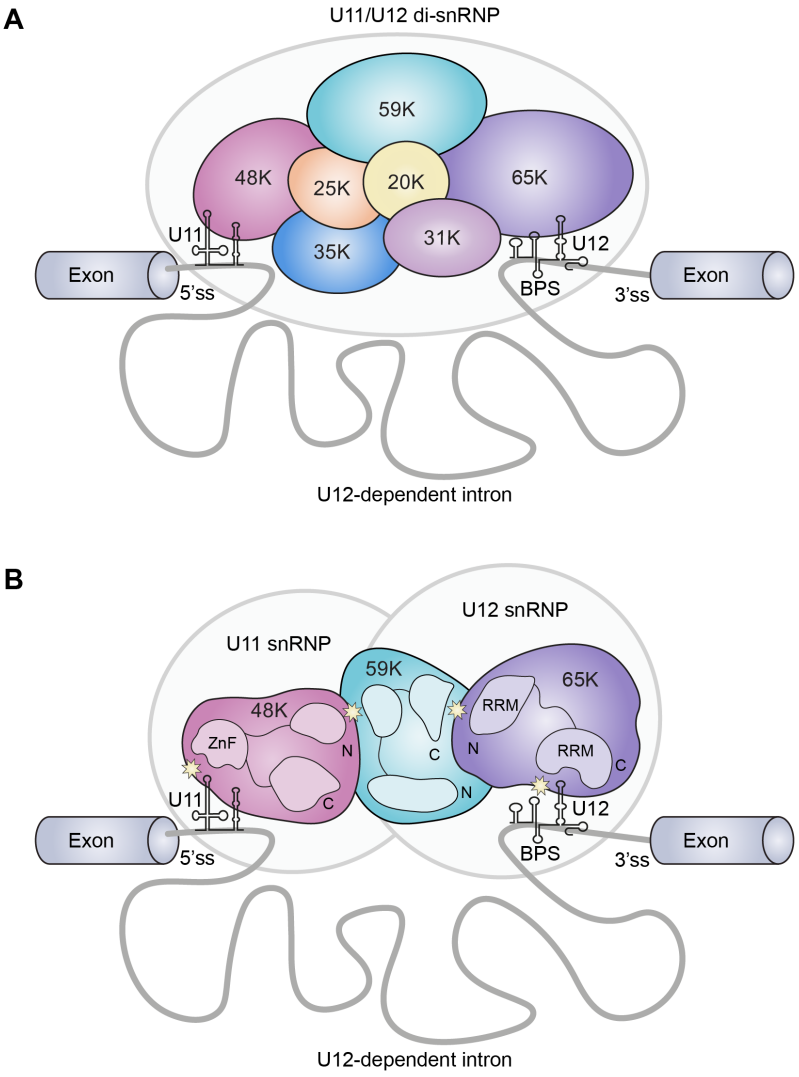

Figure 4.6 Recognition of U12-dependent introns by the U11/U12 di-snRNP

A. The U11/U12 di-snRNP contains 2 unique snRNAs U11 and U12 which cooperatively bind to the 5' splice site and branch point sequence, respectively, of U12-dependent introns. The U11/U12 di-snRNP also contains 7 protein components that are specific to the U12-dependent spliceosome: 20K, 25K, 31K, 35K, 48K, 59K and 65K. Figure adapted from Doggett et al., 2018[390]. **B.** 48K, 59K and 65K proteins have a structural function, forming a molecular bridge connecting the U11 and U12 snRNAs. Asterisks indicate RNA-protein and protein-protein interactions that have been validated experimentally. Figure adapted from Tidow et al., 2009[417].

BPS: branch point sequence, di-snRNP: di-small nuclear ribonuclear protein, RRM: RNA recognition motif, snRNAs: small nuclear RNAs, ss: splice site, ZnF: zinc finger domain.

4.1.3 Distribution of U12-dependent introns

U12-dependent splicing is necessary for the proper expression of 770 genes in humans. Despite this relative rarity, the importance of U12-dependent introns is indicated by their evolutionary conservation in early eukaryotes, fungi, plants and animals[421]. Intriguingly, U12-dependent introns are not evenly distributed throughout the genome, instead they are enriched in "information processing" genes[399]. Such genes are involved in essential cellular processes including DNA replication and repair, transcription, RNA processing and translation (Figure 4.7). Of great interest in the context of cancer, several genes that are downstream of RAS in mitogenic pathways contain U12-dependent introns. This includes the proto-oncogenes, *BRAF* and *RAF1*, and 11 out of 14 MAPK family genes, such as *ERK*, *JNK, p38* and their respective isoforms. These genes are typically highly active in rapidly proliferating cells and are frequently dysregulated in cancer. This raises the tantalising possibility that efficient U12-dependent splicing is required for cancer growth, particularly in cancers driven by RAS-MAPK pathway activation. Therefore, in this chapter I investigate whether reducing *rnpc3* gene dosage had an impact on hepatocyte hyperplasia and liver enlargement in the *TO(kras^{G12V})* zebrafish HCC model.

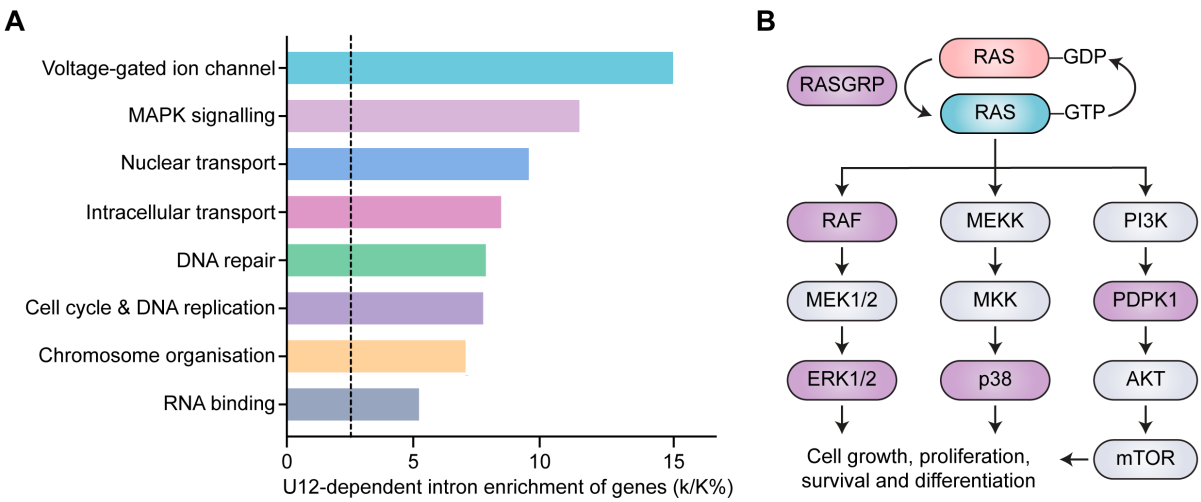

Figure 4.7 Genes containing U12-dependent introns are enriched in certain functional classes and pathways

A. U12-dependent introns are over-represented in several gene ontologies, occurring at a frequency greater than chance (3.72%), as denoted by the vertical dotted line. Enrichment = genes in overlap (k)/Genes in gene set (K) as a percentage. Figure from Doggett et al., 2018[390]. **B.** Several components of the MAPK signalling cascade, shown in purple, are encoded by genes containing U12-dependent introns.

4.2 Results

4.2.1 *rnpc3* mutation reduces *rnpc3* mRNA transcript expression

To investigate the role of U12-dependent splicing in a cancer setting, *TO(kras^{G12V})$^{T/+}$* zebrafish were crossed with the Znomics *rnpc3* mutant to generate the *rnpc3; TO(kras^{G12V})$^{T/+}$* line[176,212]. Heterozygous *rnpc3* mutation reduced *rnpc3* mRNA expression by 37% in larvae at 7 dpf (Figure 4.8). Meanwhile, *rnpc3* transcript expression was reduced by 83% in homozygous *rnpc3* mutant larvae. Both these results indicate that the retroviral insertion into intron 1 of the *rnpc3* locus triggers nonsense mediated decay, rather than expression of a truncated 65K protein.

4.2.2 *rnpc3* mutation reduces *kras^{G12V}*-driven hepatocyte hyperplasia

To determine the effect of *rnpc3* mutation on normal liver cells, the *2-CLiP* transgenic line was again employed to facilitate analysis of normal liver volume in the absence of oncogene expression. In *rnpc3$^{+/+}$*; *2-CLiP* larvae liver volume was an average of $1.75 \times 10^6 \pm 5.44 \times 10^4$ μm^3 at 7 dpf (Figure 4.9). *rnpc3* heterozygosity did not affect normal liver development in *2-CLiP* larvae. As discussed in section 1.5, homozygous *rnpc3* mutation is lethal at 9-10 dpf and larvae exhibit smaller livers at 7 dpf. As it would require an intercross and raising a generation of zebrafish to show this on the *2-CLiP* background, this experiment was not performed.

Expression of oncogenic Kras^{G12V} resulted in liver enlargement with a striking 5.5-fold increase in liver volume to $9.58 \times 10^6 \pm 2.46 \times 10^5$ in *rnpc3$^{+/+}$; TO(kras^{G12V})$^{T/+}$* larvae. Remarkably, this excess liver volume was reduced by 49% to $5.70 \times 10^6 \pm 1.34 \times 10^5$ in *rnpc3$^{+/-}$; TO(kras^{G12V})$^{T/+}$* larvae and even further restricted by 83% to $3.09 \times 10^6 \pm 1.12 \times 10^5$ in *rnpc3$^{-/-}$; TO(kras^{G12V})$^{T/+}$* larvae. These data demonstrate that while *rnpc3* heterozygosity is sufficient for normal liver growth and development, a mild reduction in *rnpc3* gene dosage (50%) is capable of restricting tumour burden in livers expressing oncogenic *kras^{G12V}* through a synthetic lethal interaction. These results suggest that oncogenic *kras^{G12V}*-driven hepatocyte hyperplasia is dependent on efficient U12-dependent splicing to sustain tumour growth.

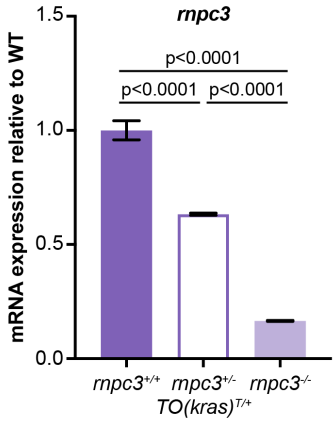

Figure 4.8 *rnpc3* mutation reduces *rnpc3* mRNA transcript expression

RT-qPCR analysis of pooled micro-dissected livers from *TO(kras^{G12V})$^{T/+}$* larvae of the indicated *rnpc3* genotype at 7 dpf. Heterozygous and homozygous mutation of *rnpc3* reduced expression of the *rnpc3* transcript by 37% and 83%, respectively, indicating that the mutated pre-mRNA molecules were subject to nonsense mediated decay. Data are expressed as mean ± SEM, n=3 biological replicates. Significance was calculated using a one-way ANOVA with Tukey's multiple comparisons test.

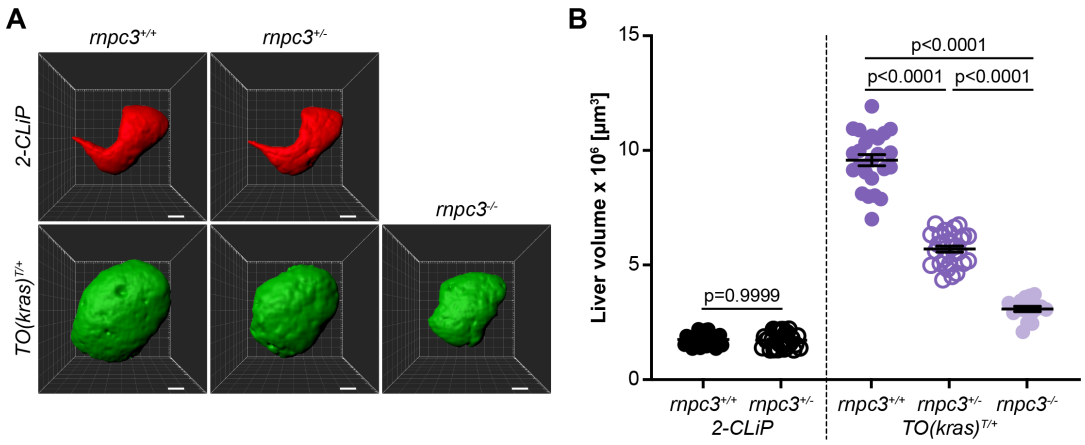

Figure 4.9 Heterozygous and homozygous *rnpc3* mutation reduces *kras^{G12V}*-driven hepatocyte hyperplasia and liver enlargement

A. Representative three-dimensional reconstructions of *2-CLiP* and *TO(kras^{G12V})$^{T/+}$* livers of the indicated *rnpc3* genotype. Scale bar 25 µm. **B.** Liver volume in *2-CLiP* larvae was not impacted by *rnpc3* heterozygosity at 7 dpf. Upon doxycycline-induced expression of the *TO(kras^{G12V})* transgene, *rnpc3* heterozygosity restricted hepatocyte hyperplasia and liver enlargement. This effect was more pronounced in *rnpc3* homozygous mutant larvae. Data are expressed as mean ± SEM, n≥16. Significance was calculated using a one-way ANOVA with Tukey's multiple comparisons test.

4.2.3 Heterozygous *rnpc3* mutation restricts DNA replication in *TO(kras^{G12V})$^{T/+}$* hepatocytes

As *rnpc3* mutant larvae were originally identified as exhibiting a growth arrest phenotype, I examined if cell cycle progression was altered in *rnpc3$^{+/-}$; TO(kras^{G12V})$^{T/+}$* larvae using an EdU incorporation assay to identify cells in S phase (Figure 4.10). In *rnpc3$^{+/+}$; TO(kras^{G12V})$^{T/+}$* larvae, 32% of hepatocytes were EdU-positive. This number was reduced by 42% in *rnpc3$^{+/-}$; TO(kras^{G12V})$^{T/+}$* larvae compared to wildtype. This suggests that *rnpc3* heterozygosity reduces tumour burden via reducing the percentage of cells in S phase of the cell cycle.

To investigate this mechanism further, mRNA levels of cell cycle inhibitors, *cdkn2a/b* (encoding p16) and *cdkn1a* (encoding p21) were analysed by RT-qPCR (Figure 4.11). *cdkn1a* transcript expression was upregulated 2.3-fold in pools of *rnpc3$^{+/-}$; TO(kras^{G12V})$^{T/+}$* micro-dissected livers. Similarly, mRNA expression of *cdkn1a* was increased 1.5-fold by *rnpc3* heterozygosity. Together, this data suggests that heterozygous *rnpc3* mutation promotes expression of cell cycle regulators that decrease the number of actively cycling cells thereby reducing tumour burden and liver enlargement.

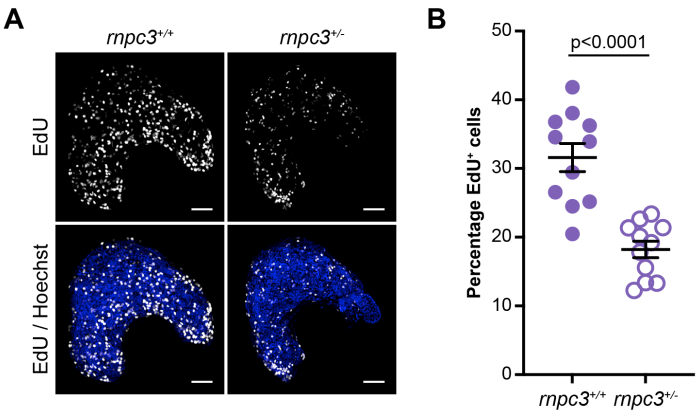

Figure 4.10 Heterozygous *rnpc3* mutation restricts the percentage of *TO(kras^{G12V})$^{T/+}$* hepatocytes in S phase of the cell cycle

A. Representative maximum intensity projection images of EdU incorporation throughout *TO(kras^{G12V})$^{T/+}$* livers of the indicated *rnpc3* genotype. Scale bar 25 µm. **B.** Quantification of the percentage of Hoechst 33342 positive nuclei with fluorescent EdU puncta. *rnpc3* heterozygosity restricted DNA replication by 42% in *TO(kras^{G12V})$^{T/+}$* livers. Data are expressed as mean ± SEM, n=11. Significance was calculated using a Student's t-test.

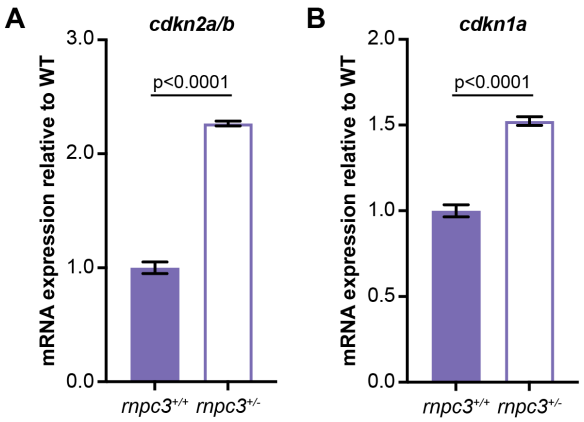

Figure 4.11 Heterozygous *rnpc3* mutation increases expression of cell cycle regulators in *TO(kras^{G12V})$^{T/+}$* hepatocytes

RT-qPCR analysis of pooled micro-dissected livers from *TO(kras^{G12V})$^{T/+}$* larvae of the indicated *rnpc3* genotype. **A.** *rnpc3* heterozygosity increased mRNA expression of *cdkn2a/b* in *TO(kras^{G12V})$^{T/+}$* larvae. **B.** *cdkn1a* transcript levels were similarly upregulated by *rnpc3* heterozygosity. Data are expressed as mean ± SEM, n=5 biological replicates. Significance was calculated using a Student's t-test.

4.2.4 Heterozygous *rnpc3* mutation triggers cell death in *TO(kras^{G12V})$^{T/+}$* hepatocytes

In the preceding sections, I demonstrated that tumour burden in *TO*(*kras^{G12V})* larvae was partially mitigated by *rnpc3* heterozygosity, which caused a reduction in EdU incorporation in hepatocytes and enhanced expression of pro-senescence genes, *cdkn2a/b* and *cdkn1a*. Another possible explanation for the observed reduction in liver volume in response to heterozygous *rnpc3* mutation is an increase in cell death. To explore this, the *Annexin 5-mKate* transgenic line was again employed to allow visualisation and quantification of apoptotic cells. In this system, foci (objects) of mKate fluorescence become visible upon binding of secreted Annexin 5-mKate fusion protein to phosphatidylserine. This phospholipid is normally inaccessible to Annexin 5-mKate binding because of its localisation on the inner leaflet of the plasma membrane bilayer. However, apoptotic cells are characterised by fragmented plasma membranes that can no longer sequester phosphatidylserine to the inner leaflet, thereby exposing it to Annexin 5-mKate binding and the formation of fluorescent puncta.

Expression of oncogenic *kras^{G12V}* on a wildtype *rnpc3* background resulted in low levels of cell death with an average abundance of 1.53 x 10^{-5} Annexin 5 fluorescent puncta/μm^3 liver volume (Figure 4.12). The number of fluorescence objects was markedly increased by 52% in *rnpc3$^{+/-}$; TO(kras^{G12V})$^{T/+}$* larvae, demonstrating that *rnpc3* heterozygosity increases cell death in the context of *kras^{G12V}* expressing hepatocytes.

As Tp53 has a central role in mediating cell death pathways and having previously shown in section 3.5.3 that expression of the *kras^{G12V}* oncogene causes elevated expression of Tp53 protein, I next examined mRNA expression levels of *tp53* and apoptosis regulators *bbc3 (puma)* and *pmaip1 (noxa)* by RT-qPCR analysis on pools of micro-dissected livers (Figure 4.13). *tp53* mRNA expression levels were unaltered in *rnpc3$^{+/-}$; TO(kras^{G12V})$^{T/+}$* larvae. However, *rnpc3* heterozygosity produced a marked increase (3.7-fold) in the expression of the *tp53* isoform, *Δ113tp53*, indicating the presence of stabilised, transcriptionally active Tp53 protein in hepatocytes. Consistent with this, the *tp53* target genes *bbc3* and *pmaip1* were upregulated 2.3-fold and 1.8-fold, respectively, in *rnpc3$^{+/-}$; TO(kras^{G12V})$^{T/+}$* larvae. Together, these data suggests that heterozygous *rnpc3* mutation induces a Tp53 transcriptional program that increases the expression of pro-apoptosis genes resulting in elevated levels of cell death and reduced liver volume.

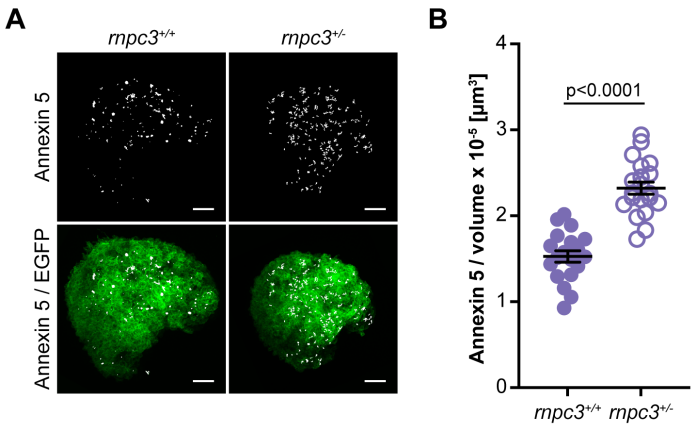

Figure 4.12 Heterozygous *rnpc3* mutation triggers cell death in *TO(kras^{G12V})$^{T/+}$* hepatocytes

A. Representative maximum intensity projection images of Annexin 5-mKate fluorescence, indicating cell death throughout *TO(kras^{G12V})$^{T/+}$* livers of the indicated *rnpc3* genotype. Scale bar 25 µm. **B.** Quantification of Annexin 5 fluorescent foci by automatic 3D simple segmentation of mKate signal. *rnpc3* heterozygosity increased cell death by 52% in *TO(kras^{G12V})$^{T/+}$* hepatocytes. Data are expressed as mean ± SEM, n≥19. Significance was calculated using a Student's t-test.

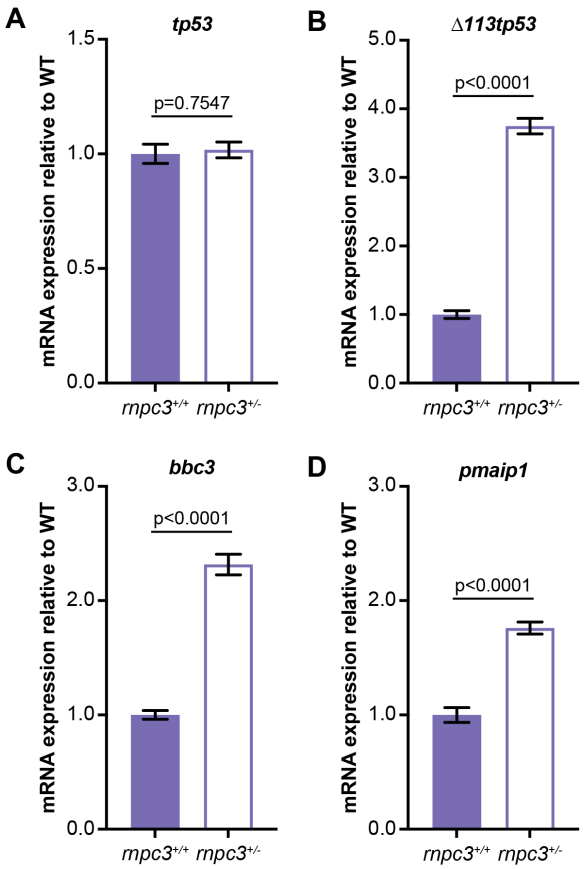

Figure 4.13 Heterozygous *rnpc3* mutation increases expression of *Δ113tp53* and pro-apoptosis genes in *TO(kras^{G12V})$^{T/+}$* hepatocytes

RT-qPCR analysis of pooled micro-dissected livers from *TO(kras^{G12V})$^{T/+}$* larvae of the indicated *rnpc3* genotype. **A.** *rnpc3* heterozygosity did not impact mRNA expression levels of *tp53*. **B.** In contrast, transcript levels of *Δ113tp53* were upregulated 3.7-fold in *rnpc3$^{+/+}$*; *TO(kras^{G12V})$^{T/+}$* livers, indicating activation of a Tp53 transcriptional program. **C, D.** *rnpc3* heterozygosity increased levels of mRNAs for *bbc3* and *pmaip1*, by 2.3-fold and 1.8-fold, respectively. Data are expressed as mean ± SEM, n=5 biological replicates. Significance was calculated using a Student's t-test.

4.2.5 *rnpc3* heterozygosity reduces hepatocyte hyperplasia and liver enlargement associated with combined *kras*^{G12V} and *tp53* mutation

To test whether activation of the Tp53 pathway was involved in the reduction of liver volume in *kras*^{G12V}-expressing larvae on a heterozygous *rnpc3* background, liver volume experiments were repeated in the presence and absence of Tp53 function (Figure 4.14). Consistent with previous results, *rnpc3* heterozygosity restricted liver hyperplasia in *tp53*$^{+/+}$; *TO(kras*^{G12V}*)*$^{T/+}$ larvae, reducing liver volume by 41%. The complete abrogation of Tp53 activity in *rnpc3*$^{+/+}$; *tp53*$^{m/m}$*; TO(kras*^{G12V}*)*$^{T/+}$ larvae supported a large increase (33%) in liver volume compared to that of livers in *rnpc3*$^{+/+}$; *tp53*$^{+/+}$; *TO(kras*^{G12V}*)*$^{T/+}$ larvae, indicating that Tp53 function normally restrains tumor growth/liver enlargement in this model. Liver volume on the *rnpc3*$^{+/-}$; *tp53*$^{m/m}$; *TO(kras*^{G12V}*)*$^{T/+}$ background was reduced by 8% compared to *rnpc3*$^{+/+}$; *tp53*$^{m/m}$; *TO(kras*^{G12V}*)*$^{T/+}$. This suggests that a 50% reduction in *rnpc3* expression produces only a mild reduction in tumour burden in the complete absence of functional Tp53.

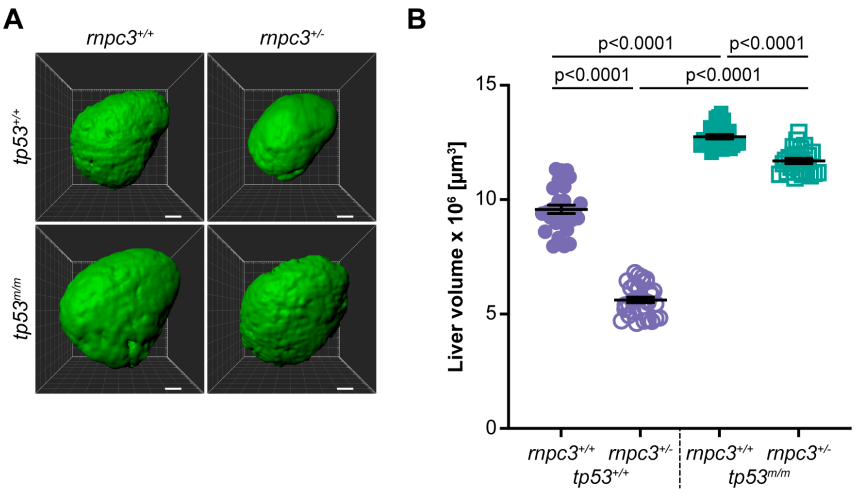

Figure 4.14 *kras*^{G12V} expression in the absence of Tp53 function (*tp53*$^{m/m}$) results in a greater increase in liver volume that is partially mitigated by *rnpc3* heterozygosity

A. Representative three-dimensional reconstructions of *TO(kras*^{G12V}*)*$^{T/+}$ livers of the indicated *rnpc3* and *tp53* genotype. Scale bar 25 µm. **B.** Liver volume was significantly reduced by *rnpc3* heterozygosity in both Tp53 proficient and deficient *TO(kras*^{G12V}*)*$^{T/+}$ larvae. Data are expressed as mean ± SEM, n≥24. Significance was calculated using a one-way ANOVA with Tukey's multiple comparisons test.

4.2.6 U12-dependent splicing is essential for cell viability

The *in vivo* pre-clinical data from the *TO(kras^{G12V})$^{T/+}$* model I have presented in this chapter suggest that hepatocarcinogenesis requires efficient U12-dependent splicing. Consistent with this notion, genome-wide CRISPR screens, curated in the DepMap portal reveal that *RNPC3* is essential for the viability of all 808 different human cancer cell lines screened[374,375]. All other genes encoding the unique protein components of the U11/U12 di-snRNP are also classified as common essential genes (Table 4.1). Consistent with this, interrogation of mutation data in The Cancer Genome Atlas (TCGA) datasets using the cBioPortal for Cancer Genomics[376,377] shows that *RNPC3* is rarely mutated in cancer. Indeed, out of 48,081 samples in the curated combined dataset across all cancers, only 79 (<0.16%) contain a potentially debilitating *RNPC3* mutation (Table 4.2). Similarly, other genes encoding the unique protein components of the U11/U12 di-snRNP are mutated in <0.2% of patient samples across all cancers. Restricting the analysis to HCC samples, *RNPC3* mutations were absent in 892 patient samples. Such rarity of *RNPC3* mutations suggest that cancers generally do not have alternative mechanisms to compensate for 65K deficiency. Collectively, these data support the idea that cancers are highly dependent upon efficient U12-dependent splicing for sustaining tumourigenesis, representing a vulnerability that may be exploited in the clinic.

Table 4.1 DepMap portal gene essentiality CRISPR screens of unique U11/U12 di-snRNP components dependency in human cancer cell lines

NUP	Dependent cell lines (%)	Classification
ZMAT5	100.00	Common essential
SNRNP25	99.88	Common essential
ZCRB1	94.68	Common essential
SNRNP35	99.63	Common essential
SNRNP48	66.46	Common essential
PDCD7	61.76	Common essential
RNPC3	100.00	Common essential

Table 4.2 Percentage of TCGA dataset samples with mutation of unique U11/U12 di-snRNP components

U11/U12 di-snRNP genes	Cancer samples with gene mutated (%)	HCC samples with gene mutated (%)
ZMAT5	0.10	0.11
SNRNP25	0.05	0.00
ZCRB1	0.19	0.11
SNRNP35	0.18	0.11
SNRNP48	0.22	0.22
PDCD7	0.21	0.45
RNPC3	0.16	0.00

4.3 Discussion

The precise splicing of introns is an essential step for correct eukaryotic gene expression. Whilst only 770 human genes contain U12-dependent introns, U12-dependent splicing is indispensable during vertebrate development and is crucial for the proper expression of genes in pathways that regulate cell growth, division and survival. In this chapter, *rnpc3* heterozygosity is identified as participating in a synthetic lethal interaction with oncogenic $Kras^{G12V}$ producing a robust anti-tumourigenic effect in the *TO(kras^{G12V})* zebrafish model of HCC. Heterozygous loss of *rnpc3* did not impact liver volume in *2-CLiP* larvae, indicating that a mild (50%) reduction in *rnpc3* expression is well tolerated by normal cells. Significantly, *rnpc3* heterozygosity substantially decreased tumour burden by 49% in *TO(kras^{G12V})$^{T/+}$* larvae. This therapeutic benefit was achieved through both a reduction in the number of cells progressing through S phase of the cell cycle and an increase in cell death. This mechanism is supported by the results showing enhanced transcription of the pro-senescence genes, *cdkn2a/b* and *cdkn1a*, and the pro-apoptosis genes, *pmaip1* and *bbc3*, in *rnpc3* heterozygous larvae.

Future RNA-seq experiments will seek to investigate if U12-dependent splicing is specifically impacted in heterozygous *rnpc3* hepatocytes and if these defects are more severe in the presence of oncogenic $Kras^{G12V}$ expression. Assessment of the impact of U12-dependent splicing on gene expression and whether *rnpc3* heterozygosity causes elevated levels of intron retention or increased rates of alternative splicing will provide valuable insight into the mechanism underlying restricted hepatocyte hyperplasia and liver enlargement. The effect of *rnpc3* heterozygosity reducing tumour burden in the *TO(kras^{G12V})$^{T/+}$* model is likely due to a more general response to disrupted splicing of U12-dependent intron containing genes (Figure 4.15). As U12-dependent introns are enriched in genes that are components of MAPK signalling, nuclear transport, DNA repair, cell cycle and DNA replication pathways, the disruption of U12-dependent splicing has a transcriptome-wide impact on gene expression. This results in enhanced replicative stress and the accumulation of DNA damage, which in turn, leads to the activation of Tp53 and induction of cell cycle arrest and cell death pathways. Combined with the inhibition of pro-proliferative signalling pathways, this results in a reduction in tumour burden.

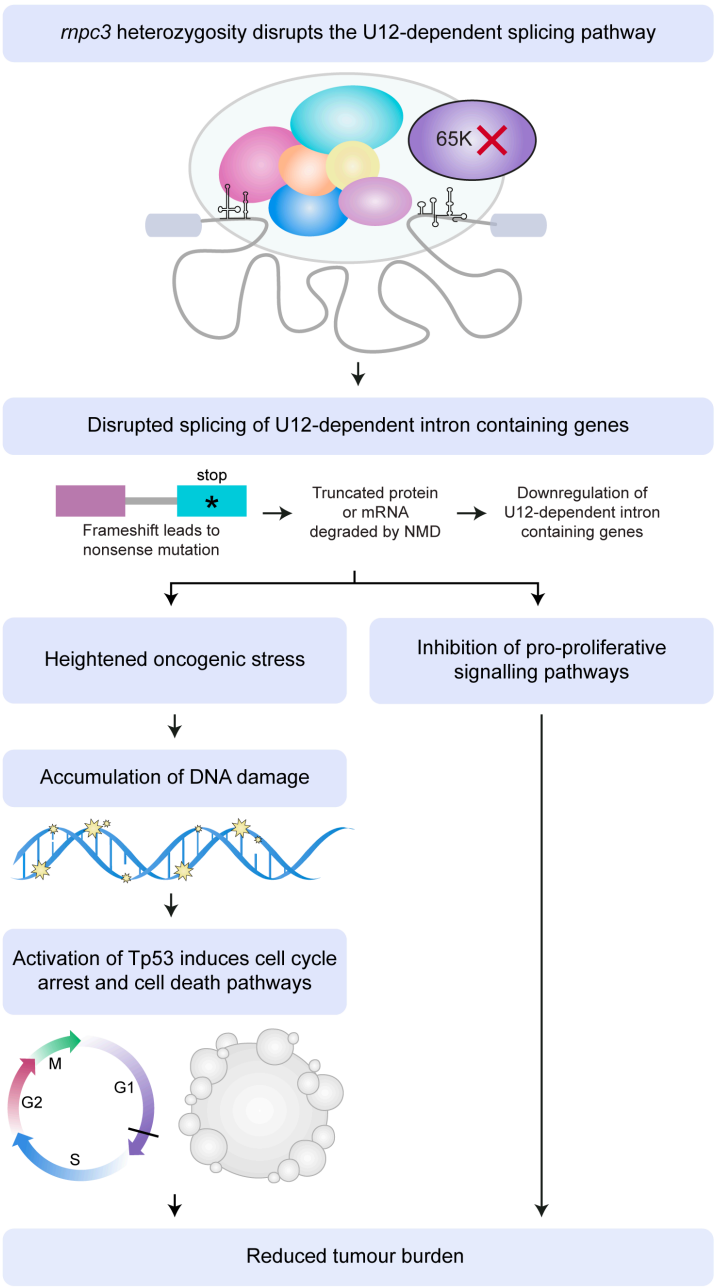

Figure 4.15 Schematic explaining the mechanism by which *rnpc3* heterozygosity reduces tumour burden

rnpc3 heterozygosity disrupts the U12-dependent splicing pathway resulting in impaired splicing of U12-dependent intron containing genes. This causes an accumulation of aberrant pre-mRNA transcripts containing retained introns or skipped exons. Such transcripts often encode frameshift mutations and premature stop codons in positions likely to trigger nonsense mediated decay (NMD) causing downregulation of U12-dependent intron containing genes. As U12-dependent introns are enriched in genes that are components of DNA repair, cell cycle and DNA replication pathways this leads to heightened oncogenic stress and the accumulation of DNA damage. This activates Tp53 which induces cell cycle arrest and cell death pathways. Additionally, as many MAPK signalling pathway components contain

U12-dependent introns, disrupted U12-dependent splicing also inhibits pro-proliferative signalling. Together, these molecular and cellular events combine to ultimately reduce tumour burden.

The previous demonstration by the Heath lab that *rnpc3* is critical for rapid cell growth and proliferation during both zebrafish[212] and mouse development[390], in conjunction with the favourable results reported here, prompted a colleague Dr. Karen Doggett to examine if impaired U12-dependent splicing was effective at restricting tumourigenesis in several mouse models of cancer. Tumour formation in a *Kras^{G12D}*-driven mouse model of lung adenocarcinoma was significantly reduced by heterozygous loss of *Rnpc3*. This vulnerability of cancer cells to impaired U12-dependent splicing was also upheld in mouse cancer models driven by signalling pathways other than RAS/MAPK. In particular heterozygous loss of *Rnpc3* reduced tumour burden in a STAT3-driven gastric cancer model and extended survival of tumour prone heterozygous *Pten* mice. Moreover, disruption of the *Rnpc3* locus in established acute myeloid leukemia (AML) cells caused impaired U12-dependent splicing and cell death. Collectively, these data show that reducing *Rnpc3* gene dosage by 50% can reduce the growth of a broad spectrum of cancers, without impacting on healthy tissues, suggesting that U12-dependent splicing represents an effective, therapeutically viable treatment for cancer.

In particular, as outlined in section 4.1.3, U12-dependent introns are often found in genes that are downstream of KRAS in mitogenic pathways, including in the proto-oncogenes, *BRAF, RAF1,* all conventional *MAPK* family genes (encoding ERK, JNK and p38) and *PDPK1*. Therefore, targeting U12-dependent splicing may be particularly promising therapeutic target for RAS/MAPK driven cancers, for which effective treatments remain an unmet clinical need. Almost all pancreatic ductal adenocarcinomas (~98%) harbour mutations in the *KRAS* gene, while 52% of colon and 32% of lung adenocarcinomas carry *KRAS* or *NRAS* mutations[422]. Direct targeting of KRAS oncoproteins in such tumours has proven extremely challenging, thus inhibiting U12-dependent splicing may prove a valuable strategy for difficult to treat tumours.

The therapeutic targeting of splicing in cancer is an area of growing interest, due to the identification in cancer genomes of frequent heterozygous point mutations in the general splicing factor genes, *SF3B1, U2AF1* and *SRSF2*[423-425]. For example, recurrent mutations in *SF3B1* occur in 20-30% patients with myelodysplastic syndrome, which frequently develops into haematological malignancies such as chronic lymphocytic leukemia, chronic myelomonocytic leukemia and acute myeloid leukemia[426,427]. Notably, these mutations usually confer an alteration of function, creating a preferential sensitivity to further disruption of splicing[425,428]. Consistent with this, *SF3B1* and *SRSF2* are synthetic lethal partners, with mutations in both genes not viable in human myeloid and leukemia cells[429]. Additionally, other synthetic lethal screens against the KRAS oncogene have identified splicing as a targetable cancer-specific vulnerability[76,430]. Together, these data support the potential usefulness of splicing inhibitors in the clinic, providing motivation for the development of compounds that disrupt splicing in particular cancer contexts. One particularly promising pharmacological splicing modulator is H3B-8800, which potently inhibits splicing and preferentially kills epithelial and haematological cancer cells with *SFB1^{K700E}* mutations

through direct interaction with the SF3b complex[431]. As a result, H3B-8800 has entered clinical trials for patients with refractory leukemias (NCT02841540). Although splicing is a fundamental step in gene expression, the capacity of H3B-8800 to selectively kill malignant cells without causing toxicity to normal cells, suggests that a U12-dependent splicing inhibitor could be useful in similar cancer contexts.

For *RNPC3/*65K or U12-dependent splicing more broadly, to be a target for cancer therapy it is necessary to examine the safety implications. U12-dependent splicing is indispensable for normal human development as revealed by the identification of patients carrying two copies of a pathogenic single nucleotide variant in *U4ATAC*, one of the U12-dependent specific snRNAs. These patients exhibit a collection of severe and closely related human developmental syndromes (microcephalic osteodysplastic primordial dwarfism type 1 (MOPD1), Roifman and Lowry-Wood syndromes)[432-435]. Pathogenic variants in another U12-dependent specific snRNA, *RNU12*, have been linked to early-onset congenital cerebral ataxia in a large consanguineous family[436]. Disrupted U12-dependent splicing, predominantly in the nervous system, is a prevalent characteristic in these Mendelian disorders[437]. One possible interpretation of these disease associations is that inhibiting 65K function for cancer treatment should be approached with caution. On the other hand, encouragement for such a strategy comes from the recent report of a family with *RNPC3* mutations. Whilst both parents are healthy, the father of this family is heterozygous for a nonsense mutation in *RNPC3* and the mother is heterozygous for a disabling nonsense mutation in *RNPC3*. Remarkably, three out of four female offspring are compound heterozygotes, yet only exhibit isolated growth hormone deficiency due to pituitary hypoplasia that is readily treatable[438,439]. This case demonstrates that despite a ubiquitous requirement for U12-dependent splicing, severe genetic disruption of an individual U12-dependent spliceosome specific component results in a mild clinical phenotype. Therefore, it is tempting to speculate that it may be possible to inhibit RNPC3/65K beyond the 50% reduction in gene dosage examined in this thesis, to achieve greater anti-cancer activity without having detrimental effects on healthy tissues.

The potential clinical utility of therapeutic strategies targeting U12-dependent splicing is further supported by interrogation of mutation data in The Cancer Genome Atlas (TCGA). Genes encoding the unique components of the U11-U12 di-snRNP were found to be rarely mutated (<1%) across a broad spectrum of cancers. Moreover, CRISPR screens have revealed that genes encoding the protein components of the U11-U12 di-snRNP are essential for the proliferation of cancer cell lines. Together these observations suggest that U12-dependent splicing is necessary for sustaining malignant growth and that this dependency may extend to diverse cancer types. Cancer cells are unlikely to develop resistance against compounds targeting the U12-dependent spliceosome as it is a unique multiprotein complex that does not contain redundant components, such as those found in signalling cascades. Therefore, I strongly believe that U12-dependent splicing inhibitors could be extremely useful in the clinic

to treat a range of cancers with a viable therapeutic window and the potential to evade the emergence of resistance. One potential small molecule inhibitor, which is selective for U12-dependent splicing, and is at a very early stage of drug development, is evaluated in Chapter 5 of this thesis.

5 Testing novel therapeutics in a zebrafish hepatocellular carcinoma model

5.1 Defining a cancer dependency map

Extensive studies of cancer genomes have revealed striking complexity in the array of mutations identified, even within the same tumour type[440]. Cancers typically contain thousands of somatic mutations which may be classified as driver or passenger mutations. A relatively small number of driver mutations confer a selective growth advantage to cells and are responsible for malignant transformation and progression. These are outnumbered by passenger mutations which do not contribute to oncogenesis[441]. Thus, only a small percentage of cancer mutations are clinically actionable and not all of these are druggable with conventional approaches. Consequently, numerous genome-scale RNAi and CRISPR screens have sought to establish cancer dependencies and synthetic lethal relationships to expand the range of drug targets and identify novel therapeutic strategies. Using short hairpin RNA (shRNA) technology, Project DRIVE characterised the viability effects of knockdown of 7,837 genes using an average of 20 shRNAs per gene in 398 cancer cell lines[442]. Similarly, Project Achilles assessed the impact of knockdown of 17,098 genes in 501 cell lines with a median coverage of 5 shRNAs per gene[443]. In addition, genome-wide viability screens have also been performed via CRISPR-Cas9 mediated gene inactivation in diverse human cancer cell lines, enabling systematic discovery of cancer dependencies. The largest screens were performed independently at the Broad and Sanger institutes, profiling a total of 17,486 genes across 908 cell lines[375,444]. As part of the Cancer Dependency Map initiative, these screens have established a comprehensive database of genetic and pharmacologic vulnerabilities of specific cancer types, identifying novel therapeutic targets which may be exploited for precision cancer therapy (Figure 5.1)[374,443]. The 769 gene dependencies identified were distributed throughout a variety of protein classes including mRNA splicing factors, kinases and transcription factors. Approximately 10% of dependencies were shared across multiple cancer contexts, suggesting that a modest number of therapeutic targets may be relevant for combating several tumour types. Significantly, 20% of genetic dependencies identified were annotated as readily druggable targets[443].

One of the most robust synthetic lethal interactions identified in large-scale screens is PRMT5 (protein arginine methyltransferase 5) dependence in cells with *MTAP* (methylthioadenosine phosphorylase) deletions[445-447]. The genomic position of *MTAP* at chromosome 9p21.3 is adjacent to that of the tumour suppressor gene, *CDKN2A* (cyclin-dependent kinase inhibitor 2A, encoding $p16^{INK4A}$ and $p14^{ARF}$). As a consequence of this proximity, *MTAP* is often co-deleted with the *CDKN2A* locus in cancer, including in 41% of glioblastomas and 21% of pancreatic adenocarcinomas[376,377]. *MTAP*-null cells accumulate high levels of the substrate MTA, which partially inhibits the essential arginine methyltransferase activity of PRMT5 (Figure 5.2). Thus, in comparison to normal cells, cancer cells harbouring MTAP deletions exhibit a heightened dependency on PRMT5 and are more susceptible to PRMT5 inhibition[445-

[447]. This dependency constitutes a type of synthetic lethality termed collateral lethality, where co-deletion of genes adjacent to tumour suppressors results in cancer-specific therapeutic vulnerabilities[448].

Whilst the identification of essential genes in cancer cell lines can help inform therapeutic approaches and identify novel targets, significant challenges remain to translate discoveries and maximise clinical benefits. For instance, currently available PRMT5 inhibitors do not recapitulate the impact of PRMT5 genetic knockdown, with pharmacological inhibition of PRMT5 not selective for MTAP-null cell lines[445-447]. However, this discrepancy is due to the SAM cooperative mechanism of action of the PRMT5 inhibitors tested, resulting in limited PRMT5 inhibition in the presence of excess MTA, rather than a failure to recapitulate the collateral synthetic lethal interaction between PRMT5 and MTAP[445,449]. Consequently, it is of utmost importance to validate synthetic lethal drug targets to fully realise the potential of such therapies.

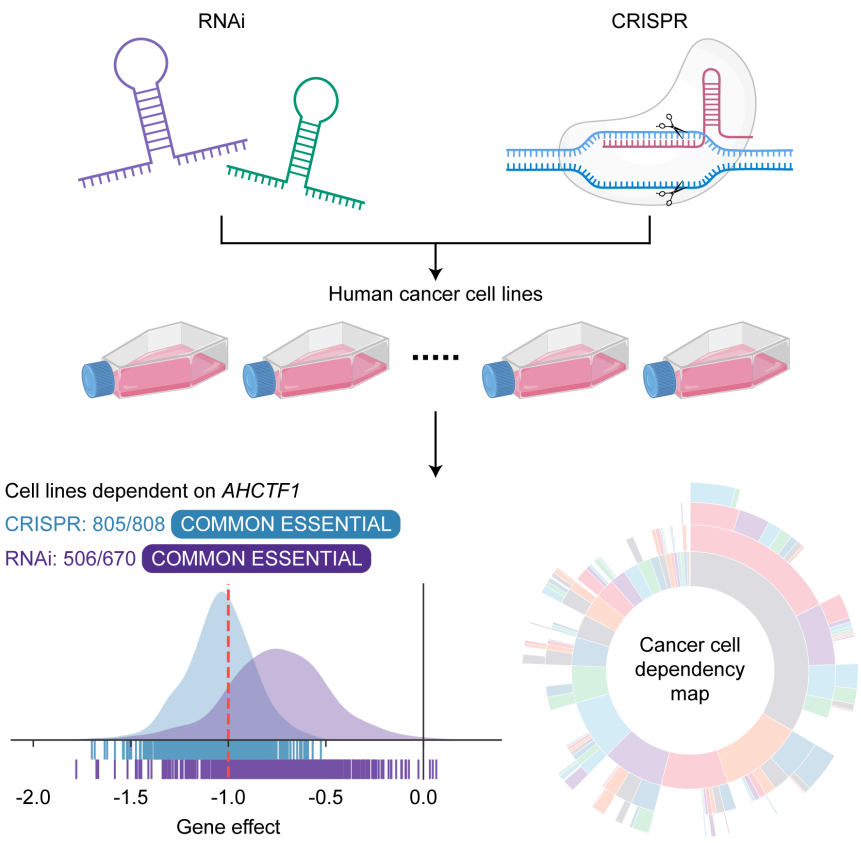

Figure 5.1 Genome-wide screens to identify cancer cell dependencies

A. Genome-scale screens utilising RNAi or CRISPR technology have enabled systematic assessment of the impact of single gene knockdown across a diverse range of cancer cell lines, revealing genes that are essential for cancer cell proliferation and survival. **B.** *AHCTF1* is classified as a common essential gene ranking amongst the topmost dependent genes in at least 90% of cell lines. The graph shown plots the calculated gene effect scores for *AHCTF1* across different cell lines in CRISPR screens (blue) and RNAi screens (purple). A lower gene effect score indicates that a gene is more likely to be indispensable in a given cell line. A score of -1 is equivalent to the median of all common essential genes whereas a score of 0 corresponds to a gene that is not essential. **C.** Integrated analyses have facilitated development of a comprehensive map of the genetic vulnerabilities of cancer that classifies the distribution of genetic dependencies by protein classes, which can be represented in a sunburst tree were the different colours correspond to distinct classes of proteins. Of the over 760 dependencies identified, a majority correspond to nucleic acid binding proteins, which may be further divided into RNA-binding proteins, DNA binding proteins, helicases and nucleases. Together, these data may be utilised to identify and prioritise novel cancer therapeutic targets. Data retrieved from DepMap Portal on 2021-02-12(https://depmap.org).

CRISPR: clustered regularly interspaced short palindromic repeats, RNAi: RNA interference.

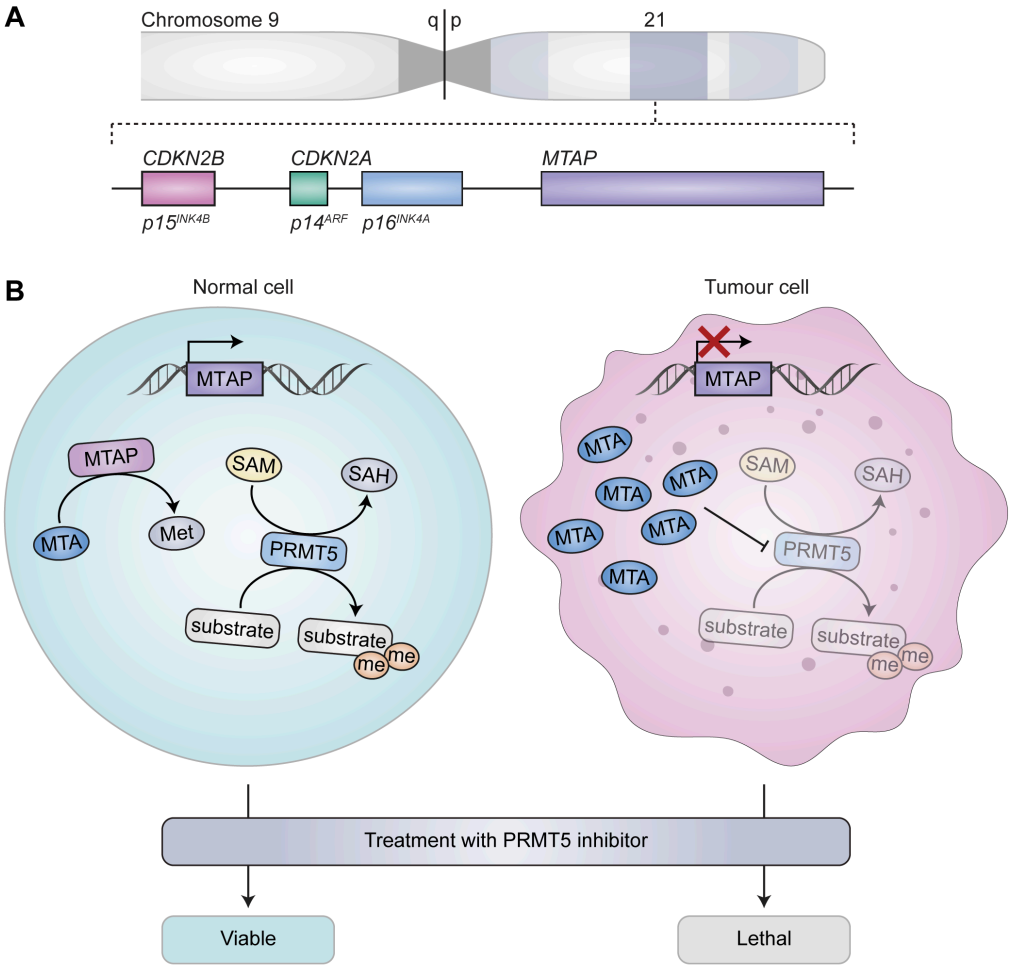

Figure 5.2 MTAP deletion confers an enhanced dependency on PRMT5 in tumour cells

A. The 9p21.3 region of chromosome 9 containing the tumour suppressor *CDKN2A* is often deleted in cancer, along with flanking genes including *CDKN2B* and *MTAP*. **B.** In normal cells, MTAP converts MTA to Met. PRMT5 functions as an essential methyltransferase, transferring a methyl group from the cofactor SAM to produce methylated substrates and SAH. In tumour cells with *CDKN2A* deletion and collateral loss of the *MTAP* gene the metabolite MTA accumulates. MTA partially inhibits PRMT5 via competing with SAM, conferring heightened sensitivity to further depletion of PRMT5 function. This vulnerability can be exploited therapeutically via treatment with PRMT5 inhibitors to selectively kill MTAP-null tumour cells while sparing normal cells. Figure adapted from Huang et al., 2020[450]

CDKN2A: cyclin-dependent kinase inhibitor 2A, CDKN2B: cycling-dependent kinase inhibitor 2B, Me: methyl, Met: methionine, MTA: methylthioadenosine, MTAP: methylthioadenosine phosphorylase, PRMT5: protein arginine methyltransferase 5, SAM: S-adenosylmethionine, SAH: S-adenosylhomocysteine.

5.2 Drug discovery and testing in zebrafish

Zebrafish provide an ideal vertebrate system for identifying and validating novel therapeutics *in vivo* as they are amenable to high-throughput screening and share genetic and physiological similarities to humans[149-151]. As versatile tools for drug discovery, zebrafish can contribute to several stages of the drug development process, including target identification, pharmacology and toxicology studies. Moreover, chemical screens performed in zebrafish have the capacity to accelerate the drug development pipeline by enabling drug discovery at the same time as assessment of toxicity[120,451]. Screens may be performed in zebrafish embryos or in adults and drugs may be administered via aqueous exposure, intraperitoneal injection or oral gavage (Figure 5.3)[452-455].

Several studies have demonstrated the value of drugs screens in zebrafish embryos for identifying molecules that specifically inhibit malignant transformation, growth or progression and for evaluating the efficacy of novel cancer therapeutics. For example, a screen of more than 16,000 compounds performed in zebrafish embryos and using phosphorylated-histone H3 as a read out, identified 14 novel cell cycle inhibitors, yet these were not detected in screens of the same library previously performed in mammalian cell lines, demonstrating the power of zebrafish *in vivo* drug discovery[456]. Another successful chemical genetic screen was performed in transgenic *Tg(hsp70:AML1-ETO)* zebrafish embryos to identify modifiers of normal and malignant haematopoiesis[457]. Among the 2,000 bioactive compounds screened, the COX-2 inhibitor nimesulide was found to suppress AML-ETO driven oncogenic cell fate transformation via inhibiting prostaglandin E2 synthesis, a strategy which may be of clinical benefit for patients with acute myeloid leukemia[457].

Based on the shared characteristics between cells in developing tissues and cancer cells, as well as the observation that embryonic developmental pathways are often reactivated during malignant transformation, multiple screens have been designed in zebrafish to find inhibitors of embryonic development phenotypes that could also be efficacious against cancer. One such screen sought to uncover inhibitors of T cell lymphoblast development with the aim of identifying targeted anti-leukemia agents[458]. In this screen, performed in the transgenic *Tg(lck:EGFP)* zebrafish line, over 26,000 compounds were evaluated for activity that suppressed EGFP expression in the thymus, indicating a reduction in the number of immature T cells. Of the 21 strong hits identified, lenaldekar was subsequently shown to induce long-term remission in a zebrafish model of T-ALL and drug efficacy was further confirmed in a human T-ALL mouse xenograft model[458]. Similarly, a screen to identify compounds that blocked embryonic development of zebrafish neural crest lineage cells, posited to also identify suppressors of melanoma, led to the discovery of leflunomide which has now entered phase I/II human clinical trials for melanoma[155]. Zebrafish models of HCC have also been used as a tool for *in vivo* drug discovery. Screening of compounds in a mifepristone-inducible *TO(kras^{G12V})* zebrafish model of HCC showed that inhibitors targeting the RAF-MEK-ERK pathway prevented liver tumourigenesis[174]. In addition, a chemical screen performed in

Tg(fabp10a:pt-β-cat) zebrafish to identify compounds that mediated β-catenin driven hepatocarcinogenesis, found two c-Jun N-terminal kinase (JNK) inhibitors and two antidepressants that suppressed the HCC phenotype[190].

Numerous drug screens performed in zebrafish have taken advantage of transgenic fluorescent reporter lines, such as *Tg(fli:EGFP)* which expresses EGFP in the blood vascular network, to facilitate identification of anti-angiogenic drugs[134,459]. Among the compounds uncovered in such screens, rosuvastatin (an FDA approved cholesterol lowering agent) was demonstrated to inhibit tumour angiogenesis and suppress tumour growth in a prostate cancer xenograft mouse model[460]. In addition, zebrafish xenograft models that enable real-time observation of tumour angiogenesis and migration, have become increasingly utilised as a platform to identify anti-angiogenic and anti-metastasis drugs[461,462]. Several transplantation-based zebrafish models have been developed via engraftment of human, murine or zebrafish tumour cells, providing a powerful tool for investigating and validating therapeutic compounds *in vivo*. For example, a pioneering study established zebrafish patient-derived xenografts (zPDX) of colorectal cancer and found that zPDX treatment response was strongly predictive of patient clinical outcomes[144]. zPDXs have since been used to evaluate outcomes of bevacizumab treatment in breast and colorectal cancer, revealing differential responses in just 4 days which could be used to rapidly inform individualised therapeutic strategies[463]. Consequently, the use of zPDXs as *in vivo* screening platforms for personalised medicine applications is an area of great promise[152]. In addition, recent development of immunodeficient zebrafish has further expanded the possibilities of transplantation studies, enabling transplant of human tumour cells into adult zebrafish[146].

As the identification and validation of novel drug targets remains a major bottleneck in drug discovery, the rapid and efficient evaluation of drug responses and kinetics *in vivo* utilising zebrafish has remarkable potential to speed up drug development and contribute to new applications in precision oncology and optimisation of combination therapy[120,149,152]. In this chapter, I set out to establish whether the *TO(kras^{G12V})* model of HCC, which exhibits robust hepatocyte hyperplasia that is highly amenable to genetic manipulation, was similarly responsive to pharmacological inhibition and could be used as a chemical screening tool.

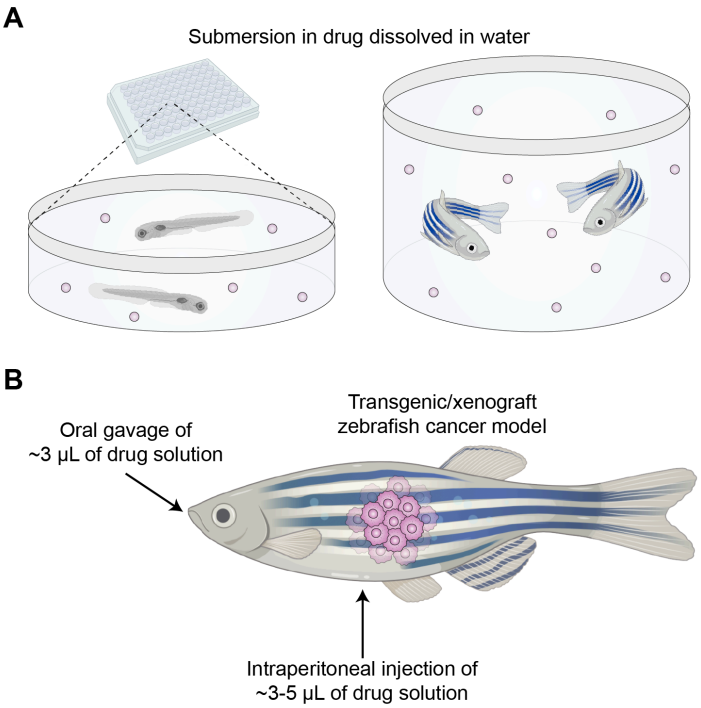

Figure 5.3 Methodologies for zebrafish cancer drug screens

Phenotype-based chemical screens for *in vivo* drug discovery may be performed in zebrafish larvae or adult fish. Screens may examine modulation of specific embryonic developmental pathways that are also relevant to tumourigenesis or utilise transgenic or transplantation-based zebrafish cancer models. **A.** Zebrafish may be treated by dissolving drugs directly in water. Such administration facilitates large-scale screening of zebrafish larvae in a 96-well plate format with relative ease. **B.** Alternatively drugs may be delivered to adult zebrafish via oral gavage or intraperitoneal injection after anaesthesia and immobilisation.

5.3 Inhibitors of protein kinases MEK1/2

The RAS-RAF-MEK-ERK signalling pathway is aberrantly activated in more than 30% of tumours[464]. Oncogenic RAS mutations cause unchecked activation of the MAPK signalling cascade via the sequential phosphorylation and activation of MEK1/2 and ERK1/2 (Figure 5.4). Activated ERK1/2 phosphorylates other protein kinases and transcription factors such as FOS, ETS and MYC, which regulate cell cycle progression by inducing expression of target genes, such as *CCND1* (encoding cyclin D1) which in turn stimulates the activity of G1 phase cyclin-dependent kinases (CDKs). In addition, ERK1/2 also regulates cell survival via phosphorylation of BCL-2 family proteins, including BIM and MCL1[465,466]. Thus, the RAS-RAF-MEK-ERK signalling cascade is a crucial mediator of several hallmark characteristics of cancer cells and much attention has been focused on developing inhibitors against components of the pathway. Targeting mutant RAS proteins directly has proven challenging due to its unremarkable molecular structure, however, novel strategies have recently emerged with the development of covalent, allele-specific $KRAS^{G12C}$ covalent inhibitors with potential therapeutic efficacy in a subset of RAS driven cancers[60,61]. A more promising approach has been therapeutic targeting of RAF and MEK. In particular, BRAF inhibitors are a validated, clinically effective therapeutic strategy in a range of cancers, especially melanomas[467-469]. MEK1/2 also holds considerable value as a therapeutic target due to its narrow substrate specificity. Unlike ERK, which phosphorylates numerous cytoplasmic and nuclear substrates, ERK1/2 are the only known physiological substrates of MEK1/2[470-472]. Thus, MEK1/2 functions as a gatekeeper to the activation of diverse cellular responses, many of which contribute to tumourigenesis, fuelling interest in the development of pharmacological inhibitors of MEK.

In 1995, the first MEK inhibitor, PD098059 was reported and since then several MEK inhibitors have been developed and progressed through clinical trials for a diverse array of tumours[473]. Trametinib was the first MEK inhibitor to receive FDA approval in 2013 for the treatment of patients with BRAF-mutant melanoma[474]. Subsequently, MEK162 (binimetinib) a potent, selective non-ATP-competitive allosteric inhibitor of MEK1/2 was developed (Figure 5.4). In phase II clinical trials, 20% of patients with NRAS and BRAF-mutant melanoma showed partial responses to MEK162[475]. MEK162 is now in clinical use for the treatment of unresectable metastatic melanoma. In addition, clinical trials are ongoing for MEK162 in BRAF-mutant metastatic colorectal cancer in combination with encorafenib (a BRAF inhibitor) and cetuximab (an EGFR inhibitor)[476]. Given the clinical relevance of MEK inhibition in RAS/RAF mutant cancers, MEK162 was selected for proof-of-principle experiments designed to explore the usefulness of the *TO(*$kras^{G12V}$*)* zebrafish HCC model for pharmacological and drug discovery studies.

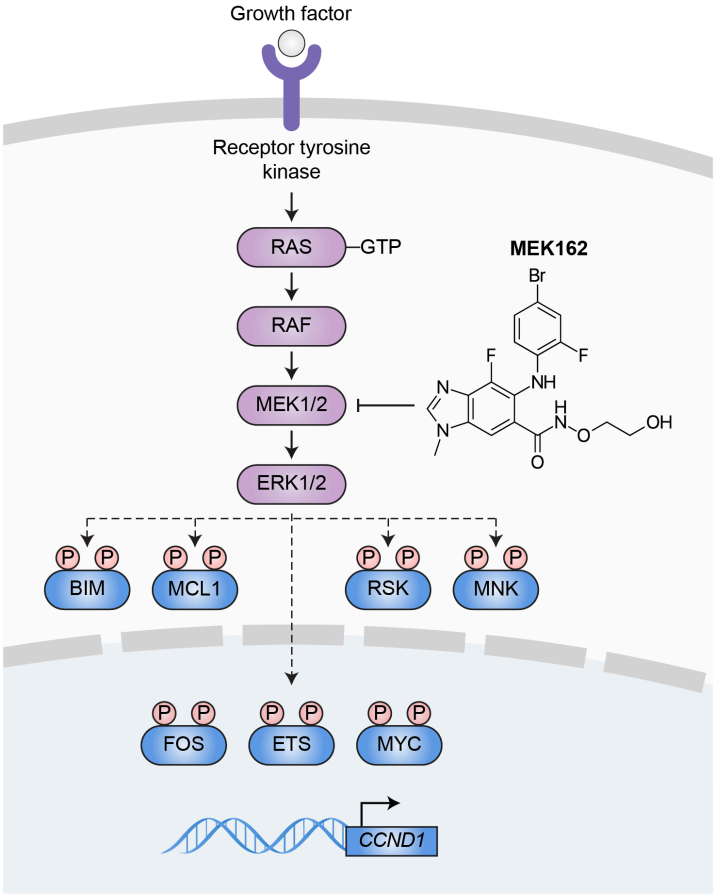

Figure 5.4 Targeting MEK1/2 for cancer therapy

The RAS/RAF/MEK/ERK pathway which is normally activated in response to growth factor signalling is aberrantly activated in many diverse cancer types, thereby driving malignant transformation and progression. As part of this signalling cascade, MEK1/2 activates ERK1/2 by phosphorylation, which contributes to the activation of many processes critical for tumourigenesis. Activated ERK1/2 catalyses the phosphorylation of several cytoplasmic and nuclear substrates. These include BCL-2 family proteins, BIM and MCL1 that regulate apoptosis and other protein kinases such as RSK and MNK. In the nucleus, ERK1/2 phosphorylates transcription factors including FOS, ETS and MYC which regulate the expression of target genes, such as *CCND1* (encoding cyclin D1) that promote cell cycle progression. As MEK1/2 has narrow substrate specificities and is crucial for activating diverse cellular responses integral for tumour growth and progression, it represents an attractive target for cancer therapy. Amongst the many MEK1/2 inhibitors developed, MEK162 has gained FDA approval for clinical use in melanoma patients. Figure adapted from Caunt et al., 2015[477].

CCND1: cyclin D1, GTP: guanosine triphosphate, MNK: MAPK interacting protein kinase, RSK: ribosomal s6 kinase.

5.4 Results

5.4.1 MEK162 reduces *kras*^{G12V}-driven hepatocyte hyperplasia

In control *2-CLiP* larvae, treatment with 1.0-20 µM MEK162 from 5 to 7 dpf did not affect normal liver development (Figure 5.5A, B). No reduction in liver volume was observed after MEK162 exposure, even at the highest concentration tested of 20 µM. In contrast, a dose-dependent reduction in liver volume was observed in *TO(kras*^{G12V}*)*$^{T/+}$ larvae (Figure 5.5C). Whilst *kras*^{G12V}-driven hepatocyte hyperplasia was significantly reduced by 81% in response to treatment with 20 µM MEK162, liver volume remained slightly greater than that of livers in *2-CLiP* larvae (Figure 5.5D). These data are consistent with the demonstrated clinical effectiveness of inhibiting the MAPK pathway via MEK162 treatment in RAS/RAF mutant cancers. Moreover, they validate the use of the *TO(kras*^{G12V}*)*$^{T/+}$ zebrafish HCC model as a highly efficient platform for evaluating impacts of drug treatment on tumourigenesis.

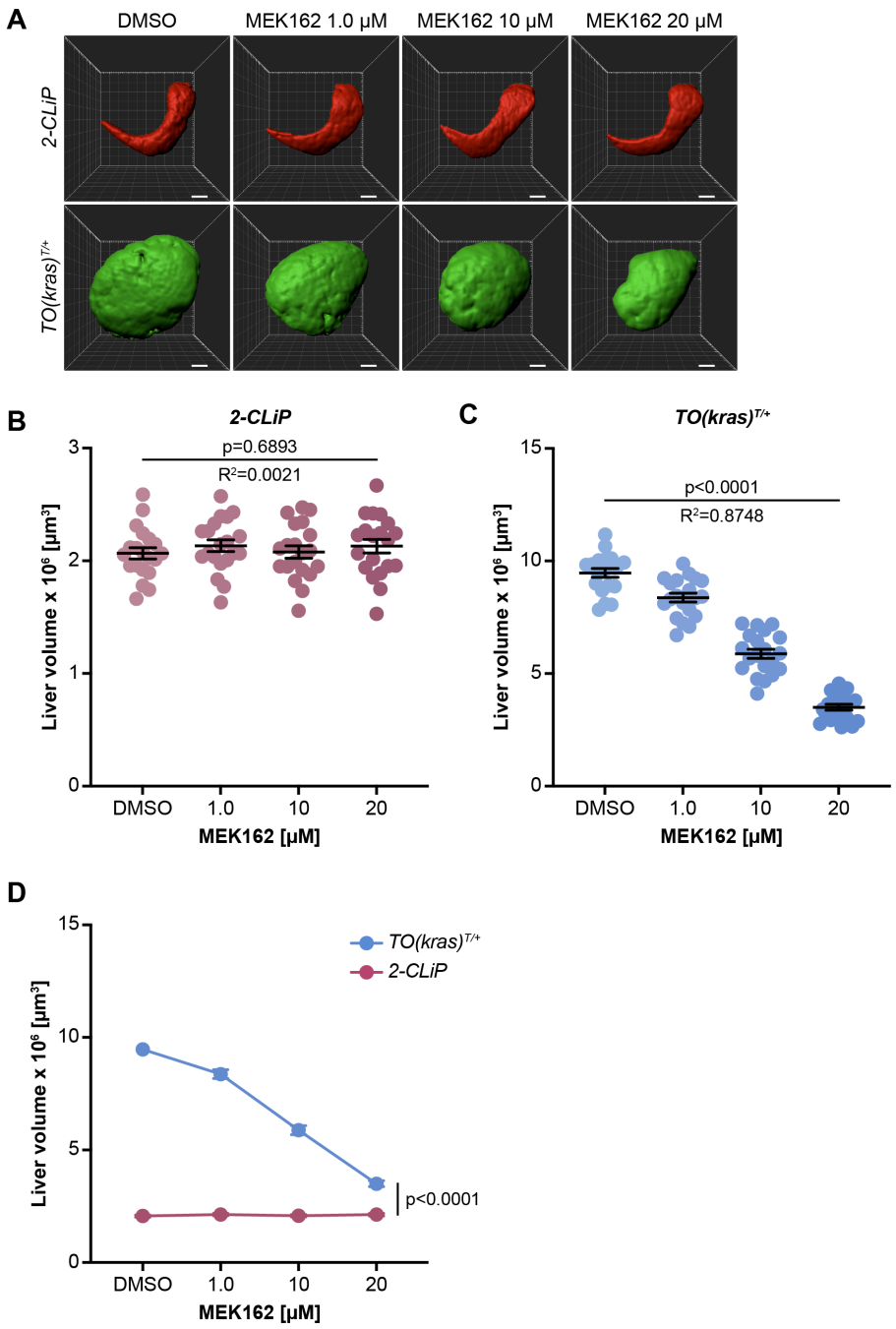

Figure 5.5 MEK162 markedly reduces *kras^{G12V}*-driven hepatocyte hyperplasia and liver enlargement

A. Representative three-dimensional reconstructions of *2-CLiP* and *TO(kras^{G12V})$^{T/+}$* livers treated with DMSO or the indicated concentration of MEK162. Scale bar 25 µm. **B.** Liver volume in *2-CLiP* larvae was not impacted by MEK162 treatment. **C.** Liver volume in *TO(kras^{G12V})$^{T/+}$* larvae was reduced in a dose-dependent manner by MEK162 treatment. **D.** Graphical representation of the results shown in panels B-C. 20 µM MEK-162 treatment caused a 81% inhibition in *kras^{G12V}*-driven liver volume, such that liver volume was only

slightly greater than that of control *2-CLiP* livers. Data are expressed as mean ± SEM, n=20. Significance was calculated by linear regression analysis.

5.5 Selective inhibitors of nuclear export

The effectiveness of another clinically approved compound, selinexor, a selective inhibitor of nuclear export (SINE), was also assessed in the *TO(kras^{G12V})* model. Dysregulation of nucleocytoplasmic transport is a common feature in a broad spectrum of diseases, including cancer[478,479]. Owing to their elevated rate of proliferation and cellular metabolism, malignant cells are hypothesised to be more dependent on nuclear transport in comparison to normal cells. Thus, inhibition of nuclear export has emerged as an important therapeutic target in cancer (Figure 5.6). Nuclear export is almost exclusively mediated by Exportin 1 (XPO1) also known as chromosome maintenance region 1 (CRM1). XPO1 is responsible for the nuclear export of over 220 proteins, including the vast majority of tumour suppressors such as pRB, tp53, APC, p27 (encoded by CDKN1B) and NF-kB[478,480]. In addition, XPO1 also mediates the export of several RNA species including small nuclear RNAs, ribosomal RNAs and a subset of messenger RNAs[481,482]. XPO1 overexpression is a frequent occurrence in diverse tumour types, including ovarian, pancreatic, gastric, brain and cervical cancer, as well as osteosarcoma, melanoma and haematological malignancies[483,484]. Significantly, elevated XPO1 is associated with disease progression, resistance to treatment and reduced survival rates[485-488]. These observations indicate that XPO1 is a promising target for therapeutic intervention, prompting the development of inhibitors of XPO1.

The first specific XPO1 inhibitor discovered was the antibiotic Leptomycin B in the 1990s[489], which binds irreversibly to the cysteine 528 residue of XPO1[490]. However, systemic toxicities were observed in phase I trials in patients with treatment-refractory cancer, as leptomycin B treatment permanently blocked nuclear export in both cancerous and normal cells[491]. The next generation of compounds developed, known collectively as SINEs (selective inhibitors of nuclear export), slowly and reversibly bind XPO1 and exhibit an improved toxicity profile *in vivo*[492-494]. These compounds bind to XPO1 for a sufficient length of time to allow tumour suppressor proteins to accumulate in the nucleus whilst also enabling a level of nuclear export that permits survival of normal cells[479]. The most prominent SINE compound, selinexor (also known as KPT-330), induces cell death in T-ALL and AML cell lines and is also effective in mouse xenograft models of leukemia[493,495]. As a result, selinexor has received FDA approval for the treatment of relapsed or refractory multiple myeloma and diffuse large B-cell lymphoma[496,497]. XPO1 is also a therapeutic vulnerability of KRAS-mutant non-small cell lung cancer. Selinexor causes nuclear accumulation of IκBα and associated inhibition of NF-κB specifically in lung cancer cell lines and this efficacy and selectivity was conserved *in vivo* in patient-derived mouse xenograft models[498]. In HCC-derived cell lines, selinexor has an anti-proliferative impact, inducing cell cycle arrest and apoptosis via upregulating protein expression of Tp53 and p27 and downregulating c-Myc and c-Met. Similarly, in HCC xenograft models, selinexor treatment significantly inhibited tumour growth[499]. Consequently, selinexor holds considerable value as a targeted cancer therapy.

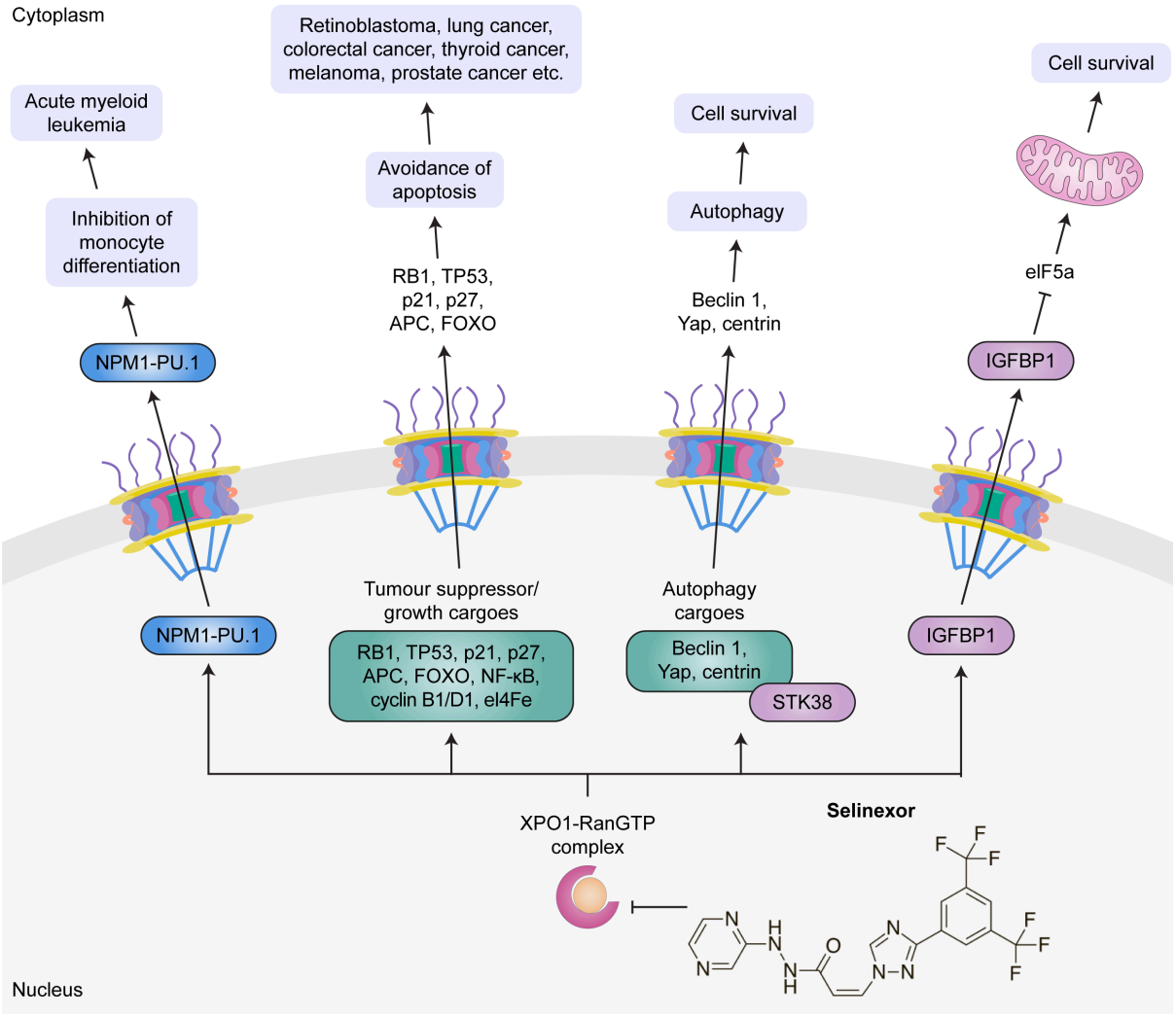

Figure 5.6 Targeting XPO1 for cancer therapy

XPO1 forms a complex with RanGTP to mediate nuclear export of a diverse array of protein and RNA cargoes. XPO1-mediated export of several cargoes has been linked to tumourigenesis. Specifically, export of NPM1 and the associated transcription factor PU.1 inhibits monocyte differentiation which contributes to the development of leukemia[500]. XPO1 also mediates export of numerous tumour suppressor proteins, including RB1, TP53 and APC amongst others, which mediate evasion of apoptosis, a hallmark characteristic of a range of cancer types. The export of growth cargoes, such as p21 and p27 by XPO1 drives cell cycle progression. In addition, XPO1 along with STK38, mediates export of the autophagy cargoes Beclin 1, Yap and centrin which promote cell survival[501]. Similarly, export of IGBP1, inhibits accumulation of eIF5a in the mitochondria, resulting in cell survival. Figure adapted from Azmi et al., 2020[478].

APC: adenomatous polyposis coli, eIF5a: eukaryotic translation initiation factor 5a, FOXO: forkhead box, IGFBP1: insulin-like growth factor binding protein 1, NPM1: nucleophosmin,

RanGTP: Ran guanosine triphosphate, STK38: serine/threonine-protein kinase 38, XPO1: exportin 1, YAP: yes-associated protein.

5.6 Results

5.6.1 Selinexor reduces *kras*^{G12V}-driven hepatocyte hyperplasia

Treatment with 0.1-2.0 µM selinexor from 5 to 7 dpf did not affect normal liver development in control *2-CLiP* larvae and had no overt visible signs of toxicity or developmental defects (Figure 5.7A, B). No reduction in liver volume was observed after selinexor exposure, even at the highest concentration tested (2.0 µM). In contrast, selinexor produced a dose-dependent reduction in liver volume in *TO(kras*^{G12V}*)*$^{T/+}$ larvae (Figure 5.7C). Whilst *kras*^{G12V}-driven liver volume was significantly reduced 56% in response to treatment with 2.0 µM selinexor, liver volume remained higher compared to *2-CLiP* larvae treated with the same dose (Figure 5.7D). These data suggest that a higher dose of selinexor may have proved to be more effective without eliciting non-specific toxicity. These results demonstrate that XPO1 inhibition suppresses tumourigenesis induced by mutant Kras and together with the MEK162 data shown in Figure 5.5, reinforce the potential usefulness of the *TO(kras*^{G12V}*)*$^{T/+}$ zebrafish HCC model as a system for testing inhibitors including novel compounds.

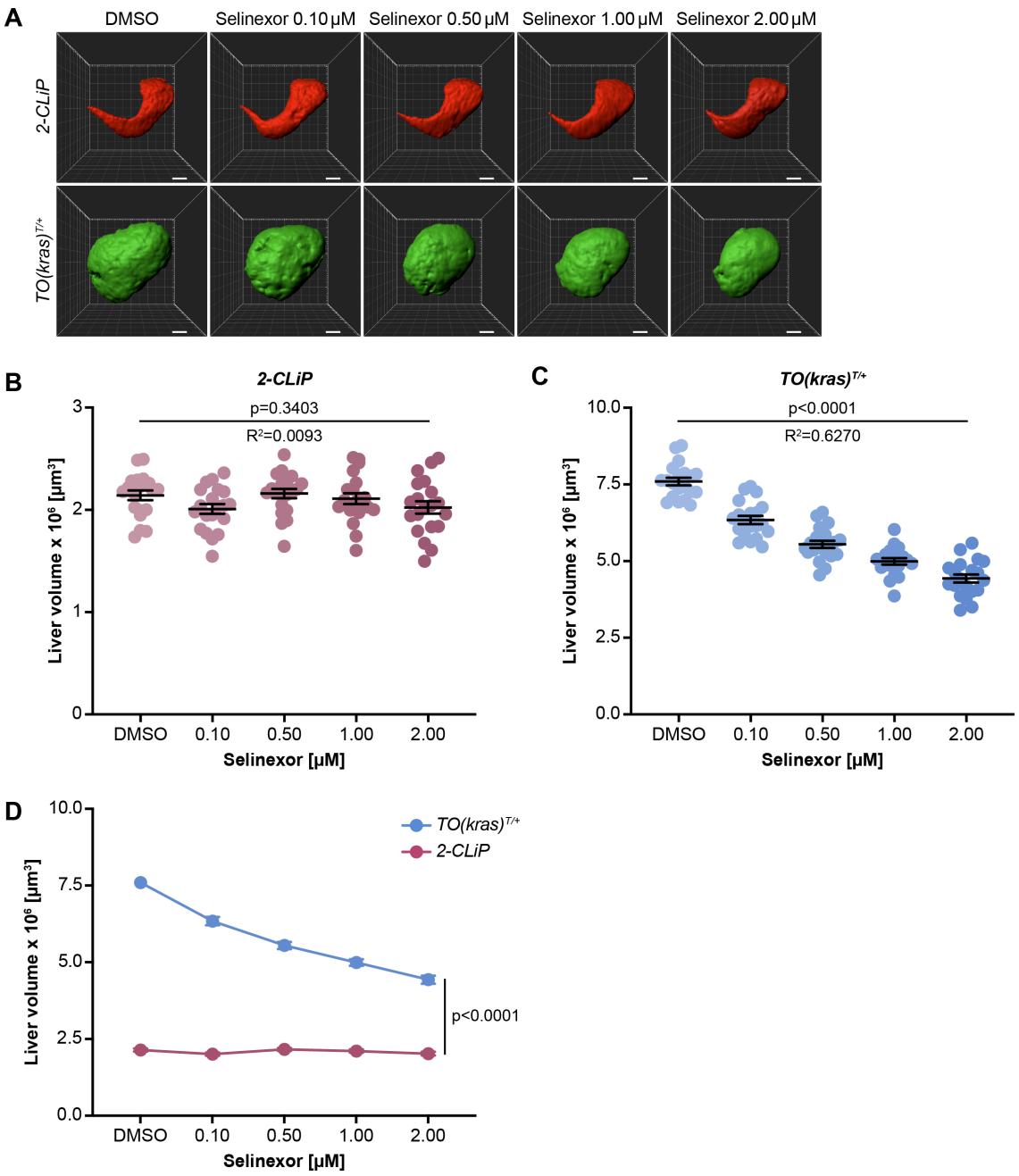

Figure 5.7 Selinexor reduces *kras*^{G12V}-driven hepatocyte hyperplasia and liver enlargement

A. Representative three-dimensional reconstructions of *2-CLiP* and *TO(kras*^{G12V}*)*$^{T/+}$ livers treated with DMSO or the indicated concentration of selinexor. Scale bar 25 µm. **B.** Liver volume in *2-CLiP* larvae was not impacted by selinexor treatment, irrespective of dose. **C.** Liver volume in *TO(kras*^{G12V}*)*$^{T/+}$ larvae was reduced in a dose-dependent manner by selinexor treatment. **D.** Graphical representation of the results shown in panels B-C. Treatment with 2.00 µM selinexor caused a 56 % reduction in excess *kras*^{G12V}-driven liver volume. Data are expressed as mean ± SEM, n=20. Significance was calculated by linear regression analysis.

After demonstrating the effectiveness of the aforementioned clinically relevant compounds in the *TO(kras^{G12V})* zebrafish HCC model, collaborators at WEHI provided inhibitors under development for *in vivo* evaluation of efficacy. These include EPZ015666 an inhibitor of protein arginine methyltransferase 5 (PRMT5), and WM-8014 an inhibitor of histone acetyltransferases KAT6A/B (also known as MOZ/QUERKOPF).

5.7 Inhibitors of protein arginine methyltransferase 5

Protein arginine methylation of histone and non-histone substrates has emerged as a frequent post-transcriptional modification that crucially regulates cell signalling and function in normal physiological and pathological states[502]. The methylation of arginine residues is catalysed by a family of nine protein arginine methyltransferases (PRMTs)[503]. PRMTs transfer a methyl group from the donor substrate, S-adenosylmethionine (SAM), to the guanidino nitrogen atoms of arginine, producing S-adenosylhomocysteine (SAH) and methylarginine (Figure 5.8)[503]. PRMTs are classified as type I, II or III depending on their catalytic activity. Type I and II PRMTs form a mono-methylarginine (MMA) intermediate before the establishment of asymmetric dimethylarginine (aDMA) or symmetric dimethylarginine (sDMA) respectively. Type III PRMTs only generate MMA[504]. PRMT5 is the primary type II enzyme, responsible for forming sDMA. PRMT5 enzymatic activity requires its binding partner and co-activator methylosome protein 50 (MEP50/WDR77) to form a hetero-octameric complex[505].

PRMT5 has integral roles in a diverse range of cellular signalling processes, methylating both nuclear and cytoplasmic targets that harbour glycine and arginine rich (GAR) motifs[504,506] (Figure 5.9). PRMT5 functions in general as a transcriptional corepressor, depositing repressive H2AR3me2s, H3R2me2s, H3R8me2s and H4R3me2s histone methylation marks in association with the SWI/SNF complex. In particular, H2AR3me2s has been implicated in repression of differentiation genes in embryonic stem cells, indicating a role in maintaining pluripotency[507]. In the cytoplasm, PRMT5 forms part of the methylosome which methylates Sm proteins, facilitating the efficient assembly of mature small nuclear ribonucleoprotein (snRNPs) into the spliceosome and thus enabling mRNA splicing. Consequently, inhibition of PRMT5 through knockdown or genetic knockout in cells causes numerous splicing defects[508,509]. Additionally, PRMT5 modulates RAS signalling via methylation of RAF proteins and plays a crucial role in apoptosis via methylation of TP53 at multiple arginine sites[506]. Importantly, deregulation of PRMT5 has been implicated in the pathogenesis of several different diseases, including cancer and metabolic, neurodegenerative and muscular disorders[503,510]. PRMT5, is overexpressed in a diverse range of cancers, including melanoma, lymphoma, glioma, lung, prostate, ovarian and breast cancer[504,511-514]. In the context of HCC specifically, PRMT5 expression is upregulated and correlated inversely with overall patient survival[515]. Moreover, knockdown of PRMT5 in HCC cell lines has been shown to inhibit growth via the downregulation of b β-catenin and cyclinD1[516]. These reports stimulated the development of potent and selective inhibitors of PRMT5, including EPZ015666[449].

EPZ015666 is a substrate competitive inhibitor of PRMT5 that binds within the peptide-binding site, including the pocket occupied by the substrate arginine side chain[449]. EPZ015666 treatment had an antiproliferative effect in both *in vitro* and *in vivo* xenograft models of mantle cell lymphoma (MCL), with more than 93% tumour growth inhibition observed in MCL tumours, corresponding with decreased levels of sDMA substrates[449]. This demonstrated target engagement and efficacy of EPZ015666, prompted further studies to evaluate the therapeutic potential of pharmacological inhibition of PRMT5 in different cancer types. In triple-negative breast cancer (TNBC) cell lines, EPZ015666 was similarly found to impair proliferation via inducing apoptosis and G2/M cell cycle arrest. In a patient-derived xenograft model of TNBC, EPZ015666 treatment reduced tumour growth by 39%[517]. In glioblastoma models, PRMT5 activity was shown to be enhanced by mTOR inhibition, conferring therapeutic resistance[518]. Following on from this, PRMT5 inhibition by EPZ015666 was shown to sensitize glioblastoma cells to mTOR inhibitors, inducing apoptosis in glioblastoma xenografts. These studies suggest that PRMT5 is a promising therapeutic target in many tumour types. To determine whether these observations may extend to HCC, the potential of EPZ015666 to inhibit hepatocyte hyperplasia and liver enlargement through pharmacological inhibition of PRMT5 was evaluated in the *TO(kras^{G12V})* zebrafish HCC model.

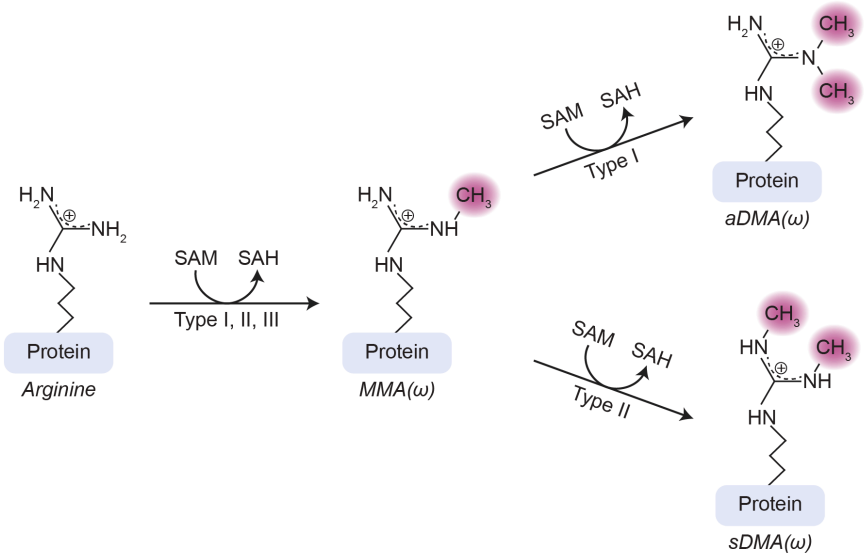

Figure 5.8 Types of protein arginine methylation

Type I, II and III protein arginine methyltransferases (PRMTs) catalyse monomethylarginine (MMA) of nitrogen atoms. Type I PRMTs also catalyse subsequent asymmetric dimethylarginine (aDMA) whereas type II PRMTs catalyse symmetric dimethylarginine (sDMA). PRMT5 is the main type II PRMT. Figure adapted from Yang et al., 2013[504].

SAM: S-adenosyl methionine, SAH: S-adenosyl homocysteine.

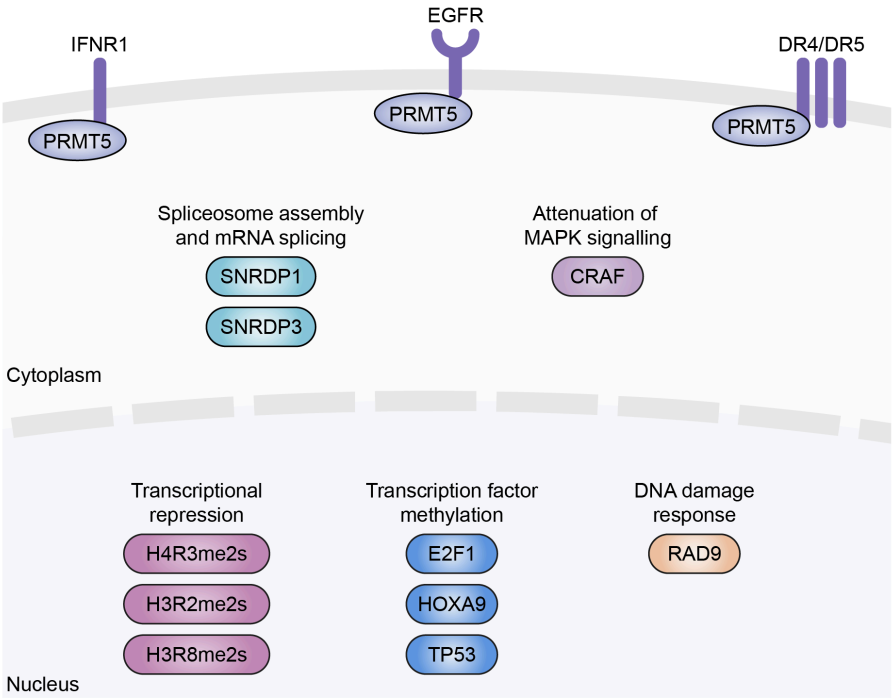

Figure 5.9 PRMT5 has integral roles in regulating diverse cellular processes

PRMT5 plays a pivotal role in mediating diverse cellular processes by methylating a wide spectrum of substrates. At the plasma membrane, PRMT5 can methylate interferon-α receptor 1 (INFR1), epidermal growth factor receptor (EGFR) and the tumour necrosis factor-related apoptosis-inducing ligand (TRAIL) receptors, death receptor 4 (DR4) and DR5.
PRMT5 can also methylate spliceosomal proteins facilitating spliceosome assembly and correct splicing. Additionally, PRMT5 modulates signal transduction pathways, such as attenuating MAPK signalling via methylation of CRAF. Within the nucleus, PRMT5 functions mainly as a transcriptional repressor by methylating histone tails H4R3me2s, H3R2me2s and H3R8me2s. It also directly regulates gene expression by methylation of transcription factors including E2F1, HOXA9 and TP53. Finally, PRMT5 also facilitates DNA repair via methylation of RAD9. Figure adapted from Yang et al., 2013[504].

5.8 Results

5.8.1 EPZ015666 reduces *kras*^{G12V}-driven hepatocyte hyperplasia

Treatment of control *2-CLiP* larvae with 0.01-10.00 µM EPZ015666 from 5 to 7 dpf did not affect normal liver development (Figure 5.10A, B). No reduction in liver volume was observed after EPZ015666 exposure, even at the highest concentration tested (10.00 µM). In contrast, a dose-dependent reduction in liver volume was observed in *TO(kras*^{G12V}*)*$^{T/+}$ larvae (Figure 5.10C). Whilst *kras*^{G12V}-driven hepatocyte hyperplasia was markedly reduced by 78% by treatment with 10.00 µM EPZ015666, liver volume remained slightly larger than that of unaffected livers in *2-CLiP* larvae (Figure 5.10D). This suggests that it may be possible to use still higher doses of EPZ015666 to achieve a complete therapeutic effect without disturbing normal tissues. These results demonstrate that EPZ015666 restricts liver volume selectively in *TO(kras*^{G12V}*)*$^{T/+}$ larvae, suggesting that PRMT5 inhibition could prove to be an effective therapeutic target in HCC.

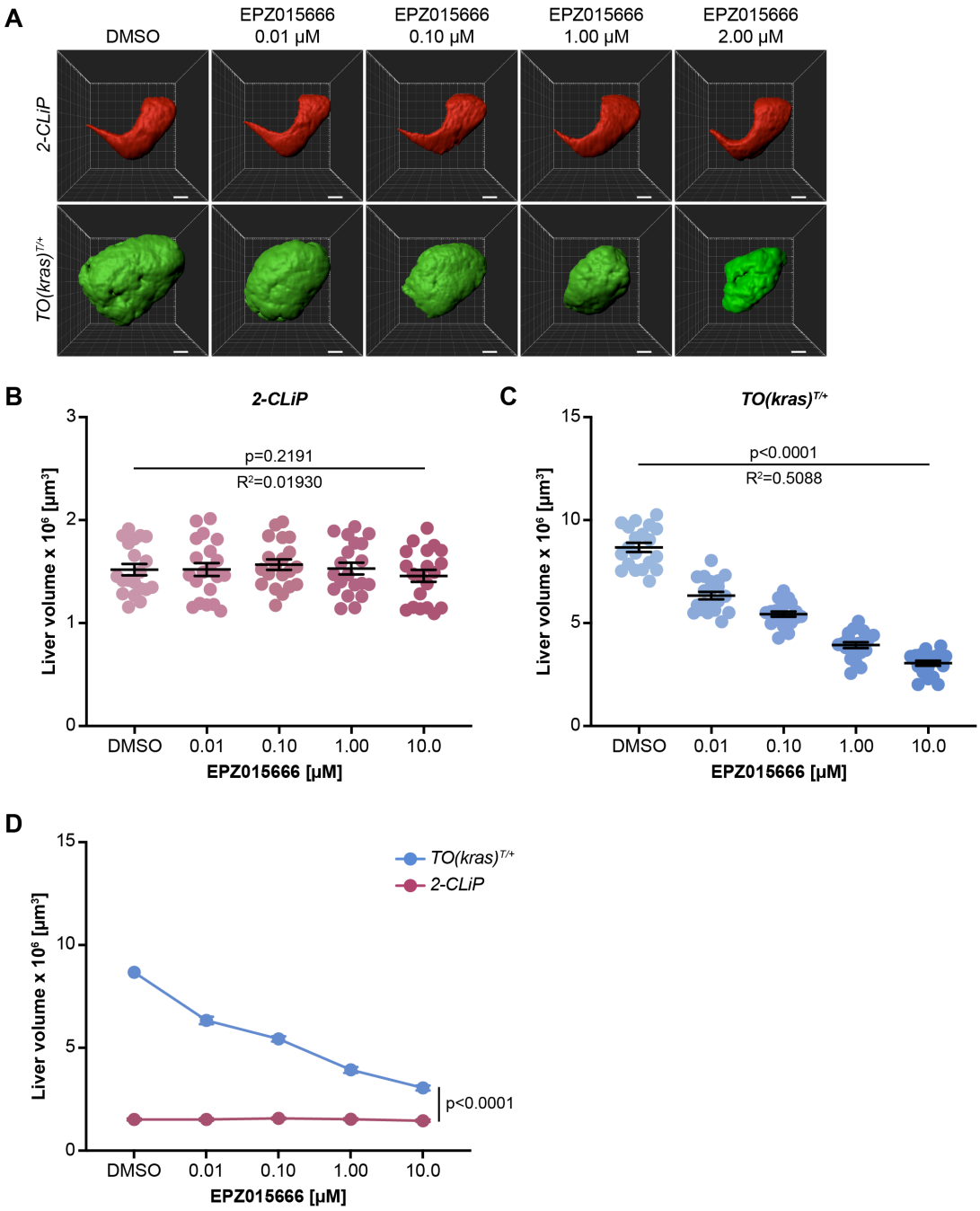

Figure 5.10 EPZ015666 reduces *kras*^{G12V}-driven hepatocyte hyperplasia and liver enlargement

A. Representative three-dimensional reconstructions of *2-CLiP* and *TO(kras*^{G12V}*)*$^{T/+}$ livers treated with DMSO or the indicated concentration of EPZ015666. Scale bar 25 µm. **B.** Liver volume in *2-CLiP* larvae was not impacted by EPZ015666 treatment. **C.** Expression of *TO(kras*^{G12V}*)*$^{T/+}$ significantly increased liver volume compared to *2-CLiP* larvae in the presence of DMSO vehicle. The elevated liver volume was reduced in a dose-dependent manner by EPZ015666 treatment. **D.** Graphical representation of the results shown in panels B-C. Whilst the highest EPZ015666 dose (10.0 µM) markedly reduced *kras*^{G12V}-driven liver enlargement,

liver volume did not quite return to the volume found in *2-CLiP* larvae treated with the same dose of EPZ015666. Data are expressed as mean ± SEM, n=20. Significance was calculated by linear regression analysis.

5.8.2 EPZ015666 restricts DNA replication in *TO(kras^{G12V})$^{T/+}$* hepatocytes

To explore the cause of the reduced liver volume in *TO(kras^{G12V})$^{T/+}$* larvae upon treatment with EPZ015666, cell cycle progression was examined using an EdU incorporation assay to identify cells in S phase (Figure 5.11). Abundant EdU positive cells were observed in the livers of *TO(kras^{G12V})$^{T/+}$* larvae treated with DMSO vehicle control. Treatment with 0.01-10.0 µM EPZ015666 resulted in a dose-dependent reduction in the percentage of EdU positive hepatocytes, with a 67% reduction in S phase cells apparent in larvae treated with 10.0 µM EPZ015666. This suggests that the reduction in liver tumour burden observed in response to EPZ015666 treatment is due, at least in part, to a decrease in the number of cycling cells.

To investigate this mechanism further, mRNA expression levels of the negative cell cycle regulators, *cdkn2a* and *cdkn1a*, were analysed by RT-qPCR analysis on pools of micro-dissected livers (Figure 5.12A,B). In *TO(kras^{G12V})$^{+/+}$* larvae, treatment with 10 µM EPZ015666 did not have an impact on the levels of *cdkn2a/b* and *cdkn1a* expression, which were indistinguishable from the DMSO vehicle controls. In *TO(kras^{G12V})$^{T/+}$* larvae*, cdkn2a/b* expression was increased by 1.4-fold, and this was further enhanced by EPZ015666 treatment. Whilst *cdkn1a* transcript levels were not upregulated by oncogenic *kras^{G12V}* expression*,* EPZ015666 treatment did increase *cdkn1a* levels by 1.8 fold in *TO(kras^{G12V})$^{T/+}$* larvae. Upregulation of these negative cell cycle regulators further supports a mechanism whereby PRMT5 inhibition reduces hepatocyte hyperplasia by decreasing the number of cells in S phase of the cell cycle.

As *cdkn2a* and *cdkn1a* are both direct transcriptional targets of Tp53 and Tp53 plays a central role in the regulation of cell cycle arrest and senescence, mRNA expression levels of *tp53* and the *tp53* isoform *Δ113tp53* were also measured (Figure 5.12C,D). Treatment with 10 µM EPZ015666 did not upregulate expression of *tp53* or *Δ113tp53* in *TO(kras^{G12V})$^{+/+}$* larvae. In contrast, induced expression of *TO(kras^{G12V})$^{T/+}$* increased mRNA transcript levels of both *tp53* and *Δ113tp53* by 2.4-fold and 2.9-fold, respectively. EPZ015666 treatment further augmented expression of *Δ113tp53* in *TO(kras^{G12V})$^{T/+}$* larvae indicating an increase in the transcriptional activity of the Tp53 protein in response to PRMT5 inhibition.

mRNA expression of *mdm2*, the negative regulator and direct transcriptional target of Tp53, was not upregulated by EPZ015666 treatment in *TO(kras^{G12V})$^{+/+}$* larvae (Figure 5.12E), consistent with the observation above that 10 µM of EPZ015666 did not upregulate expression of *Δ113tp53* mRNA in *TO(kras^{G12V})$^{T/+}$* larvae. In contrast, *mdm2* mRNA expression was increased by 1.4-fold in *TO(kras^{G12V})$^{T/+}$* larvae and this was further elevated by EPZ015666 treatment. Taken together, these data indicate that PRMT5 inhibition induces expression of *tp53* and Tp53 target genes, but only in the context of oncogenic stress. This may mean that the restriction in hepatocyte hyperplasia and liver enlargement in *TO(kras^{G12V})$^{T/+}$* larvae as a result of impaired PRMT5 function elicits a Tp53-mediated DNA damage response. This would be along the same lines as the mechanism proposed for the genetic effect of *ahctf1* and *rnpc3*

heterozygosity in this model, whereby in oncogene-expressing cells, DNA damage induces elevated levels of Tp53 protein and expression of its target genes, including *cdkn1a* and *cdkn2a/b* which together promote cell cycle arrest.

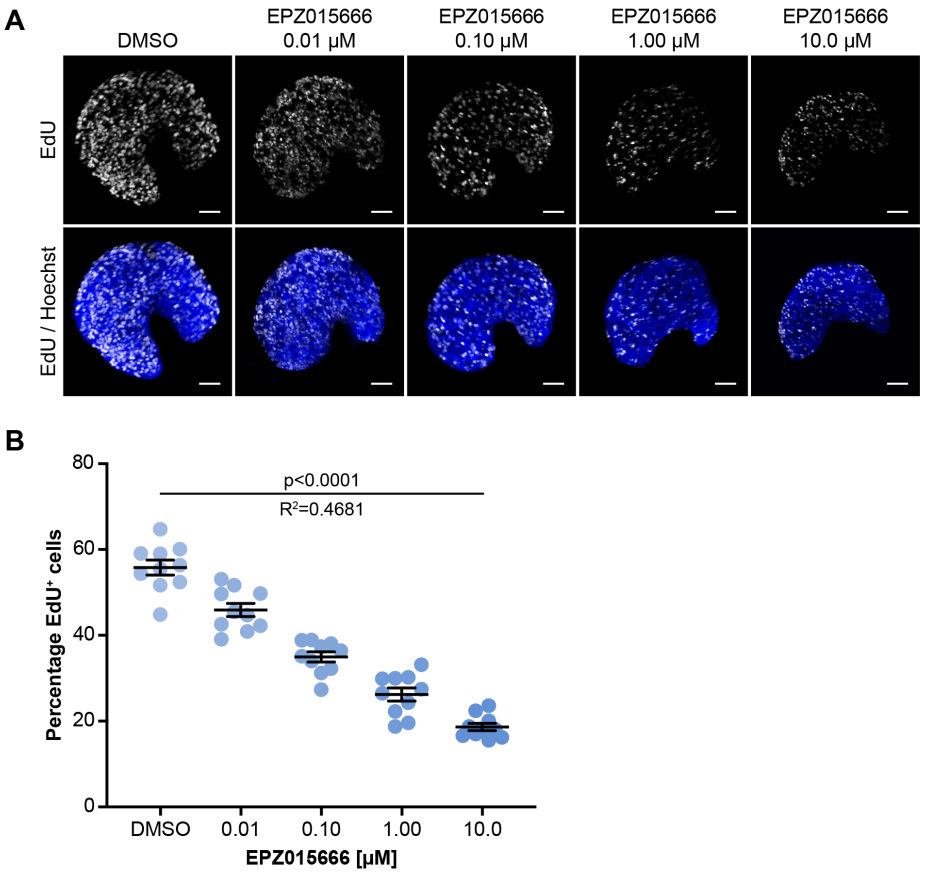

Figure 5.11 EPZ015666 treatment restricts the percentage of *TO(kras^{G12V})$^{T/+}$* hepatocytes in S phase of the cell cycle

A. Representative maximum intensity projection images of EdU incorporation throughout *TO(kras^{G12V})$^{T/+}$* livers treated with DMSO or the indicated concentration of EPZ015666. Scale bar 25 µm. **B.** Quantification of the percentage of Hoechst 33342 positive nuclei containing fluorescent EdU puncta showing DNA replication. EPZ015666 treatment significantly reduces the percentage of EdU positive nuclei. Data are expressed as mean ± SEM, n=10. Significance was calculated by linear regression analysis.

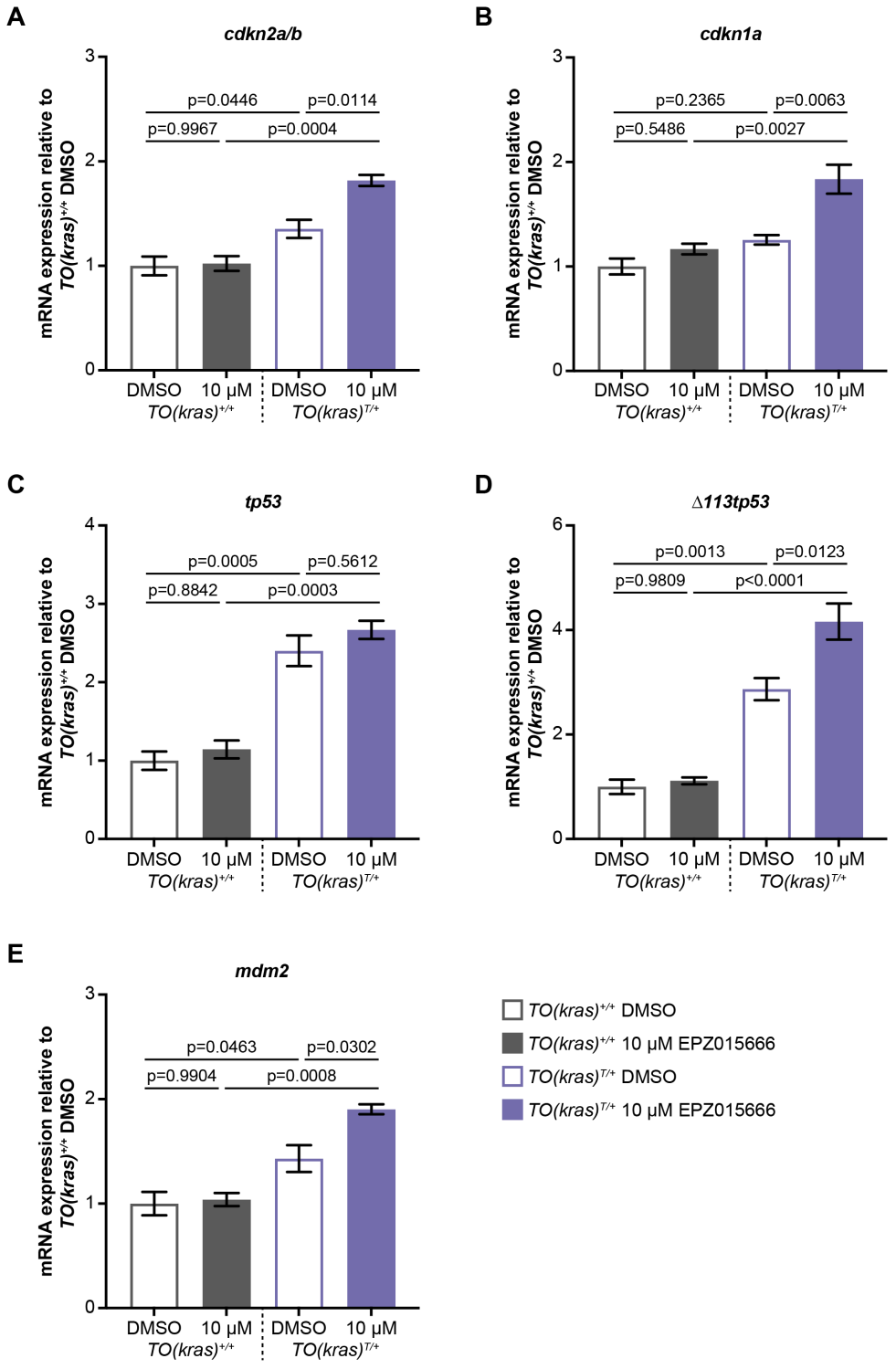

Figure 5.12 EPZ015666 treatment induces expression of Tp53 target genes in *TO(kras^{G12V})$^{T/+}$* larvae

RT-qPCR analysis of pooled micro-dissected livers from *TO(kras^{G12V})$^{+/+}$* and *TO(kras^{G12V})$^{T/+}$* larvae treated with DMSO or 10 μM EPZ015666 from 5 to 7 dpf. **A,B.** Expression of *cdkn2a/b,* and *cdkn1a* was not affected by EPZ015666 treatment in *TO(kras^{G12V})$^{+/+}$* larvae. In contrast,

the transcript levels of *cdkn2a/b* in *TO(kras^{G12V})$^{T/+}$* larvae were upregulated compared to those in *TO(kras^{G12V})$^{+/+}$* larvae treated with DMSO and this was further augmented by EPZ015666 treatment. *cdkn1a* expression was also elevated by EPZ015666 treatment in *TO(kras^{G12V})$^{T/+}$* larvae. **C,D.** Expression of *tp53* and *Δ113tp53* were not affected by EPZ015666 treatment in *TO(kras^{G12V})$^{+/+}$* larvae. Induced *TO(kras^{G12V})$^{T/+}$* expression resulted in upregulation of both *tp53* and *Δ113tp53* levels. *Δ113tp53* expression was further increased by EPZ015666 treatment. **E.** Similarly, *mdm2* expression was not altered by EPZ015666 treatment in *TO(kras^{G12V})$^{+/+}$* larvae. *mdm2* transcript levels were increased in *TO(kras^{G12V})$^{T/+}$* larvae and this was further augmented by EPZ015666 treatment. Data are expressed as mean ± SEM, n=3 biological replicates. Significance was calculated using a one-way ANOVA with Tukey's multiple comparisons test.

5.9 Novel inhibitors of histone acetyltransferases KAT6A/B

KAT6A/B (lysine acetyltransferase 6A/B) are members of the MYST family of histone acetyltransferases which catalyse the transfer of acetyl groups onto lysine residues of histones. Acetylation of histones regulates chromatin structure and assembly, which in turn impacts gene expression (Figure 5.13)[519]. KAT6A/B is found in a histone acetylation complex with ING5 (inhibitor of growth 5), one of BRPF1/2/3 (bromodomain and PHD finger containing 1/2/3) and EAF6 (Esa1-associated factor 6)[520]. KAT6A was originally discovered as part of an oncogenic fusion protein with the CREB-binding protein (CBP), which was generated by a chromosomal translocation that frequently occurs in AML[521]. Subsequently, KAT6B was identified on the basis of its structural and functional homology to KAT6A and found to occur in chromosomal translocations in a range of tumour types[522,523]. KAT6A is essential for the maintenance of hematopoietic stem cells[524-526], inhibiting senescence through repression of the *CDKN2A* locus to preserve stem cell proliferation[527,528]. *Kat6a* heterozygosity dramatically extends survival in a mouse model of lymphoma by 3.9-fold (from 105 days to 413 days)[529]. These studies, which suggest that inhibition of KAT6A/B represents a promising therapeutic target for cancer treatment, motivated a high-throughput chemical screen to identify pharmacological inhibitors of KAT6A/B performed by collaborators, Professor Anne Voss and Assoc Prof Tim Thomas, at WEHI. From a screen of 243,000 compounds and subsequent medicinal chemistry optimisation, WM-8014 was identified as a highly potent inhibitor of KAT6A/B that induces senescence *in vitro* and *in vivo* in a mouse model of lymphoma[218]. As part of this publication in *Nature*, I investigated the effects of WM-8014 in the *TO(kras^{G12V})* zebrafish HCC model.

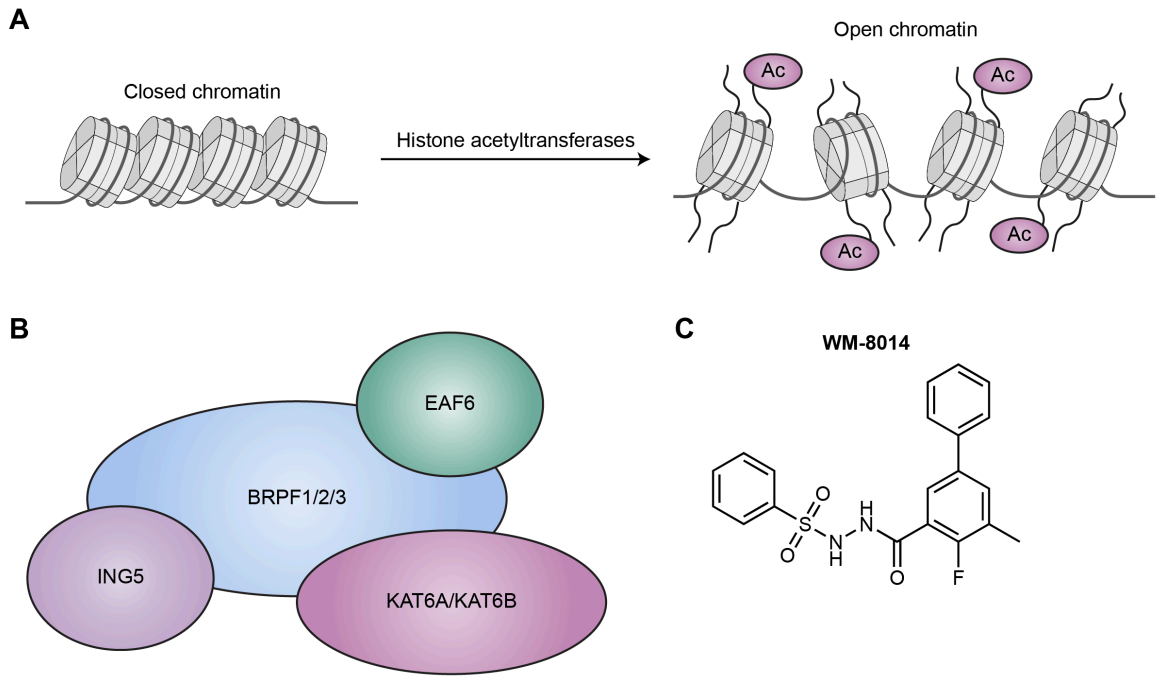

Figure 5.13 KAT6A/B catalyses histone acetylation

A. Histone acetyltransferases, such as KAT6A/B catalyse the transfer of an acetyl group to histone lysine residues. This impacts chromatin organisation and structure, generally resulting in a more open chromatin conformation and increased expression of corresponding gene loci. **B.** Schematic representation of the KAT6A/B histone acetylation complex consisting of KAT6A/B (lysine acetyl transferase 6A/B), ING5 (inhibitor of growth 5), BRPF1/2/3 (bromodomain and PHD finger containing 1/2/3) and EAF6 (Esa1-associated factor 6). **C.** Structure of WM-8014 a potent inhibitor of KAT6A/B discovered in a high-throughput chemical screen[218].

5.10 Results

5.10.1 WM-8014 reduces *kras*^{G12V}-driven hepatocyte hyperplasia

Treatment of control *2-CLiP* larvae with 10 µM WM-2474, an inactive analogue compound of WM-8014, from 5 to 7 dpf did not affect normal liver development compared with DMSO vehicle controls (Figure 5.14A, B). Similarly, treatment with 1.0-10 µM WM-8014 did not impact on liver volume in *2-CLiP* larvae. In contrast, a dose-dependent reduction in liver volume was observed in *TO(kras*^{G12V}*)*$^{T/+}$ larvae (Figure 5.14C). Whilst *kras*^{G12V}-driven hepatocyte hyperplasia was significantly reduced by 50% in response to treatment with 10 µM WM-8014, liver volume remained greater than that observed in *2-CLiP* larvae (Figure 5.14D). To determine whether an improved therapeutic effect could be achieved without causing toxicity, the response to higher concentrations of WM-8014 should be investigated. These results demonstrate that WM-8014 restricts liver volume specifically in *TO(kras*^{G12V}*)*$^{T/+}$ larvae, suggesting that KAT6A/B inhibition may be an effective therapeutic target in HCC.

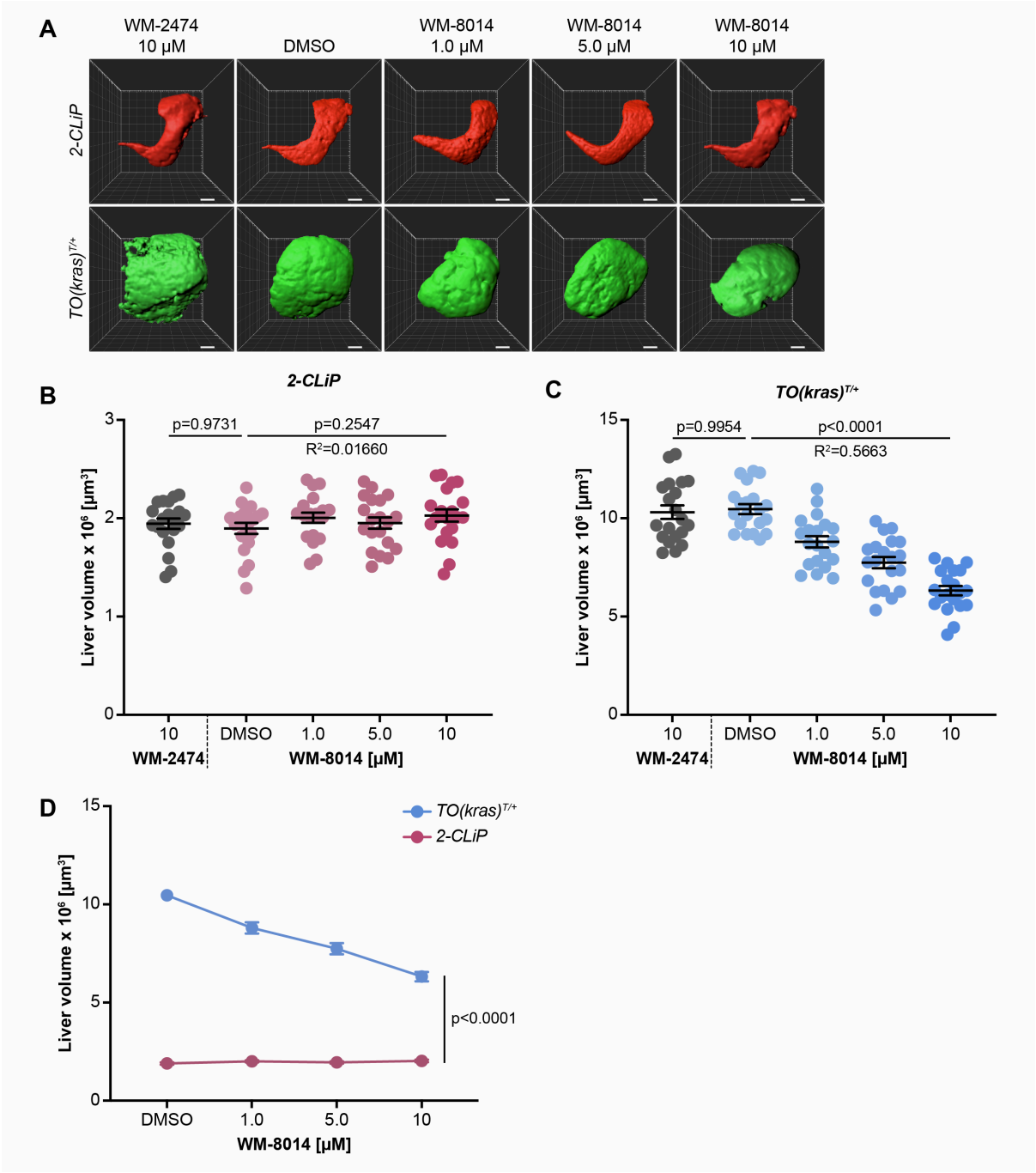

Figure 5.14 WM-8014 reduces *kras*^{G12V}-driven hepatocyte hyperplasia

A. Representative three-dimensional reconstructions of *2-CLiP* and *TO(kras*^{G12V}*)*$^{T/+}$ livers treated with 10 µM inactive compound WM-2474, DMSO or the indicated concentration of WM-8014. Scale bar 25 µm. **B.** Liver volume in *2-CLiP* larvae was not impacted by WM-2474 or WM-8014 treatment. **C.** Liver volume in *TO(kras*^{G12V}*)*$^{T/+}$ larvae was reduced in a dose-dependent manner by WM-8014 treatment. **D.** Graphical representation of the results shown in panels B-C. Expression of *TO(kras*^{G12V}*)*$^{T/+}$ significantly increased liver volume compared to *2-CLiP* larvae in the presence of DMSO vehicle. Whilst 10 µM WM-8014 treatment reduced *kras*^{G12V}-driven hepatocyte hyperplasia, liver volume was not restored to that in *2-CLiP* larvae

at a 10 μM dose of WM-8014. Data are expressed as mean ± SEM, n=20. Significance was calculated by linear regression analysis or by one-way ANOVA with Tukey's multiple comparisons test.

5.10.2 WM-8014 potentiates oncogene-induced senescence

As KAT6A functions to inhibit senescence[527,528], the ability of WM-8014 to induce cell cycle arrest in *TO(kras^{G12V})$^{T/+}$* hepatocytes was assessed using EdU incorporation to identify cells undergoing DNA replication in S phase (Figure 5.15A,B). In the absence of doxycycline, when no oncogenic Kras^{G12V} is expressed, ~4% of hepatocytes were positive for EdU and this was not impacted by WM-8014 treatment. Meanwhile, the percentage of S phase cells increased over 10-fold in Kras^{G12V}-driven livers, and this was maintained when Kras^{G12V}-driven livers were treated with the inactive analogue compound WM-2474. Treatment with WM-8014 substantially reduced the number of cycling cells by 54%. These results suggest a mechanism whereby KAT6A/B inhibition reduces hepatocyte hyperplasia and liver volume by inducing cell cycle arrest.

To investigate this further, the transcript expression levels of cell cycle regulators *cdkn2a/b* and *cdkn1a* were analysed by RT-qPCR analysis on pools of micro-dissected livers (Figure 5.16). In comparison to treatment with the inactive compound WM-2474, treatment with WM-8014 robustly upregulated *cdkn2a/b* and *cdkn1a* expression by 5.9-fold and 4.8-fold respectively, in *TO(kras^{G12V})$^{T/+}$* larvae exposed to doxycycline. Importantly, this increased expression was specific to hepatocytes expressing oncogenic Kras^{G12V} and not *TO(kras^{G12V})$^{T/+}$* hepatocytes that did not receive doxycycline. These data demonstrate that WM-8014 potentiates oncogene-induced senescence but does not impact on normal hepatocyte growth. Therefore, KAT6A/B inhibition holds great potential as an effective treatment for cancer.

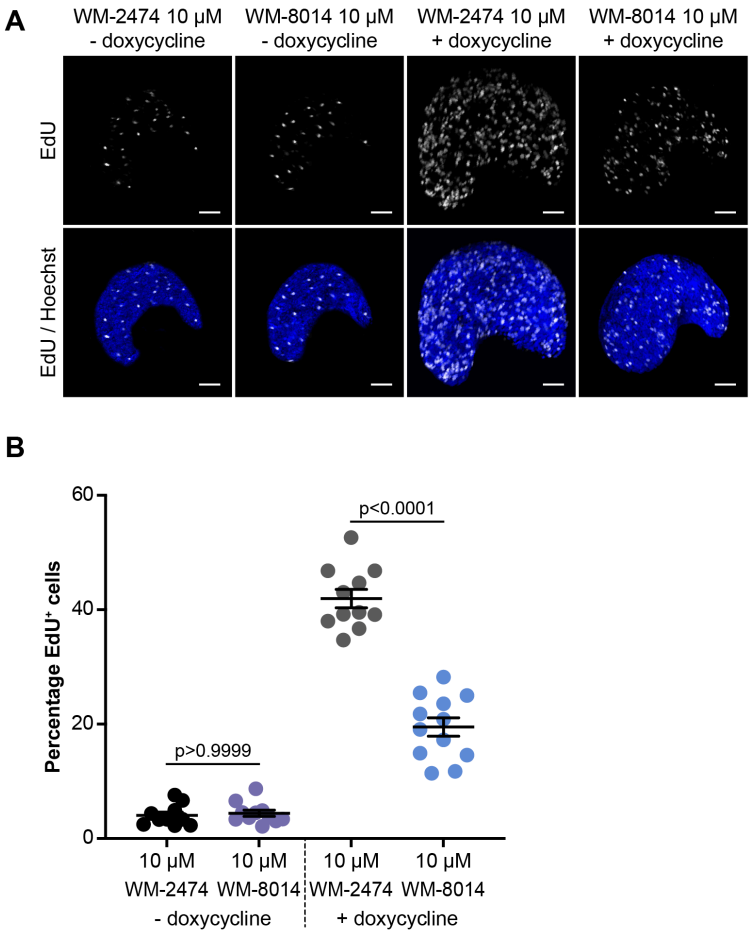

Figure 5.15 WM-8014 treatment reduces the percentage of *TO(kras^{G12V})$^{T/+}$* hepatocytes in S phase of the cell cycle

A. Representative maximum intensity projection images of EdU incorporation throughout *TO(kras^{G12V})$^{T/+}$* livers treated with 10 µM inactive compound WM-2474 or active compound WM-8014 in the absence or presence of doxycycline as indicated. Scale bar 25 µm. **B.** Quantification of the percentage of Hoechst 33342 positive nuclei containing fluorescent EdU puncta showing cells in S phase undertaking DNA replication. Doxycycline-induced expression of oncogenic Kras^{G12V} substantially increased the abundance of cycling cells. However, this was markedly mitigated by WM-8014 treatment, which significantly reduced the percentage of EdU positive nuclei. Data are expressed as mean ± SEM, n≥10. Significance was calculated by one-way ANOVA with Tukey's multiple comparisons test.

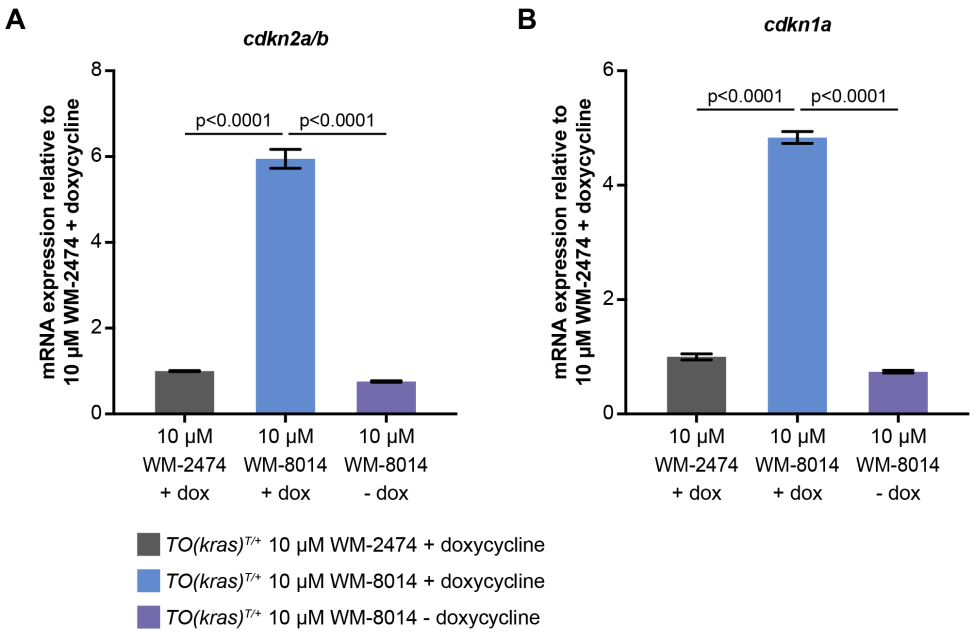

Figure 5.16 WM-8014 treatment induces expression of cell cycle regulators in *TO(kras^{G12V})$^{T/+}$* larvae

RT-qPCR analysis of pooled micro-dissected livers from *TO(kras^{G12V})$^{T/+}$* larvae treated with 10 µM active compound WM-8014 or inactive compound WM-2474 in the absence or presence of doxycycline as indicated. **A,B.** In *TO(kras^{G12V})$^{T/+}$* larvae exposed to doxycycline, treatment with 10 µM WM-8014 significantly upregulated expression of *cdkn2a/b* and *cdkn1a* compared to the inactive control compound, WM-2474. Notably, increased expression of *cdkn2a/b* and *cdkn1a* transcripts was not observed upon WM-8014 treatment in larvae not exposed to doxycycline and is therefore dependent on hepatocyte expression of oncogenic Kras^{G12V}. Data are expressed as mean ± SEM, n=4-5 biological replicates. Significance was calculated using a one-way ANOVA with Tukey's multiple comparisons test.

5.11 A novel inhibitor of U12-dependent splicing

As discussed in chapter 4 of this thesis, U12-dependent splicing represents a promising target for therapeutic inhibition of many cancers. Using a variety of genetically engineered mouse models of cancer, the Heath lab has demonstrated that reducing *rnpc3* expression genetically is effective at inhibiting tumour growth in lung and gastric adenocarcinoma, lymphoma and acute myeloid leukemia, without causing toxicity in normal tissues (Doggett et al., manuscript submitted). These *in vivo* genetic data provided the impetus to identify a small molecule inhibitor of U12-dependent splicing that could be used in a therapeutic context for a broad spectrum of malignancies.

To achieve this, a cell-based splicing reporter assay was developed by Dr. Stephen Mieruszynski in the Heath lab for the purpose of conducting a high-throughput chemical screen. He designed a luciferase splicing reporter construct, which was stably installed in HEK293 (Human Embryonic Kidney) cells, capable of distinguishing inhibitors of U2-dependent and U12-dependent splicing or pan-splicing inhibitors (Figure 5.17). A primary chemical screen of 270,000 compounds initially yielded ~3,400 potentially promising compounds, which were tested for their selectivity for U12-dependent splicing in a counter screen designed to eliminate false positives. This secondary screen was based on a different HEK293 cell line, which harboured a similar DNA construct except that the U2-dependent and U12-dependent introns were inserted in the opposite luciferase genes. In particular, this strategy eliminated compounds that interacted with the luciferase enzymes directly. This was a very important control, since the screen ultimately yielded only one *bona fide* hit compound (Hit 1) that selectively inhibited U12-dependent splicing *in vitro*. The structure of Hit 1 is not provided in this thesis for intellectual property reasons. Whilst target validation and medicinal chemistry studies are ongoing, the impact of the Hit 1 compound was evaluated in the *TO(kras^{G12V})* zebrafish HCC model.

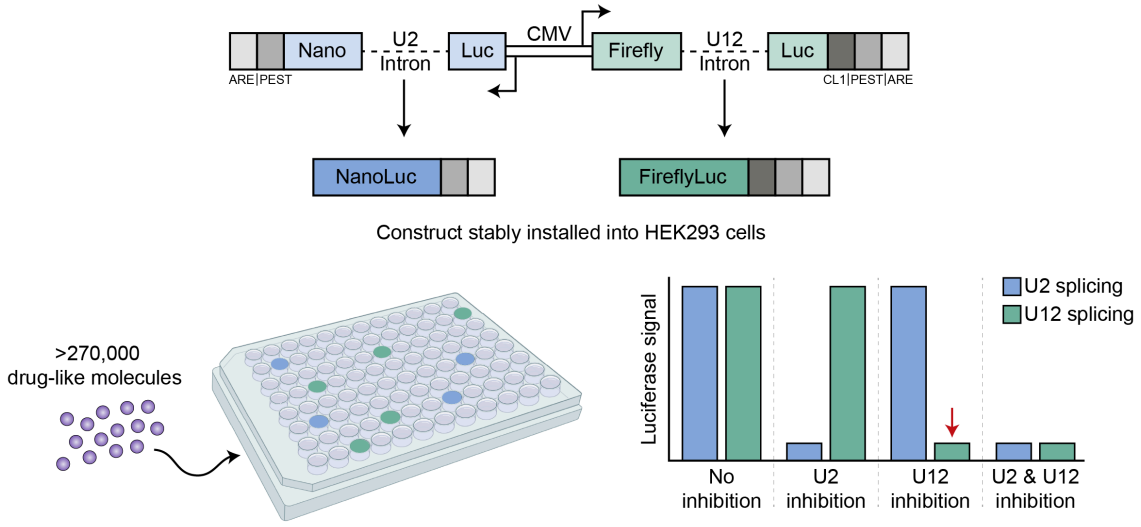

Figure 5.17 Design of a high-throughput chemical screen to identify inhibitors of U12-dependent splicing

A dynamic luciferase splicing reporter assay was designed with the purpose of identifying and distinguishing between small molecule inhibitors of U2-dependent and U12-dependent splicing. A DNA construct was created comprising a bidirectional CMV promoter driving expression of NanoLuc and FireflyLuc cDNAs interrupted by similarly sized (~750 bp) U2-dependent and U12-dependent introns from the BRAF gene. Regulatory elements (CL1, ARE and PEST) were introduced after the luciferase coding sequences to ensure rapid turnover of the encoded mRNAs and protein. This construct was stably installed in HEK293 cells which were then screened against more than 270,000 compounds. A decrease in the ratio of the FireflyLuc:NanoLuc signal (red arrow) indicated potential selective inhibitors of U12-dependent splicing, which were then re-tested in a counter screen where the U2-dependent and U12-dependent introns were placed in the opposite luciferase genes. Other luciferase signal readouts indicated that the compounds had either no effect on splicing or were selective inhibitors of U2-dependent splicing or pan-splicing inhibitors.

Figure courtesy of Dr Stephen Mieruszynski, Heath lab.

ARE: AU-rich elements, CL1: CL1 degron, CMV: cytomegalovirus, Luc: luciferase, PEST: proline, glutamic acid, serine and threonine.

5.12 Results

5.12.1 Hit 1 reduces *kras*^{G12V}-driven hepatocyte hyperplasia

Treatment of control *2-CLiP* larvae with 0.5-5.0 µM Hit 1 from 5 to 7 dpf did not affect normal liver development (Figure 5.18A, B). No reduction in liver volume was observed after Hit 1 exposure, even at the highest concentration tested (5.0 µM). In contrast, a dose-dependent reduction in liver volume was observed in *TO(kras*^{G12V}*)*$^{T/+}$ larvae (Figure 5.18C). Whilst *kras*^{G12V}-driven hepatocyte hyperplasia and excess liver volume was significantly reduced by 62% by treatment with 5.0 µM Hit 1, liver volume at the end of the experiment was significantly greater than the volume of the livers in *2-CLiP* larvae at 7 dpf (Figure 5.18D). These results demonstrate that Hit 1 restricts liver volume selectively in *TO(kras*^{G12V}*)*$^{T/+}$ larvae, suggesting that U12-dependent splicing inhibition may be an effective therapeutic target in HCC.

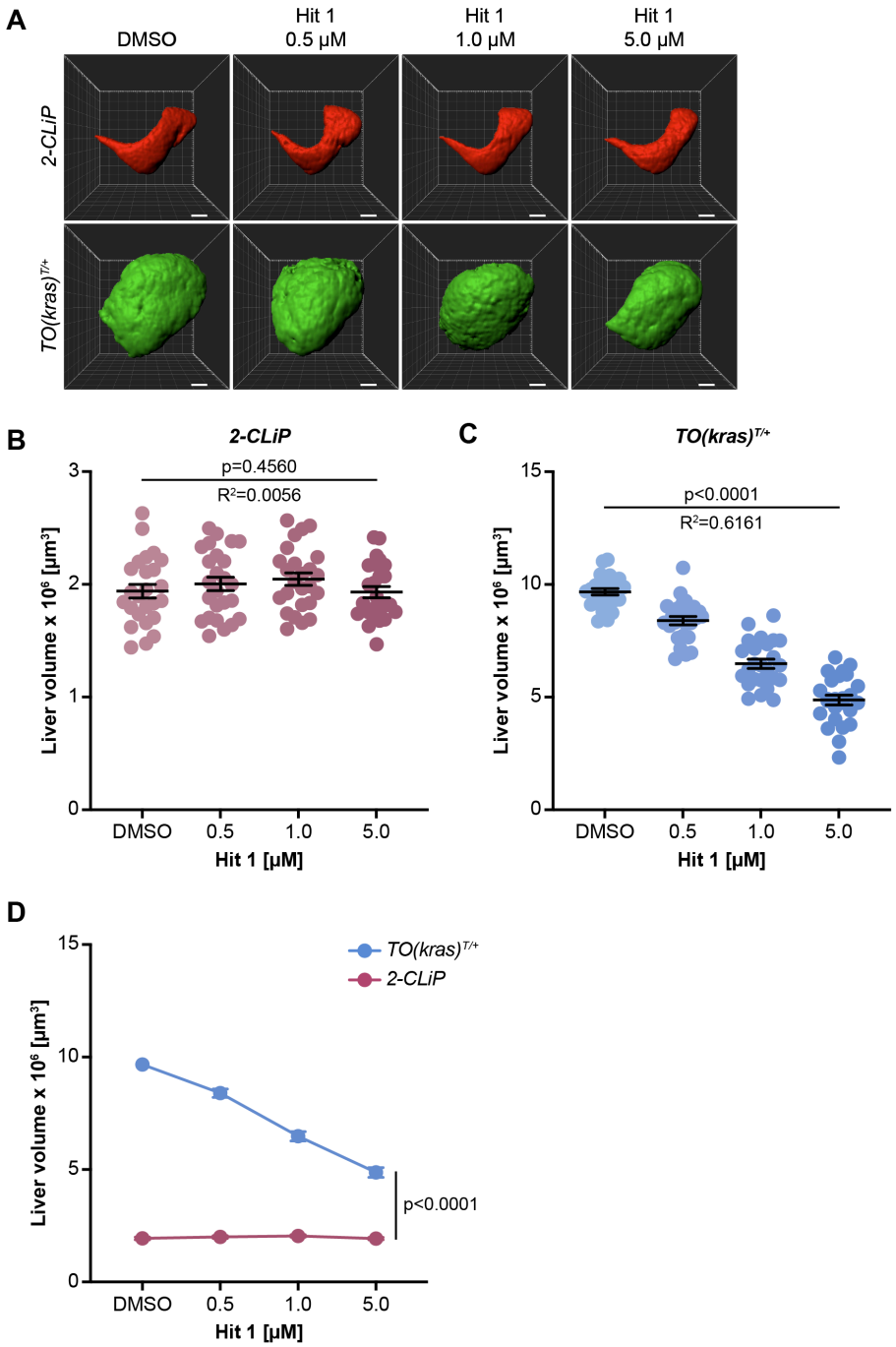

Figure 5.18 Hit 1 reduces *kras*^{G12V}-driven hepatocyte hyperplasia

A. Representative three-dimensional reconstructions of *2-CLiP* and *TO(kras*^{G12V}*)*$^{T/+}$ livers treated with DMSO or the indicated concentration of Hit 1. Scale bar 25 µm. **B.** Liver volume in *2-CLiP* larvae was not impacted by Hit 1 treatment. **C.** Liver volume in *TO(kras*^{G12V}*)*$^{T/+}$ larvae was reduced in a dose-dependent manner by Hit 1 treatment. **D.** Graphical representation of the results shown in panels B-C. Expression of *TO(kras*^{G12V}*)*$^{T/+}$ significantly increased liver volume compared to *2-CLiP* larvae in the presence of DMSO vehicle. Whilst Hit 1 treatment reduced *kras*^{G12V}-driven hepatocyte hyperplasia, liver volume was significantly higher than

that in *2-CLiP* larvae receiving a 5.0 µM dose of Hit 1. Data are expressed as mean ± SEM, n=25. Significance was calculated by linear regression analysis.

5.12.2 Hit 1 does not impact transcription of the *EGFP-kras^{G12V}* construct in *TO(kras^{G12V})$^{T/+}$* hepatocytes

One possibility that could account for the reduction in hepatocyte hyperplasia and liver volume observed in Hit 1 treated *TO(kras^{G12V})$^{T/+}$* larvae is that the Hit 1 compound interferes with the transcription of the oncogenic *EGFP-kras^{G12V}* transgene construct, for instance by inhibiting the action of doxycycline. To examine if this was occurring, RT-qPCR analysis using primers designed to amplify *EGFP* was performed on pools of micro-dissected livers. Treatment of *TO(kras^{G12V})$^{T/+}$* larvae with 0.5-5.0 µM Hit 1 from 5-7 dpf did not impact *EGFP-kras^{G12V}* mRNA expression compared to that of DMSO treated *TO(kras^{G12V})$^{T/+}$* larvae (Figure 5.19). This suggests that treatment with Hit 1 does not impact transcription of the *EGFP-kras^{G12V}* transgene and that restricted liver enlargement is not due to decreased oncogene transcription.

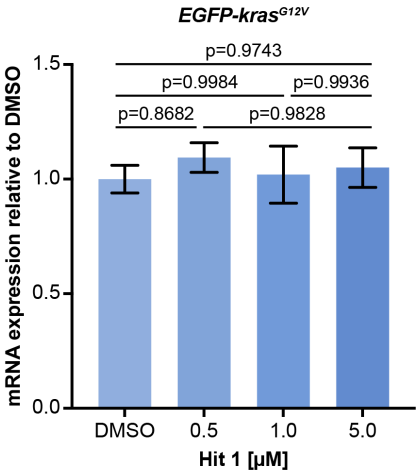

Figure 5.19 Treatment with Hit 1 does not impact transcription of the *EGFP-kras^{G12V}* construct in *TO(kras^{G12V})$^{T/+}$* hepatocytes

RT-qPCR analysis of pooled micro-dissected liver from *TO(kras^{G12V})$^{T/+}$* larvae treated with DMSO or 0.5-5.0 µM Hit 1 from 5 to 7 dpf. Primers were designed to amplify the *EGFP* portion of the *EGFP-kras^{G12V}* construct. Expression of *EGFP-kras^{G12V}* was not affected by Hit 1 treatment in *TO(kras^{G12V})$^{T/+}$* larvae. Data are expressed as mean ± SEM, n=2 biological replicates. Significance was calculated using a one-way ANOVA with Tukey's multiple comparisons test.

5.12.3 RNA-sequencing of Hit 1 treated *TO(kras^{G12V})* hepatocytes

To further investigate the mechanism by which Hit 1 reduced hepatocyte hyperplasia, I performed RNA-sequencing on individual 7 dpf micro-dissected livers to profile transcriptome-wide differences in mRNA levels between *TO(kras^{G12V})$^{T/+}$* hepatocytes treated with 5 µM Hit 1 from 5-7 dpf and *TO(kras^{G12V})$^{T/+}$* hepatocytes treated with a structurally similar but inactive compound. I extracted total RNA from individual livers and used 100 ng per sample to generate sequencing libraries using the TruSeq RNA Sample Prep Kit with Ribo-Zero depletion (Illumina). For further details, refer to Chapter 2.5.5. Following Next Seq sequencing, differential expression analysis was performed by Dr. Alexandra Garnham of the WEHI Bioinformatics Support Unit (Figure 5.20). Using a false discovery rate of (FDR) cut off of less than 0.05, treatment with Hit 1 resulted in upregulation of 478 genes and downregulation of 551 genes compared to Inactive compound treated hepatocytes. In a multi-dimension scaling plot, the samples segregated by treatment, indicating similarities between samples of the same treatment group. The top 20 upregulated and downregulated genes, ranked by significance, are shown in Table 5.1 and Table 5.2, respectively.

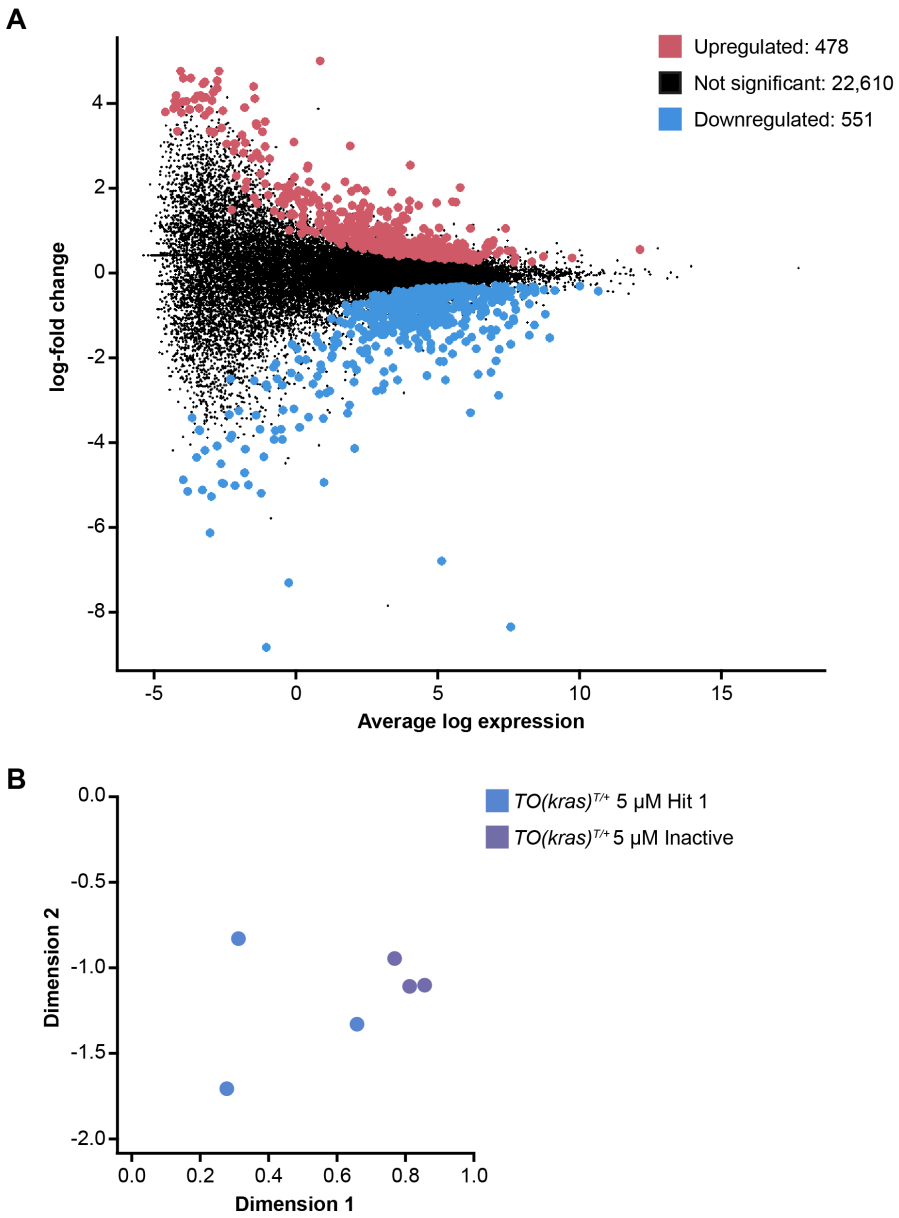

Figure 5.20 RNA-sequencing of *TO(kras^{G12V})* hepatocytes to understand the effects of Hit 1 treatment on transcriptome-wide mRNA levels in *TO(kras^{G12V})$^{T/+}$* hepatocytes

A. Mean difference plot of differentially expressed genes between *TO(kras^{G12V})$^{T/+}$* 5 µM Hit 1 treated vs. *TO(kras^{G12V})$^{T/+}$* 5 µM Inactive compound treated samples. Each point represents the average expression of a gene (x axis) against its log-fold change (y-axis). Red dots indicate genes that are significantly upregulated in Hit 1 treated *TO(kras^{G12V})$^{T/+}$* hepatocytes and blue dots represent genes that are significantly downregulated in Hit 1 treated *TO(kras^{G12V})$^{T/+}$* hepatocytes based on FDR<0.05. Black dots represent expression levels of genes that are not statistically different between Hit 1 treated and Inactive compound controls. **B.** Multi-dimensional scaling plot showing segregation of Hit 1 treated *TO(kras^{G12V})$^{T/+}$* and Inactive compound treated *TO(kras^{G12V})$^{T/+}$* samples, n=3.

Table 5.1 Top 20 upregulated genes in Hit 1 treated *TO(kras^{G12V})$^{T/+}$* hepatocytes compared to Inactive compound treated *TO(kras^{G12V})$^{T/+}$* hepatocytes

Gene	Log fold change	Average expression	False discovery rate
si:ch73-112l6.1	1.50	3.98	3.80E-09
klb	1.26	3.76	1.80E-06
abcg5	1.36	3.80	2.89E-06
si:dkey-22i16.7	3.00	1.91	3.06E-06
sccpdha.1	1.35	2.25	3.28E-06
CABZ01088484.1	1.70	4.01	5.29E-06
il20ra	1.46	3.24	8.50E-06
rps27l	0.84	5.33	1.44E-05
zgc:175280	2.53	0.42	2.26E-05
pde6b	2.46	0.39	2.44E-05
abcg8	1.45	2.98	3.59E-05
cdhr5b	2.15	1.72	4.36E-05
tmcc3	0.81	4.94	4.39E-05
zgc:92380	1.59	1.98	6.07E-05
BX248515.1	1.35	2.31	6.17E-05
tsku	0.81	3.75	6.83E-05
FADS6	1.11	3.63	9.28E-05
FP016106.1	1.74	1.46	9.28E-05
dapk2a	1.23	2.43	9.52E-05
polr2m	0.86	3.32	0.000122

Table 5.2 Top 20 downregulated genes in Hit 1 treated *TO(kras^{G12V})$^{T/+}$* hepatocytes compared to Inactive compound treated *TO(kras^{G12V})$^{T/+}$* hepatocytes

Gene	Log fold change	Average expression	False discovery rate
hist1h2ba	-1.51	5.59	3.80E-09
zgc:114046	-1.59	5.42	3.83E-08
zgc:112234	-1.40	4.60	4.85E-08
FP236812.1	-1.77	5.19	1.59E-07
CR354435.1	-1.32	3.96	5.76E-07
zgc:112234	-1.16	5.40	5.76E-07
gadd45ba	-2.09	5.07	1.31E-06
zgc:173587	-1.66	4.75	1.63E-06
ier2a	-1.33	6.89	1.81E-06
zgc:112234	-1.68	3.94	3.06E-06
FP236812.2	-1.51	4.61	3.06E-06
csrnp1b	-1.44	5.79	3.06E-06
si:dkey-23a13.22	-1.29	4.36	3.06E-06
zgc:112234	-1.23	5.29	3.06E-06
si:dkey-261m9.6	-1.05	4.92	3.06E-06
zgc:112234	-0.93	5.97	3.28E-06
zgc:171759	-1.50	4.62	3.94E-06
sema3ga	-2.53	3.58	5.29E-06
arl4ab	-1.64	4.32	5.29E-06
zgc:112234	-1.17	3.86	5.29E-06

To understand if the differentially expressed genes (DEGs) shared common functions, KEGG pathway analysis was performed. The significantly upregulated and downregulated KEGG pathways, ranked by significance, are shown in Table 5.3 and Table 5.4, respectively. ABC transporters were the most upregulated pathway in Hit 1 treated *TO(kras^{G12V})$^{T/+}$* hepatocytes, which may suggest a drug export response. Multiple components of DNA replication and cell cycle pathways were significantly downregulated (Figure 5.21-5.22), suggesting that treatment with Hit 1 restricts proliferation. Notably, MAPK signalling was also downregulated, indicating that Hit 1 treatment is effective at suppressing oncogenic Kras^{G12V} signalling cascades (Figure 5.23). Of particular interest, expression of *kras* itself is significantly downregulated by log -1.53 fold. In addition, other pro-proliferation genes *mycb*, *juna* and *junb* are also significantly downregulated in Hit 1 treated *TO(kras^{G12V})$^{T/+}$* hepatocytes, compared to Inactive compound treated *TO(kras^{G12V})$^{T/+}$* hepatocytes. Moreover, several *dusp* genes, encoding dual-specificity phosphatases including *dusp1, dusp2* and *dusp5,* which are targets of MAPK signalling, are also downregulated. Collectively, these alterations in gene expression suggest that Hit 1 has a robust anti-proliferative effect.

Further analysis of these RNA-sequencing data is required to determine the impact and selectivity of Hit 1 treatment on the expression of genes containing U12-dependent introns. These analyses are being undertaken by our collaborators, Dr. Anouk Olthof and Assoc Prof. Rahul Kanadia at the University of Connecticut. These collaborators are experts in U12-dependent splicing analysis and have developed pipelines to detect different types of aberrant splicing such as intron retention, exon skipping and alternative 5' and 3' splice site usage[530,531]. Such analysis will determine whether the beneficial effects of reducing tumour burden observed in my zebrafish HCC model were achieved by Hit 1 acting as a selective U12-dependent splicing inhibitor.

Collectively, the data assembled so far strongly support ongoing investigation of the Hit 1 compound with the goal of determining its suitability for drug development.

Table 5.3 Upregulated KEGG pathways in Hit 1 treated *TO(kras^{G12V})$^{T/+}$* hepatocytes compared to Inactive compound treated *TO(kras^{G12V})$^{T/+}$* hepatocytes

KEGG pathway	P-value
ABC transporters	5.04E-05
Glycosphingolipid biosynthesis - lacto and neolacto series	1.32E-03
Lysosome	5.02E-03
Glycosaminoglycan biosynthesis - keratan sulfate	9.69E-03
N-Glycan biosynthesis	3.16E-02

Table 5.4 Downregulated KEGG pathways in Hit 1 treated *TO(kras^{G12V})$^{T/+}$* hepatocytes compared to Inactive compound treated *TO(kras^{G12V})$^{T/+}$* hepatocytes

KEGG pathway	P-value
Necroptosis	4.12E-09
DNA replication	1.64E-06
Cell cycle	1.32E-04
Base excision repair	1.35E-03
Mismatch repair	1.48E-03
Apoptosis	1.87E-03
Ferroptosis	8.06E-03
Glutathione metabolism	9.38E-03
Arginine and proline metabolism	1.51E-02
MAPK signaling pathway	1.67E-02
Regulation of actin cytoskeleton	2.14E-02
Purine metabolism	2.43E-02
Cellular senescence	2.44E-02

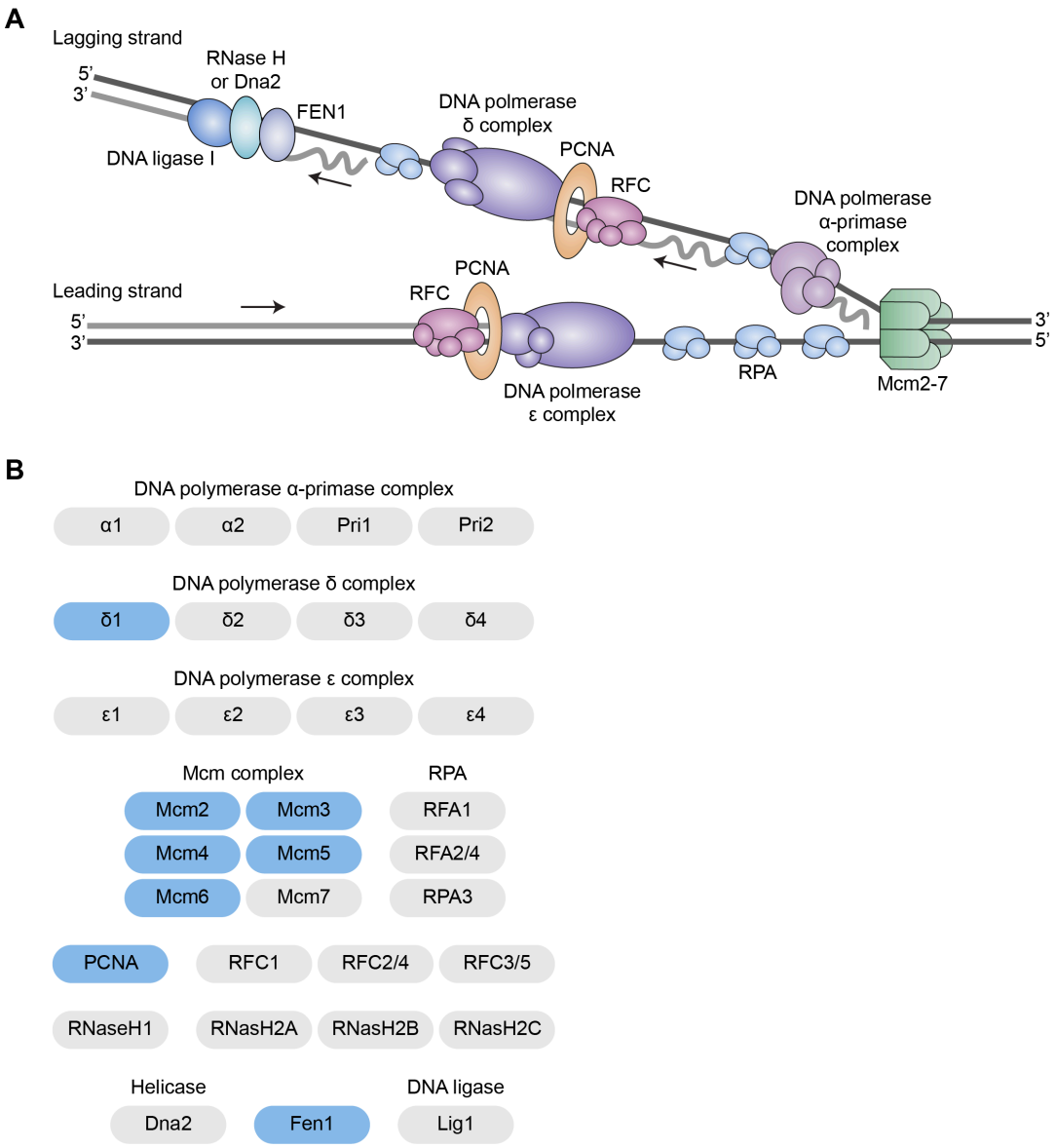

Figure 5.21 DNA replication is downregulated in Hit 1 treated *TO(kras^{G12V})$^{T/+}$* hepatocytes

A. Schematic of DNA replication machinery showing the multiple protein complexes involved. **B.** In Hit 1 treated *TO(kras^{G12V})$^{T/+}$* hepatocytes several components of the DNA replication pathway, shown in blue, are significantly downregulated (False discovery rate <0.05). Of particular interest is the finding that 5 out of 6 components of the Mcm2-7 complex (green pore-like structure in panel A), which is responsible for DNA replication fork licensing, are down-regulated.

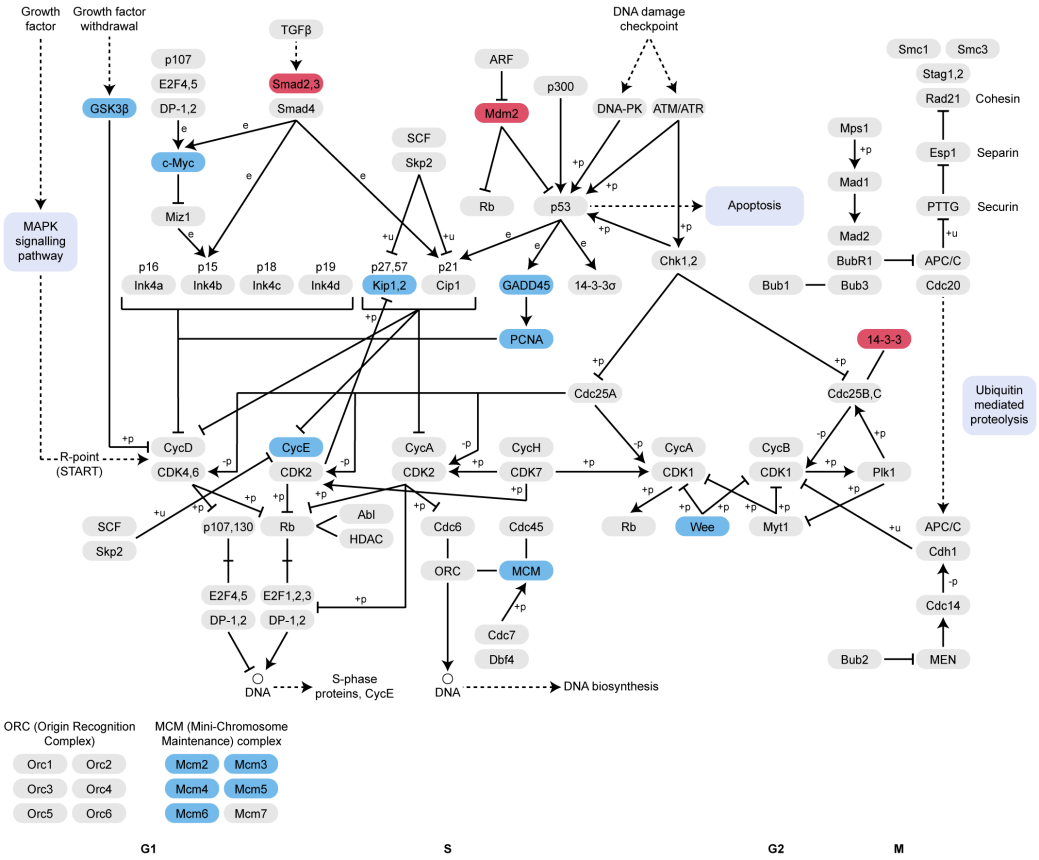

Figure 5.22 The cell cycle pathway is downregulated in Hit 1 treated *TO(kras^{G12V})$^{T/+}$* hepatocytes

In Hit 1 treated *TO(kras^{G12V})$^{T/+}$* hepatocytes several components of the cell cycle pathway, shown in blue, are significantly downregulated (False discovery rate <0.05). Whilst a few components are upregulated, as shown in red, overall the pathway is significantly downregulated resulting in reduced cell cycle progression.

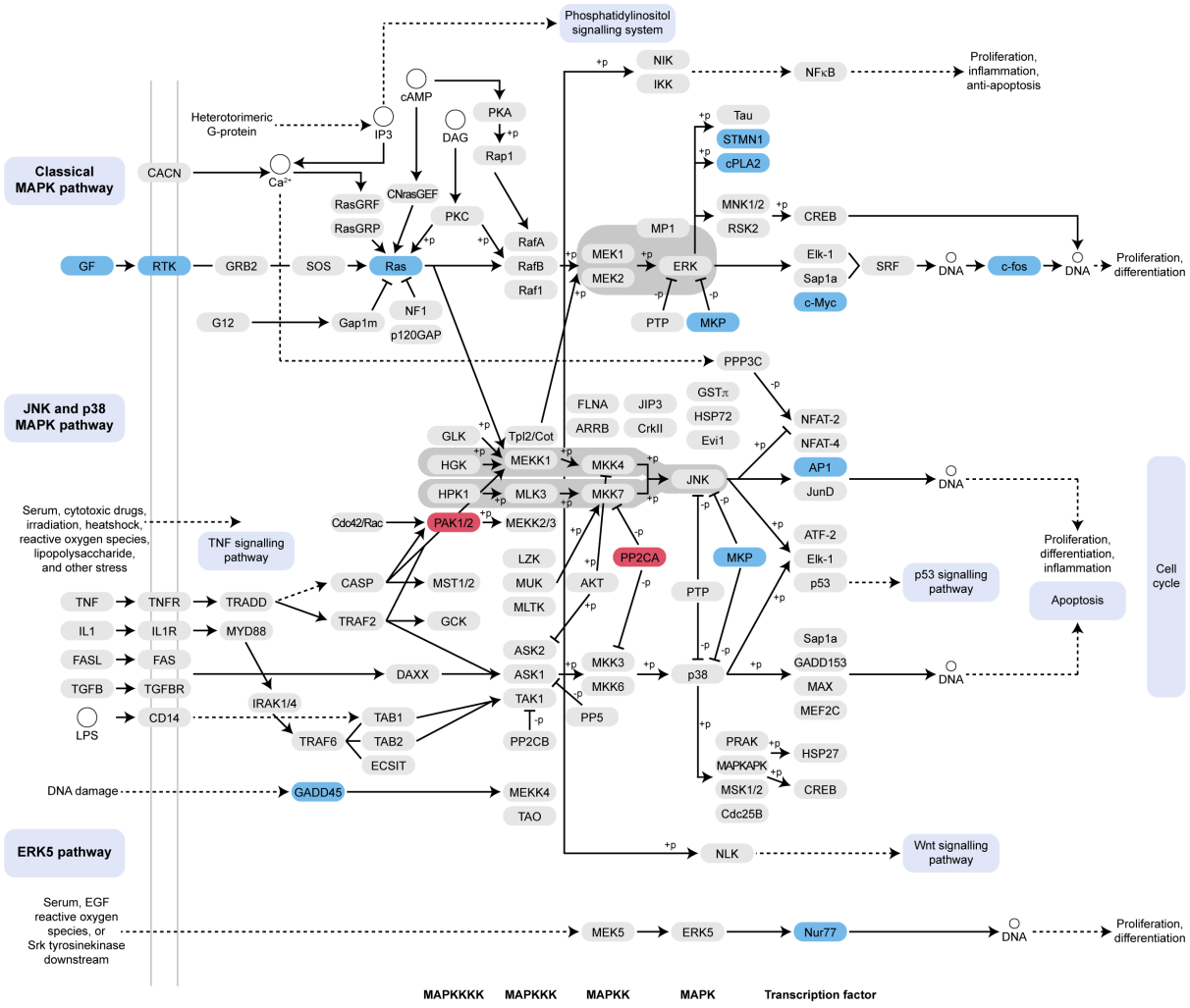

Figure 5.23 MAPK signalling pathway genes are downregulated in Hit 1 treated *TO(kras^{G12V})$^{T/+}$* hepatocytes compared to Inactive compound treated *TO(kras^{G12V})$^{T/+}$* hepatocytes

In Hit 1 treated *TO(kras^{G12V})$^{T/+}$* hepatocytes several components of the MAPK pathway, shown in blue, are significantly downregulated (False discovery rate <0.05). Whilst a few components are upregulated, as shown in red, overall the pathway is significantly downregulated resulting in reduced proliferation, differentiation and cell cycle progression.

Table 5.5 MAPK signalling pathway genes are downregulated in Hit 1 treated *TO(kras^{G12V})$^{T/+}$* hepatocytes compared to Inactive compound treated *TO(kras^{G12V})$^{T/+}$* hepatocytes

Gene	Log fold change	Average expression	False discovery rate
gadd45ba	-2.09	5.07	1.3E-06
mycb	-1.39	4.39	8.5E-06
dusp1	-1.35	7.06	7.3E-05
junbb	-1.68	7.59	7.7E-05
dusp2	-1.76	5.19	2.6E-04
fosaa	-2.86	0.82	2.7E-04
stmn1a	-1.11	3.71	1.0E-03
fosab	-3.29	6.15	1.0E-03
jun	-0.57	7.21	1.5E-03
hspa12a	-0.90	3.75	2.0E-03
fgf4	-2.16	1.80	5.3E-03
fosb	-1.83	2.28	7.2E-03
fgf18a	-0.71	3.55	9.0E-03
nr4a1	-2.62	3.12	1.7E-02
fgfr1a	-0.97	3.86	2.5E-02
dusp5	-0.73	3.04	3.3E-02
kras	-1.53	8.95	3.3E-02
junba	-1.09	4.91	4.8E-02

5.13 Overcoming drug resistance by combination therapy

As outlined in Chapter 1 of this thesis, the development of drug resistance is a major barrier to preventing complete remission in patients with cancer. After a clinical response following treatment, resistance often emerges resulting in local or distant reoccurrence of the malignancy (Figure 5.24). Therapeutic resistance in cancer is mediated through diverse mechanisms including alterations of drug targets, upregulation of drug efflux and changes in the tumour microenvironment[532-534]. Beginning in the 1960s, drug combination therapy has been a central strategy for providing maximal benefit to patients and minimising the evolution of resistance[535]. In 1965, simultaneous administration of methotrexate, vincristine, 6-MP and prednisone was demonstrated to induce long-term remission of childhood acute lymphoblastic leukemia (ALL)[536]. This clinical success was subsequently extended to Hodgkin's lymphoma and non-Hodgkin's lymphoma, with combination of four chemotherapeutic drugs shown to produce cures in patients[537,538]. Numerous combination strategies have since been developed that are capable of inducing robust treatment responses and limiting the development of drug resistance. More recently combined treatment modalities have expanded to include molecularly targeted agents. For example, the combination of HER2 inhibitors pertuzumab and trastuzumab, together with the chemotherapy agent docetaxel extends progression-free survival in patients with metastatic HER2-positive breast cancer by 6.1 months[539]. Therefore, rational combinatorial therapy has immense potential to improve clinical outcomes, even in patients at advanced disease stages. Having previously determined that heterozygous *rnpc3* and *ahctf1* mutation were effective in restricting *kras*^{G12V}-driven liver hyperplasia, I decided to explore the benefit, if any, of combining chemical inhibitors with genetic manipulation in the *TO(kras*^{G12V}*)* zebrafish HCC model.

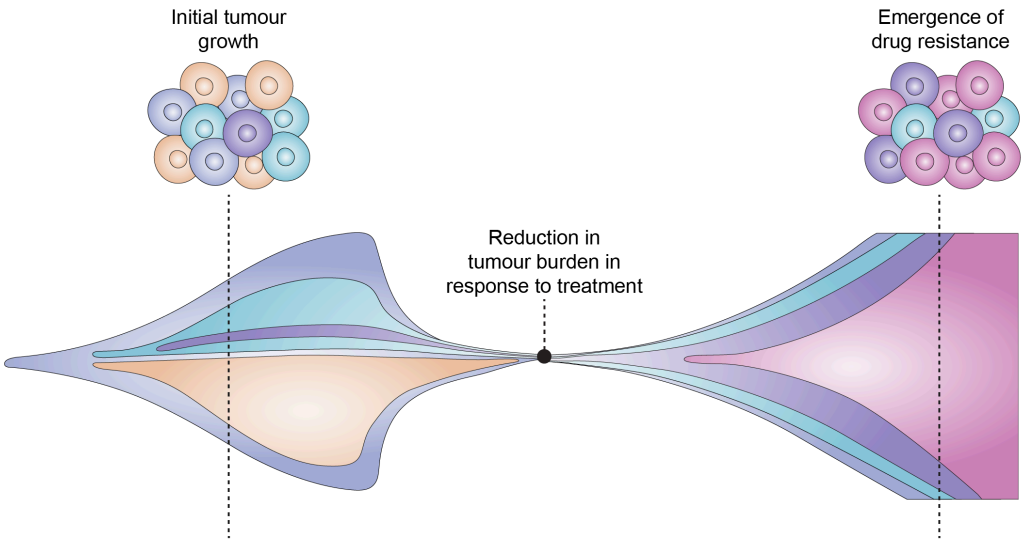

Figure 5.24 Schematic of the emergence of cancer drug resistance

During malignant transformation and tumour growth, the progressive accumulation of mutations and selective pressures including hypoxia and metabolic limitations lead to the development of intratumoural heterogeneity as indicated by the different colour tumour cells. In response to treatment, an initial reduction in tumour burden is observed. However, subpopulations of tumour cells may emerge that exhibit intrinsic resistance (purple tumour cells) or develop acquired resistance (pink tumour cells) which eventually results in disease relapse.

5.14 Results

5.14.1 *rnpc3* heterozygosity combines with MEK inhibition to completely block *kras*^{G12V}-driven hepatocyte hyperplasia

Consistent with previous results, in control *2-CLiP* larvae treatment with 1.0-20 µM MEK162 from 5 to 7 dpf did not affect normal liver development (Figure 5.25A, B). No reduction in liver volume was observed after MEK162 exposure, even at the highest concentration tested of 20 µM. In contrast, a dose-dependent reduction in liver volume was observed in *rnpc3*$^{+/+}$*; TO(kras*^{G12V}*)*$^{T/+}$ larvae (Figure 5.25C). When MEK162 treatment was combined with *rnpc3* heterozygosity, liver hyperplasia was further reduced (Figure 5.25D). Strikingly, liver volume in *rnpc3*$^{+/-}$*; TO(kras*^{G12V}*)*$^{T/+}$ larvae treated with 20 µM MEK162 was indistinguishable from that of control, non-hyperplastic livers in *2-CLiP* larvae (Figure 5.25E). This demonstrates that *rnpc3* heterozygosity combines with MEK inhibition to completely block *kras*^{G12V}-driven hepatocyte hyperplasia.

5.14.2 *rnpc3* heterozygosity combines with MEK inhibition to reduce pERK1/2 expression in *TO(kras*^{G12V}*)*$^{T/+}$ larvae

To demonstrate that the reduction in liver volume observed upon MEK162 treatment was achieved through on-target inhibition of the RAS/RAF/MEK/ERK signalling cascade the abundance of pERK1/2 proteins was quantified in pools of micro-dissected livers (Figure 5.26). MEK162 treatment resulted in a dose-dependent reduction in pERK1/2 levels, reducing protein expression by 90% in *rnpc3*$^{+/+}$*; TO(kras*^{G12V}*)*$^{T/+}$ larvae at a 20 µM dose, an effect that was enhanced in *rnpc3*$^{+/-}$*; TO(kras*^{G12V}*)*$^{T/+}$ larvae. Strikingly, *rnpc3* heterozygosity alone resulted in a 17% reduction in pERK1/2 proteins.

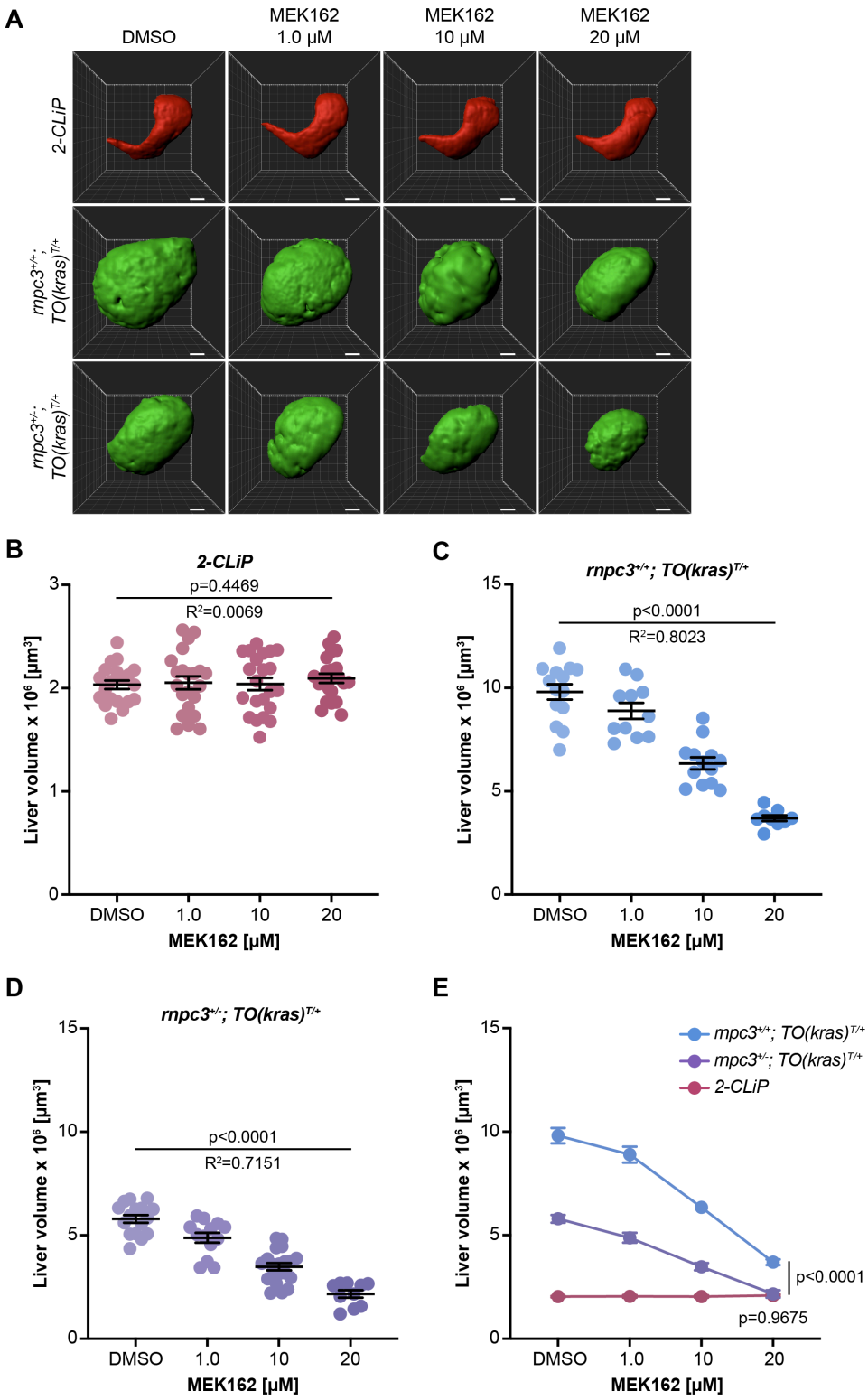

Figure 5.25 *rnpc3* heterozygosity combined with MEK162 completely restricts *kras*^{G12V}-driven hepatocyte hyperplasia and liver enlargement

A. Representative three-dimensional reconstructions of *2-CLiP* and *TO(kras*^{G12V}*)*$^{T/+}$ livers of the indicated *rnpc3* genotype treated with DMSO or the indicated concentration of MEK162. Scale bar 25 µm. **B.** Liver volume in *2-CLiP* larvae was not impacted by MEK162 treatment. **C.**

Liver volume in *rnpc3*$^{+/+}$*; TO(kras*^{G12V}*)*$^{T/+}$ larvae was reduced in a dose-dependent manner by MEK162 treatment. **D.** Similarly, MEK162 restricted liver hyperplasia in *rnpc3*$^{+/-}$*; TO(kras*^{G12V}*)*$^{T/+}$ larvae in a dose-dependent fashion. **E.** Graphical representation of the results shown in panels B-D. Expression of *TO(kras*^{G12V}*)*$^{T/+}$ significantly increased liver volume compared to *2-CLiP* larvae in the presence of DMSO vehicle and this was partially reduced by *rnpc3* heterozygosity. At a 20 µM dose of MEK162, liver volume in *rnpc3*$^{+/-}$*; TO(kras*^{G12V}*)*$^{T/+}$ larvae was reduced to that of normal *2-CLiP* larvae. Data are expressed as mean ± SEM, n≥9. Significance was calculated by linear regression analysis or by two-way ANOVA with Tukey's multiple comparisons test.

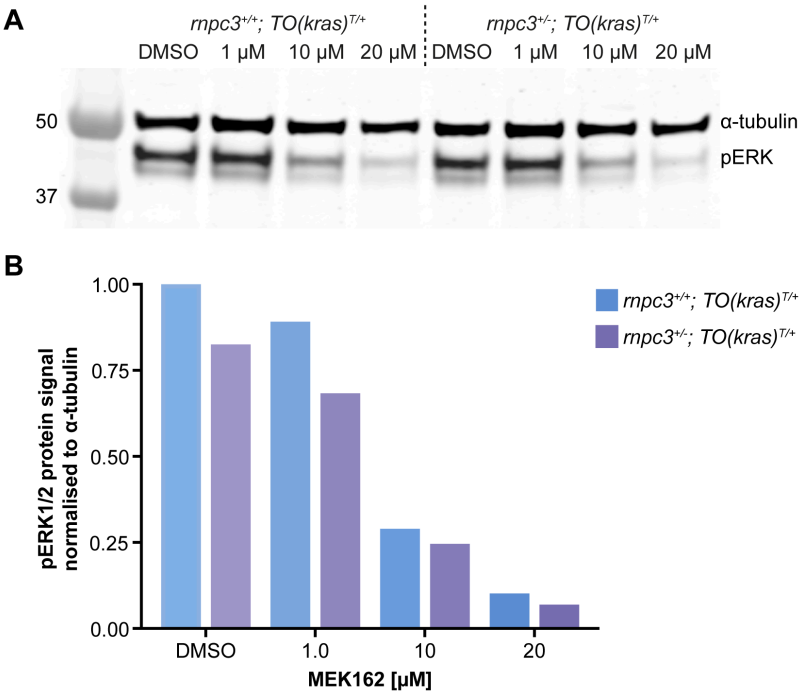

Figure 5.26 *rnpc3* heterozygosity combined with MEK162 reduces expression of pERK1/2 proteins in *TO(kras^{G12V})$^{T/+}$* larvae

A. Western blot of pERK1/2 (42 and 44 kDa) protein levels in lysates of pooled micro-dissected *TO(kras^{G12V})$^{T/+}$* livers of the indicated *rnpc3* genotype treated with DMSO or the indicated concentration of MEK162. **B.** Quantification of pERK1/2 protein levels normalised to the α-tubulin loading control in DMSO treated *rnpc3$^{+/+}$; TO(kras^{G12V})$^{T/+}$* larvae. pERK1/2 protein expression was reduced in a dose-dependent manner by MEK162 treatment and this was augmented by *rnpc3* heterozygosity.

5.14.3 *rnpc3* heterozygosity combines with MEK inhibition to induce a Tp53-mediated response in *TO(kras^{G12V})$^{T/+}$* larvae

As previously shown in chapter 4 *rnpc3* heterozygosity reduces liver volume via decreasing the number of cycling cells and increasing cell death. As these key tumour suppressive functions can be mediated by Tp53, whether a Tp53 response was induced by *rnpc3* heterozygosity and the impact of MEK162 treatment was assessed by RT-qPCR analysis on pools of micro-dissected livers. mRNA expression levels of *rnpc3* were not affected by 20 µM MEK162 treatment, however, they were reduced 50% by *rnpc3* heterozygosity as expected (Figure 5.27A). Neither MEK162 exposure, nor *rnpc3* heterozygosity, alone or in combination altered *tp53* transcript levels (Figure 5.27B). However, *Δ113tp53* expression was elevated in response to MEK162 treatment and *rnpc3* heterozygosity, indicating the presence of stabilised, transcriptionally active Tp53 protein (Figure 5.27C). Notably, in *rnpc3$^{+/-}$; TO(kras^{G12V})$^{T/+}$* larvae treated with MEK162, *Δ113tp53* levels were upregulated >7-fold.

Consistent with the activation of a Tp53-mediated response, expression of the direct Tp53 transcriptional target *mdm2* was increased by MEK162 treatment and further elevated by *rnpc3* heterozygosity (Figure 5.28A). In addition, significant upregulation of cell cycle regulators *cdkn2a/b* and *cdkn1a* was observed in *rnpc3$^{+/+}$; TO(kras^{G12V})$^{T/+}$* larvae treated with MEK162 (Figure 5.28B,C). MEK162 exposure in combination with *rnpc3* heterozygosity had an approximately additive effect, increasing *cdkn2a/b* and *cdkn1a* expression by 4.4-fold and 3.5-fold, respectively. Similarly, transcript levels of the pro-apoptosis genes, *bbc3* and *pmaip1* were elevated by MEK162 treatment (Figure 5.28D,E). Combined MEK162 treatment and *rnpc3* heterozygosity resulted in upregulation of *bbc3* and *pmaip1* by 4.6-fold and 3.0-fold, respectively. Collectively, these data indicate that *rnpc3* heterozygosity combines with MEK inhibition to restrict *kras^{G12V}*-driven liver hyperplasia via activation of a Tp53 transcriptional program that increases expression of both pro-senescence and pro-apoptosis genes. Moreover, the anti-tumour growth effect of *rnpc3* heterozygosity can be enhanced by treatment with MEK162, indicating that an inhibitor of U12-dependent splicing in combination with MEK162 could provide a combination therapy of clinical benefit to cancer patients.

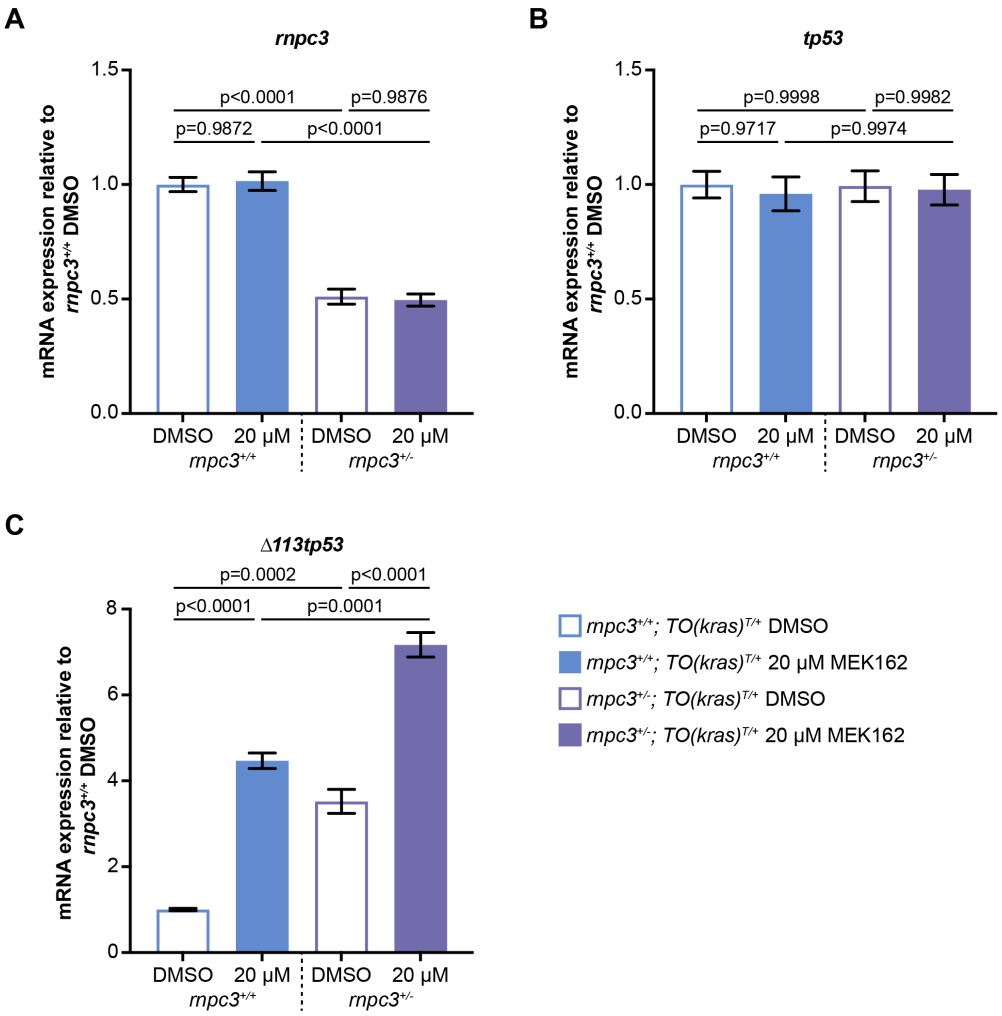

Figure 5.27 *rnpc3* heterozygosity combined with MEK162 induces expression of a Tp53 transcriptional program in the livers of *TO(kras^{G12V})$^{T/+}$* larvae

RT-qPCR analysis of pooled micro-dissected livers from *TO(kras^{G12V})$^{T/+}$* larvae of the indicated *rnpc3* genotype treated with DMSO or 20 μM MEK162. **A.** *rnpc3* transcript levels were not impacted by MEK162 treatment but were reduced by 50% in *rnpc3* heterozygous larvae. **B.** *tp53* mRNA expression was not altered by MEK162 exposure or *rnpc3* heterozygosity. **C.** *Δ113tp53* expression was upregulated by MEK162 treatment and this effect was enhanced in *rnpc3$^{+/-}$; TO(kras^{G12V})$^{T/+}$* larvae. Data are expressed as mean ± SEM, n=3 biological replicates. Significance was calculated using a one-way ANOVA with Tukey's multiple comparisons test.

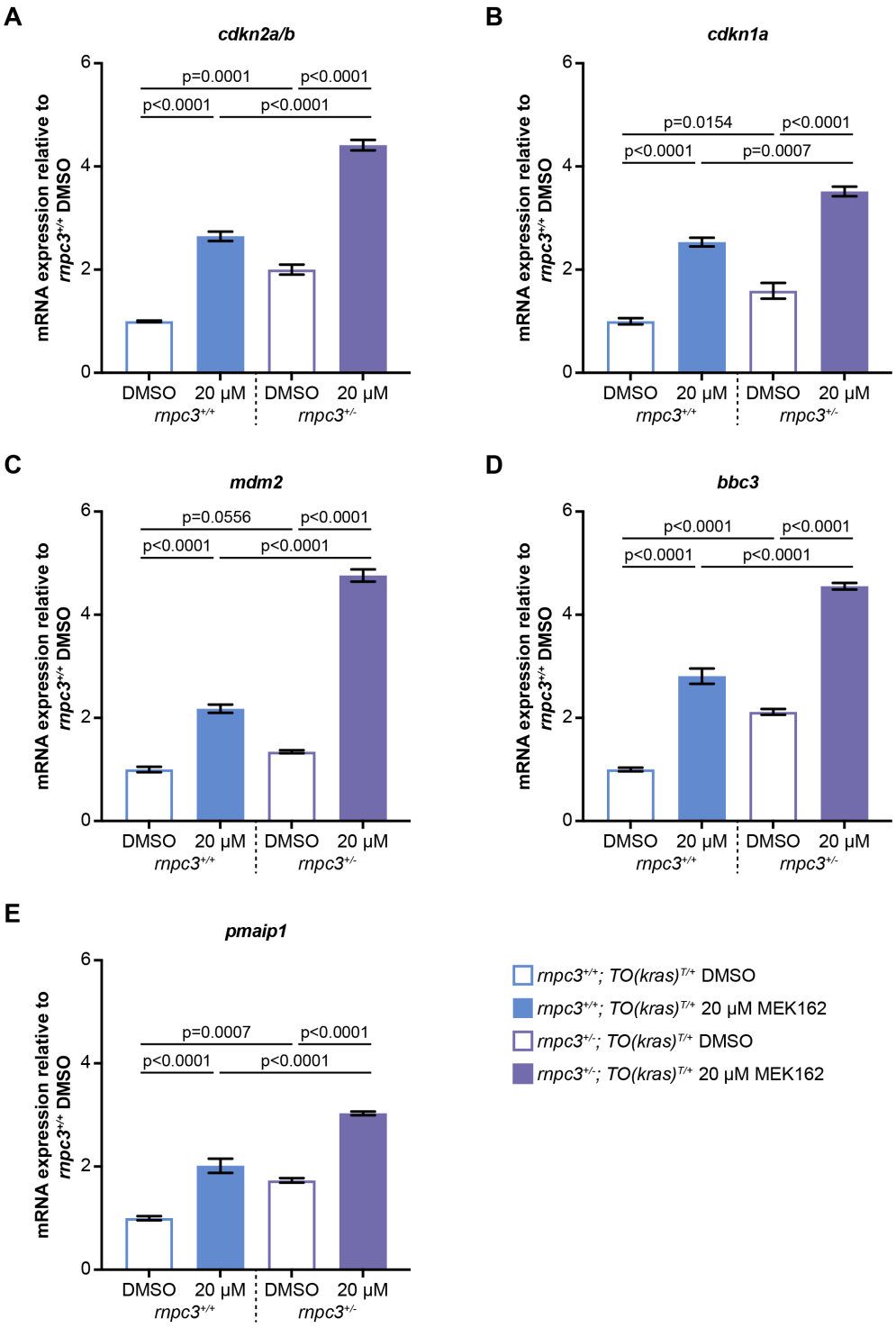

Figure 5.28 *rnpc3* heterozygosity combined with MEK162 induces expression of Tp53 target genes in *TO(kras^{G12V})$^{T/+}$* larvae

RT-qPCR analysis of pooled micro-dissected livers from *TO(kras^{G12V})$^{T/+}$* larvae of the indicated *rnpc3* genotype treated with DMSO or 20 µM MEK162. **A.** *mdm2* transcripts were upregulated by MEK162 treatment and this was augmented by *rnpc3* heterozygosity. **B,C.** Expression of cell cycle regulators *cdkn2a/b* and *cdkn1a* were similarly increased by MEK162 treatment and

this effect was further enhanced in *rnpc3*$^{+/-}$*; TO(kras*^{G12V}*)*$^{T/+}$ larvae. **D,E.** mRNA levels of *bbc3* and *pmaip1*, encoding puma and noxa, respectively, were increased by MEK162 exposure and this effect was augmented by *rnpc3* heterozygosity. Data are expressed as mean ± SEM, n=3 biological replicates. Significance was calculated using a one-way ANOVA with Tukey's multiple comparisons test.

5.14.4 *rnpc3* heterozygosity combines with Hit 1 treatment to completely block *kras*^{G12V}-driven hepatocyte hyperplasia

Having established the efficacy of *rnpc3* heterozygosity combined with MEK162 treatment at restricting *kras*^{G12V}-driven hepatocyte hyperplasia, I next investigated the impact of *rnpc3* heterozygosity combined with Hit 1 treatment. Consistent with previous results, treatment of control *2-CLiP* larvae with 0.5-5.0 µM Hit 1 from 5 to 7 dpf did not affect normal liver development (Figure 5.29A, B). No reduction in liver volume was observed after Hit 1 exposure, even at the highest concentration tested (5.0 µM). In contrast, a dose-dependent reduction in liver volume was observed in *rnpc3*$^{+/+}$*; TO(kras*^{G12V}*)*$^{T/+}$ larvae (Figure 5.29C). When Hit 1 treatment was combined with *rnpc3* heterozygosity, liver hyperplasia was further reduced (Figure 5.29D). Significantly, liver volume in *rnpc3*$^{+/-}$*; TO(kras*^{G12V}*)*$^{T/+}$ larvae treated with 5.0 µM Hit 1 was indistinguishable from that of control, non-hyperplastic livers in *2-CLiP* larvae (Figure 5.29E). This demonstrates that *rnpc3* heterozygosity combines with Hit 1 treatment to completely block *kras*^{G12V}-driven hepatocyte hyperplasia and liver enlargement.

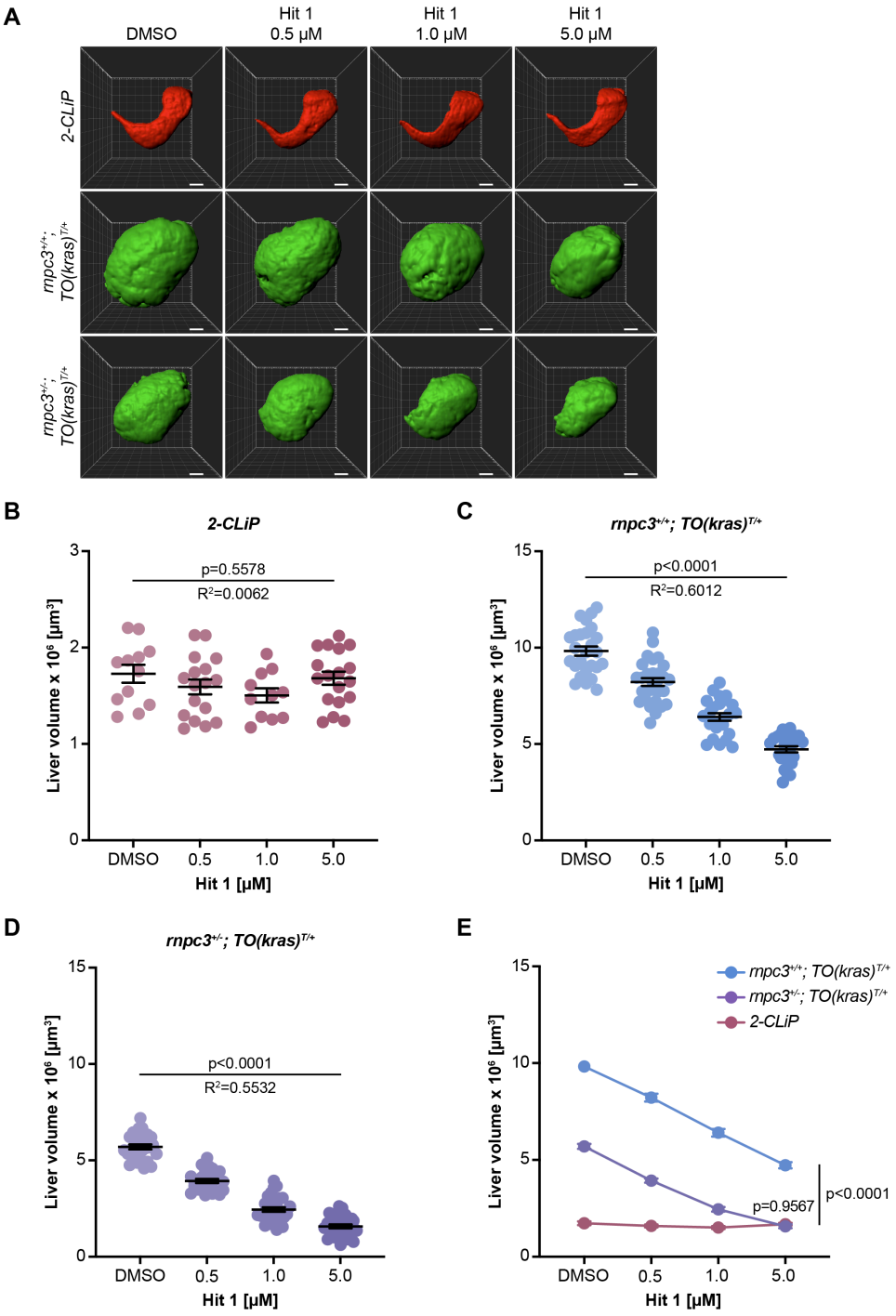

Figure 5.29 *rnpc3* heterozygosity combined with Hit 1 completely restricts *kras*^{G12V}-driven liver hyperplasia

A. Representative three-dimensional reconstructions of *2-CLiP* and *TO(kras*^{G12V}*)*$^{T/+}$ livers of the indicated *rnpc3* genotype treated with DMSO or the indicated concentration of Hit 1, a putative inhibitor of U12-dependent splicing. Scale bar 25 µm. **B.** Liver volume in *2-CLiP* larvae was not impacted by Hit 1 treatment. **C.** Liver volume in *rnpc3*$^{+/+}$*; TO(kras*^{G12V}*)*$^{T/+}$ larvae was reduced in a dose-dependent manner by Hit 1 treatment. **D.** Similarly, in *rnpc3*$^{+/-}$*; TO(kras*^{G12V}*)*$^{T/+}$ larvae, Hit 1 restricted hepatocyte hyperplasia and liver enlargement. **E.**

Graphical representation of the results shown in panels B-D. Expression of *TO(kras^{G12V})$^{T/+}$* significantly increased liver volume compared to *2-CLiP* larvae in the presence of DMSO vehicle and this was partially reduced by *rnpc3* heterozygosity. At a 5.0 µM dose of Hit 1, liver volume in *rnpc3$^{+/-}$; TO(kras^{G12V})$^{T/+}$* larvae was returned to that of normal livers in *2-CLiP* larvae. Data are expressed as mean ± SEM, n≥11. Significance was calculated by linear regression analysis or by two-way ANOVA with Tukey's multiple comparisons test.

5.14.5 *ahctf1* heterozygosity combines with XPO1 inhibition to completely block *kras*^{G12V}-driven hepatocyte hyperplasia

The next combination treatment I examined was *ahctf1* heterozygosity together with XPO1 inhibition. Consistent with previous results, treatment of control *2-CLiP* larvae with 0.10-2.00 µM selinexor from 5 to 7 dpf did not affect normal liver development (Figure 5.30A, B). No reduction in liver volume was observed after selinexor exposure, even at the highest concentration tested of 2.00 µM. In contrast, there was a dose-dependent reduction in liver volume in response to selinexor in *ahctf1*$^{+/+}$*; TO(kras*^{G12V}*)*$^{T/+}$ larvae (Figure 5.30C). When selinexor treatment was combined with *ahctf1* heterozygosity, liver volume was further reduced (Figure 5.30D). Importantly, liver volume in *ahctf1*$^{+/-}$*; TO(kras*^{G12V}*)*$^{T/+}$ larvae treated with 1.00 µM or 2.00 µM selinexor was indistinguishable from that of control, non-hyperplastic livers in *2-CLiP* larvae (Figure 5.30E). This demonstrates that *ahctf1* heterozygosity combines with XPO1 inhibition to completely block *kras*^{G12V}-driven hepatocyte hyperplasia and liver enlargement.

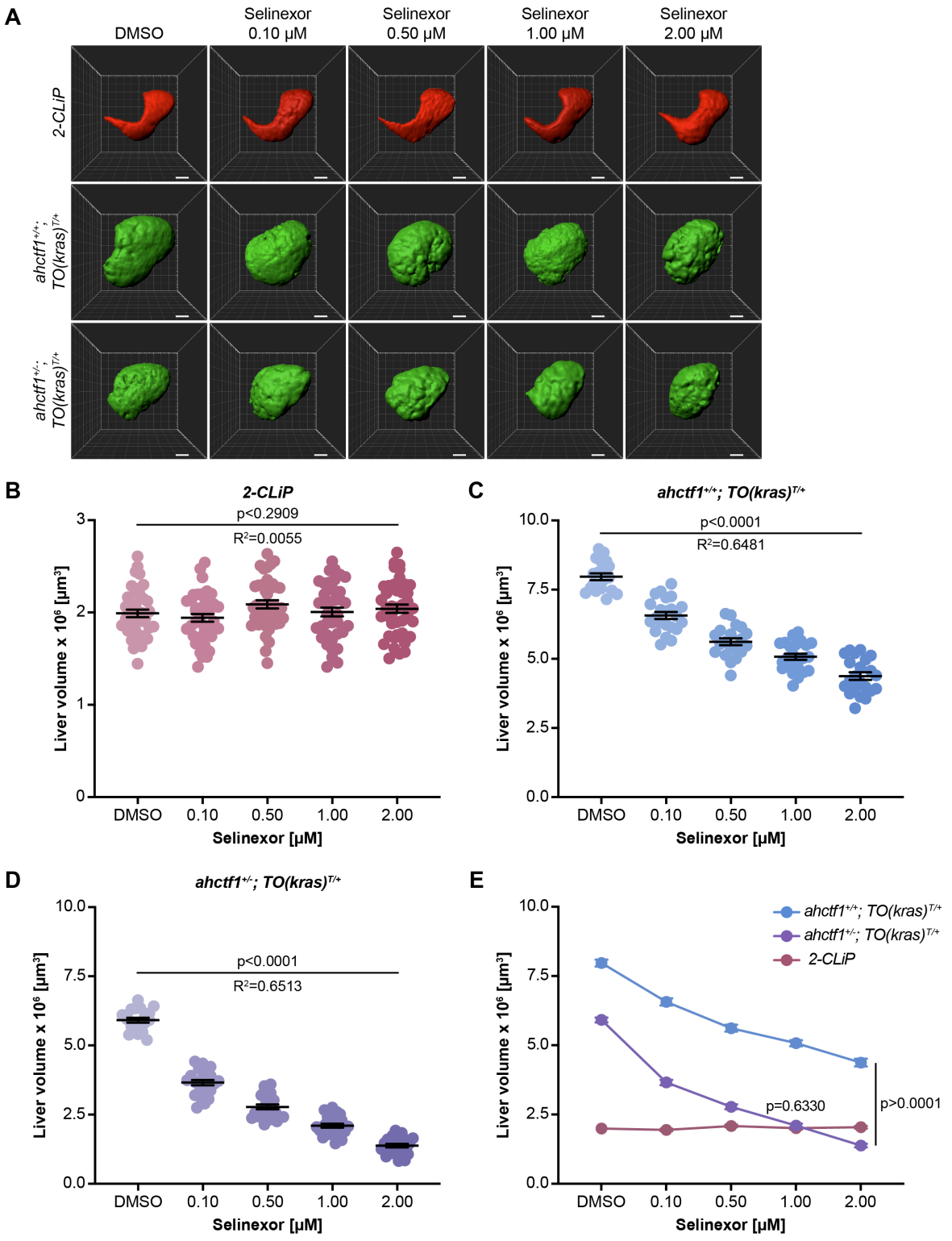

Figure 5.30 *ahctf1* heterozygosity combined with selinexor treatment completely restricts *kras*^{G12V}-driven hepatocyte hyperplasia and liver enlargement

A. Representative three-dimensional reconstructions of *2-CLiP* and *TO(kras*^{G12V}*)*$^{T/+}$ livers of the indicated *ahctf1* genotype treated with DMSO or the indicated concentration of selinexor.

Scale bar 25 µm. **B.** Liver volume in *2-CLiP* larvae was not impacted by selinexor treatment. **C.** Liver volume in *ahctf1*$^{+/+}$*; TO(kras*^{G12V}*)*$^{T/+}$ larvae was reduced in a dose-dependent manner by selinexor treatment. **D.** Selinexor restricted liver enlargement even further in *ahctf1*$^{+/-}$*; TO(kras*^{G12V}*)*$^{T/+}$ larvae **E.** Graphical representation of the results shown in panels B-D. Expression of *TO(kras*^{G12V}*)*$^{T/+}$ significantly increased liver volume compared to *2-CLiP* larvae in the presence of DMSO vehicle and this was partially reduced by *ahctf1* heterozygosity. At a 1.00 µM and 2.00 µM dose of selinexor, liver volume in *ahctf1*$^{+/-}$*; TO(kras*^{G12V}*)*$^{T/+}$ larvae was indistinguishable from that of livers in *2-CLiP* larvae. Data are expressed as mean ± SEM, n≥20. Significance was calculated by linear regression analysis or by two-way ANOVA with Tukey's multiple comparisons test.

5.15 Discussion

The current success rate of cancer drug discovery and development is insufficient to meet growing clinical demands. Moreover, the almost inevitable emergence of drug resistance to targeted therapies poses a major barrier to achieving complete cures in patients. Zebrafish provide a powerful vertebrate platform for *in vivo* drug discovery, to help overcome these obstacles and improve clinical outcomes. Due to their capacity for high-throughput applications as well as their genetic and physiological similarity to humans, zebrafish facilitate the efficient screening of novel compounds and validation of drug targets. By contributing to simultaneous target identification, pharmacology and toxicology analysis, studies in zebrafish have immense capacity to accelerate the drug development pipeline, offering a rapid path to the development of novel cancer therapies.

The efficacy of zebrafish as a tool for drug discovery is supported by the results presented in this chapter which establish that the *TO(kras^{G12V})$^{T/+}$* HCC model is highly amenable to pharmacological inhibition, thus representing a valuable system for the pre-clinical examination of drug treatments *in vivo*. Using this transgenic model alongside the *2-CLiP* zebrafish line as a control, provides early insights into toxicity, enables optimisation of drug efficacy and allows identification of compounds that selectively inhibit *kras^{G12V}*-driven hepatocyte hyperplasia without impacting normal liver growth and development. Significantly, treatment with all the drug compounds tested – MEK162, selinexor, EPZ015666, WM-8014 and Hit 1 – did not impair normal liver growth in *2-CLiP* larvae; instead anti-tumour effects were observed only in hepatocytes expressing oncogenic Kras^{G12V}. These observations suggest that a viable therapeutic window exists for these drug treatments that can be exploited for HCC treatment.

Treatment with MEK162, a clinically approved MAPK pathway inhibitor reduced *kras^{G12V}*-driven liver hyperplasia by 81%. This promising therapeutic activity was further enhanced by *rnpc3* heterozygosity which combined with MEK inhibition to reduce pERK1/2 protein expression and activate a Tp53-mediated transcriptional program. Mechanistically, this resulted in increased expression of pro-senescence and pro-apoptosis genes which reduced liver volume to non-hyperplastic *2-CLiP* levels. The efficacy of MEK162 in the *TO(kras^{G12V})$^{T/+}$* model is consistent with multiple studies which have demonstrated that MEK inhibition improves clinical outcomes in RAS/RAF mutant cancers, such as NRAS and BRAF-mutant melanoma[475]. Moreover, the capacity of *rnpc3* heterozygosity to augment the effects of MEK162 treatment further advance U12-dependent splicing disruption as a promising mechanism by which cancer growth may be restricted.

The potential of U12-dependent splicing as an effective target for cancer therapy is also supported by the ability of the Hit 1 compound, identified in a high-throughput screen for U12-dependent splicing inhibitors, to restrict *kras^{G12V}*-driven liver hyperplasia. Treatment with 5.0 µM Hit 1 treatment significantly reduced excess liver volume by 62% in

TO(kras^{G12V})$^{T/+}$ larvae and no toxicity was observed on the *2-CLiP* background. Furthermore, combination of Hit 1 exposure and *rnpc3* heterozygosity was able to completely block liver hyperplasia, reducing liver volume to that of *2-CLiP* larvae. The compound is currently the focus of medicinal chemistry efforts to improve its potency and drug-like properties. Whilst further experiments are necessary to demonstrate that U12-dependent splicing is selectively disrupted by Hit 1 treatment in this *in vivo* model system, *in vitro* experiments using HEK273, HeLa and A549 lung adenocarcinoma cells, have shown that U12 intron-containing genes are aberrantly spliced in response to Hit 1 treatment (Dr. Stephen Mieruszynski, personal communication). Together, these preliminary results support the potential clinical utility of inhibiting U12-dependent splicing as a hitherto unexplored cancer treatment.

The modulation of splicing more broadly through PRMT5 inhibition has also recently emerged as a promising therapeutic target in diverse cancer types including glioblastoma, lymphoma and leukemia[509,540]. Treatment with the PRMT5 inhibitor, EPZ015666 substantially reduced *kras^{G12V}*-driven liver hyperplasia in a concentration-dependent manner, with excess liver volume reduced by 78% in response to a 10.00 µM dose. Consistent with previous reports that the enzymatic activity of PRMT5 is required for cell proliferation *in vitro* and genetic suppression of PRMT5 impairs cancer cell growth by inducing senescence[540,541], EPZ015666 treatment restricted DNA replication in *TO(kras^{G12V})$^{T/+}$* hepatocytes and upregulated expression of pro-senescence genes. These data demonstrate that EPZ015666 is efficacious at limiting liver tumour burden by inducing senescence, providing a rationale for further development of PRMT5 inhibitors for treatment of HCC patients.

Treatment with the clinically validated XPO1 inhibitor selinexor was also investigated in the *TO(kras^{G12V})$^{T/+}$* model. Like the previous compounds analysed, selinexor treatment produced a dose-dependent reduction in tumour burden. Moreover, this therapeutic effect was strongly augmented by *ahctf1* heterozygosity, suggesting that new drugs targeting the ELYS protein could be combined effectively with drugs that target nucleocytoplasmic transport. Overexpression of XPO1 in many cancers is associated with a poor prognosis and drug resistance through excessive export of the drug from the nucleus. By reducing drug efflux, treatment with SINE compounds may indirectly sensitise cancer cells to treatment and overcome drug resistance. This approach has been shown to be successful in multiple myeloma, with selinexor treatment capable of overcoming acquired multi-drug resistance and restoring sensitivity to doxorubicin both *in vitro* and *in vivo*[542]. Therefore, XPO1 inhibition represents a promising therapeutic strategy to reverse *de novo* drug resistance and greatly improve patient outcomes.

Similarly, combination therapy is a well-established strategy to reduce the likelihood of drug resistance emerging and improve the magnitude of therapeutic responses through additive or synergistic interactions between compounds. Collectively the data presented in this chapter strongly support the use of combination therapies to maximise treatment responses.

Whilst treatment with MEK162, Hit 1 and selinexor were effective in reducing liver enlargement in a dose-dependent manner, some degree of hepatocyte hyperplasia remained, even at the highest concentrations tested. However, combining these treatment modalities with heterozygosity of *rnpc3* or *ahctf1* had a substantial impact, completely restricting *kras*^{G12V}-driven liver enlargement. Therefore, these inhibitors are likely to be most effective clinically when used in combination with other treatments rather than as single-agent therapies. Such combination therapy has been widely successful in the clinic, with treatment regimens established that are capable of inducing robust treatment responses for a diverse array of cancers, limiting the development of drug resistance. For example, multiple traditional chemotherapeutic agents are routinely used together to curatively treat leukemia and lymphoma[535]. Combination therapy has also recently been shown to be effective for HCC. Phase III trials of atezolizumab (an immune checkpoint inhibitor) plus bevacizumab (an anti-VEGFA antibody), prolonged overall survival and extended median progression-free survival by a further 2.5 months compared to sorafenib treatment[543]. Determining which dose, dosage schedule and combination of pharmacological agents will confer the greatest therapeutic outcome in patients poses a formidable challenge that could potentially be advanced by more extensive use of zebrafish cancer models such as the *TO(kras*^{G12V}*)*$^{T/+}$ HCC model at the heart of this thesis.

Notwithstanding all the observations discussed above, it is important to recognise the potential limitations of the HCC model. Cancer usually develops over decades in humans during which time there is a steady accumulation of mutations that together contribute to the malignant state. The *TO(kras*^{G12V}*)* zebrafish HCC model is solely dependent on the continuous induced expression of oncogenic Kras^{G12V} and in my doxycycline treatment regime (5 days) there is not enough time for secondary mutations to occur. Thus, the model does not fully recapitulate the complex genetic landscape of HCC tumours in patients.

In addition, despite increased recognition of the usefulness and relevance of zebrafish models to cancer research, many clinicians and biomedical scientists do not accept findings made in zebrafish until they have been recapitulated in mammalian models. For instance, in the first submission of our paper to *Nature* describing the discovery of the KAT6A/B inhibitor, WM-8014, I provided the first *in vivo* evidence of its anti-tumour potency in the *TO(kras*^{G12V}*)* model. However, before accepting this paper, the editors at *Nature* required evidence that senescence was also induced upon WM-8014 treatment in a mouse xenograft model of human lymphoma.

A further limitation of testing drug compounds in zebrafish is the difficulty in accurately estimating drug exposure concentrations. Whilst direct submersion of zebrafish in drug compounds dissolved in water permits high-throughput screening, determining drug dose, pharmacokinetics and pharmacodynamics is challenging[149,152]. However, alternative drug administration routes such as intraperitoneal injection and oral gavage can enable more

precise determination of drug doses[452-455]. In addition, the development of mass spectrometry techniques to analyse pooled blood plasma samples from zebrafish, allows evaluation of drug absorption, clearance and distribution, even in larval zebrafish, further advancing the use of zebrafish in drug discovery and validation[544,545]

In summary, zebrafish cancer models offer unique opportunities to rapidly assess and identify optimal combinatorial drug strategies. Recent technological developments facilitating generation of transgenic and transplantation-based zebrafish cancer avatars, has further broadened the potential use of zebrafish as clinical prediction tools[138,144,146,152]. Thus, drug screens in zebrafish may be utilised for precision oncology to inform individualised therapeutic strategies. The validity of this approach is currently being assessed in an ongoing co-clinical trial (NCT03668418) based on phenotypic testing of chemotherapeutic drug responses in zebrafish larval xenografts of human gastrointestinal cancers[546]. Additionally, zebrafish cancer avatars have the potential to be useful predictors of drug resistance. In particular, only short durations of drug exposure are necessary to identify primary resistance, so both larval and adult zPDXs can be used to evaluate chemosensitivity and inform clinical treatment[144,463].

6 Conclusions and general discussion

In this thesis, I report the results of experiments designed to test the paradigm that genes that are indispensable for rapid rates of cell proliferation during development may provide novel molecular targets for cancer treatment. Additionally, I evaluate the efficacy of several drug treatments *in vivo.*

Utilising advanced imaging techniques, I show that both *ahctf1* heterozygosity and *rnpc3* heterozygosity markedly reduce *kras*^{G12V}-driven hepatocyte hyperplasia and liver enlargement, while leaving non-cancerous tissues unaffected (Figure 6.1). In heterozygous *ahctf1* larvae this therapeutic effect is achieved by disrupting nuclear pore formation and impairing mitotic spindle assembly and chromosome segregation. Together these defects augment the mild oncogene-induced stress caused by expression of *kras*^{G12V} alone, ultimately producing DNA damage and a 3.5-fold activation of Tp53-dependent and independent cell death pathways. A similar interaction occurs between *kras*^{G12V} expression and impairment of U12-dependent splicing in heterozygous *rnpc3* larvae. However, in this instance, the reduction in tumour burden was produced by a less pronounced (1.5-fold) increase in apoptosis. Instead, there was a marked reduction in DNA replication and cell cycle progression, consistent with growth arrest. Thus, it is tempting to think that the precise mechanisms that produced cell death and growth arrest in *ahctf1*$^{-/-}$ and *rnpc3*$^{-/-}$ larvae, respectively, during development (as introduced in section 1.4.6) were employed again to reduce hepatocyte hyperplasia and tumour burden in the *TO(kras*^{G12V}) model of HCC. If this observation holds true, then one might infer from this that Elys may represent a superior molecular target for cancer therapy than the 65K protein encoded by *rnpc3*, since impairment of its function is more likely to kill cancer cells. Killing malignant cells is the ultimate goal of cancer treatment, potentially enabling elimination of tumours and complete patient remission rather than arresting tumour growth and producing stable disease.

Developmental signalling pathways are recapitulated during tumourigenesis and key characteristics of cells in developing tissues are shared with cancer cells. Given *ahctf1* and *rnpc3* were identified in an ENU mutagenesis screen for genes that are essential for high rates of cell proliferation during endodermal organ development, it is not surprising that they are also necessary to support the rapid proliferation of hepatocytes expressing oncogenic *kras*^{G12V}. During my Honours project I investigated the impact of another Liver^{plus} screen mutant, *setebos*, which harbours a mutation in the ribosomal RNA processing gene *nol8*. Consistent with the other mutants examined, heterozygous loss of *nol8* was also effective at restricting *kras*^{G12V}-driven hepatocyte hyperplasia and liver enlargement. Collectively this data supports the concept that processes essential for development are also necessary for tumourigenesis, revealing potential targets that may be of therapeutic benefit for improved cancer treatments.

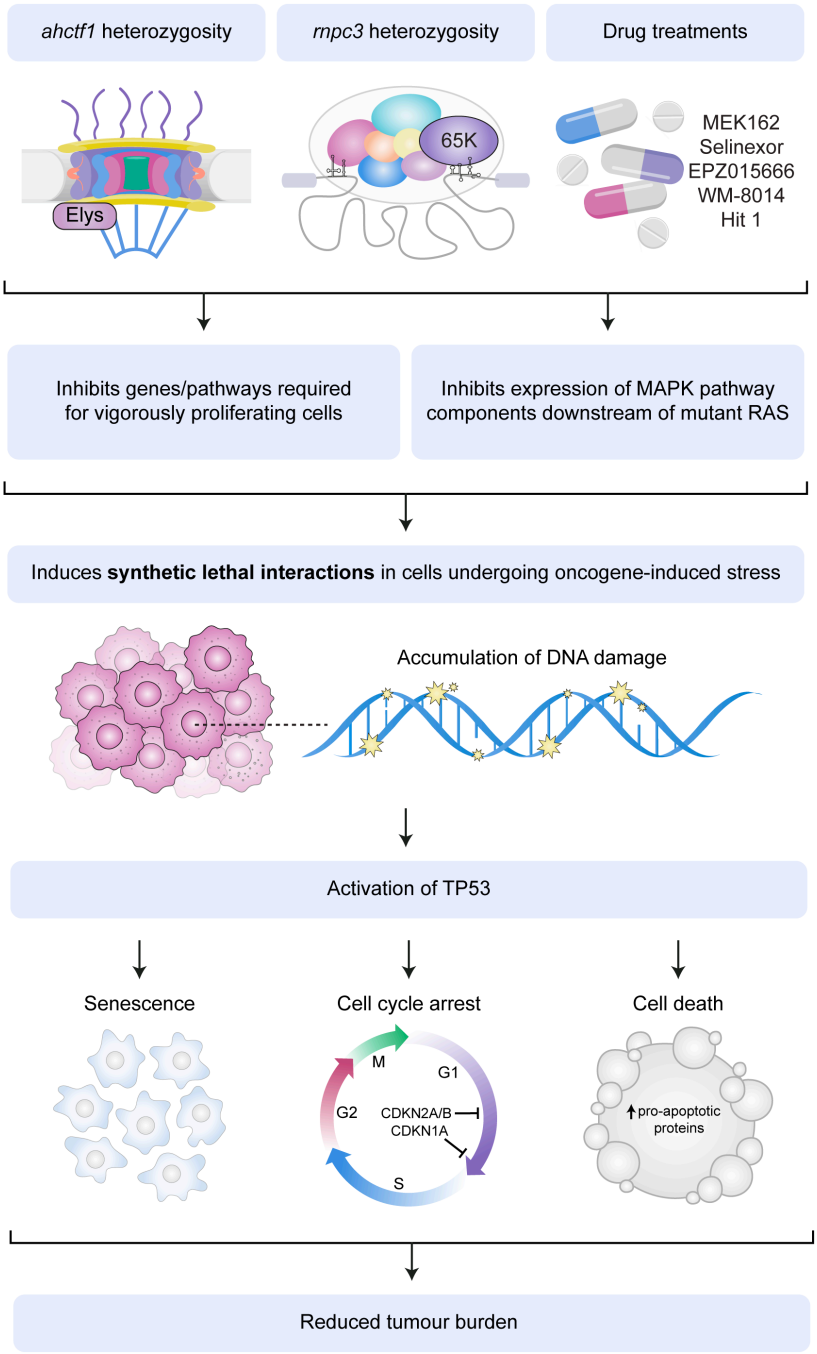

Figure 6.1 Mechanism underlying genetic mutant and drug treatment induced reduction of *kras*^{G12V}-driven hepatocyte hyperplasia

ahctf1 heterozygosity, *rnpc3* heterozygosity and drug treatments can both inhibit genes or pathways that are required for vigorously proliferating cells and inhibit expression of MAPK pathway components downstream of mutant RAS. Together, this results in synthetic lethal interactions in cells undergoing oncogene-induced stress leading to the accumulation of DNA damage. In turn, this activates TP53, which modulates diverse cellular processes such as senescence, cell cycle arrest and cell death that ultimately reduce tumour burden.

The recent success of molecularly targeted cancer therapies focused on inhibiting oncogenic pathways required for growth and/or survival has greatly improved patient outcomes. However, the relatively smooth topography of some frequently mutated oncogenes such as KRAS renders them not easily druggable by conventional approaches. In addition, the emergence of drug resistance remains a formidable challenge in improving patient outcomes. Consequently, synthetic lethality has emerged as a promising paradigm for cancer drug development with broad potential to uncover novel drug targets and rational combination therapies[65,450].

In this thesis, I present data consistent with the idea that *ahctf1* and *rnpc3* participate in synthetic lethal interactions with mutant *kras* in the *TO(kras^{G12V})* model of HCC. Moreover, these data strongly support targeting Elys and the 65K component of the U12-dependent spliceosome as promising strategies for cancer treatment. Indeed, targeting these proteins may be effective against a wide range of tumours that are driven by oncogenes that fuel high rates of cell proliferation. However, my research also raised another important issue: the role of Tp53 in executing the synthetic lethal response. My experiments clearly demonstrated that although there was a mild beneficial Tp53-independent response to *ahctf1* heterozygosity, the reduction in tumour burden was much more impressive in the presence of wildtype Tp53. This has very important implications in the stratification of patients selected for treatment with drugs designed to disable ELYS function. My data suggest that such treatments are more likely to be successful in patients carrying an intact *TP53* gene. Moreover, in this example, further beneficial outcomes would most likely be derived from selecting patients with higher levels of ELYS (and other nucleoporin) expression.

Ultimately, if such targeted therapies were developed, they would likely be utilised as part of combination treatments rather than as single agents. Such combined treatment modalities can increase the magnitude of therapeutic responses and reduce the emergence of drug resistance to achieve long term cures. This is supported by the data presented in Chapter 5 that show that combining *ahctf1* heterozygosity with selinexor, an inhibitor of nucleocytoplasmic transport, and combining *rnpc3* heterozygosity with either a MEK inhibitor or a U12-dependent splicing inhibitor produces a more robust effect, completely blocking *kras^{G12V}*-driven hepatocyte hyperplasia without impacting normal hepatocytes. These data exemplify the usefulness of combination strategies in improving therapeutic outcomes and highlight the strength of *TO(kras^{G12V})$^{T/+}$* zebrafish as a preclinical model that can be utilised for novel drug discovery and validation.

Whilst all the chemical interventions examined in this thesis were effective at reducing tumour burden driven by oncogenic *kras^{G12V}*, the utility of such treatments in the setting of established tumours harbouring multiple genetic aberrations remains to be investigated. RAS mutant tumours early in their development may exhibit an increased reliance on major cell growth, proliferation and cell death pathways and these vulnerabilities may decrease as

tumourigenesis progresses and cancer cells acquire plasticity to evade targeted treatments. Therefore, early diagnosis and treatment is of critical importance to maximise clinical responses, in addition to expanded anti-cancer strategies.

Traditionally, drug discovery efforts have focused on the development of small molecule drugs that target proteins. However, many globular proteins have characteristic low ligandability, lacking enzymatic active sites or deep binding pockets where compounds can bind with high affinity. Consequently, over 80% of the proteome is considered "undruggable" and is exceedingly difficult to target with conventional approaches[547]. Nevertheless, encouraging progress has been made with the development of proteolysis targeting chimeras (PROTACs) that are capable of inducing proteasome-mediated selective degradation of target proteins. This has greatly expanded the range of viable targets for cancer therapy, offering a promising strategy to target previously intractable proteins[386,387]. Currently, phase I clinical trials (NCT03888612) are ongoing for the first-in-class compound ARV-110, an orally bioavailable PROTAC that selectively targets the androgen receptor (AR) for degradation in patients with metastatic castration-resistant prostate cancer.

Another emerging strategy with immense potential to transform drug development and provide a new modality for the treatment of disease is targeting RNA directly. Consistent with the idea that more than 80% of the proteome is undruggable, only 0.05% of the human genome encodes proteins that are targeted by currently FDA-approved drugs[548,549]. In contrast, utilising small molecules to modulate RNA transcripts or specific RNA isoforms offers nearly unlimited therapeutic opportunities. Targeting RNA with antisense oligonucleotides (ASOs) and short interfering RNAs (siRNAs) that are designed to hybridise to specific mRNAs via base-pairing, has proven to be a successful approach to modulating expression of disease-related mRNAs[550,551]. Whilst such treatments have received regulatory approval for the treatment of Duchenne muscular dystrophy (DMD) and spinal muscular atrophy (SMA), the requirement for local delivery approaches has proven challenging[552]. Targeting RNA with small molecules that may be administered systemically would therefore help overcome these limitations. One emerging strategy is to develop small molecules that specifically interact with highly structured RNA regions[553,554]. In 2020, the first small molecule drug targeting RNA, Evrysdi (risdiplam) received FDA approval for the treatment of SMA[555]. In the context of cancer, RNA therapeutics hold immense promise, enabling the direct targeting of hitherto inaccessible oncogenes and tumour suppressors[556,557]. Moreover, growing recognition of the contribution of long non-coding RNAs (lncRNAs), small non-coding RNAs (sncRNAs), microRNAs (miRNAs) to tumourigenesis, metastasis and drug resistance, has further broadened the potential therapeutic applications of targeting RNA[558-560]. Such possibilities are particularly relevant to my research demonstrating that the 65K protein of the U12-dependent splicing machinery is a potential cancer therapeutic target. This is because as well as containing several unique protein components, the U12-dependent spliceosome also contains 4 unique snRNAs (as outlined in section 4.1.2) that are also indispensable for its

function[432-436]. Accordingly, one future direction for this aspect of my work would be to explore the possibility of directly targeting the unique snRNA components of the U12-dependent spliceosome with rationally designed small molecules[561]. Notwithstanding that small molecule RNA-targeting technology remains in its infancy, likely with a myriad of unknown challenges ahead, I believe it holds immense promise as a new frontier in drug development that is highly relevant to my pre-clinical research.

7 References

1 Sung, H. *et al.* Global Cancer Statistics 2020: GLOBOCAN Estimates of Incidence and Mortality Worldwide for 36 Cancers in 185 Countries. *CA Cancer J Clin* **71**, 209-249, doi:10.3322/caac.21660 (2021).

2 Llovet, J. M. *et al.* Hepatocellular carcinoma. *Nat Rev Dis Primers* **2**, 16018, doi:10.1038/nrdp.2016.18 (2016).

3 Yang, J. D. *et al.* A global view of hepatocellular carcinoma: trends, risk, prevention and management. *Nat Rev Gastroenterol Hepatol* **16**, 589-604, doi:10.1038/s41575-019-0186-y (2019).

4 Park, J. W. *et al.* Global patterns of hepatocellular carcinoma management from diagnosis to death: the BRIDGE Study. *Liver Int* **35**, 2155-2166, doi:10.1111/liv.12818 (2015).

5 Yang, J. D. *et al.* Hepatocellular Carcinoma Occurs at an Earlier Age in Africans, Particularly in Association With Chronic Hepatitis B. *Am J Gastroenterol* **110**, 1629-1631, doi:10.1038/ajg.2015.289 (2015).

6 Farazi, P. A. & DePinho, R. A. Hepatocellular carcinoma pathogenesis: from genes to environment. *Nat Rev Cancer* **6**, 674-687, doi:10.1038/nrc1934 (2006).

7 Craig, A. J., von Felden, J., Garcia-Lezana, T., Sarcognato, S. & Villanueva, A. Tumour evolution in hepatocellular carcinoma. *Nat Rev Gastroenterol Hepatol* **17**, 139-152, doi:10.1038/s41575-019-0229-4 (2020).

8 Kim, E. & Viatour, P. Hepatocellular carcinoma: old friends and new tricks. *Exp Mol Med* **52**, 1898-1907, doi:10.1038/s12276-020-00527-1 (2020).

9 Schulze, K. *et al.* Exome sequencing of hepatocellular carcinomas identifies new mutational signatures and potential therapeutic targets. *Nat Genet* **47**, 505-511, doi:10.1038/ng.3252 (2015).

10 Zucman-Rossi, J., Villanueva, A., Nault, J. C. & Llovet, J. M. Genetic Landscape and Biomarkers of Hepatocellular Carcinoma. *Gastroenterology* **149**, 1226-1239 e1224, doi:10.1053/j.gastro.2015.05.061 (2015).

11 Farazi, P. A. *et al.* Differential impact of telomere dysfunction on initiation and progression of hepatocellular carcinoma. *Cancer Res* **63**, 5021-5027 (2003).

12 Ryan, M. B. & Corcoran, R. B. Therapeutic strategies to target RAS-mutant cancers. *Nat Rev Clin Oncol* **15**, 709-720, doi:10.1038/s41571-018-0105-0 (2018).

13 Pylayeva-Gupta, Y., Grabocka, E. & Bar-Sagi, D. RAS oncogenes: weaving a tumorigenic web. *Nat Rev Cancer* **11**, 761-774, doi:10.1038/nrc3106 (2011).

14 Newell, P. *et al.* Ras pathway activation in hepatocellular carcinoma and anti-tumoral effect of combined sorafenib and rapamycin in vivo. *J Hepatol* **51**, 725-733, doi:10.1016/j.jhep.2009.03.028 (2009).

15 Calvisi, D. F. *et al.* Ubiquitous activation of Ras and Jak/Stat pathways in human HCC. *Gastroenterology* **130**, 1117-1128, doi:10.1053/j.gastro.2006.01.006 (2006).

16 Villanueva, A. & Llovet, J. M. Targeted therapies for hepatocellular carcinoma. *Gastroenterology* **140**, 1410-1426, doi:10.1053/j.gastro.2011.03.006 (2011).

17 Rudalska, R. *et al.* In vivo RNAi screening identifies a mechanism of sorafenib resistance in liver cancer. *Nat Med* **20**, 1138-1146, doi:10.1038/nm.3679 (2014).

18 Pai, E. F. *et al.* Refined crystal structure of the triphosphate conformation of H-ras p21 at 1.35 A resolution: implications for the mechanism of GTP hydrolysis. *EMBO J* **9**, 2351-2359 (1990).

19 Lane, D. P. Cancer. p53, guardian of the genome. *Nature* **358**, 15-16, doi:10.1038/358015a0 (1992).
20 Bieging, K. T., Mello, S. S. & Attardi, L. D. Unravelling mechanisms of p53-mediated tumour suppression. *Nat Rev Cancer* **14**, 359-370, doi:10.1038/nrc3711 (2014).
21 Vousden, K. H. & Prives, C. Blinded by the Light: The Growing Complexity of p53. *Cell* **137**, 413-431, doi:10.1016/j.cell.2009.04.037 (2009).
22 Bressac, B., Kew, M., Wands, J. & Ozturk, M. Selective G to T mutations of p53 gene in hepatocellular carcinoma from southern Africa. *Nature* **350**, 429-431, doi:10.1038/350429a0 (1991).
23 Liu, J. *et al.* Alterations of TP53 are associated with a poor outcome for patients with hepatocellular carcinoma: evidence from a systematic review and meta-analysis. *Eur J Cancer* **48**, 2328-2338, doi:10.1016/j.ejca.2012.03.001 (2012).
24 Vousden, K. H. & Lane, D. P. p53 in health and disease. *Nat Rev Mol Cell Biol* **8**, 275-283, doi:10.1038/nrm2147 (2007).
25 Hoshida, Y. *et al.* Integrative transcriptome analysis reveals common molecular subclasses of human hepatocellular carcinoma. *Cancer Res* **69**, 7385-7392, doi:10.1158/0008-5472.CAN-09-1089 (2009).
26 Villanueva, A. *et al.* Combining clinical, pathology, and gene expression data to predict recurrence of hepatocellular carcinoma. *Gastroenterology* **140**, 1501-1512 e1502, doi:10.1053/j.gastro.2011.02.006 (2011).
27 Lee, J. S. *et al.* Classification and prediction of survival in hepatocellular carcinoma by gene expression profiling. *Hepatology* **40**, 667-676, doi:10.1002/hep.20375 (2004).
28 Boyault, S. *et al.* Transcriptome classification of HCC is related to gene alterations and to new therapeutic targets. *Hepatology* **45**, 42-52, doi:10.1002/hep.21467 (2007).
29 Mao, T. L., Chu, J. S., Jeng, Y. M., Lai, P. L. & Hsu, H. C. Expression of mutant nuclear beta-catenin correlates with non-invasive hepatocellular carcinoma, absence of portal vein spread, and good prognosis. *J Pathol* **193**, 95-101, doi:10.1002/1096-9896(2000)9999:9999<::AID-PATH720>3.0.CO;2-3 (2001).
30 Llovet, J. M., Montal, R., Sia, D. & Finn, R. S. Molecular therapies and precision medicine for hepatocellular carcinoma. *Nat Rev Clin Oncol* **15**, 599-616, doi:10.1038/s41571-018-0073-4 (2018).
31 Bray, F. *et al.* Global cancer statistics 2018: GLOBOCAN estimates of incidence and mortality worldwide for 36 cancers in 185 countries. *CA Cancer J Clin* **68**, 394-424, doi:10.3322/caac.21492 (2018).
32 Villanueva, A., Minguez, B., Forner, A., Reig, M. & Llovet, J. M. Hepatocellular carcinoma: novel molecular approaches for diagnosis, prognosis, and therapy. *Annu Rev Med* **61**, 317-328, doi:10.1146/annurev.med.080608.100623 (2010).
33 Llovet, J. M., Villanueva, A., Lachenmayer, A. & Finn, R. S. Advances in targeted therapies for hepatocellular carcinoma in the genomic era. *Nat Rev Clin Oncol* **12**, 436, doi:10.1038/nrclinonc.2015.121 (2015).
34 Patel, T. & Harnois, D. Assessment of response to therapy in hepatocellular carcinoma. *Annals of medicine* **46**, 130-137, doi:10.3109/07853890.2014.891355 (2014).
35 Lo, C. M. *et al.* Randomized controlled trial of transarterial lipiodol chemoembolization for unresectable hepatocellular carcinoma. *Hepatology* **35**, 1164-1171, doi:10.1053/jhep.2002.33156 (2002).

36 Kudo, M. *et al.* Brivanib as adjuvant therapy to transarterial chemoembolization in patients with hepatocellular carcinoma: A randomized phase III trial. *Hepatology* **60**, 1697-1707, doi:10.1002/hep.27290 (2014).
37 Llovet, J. M. *et al.* Sorafenib in advanced hepatocellular carcinoma. *N Engl J Med* **359**, 378-390, doi:10.1056/NEJMoa0708857 (2008).
38 Bruix, J. *et al.* Adjuvant sorafenib for hepatocellular carcinoma after resection or ablation (STORM): a phase 3, randomised, double-blind, placebo-controlled trial. *The Lancet Oncology* **16**, 1344-1354, doi:10.1016/s1470-2045(15)00198-9 (2015).
39 Johnson, P. J. *et al.* Brivanib versus sorafenib as first-line therapy in patients with unresectable, advanced hepatocellular carcinoma: results from the randomized phase III BRISK-FL study. *J Clin Oncol* **31**, 3517-3524, doi:10.1200/JCO.2012.48.4410 (2013).
40 Cheng, A. L. *et al.* Sunitinib versus sorafenib in advanced hepatocellular cancer: results of a randomized phase III trial. *J Clin Oncol* **31**, 4067-4075, doi:10.1200/JCO.2012.45.8372 (2013).
41 Cainap, C. *et al.* Linifanib versus Sorafenib in patients with advanced hepatocellular carcinoma: results of a randomized phase III trial. *J Clin Oncol* **33**, 172-179, doi:10.1200/JCO.2013.54.3298 (2015).
42 Zhu, A. X. *et al.* SEARCH: a phase III, randomized, double-blind, placebo-controlled trial of sorafenib plus erlotinib in patients with advanced hepatocellular carcinoma. *J Clin Oncol* **33**, 559-566, doi:10.1200/JCO.2013.53.7746 (2015).
43 Llovet, J. M. *et al.* Brivanib in patients with advanced hepatocellular carcinoma who were intolerant to sorafenib or for whom sorafenib failed: results from the randomized phase III BRISK-PS study. *J Clin Oncol* **31**, 3509-3516, doi:10.1200/JCO.2012.47.3009 (2013).
44 Zhu, A. X. *et al.* Effect of everolimus on survival in advanced hepatocellular carcinoma after failure of sorafenib: the EVOLVE-1 randomized clinical trial. *JAMA* **312**, 57-67, doi:10.1001/jama.2014.7189 (2014).
45 Llovet, J. M. & Hernandez-Gea, V. Hepatocellular carcinoma: reasons for phase III failure and novel perspectives on trial design. *Clin Cancer Res* **20**, 2072-2079, doi:10.1158/1078-0432.ccr-13-0547 (2014).
46 Bruix, J., da Fonseca, L. G. & Reig, M. Insights into the success and failure of systemic therapy for hepatocellular carcinoma. *Nat Rev Gastroenterol Hepatol* **16**, 617-630, doi:10.1038/s41575-019-0179-x (2019).
47 Bruix, J. *et al.* Regorafenib for patients with hepatocellular carcinoma who progressed on sorafenib treatment (RESORCE): a randomised, double-blind, placebo-controlled, phase 3 trial. *Lancet* **389**, 56-66, doi:10.1016/S0140-6736(16)32453-9 (2017).
48 Kudo, M. *et al.* Lenvatinib versus sorafenib in first-line treatment of patients with unresectable hepatocellular carcinoma: a randomised phase 3 non-inferiority trial. *Lancet* **391**, 1163-1173, doi:10.1016/S0140-6736(18)30207-1 (2018).
49 Abou-Alfa, G. K. *et al.* Cabozantinib in Patients with Advanced and Progressing Hepatocellular Carcinoma. *N Engl J Med* **379**, 54-63, doi:10.1056/NEJMoa1717002 (2018).
50 Zhu, A. X. *et al.* Ramucirumab after sorafenib in patients with advanced hepatocellular carcinoma and increased alpha-fetoprotein concentrations (REACH-

2): a randomised, double-blind, placebo-controlled, phase 3 trial. *Lancet Oncol* **20**, 282-296, doi:10.1016/S1470-2045(18)30937-9 (2019).
51 Zhu, A. X. *et al.* Pembrolizumab in patients with advanced hepatocellular carcinoma previously treated with sorafenib (KEYNOTE-224): a non-randomised, open-label phase 2 trial. *Lancet Oncol* **19**, 940-952, doi:10.1016/S1470-2045(18)30351-6 (2018).
52 El-Khoueiry, A. B. *et al.* Nivolumab in patients with advanced hepatocellular carcinoma (CheckMate 040): an open-label, non-comparative, phase 1/2 dose escalation and expansion trial. *Lancet* **389**, 2492-2502, doi:10.1016/S0140-6736(17)31046-2 (2017).
53 Yau, T. *et al.* Efficacy and Safety of Nivolumab Plus Ipilimumab in Patients With Advanced Hepatocellular Carcinoma Previously Treated With Sorafenib: The CheckMate 040 Randomized Clinical Trial. *JAMA Oncol*, doi:10.1001/jamaoncol.2020.4564 (2020).
54 Luo, J., Solimini, N. L. & Elledge, S. J. Principles of cancer therapy: oncogene and non-oncogene addiction. *Cell* **136**, 823-837, doi:10.1016/j.cell.2009.02.024 (2009).
55 Weinstein, I. B. Cancer. Addiction to oncogenes--the Achilles heal of cancer. *Science* **297**, 63-64, doi:10.1126/science.1073096 (2002).
56 Weinstein, I. B. & Joe, A. Oncogene addiction. *Cancer Res* **68**, 3077-3080; discussion 3080, doi:10.1158/0008-5472.CAN-07-3293 (2008).
57 Huettner, C. S., Zhang, P., Van Etten, R. A. & Tenen, D. G. Reversibility of acute B-cell leukaemia induced by BCR-ABL1. *Nat Genet* **24**, 57-60, doi:10.1038/71691 (2000).
58 Druker, B. J. *et al.* Efficacy and safety of a specific inhibitor of the BCR-ABL tyrosine kinase in chronic myeloid leukemia. *N Engl J Med* **344**, 1031-1037, doi:10.1056/NEJM200104053441401 (2001).
59 Hochhaus, A. *et al.* Long-Term Outcomes of Imatinib Treatment for Chronic Myeloid Leukemia. *N Engl J Med* **376**, 917-927, doi:10.1056/NEJMoa1609324 (2017).
60 Lito, P., Solomon, M., Li, L. S., Hansen, R. & Rosen, N. Allele-specific inhibitors inactivate mutant KRAS G12C by a trapping mechanism. *Science* **351**, 604-608, doi:10.1126/science.aad6204 (2016).
61 Canon, J. *et al.* The clinical KRAS(G12C) inhibitor AMG 510 drives anti-tumour immunity. *Nature* **575**, 217-223, doi:10.1038/s41586-019-1694-1 (2019).
62 Chen, H., Liu, H. & Qing, G. Targeting oncogenic Myc as a strategy for cancer treatment. *Signal Transduct Target Ther* **3**, 5, doi:10.1038/s41392-018-0008-7 (2018).
63 Solimini, N. L., Luo, J. & Elledge, S. J. Non-oncogene addiction and the stress phenotype of cancer cells. *Cell* **130**, 986-988, doi:10.1016/j.cell.2007.09.007 (2007).
64 Kotsantis, P., Petermann, E. & Boulton, S. J. Mechanisms of Oncogene-Induced Replication Stress: Jigsaw Falling into Place. *Cancer Discov* **8**, 537-555, doi:10.1158/2159-8290.CD-17-1461 (2018).
65 Gao, S. & Lai, L. Synthetic lethality in drug development: the dawn is coming. *Future Med Chem* **10**, 2129-2132, doi:10.4155/fmc-2018-0227 (2018).
66 Kaelin, W. G., Jr. The concept of synthetic lethality in the context of anticancer therapy. *Nat Rev Cancer* **5**, 689-698, doi:10.1038/nrc1691 (2005).
67 O'Neil, N. J., Bailey, M. L. & Hieter, P. Synthetic lethality and cancer. *Nat Rev Genet* **18**, 613-623, doi:10.1038/nrg.2017.47 (2017).
68 Farmer, H. *et al.* Targeting the DNA repair defect in BRCA mutant cells as a therapeutic strategy. *Nature* **434**, 917-921, doi:10.1038/nature03445 (2005).

69 Bryant, H. E. *et al.* Specific killing of BRCA2-deficient tumours with inhibitors of poly(ADP-ribose) polymerase. *Nature* **434**, 913-917, doi:10.1038/nature03443 (2005).
70 Lord, C. J. & Ashworth, A. PARP inhibitors: Synthetic lethality in the clinic. *Science* **355**, 1152-1158, doi:10.1126/science.aam7344 (2017).
71 Lord, C. J., Tutt, A. N. & Ashworth, A. Synthetic lethality and cancer therapy: lessons learned from the development of PARP inhibitors. *Annu Rev Med* **66**, 455-470, doi:10.1146/annurev-med-050913-022545 (2015).
72 Murai, J. *et al.* Trapping of PARP1 and PARP2 by Clinical PARP Inhibitors. *Cancer Res* **72**, 5588-5599, doi:10.1158/0008-5472.CAN-12-2753 (2012).
73 Hopkins, T. A. *et al.* Mechanistic Dissection of PARP1 Trapping and the Impact on In Vivo Tolerability and Efficacy of PARP Inhibitors. *Mol Cancer Res* **13**, 1465-1477, doi:10.1158/1541-7786.MCR-15-0191-T (2015).
74 Pujade-Lauraine, E. *et al.* Olaparib tablets as maintenance therapy in patients with platinum-sensitive, relapsed ovarian cancer and a BRCA1/2 mutation (SOLO2/ENGOT-Ov21): a double-blind, randomised, placebo-controlled, phase 3 trial. *Lancet Oncol* **18**, 1274-1284, doi:10.1016/S1470-2045(17)30469-2 (2017).
75 Curtin, N. J. & Szabo, C. Poly(ADP-ribose) polymerase inhibition: past, present and future. *Nat Rev Drug Discov* **19**, 711-736, doi:10.1038/s41573-020-0076-6 (2020).
76 Luo, J. *et al.* A genome-wide RNAi screen identifies multiple synthetic lethal interactions with the Ras oncogene. *Cell* **137**, 835-848, doi:10.1016/j.cell.2009.05.006 (2009).
77 Barbie, D. A. *et al.* Systematic RNA interference reveals that oncogenic KRAS-driven cancers require TBK1. *Nature* **462**, 108-112, doi:10.1038/nature08460 (2009).
78 Steckel, M. *et al.* Determination of synthetic lethal interactions in KRAS oncogene-dependent cancer cells reveals novel therapeutic targeting strategies. *Cell Res* **22**, 1227-1245, doi:10.1038/cr.2012.82 (2012).
79 Downward, J. RAS Synthetic Lethal Screens Revisited: Still Seeking the Elusive Prize? *Clin Cancer Res* **21**, 1802-1809, doi:10.1158/1078-0432.CCR-14-2180 (2015).
80 Ryan, C. J., Bajrami, I. & Lord, C. J. Synthetic Lethality and Cancer - Penetrance as the Major Barrier. *Trends Cancer* **4**, 671-683, doi:10.1016/j.trecan.2018.08.003 (2018).
81 Mullard, A. Synthetic lethality screens point the way to new cancer drug targets. *Nat Rev Drug Discov* **16**, 736, doi:10.1038/nrd.2017.190 (2017).
82 Shalem, O. *et al.* Genome-scale CRISPR-Cas9 knockout screening in human cells. *Science* **343**, 84-87, doi:10.1126/science.1247005 (2014).
83 Wang, T. *et al.* Gene Essentiality Profiling Reveals Gene Networks and Synthetic Lethal Interactions with Oncogenic Ras. *Cell* **168**, 890-903 e815, doi:10.1016/j.cell.2017.01.013 (2017).
84 Sulahian, R. *et al.* Synthetic Lethal Interaction of SHOC2 Depletion with MEK Inhibition in RAS-Driven Cancers. *Cell Rep* **29**, 118-134 e118, doi:10.1016/j.celrep.2019.08.090 (2019).
85 Kelly, M. R. *et al.* Combined Proteomic and Genetic Interaction Mapping Reveals New RAS Effector Pathways and Susceptibilities. *Cancer Discov* **10**, 1950-1967, doi:10.1158/2159-8290.CD-19-1274 (2020).
86 Anderson, G. R. *et al.* A Landscape of Therapeutic Cooperativity in KRAS Mutant Cancers Reveals Principles for Controlling Tumor Evolution. *Cell Rep* **20**, 999-1015, doi:10.1016/j.celrep.2017.07.006 (2017).

87 Gorre, M. E. *et al.* Clinical resistance to STI-571 cancer therapy caused by BCR-ABL gene mutation or amplification. *Science* **293**, 876-880, doi:10.1126/science.1062538 (2001).
88 Barber, L. J. *et al.* Secondary mutations in BRCA2 associated with clinical resistance to a PARP inhibitor. *J Pathol* **229**, 422-429, doi:10.1002/path.4140 (2013).
89 Groenendijk, F. H. & Bernards, R. Drug resistance to targeted therapies: deja vu all over again. *Mol Oncol* **8**, 1067-1083, doi:10.1016/j.molonc.2014.05.004 (2014).
90 Aiello, N. M. & Stanger, B. Z. Echoes of the embryo: using the developmental biology toolkit to study cancer. *Dis Model Mech* **9**, 105-114, doi:10.1242/dmm.023184 (2016).
91 Takebe, N. *et al.* Targeting Notch, Hedgehog, and Wnt pathways in cancer stem cells: clinical update. *Nat Rev Clin Oncol* **12**, 445-464, doi:10.1038/nrclinonc.2015.61 (2015).
92 Klaus, A. & Birchmeier, W. Wnt signalling and its impact on development and cancer. *Nat Rev Cancer* **8**, 387-398, doi:10.1038/nrc2389 (2008).
93 Zhan, T., Rindtorff, N. & Boutros, M. Wnt signaling in cancer. *Oncogene* **36**, 1461-1473, doi:10.1038/onc.2016.304 (2017).
94 Jung, Y. S. & Park, J. I. Wnt signaling in cancer: therapeutic targeting of Wnt signaling beyond beta-catenin and the destruction complex. *Exp Mol Med* **52**, 183-191, doi:10.1038/s12276-020-0380-6 (2020).
95 Briscoe, J. & Therond, P. P. The mechanisms of Hedgehog signalling and its roles in development and disease. *Nat Rev Mol Cell Biol* **14**, 416-429, doi:10.1038/nrm3598 (2013).
96 Amakye, D., Jagani, Z. & Dorsch, M. Unraveling the therapeutic potential of the Hedgehog pathway in cancer. *Nat Med* **19**, 1410-1422, doi:10.1038/nm.3389 (2013).
97 Ng, J. M. & Curran, T. The Hedgehog's tale: developing strategies for targeting cancer. *Nat Rev Cancer* **11**, 493-501, doi:10.1038/nrc3079 (2011).
98 Epstein, E. H. Basal cell carcinomas: attack of the hedgehog. *Nat Rev Cancer* **8**, 743-754, doi:10.1038/nrc2503 (2008).
99 Andersson, E. R., Sandberg, R. & Lendahl, U. Notch signaling: simplicity in design, versatility in function. *Development* **138**, 3593-3612, doi:10.1242/dev.063610 (2011).
100 Bray, S. J. Notch signalling in context. *Nat Rev Mol Cell Biol* **17**, 722-735, doi:10.1038/nrm.2016.94 (2016).
101 Ellisen, L. W. *et al.* TAN-1, the human homolog of the Drosophila notch gene, is broken by chromosomal translocations in T lymphoblastic neoplasms. *Cell* **66**, 649-661, doi:10.1016/0092-8674(91)90111-b (1991).
102 Weng, A. P. *et al.* Activating mutations of NOTCH1 in human T cell acute lymphoblastic leukemia. *Science* **306**, 269-271, doi:10.1126/science.1102160 (2004).
103 Andersson, E. R. & Lendahl, U. Therapeutic modulation of Notch signalling--are we there yet? *Nat Rev Drug Discov* **13**, 357-378, doi:10.1038/nrd4252 (2014).
104 Aster, J. C., Pear, W. S. & Blacklow, S. C. The Varied Roles of Notch in Cancer. *Annual review of pathology* **12**, 245-275, doi:10.1146/annurev-pathol-052016-100127 (2017).
105 Nowell, C. S. & Radtke, F. Notch as a tumour suppressor. *Nat Rev Cancer* **17**, 145-159, doi:10.1038/nrc.2016.145 (2017).

106 Bugter, J. M., Fenderico, N. & Maurice, M. M. Mutations and mechanisms of WNT pathway tumour suppressors in cancer. *Nat Rev Cancer* **21**, 5-21, doi:10.1038/s41568-020-00307-z (2021).
107 Axelson, M. *et al.* U.S. Food and Drug Administration approval: vismodegib for recurrent, locally advanced, or metastatic basal cell carcinoma. *Clin Cancer Res* **19**, 2289-2293, doi:10.1158/1078-0432.CCR-12-1956 (2013).
108 Casey, D. *et al.* FDA Approval Summary: Sonidegib for Locally Advanced Basal Cell Carcinoma. *Clin Cancer Res* **23**, 2377-2381, doi:10.1158/1078-0432.CCR-16-2051 (2017).
109 Majumder, S. *et al.* Targeting Notch in oncology: the path forward. *Nat Rev Drug Discov*, doi:10.1038/s41573-020-00091-3 (2020).
110 Hanahan, D. & Weinberg, R. A. The hallmarks of cancer. *Cell* **100**, 57-70, doi:10.1016/s0092-8674(00)81683-9 (2000).
111 Hanahan, D. & Weinberg, R. A. Hallmarks of cancer: the next generation. *Cell* **144**, 646-674, doi:10.1016/j.cell.2011.02.013 (2011).
112 Acloque, H., Adams, M. S., Fishwick, K., Bronner-Fraser, M. & Nieto, M. A. Epithelial-mesenchymal transitions: the importance of changing cell state in development and disease. *J Clin Invest* **119**, 1438-1449, doi:10.1172/JCI38019 (2009).
113 Thiery, J. P. Epithelial-mesenchymal transitions in tumour progression. *Nat Rev Cancer* **2**, 442-454, doi:10.1038/nrc822 (2002).
114 Chung, A. S., Lee, J. & Ferrara, N. Targeting the tumour vasculature: insights from physiological angiogenesis. *Nat Rev Cancer* **10**, 505-514, doi:10.1038/nrc2868 (2010).
115 Voss, A. K. & Strasser, A. The essentials of developmental apoptosis. *F1000Res* **9**, doi:10.12688/f1000research.21571.1 (2020).
116 Igney, F. H. & Krammer, P. H. Death and anti-death: tumour resistance to apoptosis. *Nat Rev Cancer* **2**, 277-288, doi:10.1038/nrc776 (2002).
117 Roosen-Runge, E. C. On the early development—bipolar differentiation and cleavage—of the zebra fish, brachydanio rerio. *The Biological Bulletin* **75**, 119-133, doi:10.2307/1537678 (1938).
118 Roosen-Runge, E. C. Karyokinesis during cleavage of the zebra fish brachydanio rerio. *The Biological Bulletin* **77**, 79-91, doi:10.2307/1537846 (1939).
119 Kimmel, C. B., Ballard, W. W., Kimmel, S. R., Ullmann, B. & Schilling, T. F. Stages of embryonic development of the zebrafish. *Dev Dyn* **203**, 253-310, doi:10.1002/aja.1002030302 (1995).
120 Astone, M., Dankert, E. N., Alam, S. K. & Hoeppner, L. H. Fishing for cures: The alLURE of using zebrafish to develop precision oncology therapies. *NPJ Precis Oncol* **1**, doi:10.1038/s41698-017-0043-9 (2017).
121 Liu, S. & Leach, S. D. Zebrafish models for cancer. *Annual review of pathology* **6**, 71-93, doi:10.1146/annurev-pathol-011110-130330 (2011).
122 Howe, K. *et al.* The zebrafish reference genome sequence and its relationship to the human genome. *Nature* **496**, 498-503, doi:10.1038/nature12111 (2013).
123 Kettleborough, R. N. *et al.* A systematic genome-wide analysis of zebrafish protein-coding gene function. *Nature* **496**, 494-497, doi:10.1038/nature11992 (2013).
124 Chernyavskaya, Y., Kent, B. & Sadler, K. C. Zebrafish Discoveries in Cancer Epigenetics. *Adv Exp Med Biol* **916**, 169-197, doi:10.1007/978-3-319-30654-4_8 (2016).

125 Lieschke, G. J. & Currie, P. D. Animal models of human disease: zebrafish swim into view. *Nat Rev Genet* **8**, 353-367, doi:10.1038/nrg2091 (2007).
126 White, R., Rose, K. & Zon, L. Zebrafish cancer: the state of the art and the path forward. *Nat Rev Cancer* **13**, 624-636, doi:10.1038/nrc3589 (2013).
127 Amsterdam, A. & Hopkins, N. Mutagenesis strategies in zebrafish for identifying genes involved in development and disease. *Trends Genet* **22**, 473-478, doi:10.1016/j.tig.2006.06.011 (2006).
128 Gu, Q., Yang, X., He, X., Li, Q. & Cui, Z. Generation and characterization of a transgenic zebrafish expressing the reverse tetracycline transactivator. *Journal of genetics and genomics = Yi chuan xue bao* **40**, 523-531, doi:10.1016/j.jgg.2013.06.008 (2013).
129 Berghmans, S. *et al.* Making waves in cancer research: new models in the zebrafish. *BioTechniques* **39**, 227-237 (2005).
130 Langenau, D. M. *et al.* Myc-induced T cell leukemia in transgenic zebrafish. *Science* **299**, 887-890, doi:10.1126/science.1080280 (2003).
131 Hwang, K. L. & Goessling, W. Baiting for Cancer: Using the Zebrafish as a Model in Liver and Pancreatic Cancer. *Advances in experimental medicine and biology* **916**, 391-410, doi:10.1007/978-3-319-30654-4_17 (2016).
132 Wrighton, P. J., Oderberg, I. M. & Goessling, W. There Is Something Fishy About Liver Cancer: Zebrafish Models of Hepatocellular Carcinoma. *Cell Mol Gastroenterol Hepatol* **8**, 347-363, doi:10.1016/j.jcmgh.2019.05.002 (2019).
133 McConnell, A. M., Noonan, H. R. & Zon, L. I. Reeling in the Zebrafish Cancer Models. *Annual Review of Cancer Biology* **5**, doi:10.1146/annurev-cancerbio-051320-014135 (2020).
134 Lawson, N. D. & Weinstein, B. M. In vivo imaging of embryonic vascular development using transgenic zebrafish. *Dev Biol* **248**, 307-318, doi:10.1006/dbio.2002.0711 (2002).
135 White, R. M. *et al.* Transparent adult zebrafish as a tool for in vivo transplantation analysis. *Cell Stem Cell* **2**, 183-189, doi:10.1016/j.stem.2007.11.002 (2008).
136 Knopf, F. *et al.* Dually inducible TetON systems for tissue-specific conditional gene expression in zebrafish. *Proceedings of the National Academy of Sciences of the United States of America* **107**, 19933-19938, doi:10.1073/pnas.1007799107 (2010).
137 Yen, J., White, R. M. & Stemple, D. L. Zebrafish models of cancer: progress and future challenges. *Curr Opin Genet Dev* **24**, 38-45, doi:10.1016/j.gde.2013.11.003 (2014).
138 Callahan, S. J. *et al.* Cancer modeling by Transgene Electroporation in Adult Zebrafish (TEAZ). *Dis Model Mech* **11**, doi:10.1242/dmm.034561 (2018).
139 Nicoli, S. & Presta, M. The zebrafish/tumor xenograft angiogenesis assay. *Nat Protoc* **2**, 2918-2923, doi:10.1038/nprot.2007.412 (2007).
140 Haldi, M., Ton, C., Seng, W. L. & McGrath, P. Human melanoma cells transplanted into zebrafish proliferate, migrate, produce melanin, form masses and stimulate angiogenesis in zebrafish. *Angiogenesis* **9**, 139-151, doi:10.1007/s10456-006-9040-2 (2006).
141 Lam, S. H., Chua, H. L., Gong, Z., Lam, T. J. & Sin, Y. M. Development and maturation of the immune system in zebrafish, Danio rerio: a gene expression profiling, in situ hybridization and immunological study. *Dev Comp Immunol* **28**, 9-28, doi:10.1016/s0145-305x(03)00103-4 (2004).

142 Konantz, M. *et al.* Zebrafish xenografts as a tool for in vivo studies on human cancer. *Ann N Y Acad Sci* **1266**, 124-137, doi:10.1111/j.1749-6632.2012.06575.x (2012).
143 Lee, L. M., Seftor, E. A., Bonde, G., Cornell, R. A. & Hendrix, M. J. The fate of human malignant melanoma cells transplanted into zebrafish embryos: assessment of migration and cell division in the absence of tumor formation. *Dev Dyn* **233**, 1560-1570, doi:10.1002/dvdy.20471 (2005).
144 Fior, R. *et al.* Single-cell functional and chemosensitive profiling of combinatorial colorectal therapy in zebrafish xenografts. *Proc Natl Acad Sci U S A* **114**, E8234-E8243, doi:10.1073/pnas.1618389114 (2017).
145 Marques, I. J. *et al.* Metastatic behaviour of primary human tumours in a zebrafish xenotransplantation model. *BMC Cancer* **9**, 128, doi:10.1186/1471-2407-9-128 (2009).
146 Yan, C. *et al.* Visualizing Engrafted Human Cancer and Therapy Responses in Immunodeficient Zebrafish. *Cell* **177**, 1903-1914 e1914, doi:10.1016/j.cell.2019.04.004 (2019).
147 Sanchez-Rivera, F. J. & Jacks, T. Applications of the CRISPR-Cas9 system in cancer biology. *Nat Rev Cancer* **15**, 387-395, doi:10.1038/nrc3950 (2015).
148 Hwang, W. Y. *et al.* Efficient genome editing in zebrafish using a CRISPR-Cas system. *Nat Biotechnol* **31**, 227-229, doi:10.1038/nbt.2501 (2013).
149 MacRae, C. A. & Peterson, R. T. Zebrafish as tools for drug discovery. *Nat Rev Drug Discov* **14**, 721-731, doi:10.1038/nrd4627 (2015).
150 Zon, L. I. & Peterson, R. T. In vivo drug discovery in the zebrafish. *Nat Rev Drug Discov* **4**, 35-44, doi:10.1038/nrd1606 (2005).
151 Tat, J., Liu, M. & Wen, X. Y. Zebrafish cancer and metastasis models for in vivo drug discovery. *Drug Discov Today Technol* **10**, e83-89, doi:10.1016/j.ddtec.2012.04.006 (2013).
152 Fazio, M., Ablain, J., Chuan, Y., Langenau, D. M. & Zon, L. I. Zebrafish patient avatars in cancer biology and precision cancer therapy. *Nat Rev Cancer* **20**, 263-273, doi:10.1038/s41568-020-0252-3 (2020).
153 Patton, E. E. *et al.* BRAF mutations are sufficient to promote nevi formation and cooperate with p53 in the genesis of melanoma. *Curr Biol* **15**, 249-254, doi:10.1016/j.cub.2005.01.031 (2005).
154 Ceol, C. J. *et al.* The histone methyltransferase SETDB1 is recurrently amplified in melanoma and accelerates its onset. *Nature* **471**, 513-517, doi:10.1038/nature09806 (2011).
155 White, R. M. *et al.* DHODH modulates transcriptional elongation in the neural crest and melanoma. *Nature* **471**, 518-522, doi:10.1038/nature09882 (2011).
156 Kaufman, C. K. *et al.* A zebrafish melanoma model reveals emergence of neural crest identity during melanoma initiation. *Science* **351**, aad2197, doi:10.1126/science.aad2197 (2016).
157 Fazio, M. *et al.* SATB2 induction of a neural crest mesenchyme-like program drives melanoma invasion and drug resistance. *Elife* **10**, doi:10.7554/eLife.64370 (2021).
158 Johansson, J. A. *et al.* PRL3-DDX21 Transcriptional Control of Endolysosomal Genes Restricts Melanocyte Stem Cell Differentiation. *Dev Cell* **54**, 317-332 e319, doi:10.1016/j.devcel.2020.06.013 (2020).

159 Santoriello, C. *et al.* RNA helicase DDX21 mediates nucleotide stress responses in neural crest and melanoma cells. *Nat Cell Biol* **22**, 372-379, doi:10.1038/s41556-020-0493-0 (2020).
160 Tan, J. L. *et al.* Stress from Nucleotide Depletion Activates the Transcriptional Regulator HEXIM1 to Suppress Melanoma. *Mol Cell* **62**, 34-46, doi:10.1016/j.molcel.2016.03.013 (2016).
161 Hanson, K. *et al.* The anti-rheumatic drug, leflunomide, synergizes with MEK inhibition to suppress melanoma growth. *Oncotarget* **9**, 3815-3829, doi:10.18632/oncotarget.23378 (2018).
162 Zhang, M. *et al.* Adipocyte-Derived Lipids Mediate Melanoma Progression via FATP Proteins. *Cancer Discov* **8**, 1006-1025, doi:10.1158/2159-8290.CD-17-1371 (2018).
163 Lu, J. W. *et al.* Liver development and cancer formation in zebrafish. *Birth defects research. Part C, Embryo today : reviews* **93**, 157-172, doi:10.1002/bdrc.20205 (2011).
164 Wallace, K. N. & Pack, M. Unique and conserved aspects of gut development in zebrafish. *Developmental biology* **255**, 12-29, doi:10.1016/s0012-1606(02)00034-9 (2003).
165 Lu, J. W. *et al.* Zebrafish as a disease model for studying human hepatocellular carcinoma. *World J Gastroenterol* **21**, 12042-12058, doi:10.3748/wjg.v21.i42.12042 (2015).
166 Li, Z. *et al.* Transcriptomic analysis of a transgenic zebrafish hepatocellular carcinoma model reveals a prominent role of immune responses in tumour progression and regression. *International journal of cancer. Journal international du cancer* **135**, 1564-1573, doi:10.1002/ijc.28794 (2014).
167 Zheng, W. *et al.* Xmrk, kras and myc transgenic zebrafish liver cancer models share molecular signatures with subsets of human hepatocellular carcinoma. *PLoS One* **9**, e91179, doi:10.1371/journal.pone.0091179 (2014).
168 Lam, S. H. *et al.* Conservation of gene expression signatures between zebrafish and human liver tumors and tumor progression. *Nat Biotechnol* **24**, 73-75, doi:10.1038/nbt1169 (2006).
169 Spitsbergen, J. M. *et al.* Neoplasia in zebrafish (Danio rerio) treated with 7,12-dimethylbenz[a]anthracene by two exposure routes at different developmental stages. *Toxicol Pathol* **28**, 705-715, doi:10.1177/019262330002800511 (2000).
170 Spitsbergen, J. M. *et al.* Neoplasia in zebrafish (Danio rerio) treated with N-methyl-N'-nitro-N-nitrosoguanidine by three exposure routes at different developmental stages. *Toxicol Pathol* **28**, 716-725, doi:10.1177/019262330002800512 (2000).
171 Mudbhary, R. *et al.* UHRF1 overexpression drives DNA hypomethylation and hepatocellular carcinoma. *Cancer Cell* **25**, 196-209, doi:10.1016/j.ccr.2014.01.003 (2014).
172 Li, Z. *et al.* A transgenic zebrafish liver tumor model with inducible Myc expression reveals conserved Myc signatures with mammalian liver tumors. *Dis Model Mech* **6**, 414-423, doi:10.1242/dmm.010462 (2013).
173 Nguyen, A. T. *et al.* A high level of liver-specific expression of oncogenic Kras(V12) drives robust liver tumorigenesis in transgenic zebrafish. *Dis Model Mech* **4**, 801-813, doi:10.1242/dmm.007831 (2011).

174 Nguyen, A. T. *et al.* An inducible kras(V12) transgenic zebrafish model for liver tumorigenesis and chemical drug screening. *Dis Model Mech* **5**, 63-72, doi:10.1242/dmm.008367 (2012).
175 Li, Z. *et al.* Inducible and repressable oncogene-addicted hepatocellular carcinoma in Tet-on xmrk transgenic zebrafish. *J Hepatol* **56**, 419-425, doi:10.1016/j.jhep.2011.07.025 (2012).
176 Chew, T. W. *et al.* Crosstalk of Ras and Rho: activation of RhoA abates Kras-induced liver tumorigenesis in transgenic zebrafish models. *Oncogene* **33**, 2717-2727, doi:10.1038/onc.2013.240 (2014).
177 Huo, X. *et al.* Transcriptomic analyses of oncogenic hepatocytes reveal common and different molecular pathways of hepatocarcinogenesis in different developmental stages and genders in kras(G12V) transgenic zebrafish. *Biochem Biophys Res Commun* **510**, 558-564, doi:10.1016/j.bbrc.2019.02.008 (2019).
178 Li, Y., Li, H., Spitsbergen, J. M. & Gong, Z. Males develop faster and more severe hepatocellular carcinoma than females in kras(V12) transgenic zebrafish. *Sci Rep* **7**, 41280, doi:10.1038/srep41280 (2017).
179 Yan, C., Yang, Q. & Gong, Z. Tumor-Associated Neutrophils and Macrophages Promote Gender Disparity in Hepatocellular Carcinoma in Zebrafish. *Cancer Res* **77**, 1395-1407, doi:10.1158/0008-5472.CAN-16-2200 (2017).
180 Yang, Q., Yan, C. & Gong, Z. Interaction of hepatic stellate cells with neutrophils and macrophages in the liver following oncogenic kras activation in transgenic zebrafish. *Sci Rep* **8**, 8495, doi:10.1038/s41598-018-26612-0 (2018).
181 Yang, Q., Yan, C. & Gong, Z. Activation of liver stromal cells is associated with male-biased liver tumor initiation in xmrk and Myc transgenic zebrafish. *Sci Rep* **7**, 10315, doi:10.1038/s41598-017-10529-1 (2017).
182 Yang, Q., Yan, C., Yin, C. & Gong, Z. Serotonin Activated Hepatic Stellate Cells Contribute to Sex Disparity in Hepatocellular Carcinoma. *Cell Mol Gastroenterol Hepatol* **3**, 484-499, doi:10.1016/j.jcmgh.2017.01.002 (2017).
183 Her, G. M., Cheng, C. H., Hong, J. R., Sundaram, G. S. & Wu, J. L. Imbalance in liver homeostasis leading to hyperplasia by overexpressing either one of the Bcl-2-related genes, zfBLP1 and zfMcl-1a. *Dev Dyn* **235**, 515-523, doi:10.1002/dvdy.20624 (2006).
184 Rekha, R. D. *et al.* Thioacetamide accelerates steatohepatitis, cirrhosis and HCC by expressing HCV core protein in transgenic zebrafish Danio rerio. *Toxicology* **243**, 11-22, doi:10.1016/j.tox.2007.09.007 (2008).
185 Zhan, H. *et al.* Transgenic expression of walleye dermal sarcoma virus rv-cyclin gene in zebrafish and its suppressive effect on liver tumor development after carcinogen treatment. *Mar Biotechnol (NY)* **12**, 640-649, doi:10.1007/s10126-009-9251-9 (2010).
186 Liu, W. *et al.* A zebrafish model of intrahepatic cholangiocarcinoma by dual expression of hepatitis B virus X and hepatitis C virus core protein in liver. *Hepatology* **56**, 2268-2276, doi:10.1002/hep.25914 (2012).
187 Lu, J. W., Yang, W. Y., Lin, Y. M., Jin, S. L. & Yuh, C. H. Hepatitis B virus X antigen and aflatoxin B1 synergistically cause hepatitis, steatosis and liver hyperplasia in transgenic zebrafish. *Acta Histochem* **115**, 728-739, doi:10.1016/j.acthis.2013.02.012 (2013).

188 Lu, J. W. *et al.* Liver-specific expressions of HBx and src in the p53 mutant trigger hepatocarcinogenesis in zebrafish. *PLoS One* **8**, e76951, doi:10.1371/journal.pone.0076951 (2013).
189 Lu, J. W. *et al.* Overexpression of endothelin 1 triggers hepatocarcinogenesis in zebrafish and promotes cell proliferation and migration through the AKT pathway. *PLoS One* **9**, e85318, doi:10.1371/journal.pone.0085318 (2014).
190 Evason, K. J. *et al.* Identification of Chemical Inhibitors of β-Catenin-Driven Liver Tumorigenesis in Zebrafish. *PLoS Genet* **11**, e1005305, doi:10.1371/journal.pgen.1005305 (2015).
191 Li, Z., Zheng, W., Li, H., Li, C. & Gong, Z. Synergistic Induction of Potential Warburg Effect in Zebrafish Hepatocellular Carcinoma by Co-Transgenic Expression of Myc and xmrk Oncogenes. *PLoS One* **10**, e0132319, doi:10.1371/journal.pone.0132319 (2015).
192 Sun, L., Nguyen, A. T., Spitsbergen, J. M. & Gong, Z. Myc-induced liver tumors in transgenic zebrafish can regress in tp53 null mutation. *PLoS One* **10**, e0117249, doi:10.1371/journal.pone.0117249 (2015).
193 Nguyen, A. T., Koh, V., Spitsbergen, J. M. & Gong, Z. Development of a conditional liver tumor model by mifepristone-inducible Cre recombination to control oncogenic kras V12 expression in transgenic zebrafish. *Sci Rep* **6**, 19559, doi:10.1038/srep19559 (2016).
194 Wang, J., Leng, X., Wang, G., Wan, X. & Cao, H. The construction of intrahepatic cholangiocarcinoma model in zebrafish. *Sci Rep* **7**, 13419, doi:10.1038/s41598-017-13815-0 (2017).
195 Yan, C., Yang, Q., Shen, H. M., Spitsbergen, J. M. & Gong, Z. Chronically high level of tgfb1a induction causes both hepatocellular carcinoma and cholangiocarcinoma via a dominant Erk pathway in zebrafish. *Oncotarget* **8**, 77096-77109, doi:10.18632/oncotarget.20357 (2017).
196 Chou, Y. T. *et al.* Ribose-5-phosphate isomerase A overexpression promotes liver cancer development in transgenic zebrafish via activation of ERK and β-catenin pathways. *Carcinogenesis* **40**, 461-473, doi:10.1093/carcin/bgy155 (2019).
197 Kalasekar, S. M. *et al.* Heterogeneous beta-catenin activation is sufficient to cause hepatocellular carcinoma in zebrafish. *Biol Open* **8**, doi:10.1242/bio.047829 (2019).
198 Li, H., Li, Y., Lu, J. W., Huo, X. & Gong, Z. Liver-specific androgen receptor knockout attenuates early liver tumor development in zebrafish. *Sci Rep* **9**, 10645, doi:10.1038/s41598-019-46378-3 (2019).
199 Li, Y., Agrawal, I. & Gong, Z. Reversion of tumor hepatocytes to normal hepatocytes during liver tumor regression in an oncogene-expressing transgenic zebrafish model. *Dis Model Mech* **12**, doi:10.1242/dmm.039578 (2019).
200 Yang, W. Y. *et al.* Omics-based Investigation of Diet-induced Obesity Synergized with HBx, Src, and p53 Mutation Accelerating Hepatocarcinogenesis in Zebrafish Model. *Cancers (Basel)* **11**, doi:10.3390/cancers11121899 (2019).
201 Nakayama, J., Lu, J. W., Makinoshima, H. & Gong, Z. A Novel Zebrafish Model of Metastasis Identifies the HSD11β1 Inhibitor Adrenosterone as a Suppressor of Epithelial-Mesenchymal Transition and Metastatic Dissemination. *Mol Cancer Res* **18**, 477-487, doi:10.1158/1541-7786.Mcr-19-0759 (2020).

202 Streisinger, G., Walker, C., Dower, N., Knauber, D. & Singer, F. Production of clones of homozygous diploid zebra fish (Brachydanio rerio). *Nature* **291**, 293-296, doi:10.1038/291293a0 (1981).
203 Haffter, P. *et al.* The identification of genes with unique and essential functions in the development of the zebrafish, Danio rerio. *Development* **123**, 1-36 (1996).
204 Driever, W. *et al.* A genetic screen for mutations affecting embryogenesis in zebrafish. *Development* **123**, 37-46 (1996).
205 Chen, J. N. *et al.* Mutations affecting the cardiovascular system and other internal organs in zebrafish. *Development* **123**, 293-302 (1996).
206 Patton, E. E. & Zon, L. I. The art and design of genetic screens: zebrafish. *Nat Rev Genet* **2**, 956-966, doi:10.1038/35103567 (2001).
207 Pack, M. *et al.* Mutations affecting development of zebrafish digestive organs. *Development* **123**, 321-328 (1996).
208 Ober, E. A., Verkade, H., Field, H. A. & Stainier, D. Y. Mesodermal Wnt2b signalling positively regulates liver specification. *Nature* **442**, 688-691, doi:10.1038/nature04888 (2006).
209 Field, H. A., Ober, E. A., Roeser, T. & Stainier, D. Y. Formation of the digestive system in zebrafish. I. Liver morphogenesis. *Dev Biol* **253**, 279-290 (2003).
210 Ober, E. A., Field, H. A. & Stainier, D. Y. From endoderm formation to liver and pancreas development in zebrafish. *Mech Dev* **120**, 5-18 (2003).
211 de Jong-Curtain, T. A. *et al.* Abnormal nuclear pore formation triggers apoptosis in the intestinal epithelium of elys-deficient zebrafish. *Gastroenterology* **136**, 902-911, doi:10.1053/j.gastro.2008.11.012 (2009).
212 Markmiller, S. *et al.* Minor class splicing shapes the zebrafish transcriptome during development. *Proc Natl Acad Sci U S A* **111**, 3062-3067, doi:10.1073/pnas.1305536111 (2014).
213 Davuluri, G. *et al.* Mutation of the zebrafish nucleoporin elys sensitizes tissue progenitors to replication stress. *PLoS Genet* **4**, e1000240, doi:10.1371/journal.pgen.1000240 (2008).
214 Westerfield, M. *The Zebrafish Book: A Guide for the Laboratory Use of Zebrafish (Danio Rerio)*. (University of Oregon Press, 2000).
215 Berghmans, S. *et al.* tp53 mutant zebrafish develop malignant peripheral nerve sheath tumors. *Proc Natl Acad Sci U S A* **102**, 407-412, doi:10.1073/pnas.0406252102 (2005).
216 Korzh, S. *et al.* Requirement of vasculogenesis and blood circulation in late stages of liver growth in zebrafish. *BMC Dev Biol* **8**, 84, doi:10.1186/1471-213X-8-84 (2008).
217 Hall, T. E. *et al.* Cellular rescue in a zebrafish model of congenital muscular dystrophy type 1A. *NPJ Regen Med* **4**, 21, doi:10.1038/s41536-019-0084-5 (2019).
218 Baell, J. B. *et al.* Inhibitors of histone acetyltransferases KAT6A/B induce senescence and arrest tumour growth. *Nature* **560**, 253-257, doi:10.1038/s41586-018-0387-5 (2018).
219 Ruijter, J. M. *et al.* Amplification efficiency: linking baseline and bias in the analysis of quantitative PCR data. *Nucleic Acids Res* **37**, e45, doi:10.1093/nar/gkp045 (2009).
220 Liao, Y., Smyth, G. K. & Shi, W. The R package Rsubread is easier, faster, cheaper and better for alignment and quantification of RNA sequencing reads. *Nucleic Acids Res* **47**, e47, doi:10.1093/nar/gkz114 (2019).

221 Ritchie, M. E. *et al.* limma powers differential expression analyses for RNA-sequencing and microarray studies. *Nucleic Acids Res* **43**, e47, doi:10.1093/nar/gkv007 (2015).
222 Robinson, M. D., McCarthy, D. J. & Smyth, G. K. edgeR: a Bioconductor package for differential expression analysis of digital gene expression data. *Bioinformatics* **26**, 139-140, doi:10.1093/bioinformatics/btp616 (2010).
223 Robinson, M. D. & Oshlack, A. A scaling normalization method for differential expression analysis of RNA-seq data. *Genome Biol* **11**, R25, doi:10.1186/gb-2010-11-3-r25 (2010).
224 Law, C. W., Chen, Y., Shi, W. & Smyth, G. K. voom: Precision weights unlock linear model analysis tools for RNA-seq read counts. *Genome Biol* **15**, R29, doi:10.1186/gb-2014-15-2-r29 (2014).
225 Phipson, B., Lee, S., Majewski, I. J., Alexander, W. S. & Smyth, G. K. Robust Hyperparameter Estimation Protects against Hypervariable Genes and Improves Power to Detect Differential Expression. *Ann Appl Stat* **10**, 946-963, doi:10.1214/16-AOAS920 (2016).
226 Kimura, N. *et al.* Identification of a novel transcription factor, ELYS, expressed predominantly in mouse foetal haematopoietic tissues. *Genes Cells* **7**, 435-446, doi:10.1046/j.1365-2443.2002.00529.x (2002).
227 Okita, K. *et al.* Targeted disruption of the mouse ELYS gene results in embryonic death at peri-implantation development. *Genes Cells* **9**, 1083-1091, doi:10.1111/j.1365-2443.2004.00791.x (2004).
228 Rasala, B. A., Orjalo, A. V., Shen, Z., Briggs, S. & Forbes, D. J. ELYS is a dual nucleoporin/kinetochore protein required for nuclear pore assembly and proper cell division. *Proc Natl Acad Sci U S A* **103**, 17801-17806, doi:10.1073/pnas.0608484103 (2006).
229 Fernandez, A. G. & Piano, F. MEL-28 is downstream of the Ran cycle and is required for nuclear-envelope function and chromatin maintenance. *Curr Biol* **16**, 1757-1763, doi:10.1016/j.cub.2006.07.071 (2006).
230 Franz, C. *et al.* MEL-28/ELYS is required for the recruitment of nucleoporins to chromatin and postmitotic nuclear pore complex assembly. *EMBO Rep* **8**, 165-172, doi:10.1038/sj.embor.7400889 (2007).
231 Galy, V., Askjaer, P., Franz, C., Lopez-Iglesias, C. & Mattaj, I. W. MEL-28, a novel nuclear-envelope and kinetochore protein essential for zygotic nuclear-envelope assembly in C. elegans. *Curr Biol* **16**, 1748-1756, doi:10.1016/j.cub.2006.06.067 (2006).
232 Ng, A. N. *et al.* Formation of the digestive system in zebrafish: III. Intestinal epithelium morphogenesis. *Dev Biol* **286**, 114-135, doi:10.1016/j.ydbio.2005.07.013 (2005).
233 Wallace, K. N., Akhter, S., Smith, E. M., Lorent, K. & Pack, M. Intestinal growth and differentiation in zebrafish. *Mech Dev* **122**, 157-173, doi:10.1016/j.mod.2004.10.009 (2005).
234 Yee, N. S., Lorent, K. & Pack, M. Exocrine pancreas development in zebrafish. *Dev Biol* **284**, 84-101, doi:10.1016/j.ydbio.2005.04.035 (2005).
235 Lin, D. H. & Hoelz, A. The Structure of the Nuclear Pore Complex (An Update). *Annu Rev Biochem* **88**, 725-783, doi:10.1146/annurev-biochem-062917-011901 (2019).

236 Beck, M. & Hurt, E. The nuclear pore complex: understanding its function through structural insight. *Nat Rev Mol Cell Biol* **18**, 73-89, doi:10.1038/nrm.2016.147 (2017).
237 Callan, H. G. & Tomlin, S. G. Experimental studies on amphibian oocyte nuclei. I. Investigation of the structure of the nuclear membrane by means of the electron microscope. *Proc R Soc Lond B Biol Sci* **137**, 367-378, doi:10.1098/rspb.1950.0047 (1950).
238 Watson, M. L. The nuclear envelope; its structure and relation to cytoplasmic membranes. *J Biophys Biochem Cytol* **1**, 257-270, doi:10.1083/jcb.1.3.257 (1955).
239 Gall, J. G. Octagonal nuclear pores. *J Cell Biol* **32**, 391-399, doi:10.1083/jcb.32.2.391 (1967).
240 Rout, M. P. *et al.* The yeast nuclear pore complex: composition, architecture, and transport mechanism. *J Cell Biol* **148**, 635-651, doi:10.1083/jcb.148.4.635 (2000).
241 Schwartz, T. U. The Structure Inventory of the Nuclear Pore Complex. *J Mol Biol* **428**, 1986-2000, doi:10.1016/j.jmb.2016.03.015 (2016).
242 Cronshaw, J. M., Krutchinsky, A. N., Zhang, W., Chait, B. T. & Matunis, M. J. Proteomic analysis of the mammalian nuclear pore complex. *J Cell Biol* **158**, 915-927, doi:10.1083/jcb.200206106 (2002).
243 Rabut, G., Doye, V. & Ellenberg, J. Mapping the dynamic organization of the nuclear pore complex inside single living cells. *Nat Cell Biol* **6**, 1114-1121, doi:10.1038/ncb1184 (2004).
244 Lutzmann, M., Kunze, R., Buerer, A., Aebi, U. & Hurt, E. Modular self-assembly of a Y-shaped multiprotein complex from seven nucleoporins. *EMBO J* **21**, 387-397, doi:10.1093/emboj/21.3.387 (2002).
245 Siniossoglou, S. *et al.* Structure and assembly of the Nup84p complex. *J Cell Biol* **149**, 41-54, doi:10.1083/jcb.149.1.41 (2000).
246 von Appen, A. *et al.* In situ structural analysis of the human nuclear pore complex. *Nature* **526**, 140-143, doi:10.1038/nature15381 (2015).
247 Mosalaganti, S. *et al.* In situ architecture of the algal nuclear pore complex. *Nat Commun* **9**, 2361, doi:10.1038/s41467-018-04739-y (2018).
248 Kim, S. J. *et al.* Integrative structure and functional anatomy of a nuclear pore complex. *Nature* **555**, 475-482, doi:10.1038/nature26003 (2018).
249 Lin, D. H. *et al.* Architecture of the symmetric core of the nuclear pore. *Science* **352**, aaf1015, doi:10.1126/science.aaf1015 (2016).
250 Fontoura, B. M., Blobel, G. & Matunis, M. J. A conserved biogenesis pathway for nucleoporins: proteolytic processing of a 186-kilodalton precursor generates Nup98 and the novel nucleoporin, Nup96. *J Cell Biol* **144**, 1097-1112, doi:10.1083/jcb.144.6.1097 (1999).
251 Belgareh, N. *et al.* An evolutionarily conserved NPC subcomplex, which redistributes in part to kinetochores in mammalian cells. *J Cell Biol* **154**, 1147-1160, doi:10.1083/jcb.200101081 (2001).
252 Loiodice, I. *et al.* The entire Nup107-160 complex, including three new members, is targeted as one entity to kinetochores in mitosis. *Mol Biol Cell* **15**, 3333-3344, doi:10.1091/mbc.e03-12-0878 (2004).
253 Siniossoglou, S. *et al.* A novel complex of nucleoporins, which includes Sec13p and a Sec13p homolog, is essential for normal nuclear pores. *Cell* **84**, 265-275, doi:10.1016/s0092-8674(00)80981-2 (1996).

254 Bilokapic, S. & Schwartz, T. U. Molecular basis for Nup37 and ELY5/ELYS recruitment to the nuclear pore complex. *Proc Natl Acad Sci U S A* **109**, 15241-15246, doi:10.1073/pnas.1205151109 (2012).
255 Thierbach, K. *et al.* Protein interfaces of the conserved Nup84 complex from Chaetomium thermophilum shown by crosslinking mass spectrometry and electron microscopy. *Structure* **21**, 1672-1682, doi:10.1016/j.str.2013.07.004 (2013).
256 Liu, H. L., De Souza, C. P., Osmani, A. H. & Osmani, S. A. The three fungal transmembrane nuclear pore complex proteins of Aspergillus nidulans are dispensable in the presence of an intact An-Nup84-120 complex. *Mol Biol Cell* **20**, 616-630, doi:10.1091/mbc.E08-06-0628 (2009).
257 Bilokapic, S. & Schwartz, T. U. Structural and functional studies of the 252 kDa nucleoporin ELYS reveal distinct roles for its three tethered domains. *Structure* **21**, 572-580, doi:10.1016/j.str.2013.02.006 (2013).
258 Neumann, N., Lundin, D. & Poole, A. M. Comparative genomic evidence for a complete nuclear pore complex in the last eukaryotic common ancestor. *PLoS One* **5**, e13241, doi:10.1371/journal.pone.0013241 (2010).
259 Ori, A. *et al.* Cell type-specific nuclear pores: a case in point for context-dependent stoichiometry of molecular machines. *Mol Syst Biol* **9**, 648, doi:10.1038/msb.2013.4 (2013).
260 Kosinski, J. *et al.* Molecular architecture of the inner ring scaffold of the human nuclear pore complex. *Science* **352**, 363-365, doi:10.1126/science.aaf0643 (2016).
261 Mansfeld, J. *et al.* The conserved transmembrane nucleoporin NDC1 is required for nuclear pore complex assembly in vertebrate cells. *Mol Cell* **22**, 93-103, doi:10.1016/j.molcel.2006.02.015 (2006).
262 Goldberg, M. W. & Allen, T. D. High resolution scanning electron microscopy of the nuclear envelope: demonstration of a new, regular, fibrous lattice attached to the baskets of the nucleoplasmic face of the nuclear pores. *J Cell Biol* **119**, 1429-1440, doi:10.1083/jcb.119.6.1429 (1992).
263 Krull, S. *et al.* Protein Tpr is required for establishing nuclear pore-associated zones of heterochromatin exclusion. *EMBO J* **29**, 1659-1673, doi:10.1038/emboj.2010.54 (2010).
264 Kohler, A. & Hurt, E. Gene regulation by nucleoporins and links to cancer. *Mol Cell* **38**, 6-15, doi:10.1016/j.molcel.2010.01.040 (2010).
265 Meszaros, N. *et al.* Nuclear pore basket proteins are tethered to the nuclear envelope and can regulate membrane curvature. *Dev Cell* **33**, 285-298, doi:10.1016/j.devcel.2015.02.017 (2015).
266 Wu, J., Matunis, M. J., Kraemer, D., Blobel, G. & Coutavas, E. Nup358, a cytoplasmically exposed nucleoporin with peptide repeats, Ran-GTP binding sites, zinc fingers, a cyclophilin A homologous domain, and a leucine-rich region. *J Biol Chem* **270**, 14209-14213, doi:10.1074/jbc.270.23.14209 (1995).
267 Lin, D. H. *et al.* Structural and functional analysis of mRNA export regulation by the nuclear pore complex. *Nat Commun* **9**, 2319, doi:10.1038/s41467-018-04459-3 (2018).
268 Napetschnig, J. *et al.* Structural and functional analysis of the interaction between the nucleoporin Nup214 and the DEAD-box helicase Ddx19. *Proc Natl Acad Sci U S A* **106**, 3089-3094, doi:10.1073/pnas.0813267106 (2009).

269 Frey, S., Richter, R. P. & Gorlich, D. FG-rich repeats of nuclear pore proteins form a three-dimensional meshwork with hydrogel-like properties. *Science* **314**, 815-817, doi:10.1126/science.1132516 (2006).
270 Terry, L. J. & Wente, S. R. Flexible gates: dynamic topologies and functions for FG nucleoporins in nucleocytoplasmic transport. *Eukaryot Cell* **8**, 1814-1827, doi:10.1128/EC.00225-09 (2009).
271 Strawn, L. A., Shen, T., Shulga, N., Goldfarb, D. S. & Wente, S. R. Minimal nuclear pore complexes define FG repeat domains essential for transport. *Nat Cell Biol* **6**, 197-206, doi:10.1038/ncb1097 (2004).
272 Aramburu, I. V. & Lemke, E. A. Floppy but not sloppy: Interaction mechanism of FG-nucleoporins and nuclear transport receptors. *Semin Cell Dev Biol* **68**, 34-41, doi:10.1016/j.semcdb.2017.06.026 (2017).
273 Grossman, E., Medalia, O. & Zwerger, M. Functional architecture of the nuclear pore complex. *Annu Rev Biophys* **41**, 557-584, doi:10.1146/annurev-biophys-050511-102328 (2012).
274 Ptak, C., Aitchison, J. D. & Wozniak, R. W. The multifunctional nuclear pore complex: a platform for controlling gene expression. *Curr Opin Cell Biol* **28**, 46-53, doi:10.1016/j.ceb.2014.02.001 (2014).
275 Hezwani, M. & Fahrenkrog, B. The functional versatility of the nuclear pore complex proteins. *Semin Cell Dev Biol* **68**, 2-9, doi:10.1016/j.semcdb.2017.05.004 (2017).
276 Chatel, G. & Fahrenkrog, B. Nucleoporins: leaving the nuclear pore complex for a successful mitosis. *Cell Signal* **23**, 1555-1562, doi:10.1016/j.cellsig.2011.05.023 (2011).
277 Chatel, G. & Fahrenkrog, B. Dynamics and diverse functions of nuclear pore complex proteins. *Nucleus* **3**, 162-171, doi:10.4161/nucl.19674 (2012).
278 Palancade, B. *et al.* Nucleoporins prevent DNA damage accumulation by modulating Ulp1-dependent sumoylation processes. *Mol Biol Cell* **18**, 2912-2923, doi:10.1091/mbc.e07-02-0123 (2007).
279 Ibarra, A. & Hetzer, M. W. Nuclear pore proteins and the control of genome functions. *Genes Dev* **29**, 337-349, doi:10.1101/gad.256495.114 (2015).
280 Khadaroo, B. *et al.* The DNA damage response at eroded telomeres and tethering to the nuclear pore complex. *Nat Cell Biol* **11**, 980-987, doi:10.1038/ncb1910 (2009).
281 Griffis, E. R., Altan, N., Lippincott-Schwartz, J. & Powers, M. A. Nup98 is a mobile nucleoporin with transcription-dependent dynamics. *Mol Biol Cell* **13**, 1282-1297, doi:10.1091/mbc.01-11-0538 (2002).
282 Morchoisne-Bolhy, S. *et al.* Intranuclear dynamics of the Nup107-160 complex. *Mol Biol Cell* **26**, 2343-2356, doi:10.1091/mbc.E15-02-0060 (2015).
283 Yang, W., Gelles, J. & Musser, S. M. Imaging of single-molecule translocation through nuclear pore complexes. *Proc Natl Acad Sci U S A* **101**, 12887-12892, doi:10.1073/pnas.0403675101 (2004).
284 Ribbeck, K. & Gorlich, D. Kinetic analysis of translocation through nuclear pore complexes. *EMBO J* **20**, 1320-1330, doi:10.1093/emboj/20.6.1320 (2001).
285 Kau, T. R., Way, J. C. & Silver, P. A. Nuclear transport and cancer: from mechanism to intervention. *Nat Rev Cancer* **4**, 106-117, doi:10.1038/nrc1274 (2004).
286 Strambio-De-Castillia, C., Niepel, M. & Rout, M. P. The nuclear pore complex: bridging nuclear transport and gene regulation. *Nat Rev Mol Cell Biol* **11**, 490-501, doi:10.1038/nrm2928 (2010).

287 Clarke, P. R. & Zhang, C. Spatial and temporal coordination of mitosis by Ran GTPase. *Nat Rev Mol Cell Biol* **9**, 464-477, doi:10.1038/nrm2410 (2008).
288 Buchwalter, A., Kaneshiro, J. M. & Hetzer, M. W. Coaching from the sidelines: the nuclear periphery in genome regulation. *Nat Rev Genet* **20**, 39-50, doi:10.1038/s41576-018-0063-5 (2019).
289 Sun, J., Shi, Y. & Yildirim, E. The Nuclear Pore Complex in Cell Type-Specific Chromatin Structure and Gene Regulation. *Trends Genet* **35**, 579-588, doi:10.1016/j.tig.2019.05.006 (2019).
290 Zierhut, C., Jenness, C., Kimura, H. & Funabiki, H. Nucleosomal regulation of chromatin composition and nuclear assembly revealed by histone depletion. *Nat Struct Mol Biol* **21**, 617-625, doi:10.1038/nsmb.2845 (2014).
291 Pascual-Garcia, P. *et al.* Metazoan Nuclear Pores Provide a Scaffold for Poised Genes and Mediate Induced Enhancer-Promoter Contacts. *Mol Cell* **66**, 63-76 e66, doi:10.1016/j.molcel.2017.02.020 (2017).
292 Gozalo, A. *et al.* Core Components of the Nuclear Pore Bind Distinct States of Chromatin and Contribute to Polycomb Repression. *Mol Cell* **77**, 67-81 e67, doi:10.1016/j.molcel.2019.10.017 (2020).
293 Kuhn, T. M., Pascual-Garcia, P., Gozalo, A., Little, S. C. & Capelson, M. Chromatin targeting of nuclear pore proteins induces chromatin decondensation. *J Cell Biol* **218**, 2945-2961, doi:10.1083/jcb.201807139 (2019).
294 Ertl, I. *et al.* Functional Interplay of Two Paralogs Encoding SWI/SNF Chromatin-Remodeling Accessory Subunits During Caenorhabditis elegans Development. *Genetics* **202**, 961-975, doi:10.1534/genetics.115.183533 (2016).
295 Bennett, C. B. *et al.* Genes required for ionizing radiation resistance in yeast. *Nat Genet* **29**, 426-434, doi:10.1038/ng778 (2001).
296 Loeillet, S. *et al.* Genetic network interactions among replication, repair and nuclear pore deficiencies in yeast. *DNA Repair (Amst)* **4**, 459-468, doi:10.1016/j.dnarep.2004.11.010 (2005).
297 Nagai, S. *et al.* Functional targeting of DNA damage to a nuclear pore-associated SUMO-dependent ubiquitin ligase. *Science* **322**, 597-602, doi:10.1126/science.1162790 (2008).
298 Therizols, P. *et al.* Telomere tethering at the nuclear periphery is essential for efficient DNA double strand break repair in subtelomeric region. *J Cell Biol* **172**, 189-199, doi:10.1083/jcb.200505159 (2006).
299 Oza, P., Jaspersen, S. L., Miele, A., Dekker, J. & Peterson, C. L. Mechanisms that regulate localization of a DNA double-strand break to the nuclear periphery. *Genes Dev* **23**, 912-927, doi:10.1101/gad.1782209 (2009).
300 Geli, V. & Lisby, M. Recombinational DNA repair is regulated by compartmentalization of DNA lesions at the nuclear pore complex. *Bioessays* **37**, 1287-1292, doi:10.1002/bies.201500084 (2015).
301 Paulsen, R. D. *et al.* A genome-wide siRNA screen reveals diverse cellular processes and pathways that mediate genome stability. *Mol Cell* **35**, 228-239, doi:10.1016/j.molcel.2009.06.021 (2009).
302 Lemaitre, C. *et al.* The nucleoporin 153, a novel factor in double-strand break repair and DNA damage response. *Oncogene* **31**, 4803-4809, doi:10.1038/onc.2011.638 (2012).

303 Duheron, V., Nilles, N., Pecenko, S., Martinelli, V. & Fahrenkrog, B. Localisation of Nup153 and SENP1 to nuclear pore complexes is required for 53BP1-mediated DNA double-strand break repair. *J Cell Sci* **130**, 2306-2316, doi:10.1242/jcs.198390 (2017).
304 Glavy, J. S. *et al.* Cell-cycle-dependent phosphorylation of the nuclear pore Nup107-160 subcomplex. *Proc Natl Acad Sci U S A* **104**, 3811-3816, doi:10.1073/pnas.0700058104 (2007).
305 Laurell, E. *et al.* Phosphorylation of Nup98 by multiple kinases is crucial for NPC disassembly during mitotic entry. *Cell* **144**, 539-550, doi:10.1016/j.cell.2011.01.012 (2011).
306 Guttinger, S., Laurell, E. & Kutay, U. Orchestrating nuclear envelope disassembly and reassembly during mitosis. *Nat Rev Mol Cell Biol* **10**, 178-191, doi:10.1038/nrm2641 (2009).
307 Dultz, E. *et al.* Systematic kinetic analysis of mitotic dis- and reassembly of the nuclear pore in living cells. *J Cell Biol* **180**, 857-865, doi:10.1083/jcb.200707026 (2008).
308 Daigle, N. *et al.* Nuclear pore complexes form immobile networks and have a very low turnover in live mammalian cells. *J Cell Biol* **154**, 71-84, doi:10.1083/jcb.200101089 (2001).
309 Belmont, A. S. Mitotic chromosome structure and condensation. *Curr Opin Cell Biol* **18**, 632-638, doi:10.1016/j.ceb.2006.09.007 (2006).
310 Wong, R. W., Blobel, G. & Coutavas, E. Rae1 interaction with NuMA is required for bipolar spindle formation. *Proc Natl Acad Sci U S A* **103**, 19783-19787, doi:10.1073/pnas.0609582104 (2006).
311 Blower, M. D., Nachury, M., Heald, R. & Weis, K. A Rae1-containing ribonucleoprotein complex is required for mitotic spindle assembly. *Cell* **121**, 223-234, doi:10.1016/j.cell.2005.02.016 (2005).
312 Orjalo, A. V. *et al.* The Nup107-160 nucleoporin complex is required for correct bipolar spindle assembly. *Mol Biol Cell* **17**, 3806-3818, doi:10.1091/mbc.e05-11-1061 (2006).
313 Mishra, R. K., Chakraborty, P., Arnaoutov, A., Fontoura, B. M. & Dasso, M. The Nup107-160 complex and gamma-TuRC regulate microtubule polymerization at kinetochores. *Nat Cell Biol* **12**, 164-169, doi:10.1038/ncb2016 (2010).
314 Zuccolo, M. *et al.* The human Nup107-160 nuclear pore subcomplex contributes to proper kinetochore functions. *EMBO J* **26**, 1853-1864, doi:10.1038/sj.emboj.7601642 (2007).
315 Gomez-Saldivar, G. *et al.* Identification of Conserved MEL-28/ELYS Domains with Essential Roles in Nuclear Assembly and Chromosome Segregation. *PLoS Genet* **12**, e1006131, doi:10.1371/journal.pgen.1006131 (2016).
316 Salina, D., Enarson, P., Rattner, J. B. & Burke, B. Nup358 integrates nuclear envelope breakdown with kinetochore assembly. *J Cell Biol* **162**, 991-1001, doi:10.1083/jcb.200304080 (2003).
317 Joseph, J., Liu, S. T., Jablonski, S. A., Yen, T. J. & Dasso, M. The RanGAP1-RanBP2 complex is essential for microtubule-kinetochore interactions in vivo. *Curr Biol* **14**, 611-617, doi:10.1016/j.cub.2004.03.031 (2004).
318 Hashizume, C., Kobayashi, A. & Wong, R. W. Down-modulation of nucleoporin RanBP2/Nup358 impaired chromosomal alignment and induced mitotic catastrophe. *Cell Death Dis* **4**, e854, doi:10.1038/cddis.2013.370 (2013).

319 Weberruss, M. & Antonin, W. Perforating the nuclear boundary - how nuclear pore complexes assemble. *J Cell Sci* **129**, 4439-4447, doi:10.1242/jcs.194753 (2016).
320 Otsuka, S. *et al.* Postmitotic nuclear pore assembly proceeds by radial dilation of small membrane openings. *Nat Struct Mol Biol* **25**, 21-28, doi:10.1038/s41594-017-0001-9 (2018).
321 Otsuka, S., Szymborska, A. & Ellenberg, J. Imaging the assembly, structure, and function of the nuclear pore inside cells. *Methods Cell Biol* **122**, 219-238, doi:10.1016/B978-0-12-417160-2.00010-2 (2014).
322 Schellhaus, A. K., De Magistris, P. & Antonin, W. Nuclear Reformation at the End of Mitosis. *J Mol Biol* **428**, 1962-1985, doi:10.1016/j.jmb.2015.09.016 (2016).
323 Hetzer, M., Bilbao-Cortes, D., Walther, T. C., Gruss, O. J. & Mattaj, I. W. GTP hydrolysis by Ran is required for nuclear envelope assembly. *Mol Cell* **5**, 1013-1024, doi:10.1016/s1097-2765(00)80266-x (2000).
324 Harel, A. *et al.* Importin beta negatively regulates nuclear membrane fusion and nuclear pore complex assembly. *Mol Biol Cell* **14**, 4387-4396, doi:10.1091/mbc.e03-05-0275 (2003).
325 Walther, T. C. *et al.* RanGTP mediates nuclear pore complex assembly. *Nature* **424**, 689-694, doi:10.1038/nature01898 (2003).
326 Rasala, B. A., Ramos, C., Harel, A. & Forbes, D. J. Capture of AT-rich chromatin by ELYS recruits POM121 and NDC1 to initiate nuclear pore assembly. *Mol Biol Cell* **19**, 3982-3996, doi:10.1091/mbc.E08-01-0012 (2008).
327 Kobayashi, W. *et al.* Structural and biochemical analyses of the nuclear pore complex component ELYS identify residues responsible for nucleosome binding. *Commun Biol* **2**, 163, doi:10.1038/s42003-019-0385-7 (2019).
328 Gillespie, P. J., Khoudoli, G. A., Stewart, G., Swedlow, J. R. & Blow, J. J. ELYS/MEL-28 chromatin association coordinates nuclear pore complex assembly and replication licensing. *Curr Biol* **17**, 1657-1662, doi:10.1016/j.cub.2007.08.041 (2007).
329 Anderson, D. J., Vargas, J. D., Hsiao, J. P. & Hetzer, M. W. Recruitment of functionally distinct membrane proteins to chromatin mediates nuclear envelope formation in vivo. *J Cell Biol* **186**, 183-191, doi:10.1083/jcb.200901106 (2009).
330 Vollmer, B. *et al.* Dimerization and direct membrane interaction of Nup53 contribute to nuclear pore complex assembly. *EMBO J* **31**, 4072-4084, doi:10.1038/emboj.2012.256 (2012).
331 Eisenhardt, N., Redolfi, J. & Antonin, W. Interaction of Nup53 with Ndc1 and Nup155 is required for nuclear pore complex assembly. *J Cell Sci* **127**, 908-921, doi:10.1242/jcs.141739 (2014).
332 Sachdev, R., Sieverding, C., Flotenmeyer, M. & Antonin, W. The C-terminal domain of Nup93 is essential for assembly of the structural backbone of nuclear pore complexes. *Mol Biol Cell* **23**, 740-749, doi:10.1091/mbc.E11-09-0761 (2012).
333 Blow, J. J. & Hodgson, B. Replication licensing--defining the proliferative state? *Trends Cell Biol* **12**, 72-78, doi:10.1016/s0962-8924(01)02203-6 (2002).
334 Fragkos, M., Ganier, O., Coulombe, P. & Mechali, M. DNA replication origin activation in space and time. *Nat Rev Mol Cell Biol* **16**, 360-374, doi:10.1038/nrm4002 (2015).
335 Blow, J. J. & Gillespie, P. J. Replication licensing and cancer--a fatal entanglement? *Nat Rev Cancer* **8**, 799-806, doi:10.1038/nrc2500 (2008).

336 Arias, E. E. & Walter, J. C. Strength in numbers: preventing rereplication via multiple mechanisms in eukaryotic cells. *Genes Dev* **21**, 497-518, doi:10.1101/gad.1508907 (2007).
337 Hodgson, B., Li, A., Tada, S. & Blow, J. J. Geminin becomes activated as an inhibitor of Cdt1/RLF-B following nuclear import. *Curr Biol* **12**, 678-683, doi:10.1016/s0960-9822(02)00778-9 (2002).
338 Khoudoli, G. A. *et al.* Temporal profiling of the chromatin proteome reveals system-wide responses to replication inhibition. *Curr Biol* **18**, 838-843, doi:10.1016/j.cub.2008.04.075 (2008).
339 Gao, N. *et al.* The nuclear pore complex protein Elys is required for genome stability in mouse intestinal epithelial progenitor cells. *Gastroenterology* **140**, 1547-1555 e1510, doi:10.1053/j.gastro.2011.01.048 (2011).
340 Doucet, C. M., Talamas, J. A. & Hetzer, M. W. Cell cycle-dependent differences in nuclear pore complex assembly in metazoa. *Cell* **141**, 1030-1041, doi:10.1016/j.cell.2010.04.036 (2010).
341 Dultz, E. & Ellenberg, J. Live imaging of single nuclear pores reveals unique assembly kinetics and mechanism in interphase. *J Cell Biol* **191**, 15-22, doi:10.1083/jcb.201007076 (2010).
342 D'Angelo, M. A., Anderson, D. J., Richard, E. & Hetzer, M. W. Nuclear pores form de novo from both sides of the nuclear envelope. *Science* **312**, 440-443, doi:10.1126/science.1124196 (2006).
343 Funakoshi, T., Clever, M., Watanabe, A. & Imamoto, N. Localization of Pom121 to the inner nuclear membrane is required for an early step of interphase nuclear pore complex assembly. *Mol Biol Cell* **22**, 1058-1069, doi:10.1091/mbc.E10-07-0641 (2011).
344 Otsuka, S. *et al.* Nuclear pore assembly proceeds by an inside-out extrusion of the nuclear envelope. *Elife* **5**, doi:10.7554/eLife.19071 (2016).
345 Doucet, C. M. & Hetzer, M. W. Nuclear pore biogenesis into an intact nuclear envelope. *Chromosoma* **119**, 469-477, doi:10.1007/s00412-010-0289-2 (2010).
346 Vollmer, B. *et al.* Nup153 Recruits the Nup107-160 Complex to the Inner Nuclear Membrane for Interphasic Nuclear Pore Complex Assembly. *Dev Cell* **33**, 717-728, doi:10.1016/j.devcel.2015.04.027 (2015).
347 Hampoelz, B., Andres-Pons, A., Kastritis, P. & Beck, M. Structure and Assembly of the Nuclear Pore Complex. *Annu Rev Biophys* **48**, 515-536, doi:10.1146/annurev-biophys-052118-115308 (2019).
348 Sakuma, S. & D'Angelo, M. A. The roles of the nuclear pore complex in cellular dysfunction, aging and disease. *Semin Cell Dev Biol* **68**, 72-84, doi:10.1016/j.semcdb.2017.05.006 (2017).
349 Raices, M. & D'Angelo, M. A. Nuclear pore complex composition: a new regulator of tissue-specific and developmental functions. *Nat Rev Mol Cell Biol* **13**, 687-699, doi:10.1038/nrm3461 (2012).
350 Zhang, X. *et al.* Mutation in nuclear pore component NUP155 leads to atrial fibrillation and early sudden cardiac death. *Cell* **135**, 1017-1027, doi:10.1016/j.cell.2008.10.022 (2008).
351 Haskell, G. T. *et al.* Whole Exome Sequencing Identifies Truncating Variants in Nuclear Envelope Genes in Patients With Cardiovascular Disease. *Circ Cardiovasc Genet* **10**, doi:10.1161/CIRCGENETICS.116.001443 (2017).

352 Miyake, N. *et al.* Biallelic Mutations in Nuclear Pore Complex Subunit NUP107 Cause Early-Childhood-Onset Steroid-Resistant Nephrotic Syndrome. *Am J Hum Genet* **97**, 555-566, doi:10.1016/j.ajhg.2015.08.013 (2015).
353 Park, E. *et al.* NUP107 mutations in children with steroid-resistant nephrotic syndrome. *Nephrol Dial Transplant* **32**, 1013-1017, doi:10.1093/ndt/gfw103 (2017).
354 Braun, D. A. *et al.* Mutations in multiple components of the nuclear pore complex cause nephrotic syndrome. *J Clin Invest* **128**, 4313-4328, doi:10.1172/JCI98688 (2018).
355 Braun, D. A. *et al.* Mutations in nuclear pore genes NUP93, NUP205 and XPO5 cause steroid-resistant nephrotic syndrome. *Nat Genet* **48**, 457-465, doi:10.1038/ng.3512 (2016).
356 Cronshaw, J. M. & Matunis, M. J. The nuclear pore complex protein ALADIN is mislocalized in triple A syndrome. *Proc Natl Acad Sci U S A* **100**, 5823-5827, doi:10.1073/pnas.1031047100 (2003).
357 Hirano, M., Furiya, Y., Asai, H., Yasui, A. & Ueno, S. ALADINI482S causes selective failure of nuclear protein import and hypersensitivity to oxidative stress in triple A syndrome. *Proc Natl Acad Sci U S A* **103**, 2298-2303, doi:10.1073/pnas.0505598103 (2006).
358 Xu, S. & Powers, M. A. Nuclear pore proteins and cancer. *Semin Cell Dev Biol* **20**, 620-630, doi:10.1016/j.semcdb.2009.03.003 (2009).
359 Nakamura, T. *et al.* Fusion of the nucleoporin gene NUP98 to HOXA9 by the chromosome translocation t(7;11)(p15;p15) in human myeloid leukaemia. *Nat Genet* **12**, 154-158, doi:10.1038/ng0296-154 (1996).
360 Gough, S. M., Slape, C. I. & Aplan, P. D. NUP98 gene fusions and hematopoietic malignancies: common themes and new biologic insights. *Blood* **118**, 6247-6257, doi:10.1182/blood-2011-07-328880 (2011).
361 Simon, D. N. & Rout, M. P. Cancer and the nuclear pore complex. *Advances in experimental medicine and biology* **773**, 285-307, doi:10.1007/978-1-4899-8032-8_13 (2014).
362 Gould, V. E. *et al.* Nup88 (karyoporin) in human malignant neoplasms and dysplasias: correlations of immunostaining of tissue sections, cytologic smears, and immunoblot analysis. *Hum Pathol* **33**, 536-544, doi:10.1053/hupa.2002.124785 (2002).
363 Knoess, M. *et al.* Nucleoporin 88 expression in hepatitis B and C virus-related liver diseases. *World J Gastroenterol* **12**, 5870-5874, doi:10.3748/wjg.v12.i36.5870 (2006).
364 Naylor, R. M., Jeganathan, K. B., Cao, X. & van Deursen, J. M. Nuclear pore protein NUP88 activates anaphase-promoting complex to promote aneuploidy. *J Clin Invest* **126**, 543-559, doi:10.1172/JCI82277 (2016).
365 Rodriguez-Bravo, V. *et al.* Nuclear Pores Promote Lethal Prostate Cancer by Increasing POM121-Driven E2F1, MYC, and AR Nuclear Import. *Cell* **174**, 1200-1215 e1220, doi:10.1016/j.cell.2018.07.015 (2018).
366 Vecchione, L. *et al.* A Vulnerability of a Subset of Colon Cancers with Potential Clinical Utility. *Cell* **165**, 317-330, doi:10.1016/j.cell.2016.02.059 (2016).
367 Joseph, J. & Dasso, M. The nucleoporin Nup358 associates with and regulates interphase microtubules. *FEBS Lett* **582**, 190-196, doi:10.1016/j.febslet.2007.11.087 (2008).

368 Chiang, D. Y. *et al.* Focal gains of VEGFA and molecular classification of hepatocellular carcinoma. *Cancer Res* **68**, 6779-6788, doi:10.1158/0008-5472.CAN-08-0742 (2008).
369 Levrero, M. *et al.* The p53/p63/p73 family of transcription factors: overlapping and distinct functions. *J Cell Sci* **113 (Pt 10)**, 1661-1670 (2000).
370 Suh, E. K. *et al.* p63 protects the female germ line during meiotic arrest. *Nature* **444**, 624-628, doi:10.1038/nature05337 (2006).
371 Chen, J. *et al.* p53 isoform delta113p53 is a p53 target gene that antagonizes p53 apoptotic activity via BclxL activation in zebrafish. *Genes Dev* **23**, 278-290, doi:10.1101/gad.1761609 (2009).
372 Leshchiner, I. *et al.* Mutation mapping and identification by whole-genome sequencing. *Genome Res* **22**, 1541-1548, doi:10.1101/gr.135541.111 (2012).
373 Voz, M. L. *et al.* Fast homozygosity mapping and identification of a zebrafish ENU-induced mutation by whole-genome sequencing. *PLoS One* **7**, e34671, doi:10.1371/journal.pone.0034671 (2012).
374 Dempster, J. M. *et al.* Extracting Biological Insights from the Project Achilles Genome-Scale CRISPR Screens in Cancer Cell Lines. doi:10.1101/720243 (2019).
375 Meyers, R. M. *et al.* Computational correction of copy number effect improves specificity of CRISPR-Cas9 essentiality screens in cancer cells. *Nat Genet* **49**, 1779-1784, doi:10.1038/ng.3984 (2017).
376 Cerami, E. *et al.* The cBio cancer genomics portal: an open platform for exploring multidimensional cancer genomics data. *Cancer Discov* **2**, 401-404, doi:10.1158/2159-8290.CD-12-0095 (2012).
377 Gao, J. *et al.* Integrative analysis of complex cancer genomics and clinical profiles using the cBioPortal. *Sci Signal* **6**, pl1, doi:10.1126/scisignal.2004088 (2013).
378 Kerr, J. B. *et al.* DNA damage-induced primordial follicle oocyte apoptosis and loss of fertility require TAp63-mediated induction of Puma and Noxa. *Mol Cell* **48**, 343-352, doi:10.1016/j.molcel.2012.08.017 (2012).
379 Dotsch, V., Bernassola, F., Coutandin, D., Candi, E. & Melino, G. p63 and p73, the ancestors of p53. *Cold Spring Harb Perspect Biol* **2**, a004887, doi:10.1101/cshperspect.a004887 (2010).
380 Sakuma, S. *et al.* Inhibition of Nuclear Pore Complex Formation Selectively Induces Cancer Cell Death. *Cancer Discov*, doi:10.1158/2159-8290.CD-20-0581 (2020).
381 D'Angelo, M. A., Raices, M., Panowski, S. H. & Hetzer, M. W. Age-dependent deterioration of nuclear pore complexes causes a loss of nuclear integrity in postmitotic cells. *Cell* **136**, 284-295, doi:10.1016/j.cell.2008.11.037 (2009).
382 Toyama, B. H. *et al.* Identification of long-lived proteins reveals exceptional stability of essential cellular structures. *Cell* **154**, 971-982, doi:10.1016/j.cell.2013.07.037 (2013).
383 Beck, M., Schirmacher, P. & Singer, S. Alterations of the nuclear transport system in hepatocellular carcinoma - New basis for therapeutic strategies. *J Hepatol* **67**, 1051-1061, doi:10.1016/j.jhep.2017.06.021 (2017).
384 Martinez, N., Alonso, A., Moragues, M. D., Ponton, J. & Schneider, J. The nuclear pore complex protein Nup88 is overexpressed in tumor cells. *Cancer Res* **59**, 5408-5411 (1999).

385 Agudo, D. *et al.* Nup88 mRNA overexpression is associated with high aggressiveness of breast cancer. *International journal of cancer. Journal international du cancer* **109**, 717-720, doi:10.1002/ijc.20034 (2004).
386 Ocana, A. & Pandiella, A. Proteolysis targeting chimeras (PROTACs) in cancer therapy. *Journal of experimental & clinical cancer research : CR* **39**, 189, doi:10.1186/s13046-020-01672-1 (2020).
387 Zeng, S. *et al.* Proteolysis targeting chimera (PROTAC) in drug discovery paradigm: Recent progress and future challenges. *Eur J Med Chem* **210**, 112981, doi:10.1016/j.ejmech.2020.112981 (2021).
388 Hall, S. L. & Padgett, R. A. Requirement of U12 snRNA for in vivo splicing of a minor class of eukaryotic nuclear pre-mRNA introns. *Science* **271**, 1716-1718, doi:10.1126/science.271.5256.1716 (1996).
389 Tarn, W. Y. & Steitz, J. A. A novel spliceosome containing U11, U12, and U5 snRNPs excises a minor class (AT-AC) intron in vitro. *Cell* **84**, 801-811, doi:10.1016/s0092-8674(00)81057-0 (1996).
390 Doggett, K. *et al.* Early developmental arrest and impaired gastrointestinal homeostasis in U12-dependent splicing-defective Rnpc3-deficient mice. *RNA* **24**, 1856-1870, doi:10.1261/rna.068221.118 (2018).
391 Park, S. J., Jung, H. J., Nguyen Dinh, S. & Kang, H. Structural features important for the U12 snRNA binding and minor spliceosome assembly of Arabidopsis U11/U12-small nuclear ribonucleoproteins. *RNA Biol* **13**, 670-679, doi:10.1080/15476286.2016.1191736 (2016).
392 Jung, H. J. & Kang, H. The Arabidopsis U11/U12-65K is an indispensible component of minor spliceosome and plays a crucial role in U12 intron splicing and plant development. *Plant J* **78**, 799-810, doi:10.1111/tpj.12498 (2014).
393 Berget, S. M., Moore, C. & Sharp, P. A. Spliced segments at the 5' terminus of adenovirus 2 late mRNA. *Proc Natl Acad Sci U S A* **74**, 3171-3175, doi:10.1073/pnas.74.8.3171 (1977).
394 Chow, L. T., Gelinas, R. E., Broker, T. R. & Roberts, R. J. An amazing sequence arrangement at the 5' ends of adenovirus 2 messenger RNA. *Cell* **12**, 1-8, doi:10.1016/0092-8674(77)90180-5 (1977).
395 Roy, S. W. & Gilbert, W. The evolution of spliceosomal introns: patterns, puzzles and progress. *Nat Rev Genet* **7**, 211-221, doi:10.1038/nrg1807 (2006).
396 Sharp, P. A. & Burge, C. B. Classification of introns: U2-type or U12-type. *Cell* **91**, 875-879, doi:10.1016/s0092-8674(00)80479-1 (1997).
397 Jackson, I. J. A reappraisal of non-consensus mRNA splice sites. *Nucleic Acids Res* **19**, 3795-3798, doi:10.1093/nar/19.14.3795 (1991).
398 Brent, M. R. & Guigo, R. Recent advances in gene structure prediction. *Curr Opin Struct Biol* **14**, 264-272, doi:10.1016/j.sbi.2004.05.007 (2004).
399 Burge, C. B., Padgett, R. A. & Sharp, P. A. Evolutionary fates and origins of U12-type introns. *Mol Cell* **2**, 773-785, doi:10.1016/s1097-2765(00)80292-0 (1998).
400 Padgett, R. A., Konarska, M. M., Grabowski, P. J., Hardy, S. F. & Sharp, P. A. Lariat RNA's as intermediates and products in the splicing of messenger RNA precursors. *Science* **225**, 898-903, doi:10.1126/science.6206566 (1984).
401 Domdey, H. *et al.* Lariat structures are in vivo intermediates in yeast pre-mRNA splicing. *Cell* **39**, 611-621, doi:10.1016/0092-8674(84)90468-9 (1984).

402 Ruskin, B., Krainer, A. R., Maniatis, T. & Green, M. R. Excision of an intact intron as a novel lariat structure during pre-mRNA splicing in vitro. *Cell* **38**, 317-331, doi:10.1016/0092-8674(84)90553-1 (1984).
403 Rodriguez, J. R., Pikielny, C. W. & Rosbash, M. In vivo characterization of yeast mRNA processing intermediates. *Cell* **39**, 603-610, doi:10.1016/0092-8674(84)90467-7 (1984).
404 Will, C. L. & Luhrmann, R. Spliceosome structure and function. *Cold Spring Harb Perspect Biol* **3**, doi:10.1101/cshperspect.a003707 (2011).
405 Shi, Y. Mechanistic insights into precursor messenger RNA splicing by the spliceosome. *Nat Rev Mol Cell Biol* **18**, 655-670, doi:10.1038/nrm.2017.86 (2017).
406 Wahl, M. C., Will, C. L. & Luhrmann, R. The spliceosome: design principles of a dynamic RNP machine. *Cell* **136**, 701-718, doi:10.1016/j.cell.2009.02.009 (2009).
407 Kastner, B., Will, C. L., Stark, H. & Luhrmann, R. Structural Insights into Nuclear pre-mRNA Splicing in Higher Eukaryotes. *Cold Spring Harb Perspect Biol* **11**, doi:10.1101/cshperspect.a032417 (2019).
408 Mount, S. M., Pettersson, I., Hinterberger, M., Karmas, A. & Steitz, J. A. The U1 small nuclear RNA-protein complex selectively binds a 5' splice site in vitro. *Cell* **33**, 509-518, doi:10.1016/0092-8674(83)90432-4 (1983).
409 Rogers, J. & Wall, R. A mechanism for RNA splicing. *Proc Natl Acad Sci U S A* **77**, 1877-1879, doi:10.1073/pnas.77.4.1877 (1980).
410 Black, D. L., Chabot, B. & Steitz, J. A. U2 as well as U1 small nuclear ribonucleoproteins are involved in premessenger RNA splicing. *Cell* **42**, 737-750, doi:10.1016/0092-8674(85)90270-3 (1985).
411 Frilander, M. J. & Steitz, J. A. Initial recognition of U12-dependent introns requires both U11/5' splice-site and U12/branchpoint interactions. *Genes Dev* **13**, 851-863, doi:10.1101/gad.13.7.851 (1999).
412 Turunen, J. J., Niemela, E. H., Verma, B. & Frilander, M. J. The significant other: splicing by the minor spliceosome. *Wiley Interdiscip Rev RNA* **4**, 61-76, doi:10.1002/wrna.1141 (2013).
413 Will, C. L. & Luhrmann, R. Splicing of a rare class of introns by the U12-dependent spliceosome. *Biol Chem* **386**, 713-724, doi:10.1515/BC.2005.084 (2005).
414 Will, C. L. *et al.* The human 18S U11/U12 snRNP contains a set of novel proteins not found in the U2-dependent spliceosome. *RNA* **10**, 929-941, doi:10.1261/rna.7320604 (2004).
415 Will, C. L., Schneider, C., Reed, R. & Luhrmann, R. Identification of both shared and distinct proteins in the major and minor spliceosomes. *Science* **284**, 2003-2005, doi:10.1126/science.284.5422.2003 (1999).
416 Turunen, J. J., Will, C. L., Grote, M., Luhrmann, R. & Frilander, M. J. The U11-48K protein contacts the 5' splice site of U12-type introns and the U11-59K protein. *Mol Cell Biol* **28**, 3548-3560, doi:10.1128/MCB.01928-07 (2008).
417 Tidow, H., Andreeva, A., Rutherford, T. J. & Fersht, A. R. Solution structure of the U11-48K CHHC zinc-finger domain that specifically binds the 5' splice site of U12-type introns. *Structure* **17**, 294-302, doi:10.1016/j.str.2008.11.013 (2009).
418 Benecke, H., Luhrmann, R. & Will, C. L. The U11/U12 snRNP 65K protein acts as a molecular bridge, binding the U12 snRNA and U11-59K protein. *EMBO J* **24**, 3057-3069, doi:10.1038/sj.emboj.7600765 (2005).

419 Bentley, D. L. Coupling mRNA processing with transcription in time and space. *Nat Rev Genet* **15**, 163-175, doi:10.1038/nrg3662 (2014).
420 Wahl, M. C. & Luhrmann, R. SnapShot: Spliceosome Dynamics I. *Cell* **161**, 1474-e1471, doi:10.1016/j.cell.2015.05.050 (2015).
421 Russell, A. G., Charette, J. M., Spencer, D. F. & Gray, M. W. An early evolutionary origin for the minor spliceosome. *Nature* **443**, 863-866, doi:10.1038/nature05228 (2006).
422 Cox, A. D., Fesik, S. W., Kimmelman, A. C., Luo, J. & Der, C. J. Drugging the undruggable RAS: Mission possible? *Nat Rev Drug Discov* **13**, 828-851, doi:10.1038/nrd4389 (2014).
423 Bonnal, S. C., Lopez-Oreja, I. & Valcarcel, J. Roles and mechanisms of alternative splicing in cancer - implications for care. *Nat Rev Clin Oncol* **17**, 457-474, doi:10.1038/s41571-020-0350-x (2020).
424 Wang, E. & Aifantis, I. RNA Splicing and Cancer. *Trends Cancer* **6**, 631-644, doi:10.1016/j.trecan.2020.04.011 (2020).
425 Lee, S. C. & Abdel-Wahab, O. Therapeutic targeting of splicing in cancer. *Nat Med* **22**, 976-986, doi:10.1038/nm.4165 (2016).
426 Yoshida, K. *et al.* Frequent pathway mutations of splicing machinery in myelodysplasia. *Nature* **478**, 64-69, doi:10.1038/nature10496 (2011).
427 Wang, L. *et al.* SF3B1 and other novel cancer genes in chronic lymphocytic leukemia. *N Engl J Med* **365**, 2497-2506, doi:10.1056/NEJMoa1109016 (2011).
428 Obeng, E. A. *et al.* Physiologic Expression of Sf3b1(K700E) Causes Impaired Erythropoiesis, Aberrant Splicing, and Sensitivity to Therapeutic Spliceosome Modulation. *Cancer Cell* **30**, 404-417, doi:10.1016/j.ccell.2016.08.006 (2016).
429 Lee, S. C. *et al.* Synthetic Lethal and Convergent Biological Effects of Cancer-Associated Spliceosomal Gene Mutations. *Cancer Cell* **34**, 225-241 e228, doi:10.1016/j.ccell.2018.07.003 (2018).
430 Fraile, J. M. *et al.* USP39 Deubiquitinase Is Essential for KRAS Oncogene-driven Cancer. *J Biol Chem* **292**, 4164-4175, doi:10.1074/jbc.M116.762757 (2017).
431 Seiler, M. *et al.* H3B-8800, an orally available small-molecule splicing modulator, induces lethality in spliceosome-mutant cancers. *Nat Med* **24**, 497-504, doi:10.1038/nm.4493 (2018).
432 Merico, D. *et al.* Compound heterozygous mutations in the noncoding RNU4ATAC cause Roifman Syndrome by disrupting minor intron splicing. *Nat Commun* **6**, 8718, doi:10.1038/ncomms9718 (2015).
433 Edery, P. *et al.* Association of TALS developmental disorder with defect in minor splicing component U4atac snRNA. *Science* **332**, 240-243, doi:10.1126/science.1202205 (2011).
434 He, H. *et al.* Mutations in U4atac snRNA, a component of the minor spliceosome, in the developmental disorder MOPD I. *Science* **332**, 238-240, doi:10.1126/science.1200587 (2011).
435 Farach, L. S. *et al.* The expanding phenotype of RNU4ATAC pathogenic variants to Lowry Wood syndrome. *Am J Med Genet A* **176**, 465-469, doi:10.1002/ajmg.a.38581 (2018).
436 Elsaid, M. F. *et al.* Mutation in noncoding RNA RNU12 causes early onset cerebellar ataxia. *Ann Neurol* **81**, 68-78, doi:10.1002/ana.24826 (2017).

437 Olthof, A. M., Rasmussen, J. S., Campeau, P. M. & Kanadia, R. N. Disrupted minor intron splicing is prevalent in Mendelian disorders. *Mol Genet Genomic Med* **8**, e1374, doi:10.1002/mgg3.1374 (2020).
438 Argente, J. *et al.* Defective minor spliceosome mRNA processing results in isolated familial growth hormone deficiency. *EMBO Mol Med* **6**, 299-306, doi:10.1002/emmm.201303573 (2014).
439 Martos-Moreno, G. A. *et al.* Response to growth hormone in patients with RNPC3 mutations. *EMBO Mol Med* **10**, doi:10.15252/emmm.201809143 (2018).
440 Consortium, I. T. P.-C. A. o. W. G. Pan-cancer analysis of whole genomes. *Nature* **578**, 82-93, doi:10.1038/s41586-020-1969-6 (2020).
441 Pon, J. R. & Marra, M. A. Driver and passenger mutations in cancer. *Annual review of pathology* **10**, 25-50, doi:10.1146/annurev-pathol-012414-040312 (2015).
442 McDonald, E. R., 3rd *et al.* Project DRIVE: A Compendium of Cancer Dependencies and Synthetic Lethal Relationships Uncovered by Large-Scale, Deep RNAi Screening. *Cell* **170**, 577-592 e510, doi:10.1016/j.cell.2017.07.005 (2017).
443 Tsherniak, A. *et al.* Defining a Cancer Dependency Map. *Cell* **170**, 564-576 e516, doi:10.1016/j.cell.2017.06.010 (2017).
444 Behan, F. M. *et al.* Prioritization of cancer therapeutic targets using CRISPR-Cas9 screens. *Nature* **568**, 511-516, doi:10.1038/s41586-019-1103-9 (2019).
445 Mavrakis, K. J. *et al.* Disordered methionine metabolism in MTAP/CDKN2A-deleted cancers leads to dependence on PRMT5. *Science* **351**, 1208-1213, doi:10.1126/science.aad5944 (2016).
446 Kryukov, G. V. *et al.* MTAP deletion confers enhanced dependency on the PRMT5 arginine methyltransferase in cancer cells. *Science* **351**, 1214-1218, doi:10.1126/science.aad5214 (2016).
447 Marjon, K. *et al.* MTAP Deletions in Cancer Create Vulnerability to Targeting of the MAT2A/PRMT5/RIOK1 Axis. *Cell Rep* **15**, 574-587, doi:10.1016/j.celrep.2016.03.043 (2016).
448 Muller, F. L., Aquilanti, E. A. & DePinho, R. A. Collateral Lethality: A new therapeutic strategy in oncology. *Trends Cancer* **1**, 161-173, doi:10.1016/j.trecan.2015.10.002 (2015).
449 Chan-Penebre, E. *et al.* A selective inhibitor of PRMT5 with in vivo and in vitro potency in MCL models. *Nat Chem Biol* **11**, 432-437, doi:10.1038/nchembio.1810 (2015).
450 Huang, A., Garraway, L. A., Ashworth, A. & Weber, B. Synthetic lethality as an engine for cancer drug target discovery. *Nat Rev Drug Discov* **19**, 23-38, doi:10.1038/s41573-019-0046-z (2020).
451 Letrado, P., de Miguel, I., Lamberto, I., Diez-Martinez, R. & Oyarzabal, J. Zebrafish: Speeding Up the Cancer Drug Discovery Process. *Cancer Res* **78**, 6048-6058, doi:10.1158/0008-5472.CAN-18-1029 (2018).
452 Parng, C., Seng, W. L., Semino, C. & McGrath, P. Zebrafish: a preclinical model for drug screening. *Assay Drug Dev Technol* **1**, 41-48, doi:10.1089/154065802761001293 (2002).
453 Kari, G., Rodeck, U. & Dicker, A. P. Zebrafish: an emerging model system for human disease and drug discovery. *Clin Pharmacol Ther* **82**, 70-80, doi:10.1038/sj.clpt.6100223 (2007).

454 Dang, M., Henderson, R. E., Garraway, L. A. & Zon, L. I. Long-term drug administration in the adult zebrafish using oral gavage for cancer preclinical studies. *Dis Model Mech* **9**, 811-820, doi:10.1242/dmm.024166 (2016).
455 Samaee, S. M., Seyedin, S. & Varga, Z. M. An Affordable Intraperitoneal Injection Setup for Juvenile and Adult Zebrafish. *Zebrafish* **14**, 77-79, doi:10.1089/zeb.2016.1322 (2017).
456 Murphey, R. D., Stern, H. M., Straub, C. T. & Zon, L. I. A chemical genetic screen for cell cycle inhibitors in zebrafish embryos. *Chemical biology & drug design* **68**, 213-219, doi:10.1111/j.1747-0285.2006.00439.x (2006).
457 Yeh, J. R. *et al.* Discovering chemical modifiers of oncogene-regulated hematopoietic differentiation. *Nat Chem Biol* **5**, 236-243, doi:10.1038/nchembio.147 (2009).
458 Ridges, S. *et al.* Zebrafish screen identifies novel compound with selective toxicity against leukemia. *Blood* **119**, 5621-5631, doi:10.1182/blood-2011-12-398818 (2012).
459 Santoro, M. M. Antiangiogenic cancer drug using the zebrafish model. *Arterioscler Thromb Vasc Biol* **34**, 1846-1853, doi:10.1161/ATVBAHA.114.303221 (2014).
460 Wang, C. *et al.* Rosuvastatin, identified from a zebrafish chemical genetic screen for antiangiogenic compounds, suppresses the growth of prostate cancer. *Eur Urol* **58**, 418-426, doi:10.1016/j.eururo.2010.05.024 (2010).
461 Zhao, C. *et al.* A novel xenograft model in zebrafish for high-resolution investigating dynamics of neovascularization in tumors. *PLoS One* **6**, e21768, doi:10.1371/journal.pone.0021768 (2011).
462 Veinotte, C. J., Dellaire, G. & Berman, J. N. Hooking the big one: the potential of zebrafish xenotransplantation to reform cancer drug screening in the genomic era. *Dis Model Mech* **7**, 745-754, doi:10.1242/dmm.015784 (2014).
463 Rebelo de Almeida, C. *et al.* Zebrafish xenografts as a fast screening platform for bevacizumab cancer therapy. *Commun Biol* **3**, 299, doi:10.1038/s42003-020-1015-0 (2020).
464 Zhao, Y. & Adjei, A. A. The clinical development of MEK inhibitors. *Nat Rev Clin Oncol* **11**, 385-400, doi:10.1038/nrclinonc.2014.83 (2014).
465 Balmanno, K. & Cook, S. J. Tumour cell survival signalling by the ERK1/2 pathway. *Cell Death Differ* **16**, 368-377, doi:10.1038/cdd.2008.148 (2009).
466 Lavoie, H., Gagnon, J. & Therrien, M. ERK signalling: a master regulator of cell behaviour, life and fate. *Nat Rev Mol Cell Biol* **21**, 607-632, doi:10.1038/s41580-020-0255-7 (2020).
467 Hauschild, A. *et al.* Dabrafenib in BRAF-mutated metastatic melanoma: a multicentre, open-label, phase 3 randomised controlled trial. *Lancet* **380**, 358-365, doi:10.1016/S0140-6736(12)60868-X (2012).
468 Chapman, P. B. *et al.* Improved survival with vemurafenib in melanoma with BRAF V600E mutation. *N Engl J Med* **364**, 2507-2516, doi:10.1056/NEJMoa1103782 (2011).
469 Bollag, G. *et al.* Clinical efficacy of a RAF inhibitor needs broad target blockade in BRAF-mutant melanoma. *Nature* **467**, 596-599, doi:10.1038/nature09454 (2010).
470 Roskoski, R., Jr. ERK1/2 MAP kinases: structure, function, and regulation. *Pharmacol Res* **66**, 105-143, doi:10.1016/j.phrs.2012.04.005 (2012).
471 Yoon, S. & Seger, R. The extracellular signal-regulated kinase: multiple substrates regulate diverse cellular functions. *Growth Factors* **24**, 21-44, doi:10.1080/02699050500284218 (2006).

472 von Kriegsheim, A. *et al.* Cell fate decisions are specified by the dynamic ERK interactome. *Nat Cell Biol* **11**, 1458-1464, doi:10.1038/ncb1994 (2009).
473 Alessi, D. R., Cuenda, A., Cohen, P., Dudley, D. T. & Saltiel, A. R. PD 098059 is a specific inhibitor of the activation of mitogen-activated protein kinase kinase in vitro and in vivo. *J Biol Chem* **270**, 27489-27494, doi:10.1074/jbc.270.46.27489 (1995).
474 Flaherty, K. T. *et al.* Improved survival with MEK inhibition in BRAF-mutated melanoma. *N Engl J Med* **367**, 107-114, doi:10.1056/NEJMoa1203421 (2012).
475 Ascierto, P. A. *et al.* MEK162 for patients with advanced melanoma harbouring NRAS or Val600 BRAF mutations: a non-randomised, open-label phase 2 study. *Lancet Oncol* **14**, 249-256, doi:10.1016/S1470-2045(13)70024-X (2013).
476 Shahjehan, F., Kamatham, S., Chandrasekharan, C. & Kasi, P. M. Binimetinib, encorafenib and cetuximab (BEACON Trial) combination therapy for patients with BRAF V600E-mutant metastatic colorectal cancer. *Drugs Today (Barc)* **55**, 683-693, doi:10.1358/dot.2019.55.11.3035584 (2019).
477 Caunt, C. J., Sale, M. J., Smith, P. D. & Cook, S. J. MEK1 and MEK2 inhibitors and cancer therapy: the long and winding road. *Nat Rev Cancer* **15**, 577-592, doi:10.1038/nrc4000 (2015).
478 Azmi, A. S., Uddin, M. H. & Mohammad, R. M. The nuclear export protein XPO1 - from biology to targeted therapy. *Nat Rev Clin Oncol*, doi:10.1038/s41571-020-00442-4 (2020).
479 Jans, D. A., Martin, A. J. & Wagstaff, K. M. Inhibitors of nuclear transport. *Curr Opin Cell Biol* **58**, 50-60, doi:10.1016/j.ceb.2019.01.001 (2019).
480 Xu, D. *et al.* LocNES: a computational tool for locating classical NESs in CRM1 cargo proteins. *Bioinformatics* **31**, 1357-1365, doi:10.1093/bioinformatics/btu826 (2015).
481 Kohler, A. & Hurt, E. Exporting RNA from the nucleus to the cytoplasm. *Nat Rev Mol Cell Biol* **8**, 761-773, doi:10.1038/nrm2255 (2007).
482 Hutten, S. & Kehlenbach, R. H. CRM1-mediated nuclear export: to the pore and beyond. *Trends Cell Biol* **17**, 193-201, doi:10.1016/j.tcb.2007.02.003 (2007).
483 Gravina, G. L. *et al.* Nucleo-cytoplasmic transport as a therapeutic target of cancer. *J Hematol Oncol* **7**, 85, doi:10.1186/s13045-014-0085-1 (2014).
484 Tan, D. S., Bedard, P. L., Kuruvilla, J., Siu, L. L. & Razak, A. R. Promising SINEs for embargoing nuclear-cytoplasmic export as an anticancer strategy. *Cancer Discov* **4**, 527-537, doi:10.1158/2159-8290.CD-13-1005 (2014).
485 Saulino, D. M., Younes, P. S., Bailey, J. M. & Younes, M. CRM1/XPO1 expression in pancreatic adenocarcinoma correlates with survivin expression and the proliferative activity. *Oncotarget* **9**, 21289-21295, doi:10.18632/oncotarget.25088 (2018).
486 Subhash, V. V. *et al.* Anti-tumor efficacy of Selinexor (KPT-330) in gastric cancer is dependent on nuclear accumulation of p53 tumor suppressor. *Sci Rep* **8**, 12248, doi:10.1038/s41598-018-30686-1 (2018).
487 Gravina, G. L. *et al.* KPT-330, a potent and selective exportin-1 (XPO-1) inhibitor, shows antitumor effects modulating the expression of cyclin D1 and survivin [corrected] in prostate cancer models. *BMC Cancer* **15**, 941, doi:10.1186/s12885-015-1936-z (2015).
488 Aladhraei, M., Kassem Al-Thobhani, A., Poungvarin, N. & Suwannalert, P. Association of XPO1 Overexpression with NF-kappaB and Ki67 in Colorectal Cancer. *Asian Pac J Cancer Prev* **20**, 3747-3754, doi:10.31557/APJCP.2019.20.12.3747 (2019).

489 Nishi, K. *et al.* Leptomycin B targets a regulatory cascade of crm1, a fission yeast nuclear protein, involved in control of higher order chromosome structure and gene expression. *J Biol Chem* **269**, 6320-6324 (1994).
490 Kudo, N. *et al.* Leptomycin B inactivates CRM1/exportin 1 by covalent modification at a cysteine residue in the central conserved region. *Proc Natl Acad Sci U S A* **96**, 9112-9117, doi:10.1073/pnas.96.16.9112 (1999).
491 Sun, Q. *et al.* Nuclear export inhibition through covalent conjugation and hydrolysis of Leptomycin B by CRM1. *Proc Natl Acad Sci U S A* **110**, 1303-1308, doi:10.1073/pnas.1217203110 (2013).
492 Parikh, K., Cang, S., Sekhri, A. & Liu, D. Selective inhibitors of nuclear export (SINE)--a novel class of anti-cancer agents. *J Hematol Oncol* **7**, 78, doi:10.1186/s13045-014-0078-0 (2014).
493 Ranganathan, P. *et al.* Preclinical activity of a novel CRM1 inhibitor in acute myeloid leukemia. *Blood* **120**, 1765-1773, doi:10.1182/blood-2012-04-423160 (2012).
494 Zhang, K. *et al.* Novel selective inhibitors of nuclear export CRM1 antagonists for therapy in mantle cell lymphoma. *Exp Hematol* **41**, 67-78 e64, doi:10.1016/j.exphem.2012.09.002 (2013).
495 Etchin, J. *et al.* Activity of a selective inhibitor of nuclear export, selinexor (KPT-330), against AML-initiating cells engrafted into immunosuppressed NSG mice. *Leukemia* **30**, 190-199, doi:10.1038/leu.2015.194 (2016).
496 Lapalombella, R. *et al.* Selective inhibitors of nuclear export show that CRM1/XPO1 is a target in chronic lymphocytic leukemia. *Blood* **120**, 4621-4634, doi:10.1182/blood-2012-05-429506 (2012).
497 Etchin, J. *et al.* Antileukemic activity of nuclear export inhibitors that spare normal hematopoietic cells. *Leukemia* **27**, 66-74, doi:10.1038/leu.2012.219 (2013).
498 Kim, J. *et al.* XPO1-dependent nuclear export is a druggable vulnerability in KRAS-mutant lung cancer. *Nature* **538**, 114-117, doi:10.1038/nature19771 (2016).
499 Zheng, Y. *et al.* KPT-330 inhibitor of XPO1-mediated nuclear export has anti-proliferative activity in hepatocellular carcinoma. *Cancer Chemother Pharmacol* **74**, 487-495, doi:10.1007/s00280-014-2495-8 (2014).
500 Gu, X. *et al.* Leukemogenic nucleophosmin mutation disrupts the transcription factor hub that regulates granulomonocytic fates. *J Clin Invest* **128**, 4260-4279, doi:10.1172/JCI97117 (2018).
501 Martin, A. P. *et al.* STK38 kinase acts as XPO1 gatekeeper regulating the nuclear export of autophagy proteins and other cargoes. *EMBO Rep* **20**, e48150, doi:10.15252/embr.201948150 (2019).
502 Blanc, R. S. & Richard, S. Arginine Methylation: The Coming of Age. *Mol Cell* **65**, 8-24, doi:10.1016/j.molcel.2016.11.003 (2017).
503 Bedford, M. T. & Clarke, S. G. Protein arginine methylation in mammals: who, what, and why. *Mol Cell* **33**, 1-13, doi:10.1016/j.molcel.2008.12.013 (2009).
504 Yang, Y. & Bedford, M. T. Protein arginine methyltransferases and cancer. *Nat Rev Cancer* **13**, 37-50, doi:10.1038/nrc3409 (2013).
505 Antonysamy, S. *et al.* Crystal structure of the human PRMT5:MEP50 complex. *Proc Natl Acad Sci U S A* **109**, 17960-17965, doi:10.1073/pnas.1209814109 (2012).
506 Stopa, N., Krebs, J. E. & Shechter, D. The PRMT5 arginine methyltransferase: many roles in development, cancer and beyond. *Cell Mol Life Sci* **72**, 2041-2059, doi:10.1007/s00018-015-1847-9 (2015).

507 Tee, W. W. *et al.* Prmt5 is essential for early mouse development and acts in the cytoplasm to maintain ES cell pluripotency. *Genes Dev* **24**, 2772-2777, doi:10.1101/gad.606110 (2010).
508 Bezzi, M. *et al.* Regulation of constitutive and alternative splicing by PRMT5 reveals a role for Mdm4 pre-mRNA in sensing defects in the spliceosomal machinery. *Genes Dev* **27**, 1903-1916, doi:10.1101/gad.219899.113 (2013).
509 Tan, D. Q. *et al.* PRMT5 Modulates Splicing for Genome Integrity and Preserves Proteostasis of Hematopoietic Stem Cells. *Cell Rep* **26**, 2316-2328 e2316, doi:10.1016/j.celrep.2019.02.001 (2019).
510 Wei, H., Mundade, R., Lange, K. C. & Lu, T. Protein arginine methylation of non-histone proteins and its role in diseases. *Cell Cycle* **13**, 32-41, doi:10.4161/cc.27353 (2014).
511 Chung, J. *et al.* Protein arginine methyltransferase 5 (PRMT5) inhibition induces lymphoma cell death through reactivation of the retinoblastoma tumor suppressor pathway and polycomb repressor complex 2 (PRC2) silencing. *J Biol Chem* **288**, 35534-35547, doi:10.1074/jbc.M113.510669 (2013).
512 Wang, L., Pal, S. & Sif, S. Protein arginine methyltransferase 5 suppresses the transcription of the RB family of tumor suppressors in leukemia and lymphoma cells. *Mol Cell Biol* **28**, 6262-6277, doi:10.1128/MCB.00923-08 (2008).
513 Wei, T. Y. *et al.* Protein arginine methyltransferase 5 is a potential oncoprotein that upregulates G1 cyclins/cyclin-dependent kinases and the phosphoinositide 3-kinase/AKT signaling cascade. *Cancer Sci* **103**, 1640-1650, doi:10.1111/j.1349-7006.2012.02367.x (2012).
514 Powers, M. A., Fay, M. M., Factor, R. E., Welm, A. L. & Ullman, K. S. Protein arginine methyltransferase 5 accelerates tumor growth by arginine methylation of the tumor suppressor programmed cell death 4. *Cancer Res* **71**, 5579-5587, doi:10.1158/0008-5472.CAN-11-0458 (2011).
515 Shimizu, D. *et al.* The protein arginine methyltransferase 5 promotes malignant phenotype of hepatocellular carcinoma cells and is associated with adverse patient outcomes after curative hepatectomy. *Int J Oncol* **50**, 381-386, doi:10.3892/ijo.2017.3833 (2017).
516 Zhang, B. *et al.* Targeting protein arginine methyltransferase 5 inhibits human hepatocellular carcinoma growth via the downregulation of beta-catenin. *J Transl Med* **13**, 349, doi:10.1186/s12967-015-0721-8 (2015).
517 Vinet, M. *et al.* Protein arginine methyltransferase 5: A novel therapeutic target for triple-negative breast cancers. *Cancer Med* **8**, 2414-2428, doi:10.1002/cam4.2114 (2019).
518 Holmes, B. *et al.* The protein arginine methyltransferase PRMT5 confers therapeutic resistance to mTOR inhibition in glioblastoma. *J Neurooncol* **145**, 11-22, doi:10.1007/s11060-019-03274-0 (2019).
519 Lee, K. K. & Workman, J. L. Histone acetyltransferase complexes: one size doesn't fit all. *Nat Rev Mol Cell Biol* **8**, 284-295, doi:10.1038/nrm2145 (2007).
520 Doyon, Y. *et al.* ING tumor suppressor proteins are critical regulators of chromatin acetylation required for genome expression and perpetuation. *Mol Cell* **21**, 51-64, doi:10.1016/j.molcel.2005.12.007 (2006).

521 Borrow, J. *et al.* The translocation t(8;16)(p11;p13) of acute myeloid leukaemia fuses a putative acetyltransferase to the CREB-binding protein. *Nat Genet* **14**, 33-41, doi:10.1038/ng0996-33 (1996).
522 Champagne, N. *et al.* Identification of a human histone acetyltransferase related to monocytic leukemia zinc finger protein. *J Biol Chem* **274**, 28528-28536, doi:10.1074/jbc.274.40.28528 (1999).
523 Huang, F., Abmayr, S. M. & Workman, J. L. Regulation of KAT6 Acetyltransferases and Their Roles in Cell Cycle Progression, Stem Cell Maintenance, and Human Disease. *Mol Cell Biol* **36**, 1900-1907, doi:10.1128/MCB.00055-16 (2016).
524 Katsumoto, T. *et al.* MOZ is essential for maintenance of hematopoietic stem cells. *Genes Dev* **20**, 1321-1330, doi:10.1101/gad.1393106 (2006).
525 Thomas, T. *et al.* Monocytic leukemia zinc finger protein is essential for the development of long-term reconstituting hematopoietic stem cells. *Genes Dev* **20**, 1175-1186, doi:10.1101/gad.1382606 (2006).
526 Sheikh, B. N. *et al.* MOZ (KAT6A) is essential for the maintenance of classically defined adult hematopoietic stem cells. *Blood* **128**, 2307-2318, doi:10.1182/blood-2015-10-676072 (2016).
527 Sheikh, B. N. *et al.* MOZ (MYST3, KAT6A) inhibits senescence via the INK4A-ARF pathway. *Oncogene* **34**, 5807-5820, doi:10.1038/onc.2015.33 (2015).
528 Perez-Campo, F. M. *et al.* MOZ-mediated repression of p16(INK) (4) (a) is critical for the self-renewal of neural and hematopoietic stem cells. *Stem Cells* **32**, 1591-1601, doi:10.1002/stem.1606 (2014).
529 Sheikh, B. N. *et al.* MOZ regulates B-cell progenitors and, consequently, Moz haploinsufficiency dramatically retards MYC-induced lymphoma development. *Blood* **125**, 1910-1921, doi:10.1182/blood-2014-08-594655 (2015).
530 Olthof, A. M., Hyatt, K. C. & Kanadia, R. N. Minor intron splicing revisited: identification of new minor intron-containing genes and tissue-dependent retention and alternative splicing of minor introns. *BMC Genomics* **20**, 686, doi:10.1186/s12864-019-6046-x (2019).
531 Olthof, A. M. *et al.* Disruption of exon-bridging interactions between the minor and major spliceosomes results in alternative splicing around minor introns. *Nucleic Acids Res*, doi:10.1093/nar/gkab118 (2021).
532 Marine, J. C., Dawson, S. J. & Dawson, M. A. Non-genetic mechanisms of therapeutic resistance in cancer. *Nat Rev Cancer* **20**, 743-756, doi:10.1038/s41568-020-00302-4 (2020).
533 Vasan, N., Baselga, J. & Hyman, D. M. A view on drug resistance in cancer. *Nature* **575**, 299-309, doi:10.1038/s41586-019-1730-1 (2019).
534 Holohan, C., Van Schaeybroeck, S., Longley, D. B. & Johnston, P. G. Cancer drug resistance: an evolving paradigm. *Nat Rev Cancer* **13**, 714-726, doi:10.1038/nrc3599 (2013).
535 DeVita, V. T., Jr. & Chu, E. A history of cancer chemotherapy. *Cancer Res* **68**, 8643-8653, doi:10.1158/0008-5472.CAN-07-6611 (2008).
536 Frei, E., 3rd *et al.* The effectiveness of combinations of antileukemic agents in inducing and maintaining remission in children with acute leukemia. *Blood* **26**, 642-656 (1965).

537 Devita, V. T., Jr., Serpick, A. A. & Carbone, P. P. Combination chemotherapy in the treatment of advanced Hodgkin's disease. *Ann Intern Med* **73**, 881-895, doi:10.7326/0003-4819-73-6-881 (1970).
538 Moxley, J. H., 3rd, De Vita, V. T., Brace, K. & Frei, E., 3rd. Intensive combination chemotherapy and X-irradiation in Hodgkin's disease. *Cancer Res* **27**, 1258-1263 (1967).
539 Baselga, J. *et al.* Pertuzumab plus trastuzumab plus docetaxel for metastatic breast cancer. *N Engl J Med* **366**, 109-119, doi:10.1056/NEJMoa1113216 (2012).
540 Sachamitr, P. *et al.* PRMT5 inhibition disrupts splicing and stemness in glioblastoma. *Nat Commun* **12**, 979, doi:10.1038/s41467-021-21204-5 (2021).
541 Radzisheuskaya, A. *et al.* PRMT5 methylome profiling uncovers a direct link to splicing regulation in acute myeloid leukemia. *Nat Struct Mol Biol* **26**, 999-1012, doi:10.1038/s41594-019-0313-z (2019).
542 Turner, J. G. *et al.* Treatment of acquired drug resistance in multiple myeloma by combination therapy with XPO1 and topoisomerase II inhibitors. *J Hematol Oncol* **9**, 73, doi:10.1186/s13045-016-0304-z (2016).
543 Finn, R. S. *et al.* Atezolizumab plus Bevacizumab in Unresectable Hepatocellular Carcinoma. *N Engl J Med* **382**, 1894-1905, doi:10.1056/NEJMoa1915745 (2020).
544 Kuhnert, A., Vogs, C., Altenburger, R. & Kuster, E. The internal concentration of organic substances in fish embryos--a toxicokinetic approach. *Environ Toxicol Chem* **32**, 1819-1827, doi:10.1002/etc.2239 (2013).
545 Kantae, V. *et al.* Pharmacokinetic Modeling of Paracetamol Uptake and Clearance in Zebrafish Larvae: Expanding the Allometric Scale in Vertebrates with Five Orders of Magnitude. *Zebrafish* **13**, 504-510, doi:10.1089/zeb.2016.1313 (2016).
546 Usai, A. *et al.* A Model of a Zebrafish Avatar for Co-Clinical Trials. *Cancers (Basel)* **12**, doi:10.3390/cancers12030677 (2020).
547 Crews, C. M. Targeting the undruggable proteome: the small molecules of my dreams. *Chem Biol* **17**, 551-555, doi:10.1016/j.chembiol.2010.05.011 (2010).
548 Santos, R. *et al.* A comprehensive map of molecular drug targets. *Nat Rev Drug Discov* **16**, 19-34, doi:10.1038/nrd.2016.230 (2017).
549 Warner, K. D., Hajdin, C. E. & Weeks, K. M. Principles for targeting RNA with drug-like small molecules. *Nat Rev Drug Discov* **17**, 547-558, doi:10.1038/nrd.2018.93 (2018).
550 Kole, R., Krainer, A. R. & Altman, S. RNA therapeutics: beyond RNA interference and antisense oligonucleotides. *Nat Rev Drug Discov* **11**, 125-140, doi:10.1038/nrd3625 (2012).
551 Bennett, C. F. & Swayze, E. E. RNA targeting therapeutics: molecular mechanisms of antisense oligonucleotides as a therapeutic platform. *Annu Rev Pharmacol Toxicol* **50**, 259-293, doi:10.1146/annurev.pharmtox.010909.105654 (2010).
552 Crooke, S. T., Baker, B. F., Crooke, R. M. & Liang, X. H. Antisense technology: an overview and prospectus. *Nat Rev Drug Discov*, doi:10.1038/s41573-021-00162-z (2021).
553 Disney, M. D. Targeting RNA with Small Molecules To Capture Opportunities at the Intersection of Chemistry, Biology, and Medicine. *J Am Chem Soc* **141**, 6776-6790, doi:10.1021/jacs.8b13419 (2019).
554 Disney, M. D., Suresh, B. M., Benhamou, R. I. & Childs-Disney, J. L. Progress toward the development of the small molecule equivalent of small interfering RNA. *Curr Opin Chem Biol* **56**, 63-71, doi:10.1016/j.cbpa.2020.01.001 (2020).

555 Sheridan, C. First small-molecule drug targeting RNA gains momentum. *Nat Biotechnol* **39**, 6-8, doi:10.1038/s41587-020-00788-1 (2021).
556 Liang, X., Li, D., Leng, S. & Zhu, X. RNA-based pharmacotherapy for tumors: From bench to clinic and back. *Biomed Pharmacother* **125**, 109997, doi:10.1016/j.biopha.2020.109997 (2020).
557 Falese, J. P., Donlic, A. & Hargrove, A. E. Targeting RNA with small molecules: from fundamental principles towards the clinic. *Chem Soc Rev* **50**, 2224-2243, doi:10.1039/d0cs01261k (2021).
558 Zhang, Z., Zhang, J., Diao, L. & Han, L. Small non-coding RNAs in human cancer: function, clinical utility, and characterization. *Oncogene* **40**, 1570-1577, doi:10.1038/s41388-020-01630-3 (2021).
559 Schmitt, A. M. & Chang, H. Y. Long Noncoding RNAs in Cancer Pathways. *Cancer Cell* **29**, 452-463, doi:10.1016/j.ccell.2016.03.010 (2016).
560 Ling, H., Fabbri, M. & Calin, G. A. MicroRNAs and other non-coding RNAs as targets for anticancer drug development. *Nat Rev Drug Discov* **12**, 847-865, doi:10.1038/nrd4140 (2013).
561 Mukherjee, H. *et al.* PEARL-seq: A Photoaffinity Platform for the Analysis of Small Molecule-RNA Interactions. *ACS Chem Biol* **15**, 2374-2381, doi:10.1021/acschembio.0c00357 (2020).